# Abstract

**"Experimental and Computational Studies of Hydrogenous Materials"**

Ph.D. Thesis                        Samantha Ford                        November 2011

**Chapter 1** gives an introduction to hydrogen bonding and the existing research surrounding short strong hydrogen bonds. The concept of a reversible, temperature dependent, proton migration is introduced and a selection of systems in which this proton migration has been observed to date is discussed.

**Chapter 2** describes the synthetic techniques, characterisation methods and computational procedures used throughout this work.

**Chapter 3** describes the variable temperature structural studies on 3,5-pyridinedicarboxylic acid and its deuterated analogues. The fully deuterated analogue undergoes a non-classical, first order, isosymmetric phase transition between 150 and 200 K and DFT calculations have identified vibrational free-energy changes as the driving force for this. Although similar behaviour is exhibited by two partially deuterated isotopologues, no such transition is observed in the fully protonated form.

**Chapter 4** presents a combined spectroscopic and computational study of three isotopologues of 3,5-pyridinedicarboxylic acid. Whilst spectral observations and diffraction data are coincident for the fully deuterated form, the advantage of spectroscopy over diffraction for describing migration in the fully protonated and a partially deuterated isotopologue is demonstrated.

**Chapter 5** explores the role of vibrational coordinates in the PES governing proton dynamics in light of NMR relaxometry measurements, which reveal a non-zero dynamical rate at temperatures close to 0 K, indicative of proton tunnelling. Tunnelling is confirmed by the presence of a 2-well potential in the system, and described based on reorganisations within the structure as a whole.

**Chapter 6** reports the synthesis of further short strong hydrogen bond systems. The variable temperature structural properties for each of these compounds are discussed, and comparisons with other well known proton migration compounds are drawn.

**Chapter 7** presents the attempted synthesis of a series of new co-crystals, with components based on those of 4-methylpyridine-pentachlorophenol; the successful products were found to possess medium-length hydrogen bonds. Variable temperature diffraction studies for one of these products are discussed and show that it undergoes a phase transition on cooling resulting from slight rotations of its components.

**Chapter 8** gives the main conclusions of this thesis and outlines a number of opportunities for further work.

# Experimental and Computational Studies of Hydrogenous Materials

Samantha Jane Ford
University College
Durham University

Supervisors: Dr. Ivana Evans & Prof. Mark Johnson

A thesis submitted in partial fulfilment of the requirements for the degree of
Doctor of Philosophy.

Department of Chemistry
Durham University
2011

# Contents

# Abbreviations

| | |
|---|---|
| 4ABNA | 4-Aminobenzoic Acid and Nicotinic Acid co-crystal |
| 2APP | 2-Aminopyridine Dihydrogen Phosphate |
| 35DBNA | 3,5-Dinitrobenzoic Acid and Nicotinic Acid co-crystal |
| 23PDCA | 2,3-Pyridinedicarboxylic Acid |
| 34PDCA | 3,4-Pyridinedicarboxylic Acid |
| 35PDCA | 3,5-Pyridinedicarboxylic Acid |
| 24PDNB | Pyridinium 2,4-Dinitrobenzoate |
| ADP | Anisotropic Displacement Parameter |
| AIMD | Ab-initio Molecular Dynamics |
| AO | Atomic Orbitals |
| BHPM | Benzimidazolium Hydrogen Phenylmalonate |
| BTA-BPY | Benzene-1,2,4,5-Tetracarboxylic Acid and 4,4'-Bipyridine co-crystal |
| CIF | Crystallographic Information File |
| CCD | Charge Coupled Device |
| CSD | Cambridge Structural Database |
| CW | Constant Wavelength |
| DFT | Density Functional Theory |
| DM | Dynamical Matrix |
| DMSO | Dimethylsulphoxide |
| DOS | Density of States |
| EI | Electron Impact |
| FTIR | Fourier Transform Infra-Red |
| GGA | Generalised Gradient Approximation |
| GOF | Goodness-of-Fit |
| $H_2$ca-Phz | Chloranilic acid and Phenazine co-crystal |
| HRPD | High Resolution Powder Diffractometer |
| HT | High Temperature |
| INH-PAS | Isonicotinic acid hydrazide and 4-aminosalicylic acid co-crystal |
| INS | Inelastic Neutron Scattering |
| IR | Infra-Red Spectroscopy |
| KDP | Potassium Hydrogen Phosphate |
| LD | Lattice Dynamics |
| LDA | Local Density Approximation |
| LT | Low Temperature |
| MD | Molecular Dynamics |
| MP-PCP | 4-Methylpyridine and Pentachlorophenol co-crystal |
| MP-TCHQ | 4-Methylpyridine and Tetrachlorohydroquinone co-crystal |
| MS | Mass Spectrometry |
| NM | Normal Modes |
| NMR | Nuclear Magnetic Resonance |
| PAW | Projector Augmented Wave |
| PBE | Perdew, Burke and Ernzerhof functional |
| PCP-PZ | Pentachlorophenol and Pyrazine co-crystal |
| PES | Potential Energy Surface |
| PV | Pseudo-Voigt (peak shape) |
| PW | Plane Wave |
| QENS | Quasi-Elastic Neutron Scattering |
| RTP | Room Temperature and Pressure |

| | |
|---|---|
| SSHB | Short Strong Hydrogen Bond |
| TCHQ-PZ | Tetrachlorohydroquinone and Pyrazine co-crystal |
| TCHZ | Thomson-Cox-Hastings (peak shape) |
| TOF | Time-of-Flight |
| TOPAS | TOtal Pattern Analysis System |
| TB | Tuberculosis |
| TS | Transition State |
| UPA | Urea-Phosphoric Acid |
| VIVALDI | Very Intense Vertical Axis Laue Diffractometer |
| VT | Variable Temperature |
| XRD | X-ray Diffraction |
| ZPVE | Zero-Point Vibrational Energy |

# Declaration & Statement of Copyright

The work submitted in this thesis is entirely my own, except where I have acknowledged help from, or collaboration with, a named person, or given reference to a published source or thesis.

The research presented was performed in the Department of Chemistry, Durham University, and at the Institut Laue Langevin, between October 2008 and October 2011, the results of which have not been submitted for a degree in this or any other university.

This thesis conformed to the word limit set out in the Degree Regulations.

# Acknowledgements

Firstly I would like to thank my supervisors, Mark and Ivana, for their continued guidance and support.

I would also like to thank those people who have helped and supported me in a scientific capacity throughout the course of my Ph.D., particularly John Evans, Garry McIntyre, Peter Trommsdorff, Jacek Waluk, Sylwester Gavinowski, Tony Horsewill and Paul Freeman.

# 1   Introduction and Literature Review

Hydrogen is the most abundant element in the universe and, as such, has an essential role in an extensive number of fields. Its vast range of practical applications extends from organic chemistry (catalysts, amino acids and organometallics) to materials science (fuel cells, hydrogen storage media and ferroelectrics). One of the most significant roles of hydrogen, however, is in the formation of the hydrogen bond.

Discovered almost a hundred years ago, the hydrogen bond is one of the fundamental physiochemical interactions in nature and greatly influences the structure, function and properties of a large range of systems, including water and DNA. A classical hydrogen bond is a donor-acceptor interaction of the form, X–H···Y, where X–H acts as a proton donor to Y, and H···Y constitutes a local interaction. Hydrogen bonds exist with a range of strengths, with energies varying from 1 to 180 kJmol$^{-1}$ and interactions ranging from partially covalent to ionic (with some closer to weak cation-$\pi$ and van der Waals interactions).[1] It is useful for practical reasons to classify hydrogen bonds as "weak", "moderate" or "strong", where some of the properties of these different bond strengths are given in Table 1.1.[1]

*Table 1.1: Rough guideline values for strong, moderate and weak hydrogen bonds.*[1]

| Hydrogen Bond Classification | Strong | Moderate | Weak |
|---|---|---|---|
| **Interaction Type** | strongly covalent | mostly electrostatic | electrostatic |
| **X···Y Bond Length/Å** | 2.2 - 2.5 | 2.5 - 3.2 | > 3.2 |
| **Bond Angles/°** | 170 - 180 | > 130 | > 90 |
| **Bond Energy/kJmol$^{-1}$** | 60 - 170 | 15 - 60 | < 15 |

The distribution of donor-acceptor bond lengths for O···H···O and N···H···O hydrogen bonds, obtained from a database study of the compounds in the CSD[2, 3] is given in Figure 1.1. In these studies, simple O···H···O and O···H···N fragments were searched, with the non-bonded O···O and O···N distances defined as contacts. Furthermore the searches were constrained to find only organic, single crystal structures in which 3D coordinates had been determined and no disorder was present. The histograms given in Figure 1.1 show the frequency of hydrogen bond lengths for each of these classes and it

can be seen that short hydrogen bonds, those with donor-acceptor distances of less than approximately 2.50 Å for O···H···O and 2.56 Å for N···H···O, are rare.
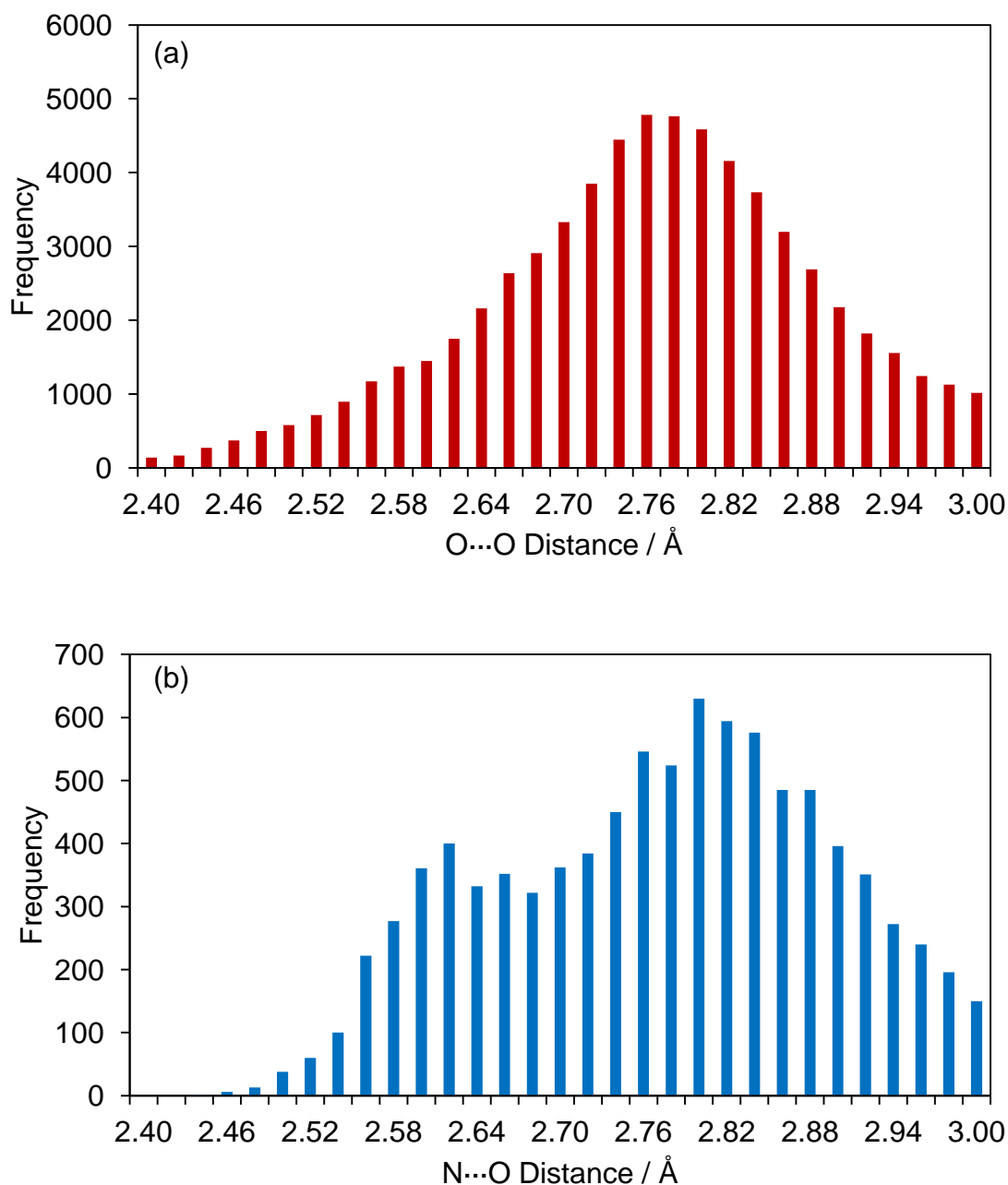
*Figure 1.1: The distribution of donor-acceptor distances for a) O···H···O and b) N···H···O hydrogen bonds.*

The characteristics of a hydrogen bond can be understood in terms of a one-dimensional single well potential. For weak hydrogen bonds there are two preferred arrangements, one in which the hydrogen atom lies closer to the acceptor and one in which it lies

closer to the donor. The potential therefore consists of two wells, the depths of which are dependent on the comparable stabilities of the X–H and H–Y interactions, with a large potential energy barrier separating them. If X and Y are identical, the two potential wells would be symmetrical (dotted lines in Figure 1.2a), whereas if X and Y differ, it is more likely that the two potential wells would be unsymmetrical (Figure 1.2b). As the X···Y separation decreases, and hence the hydrogen bonds get stronger, the potential energy barrier becomes lower and narrower (solid line in Figure 1.2a in the symmetrical case) until, for the shortest bonds, the wells merge and a single well is produced; in the symmetrical case this is represented by Figure 1.2c, whereas in the unsymmetrical case this would be an asymmetric single well potential.[4, 5]
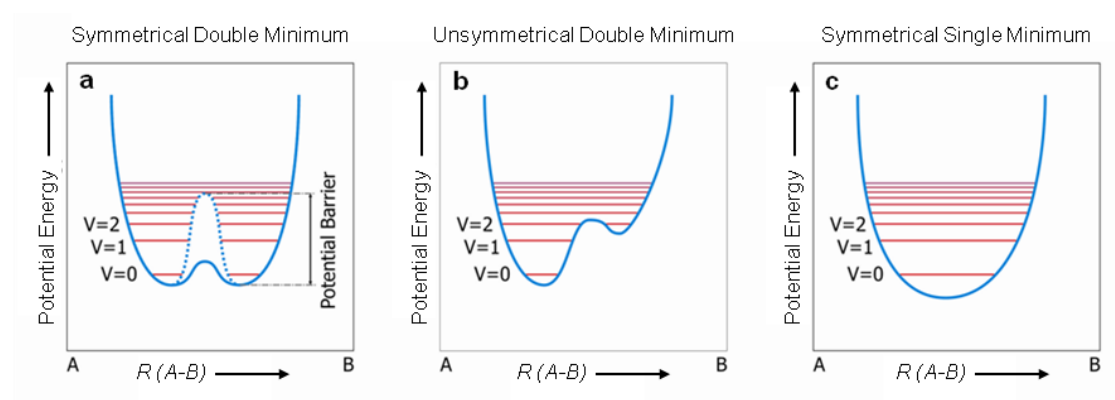


*Figure 1.2: Potential energy surfaces for the motion of hydrogen atoms in a hydrogen bond:[6] a) the symmetrical case, with a large energy separation between the wells (dotted) and a low energy separation (solid) as the X···Y separation decreases, b) the unsymmetrical case with a large energy separation and c) a single minimum for a short X···Y separation in the symmetrical case.*

It is the very shortest and strongest bonds that are the focus of this work, and these are discussed in greater detail in the following section.

## 1.1  Short Strong Hydrogen Bonds

In contrast to the primarily electrostatic $X^{\delta-}–H^{\delta+}···Y^{\delta-}$ nature of their weaker counterparts, short strong hydrogen bonds (SSHBs) possess a quasi-covalent character;[7] the position of hydrogen in the bond is close to symmetric and, consequently, the covalent X–H bonds are consistently longer than normal and the H···Y separation is

consistently shorter.[8] Such a situation is described as a three-centre, four electron bond with the hydrogen atom involved in two partial covalent bonds with comparable bond orders.

An important condition for the formation of intermolecular SSHBs is that both hydrogen bonded molecules have a similar proton affinity. In solution strong hydrogen bonds form if there is a sufficiently small difference between the donor and acceptor $pK_a$ values. Although in the solid state $pK_a$ dependencies are not strictly valid, when hydrogen bonds are isolated from strong polar interactions they can exhibit very similar behaviour to those in solution.[1, 8, 9] In addition, the strongest hydrogen bonds tend to have an almost linear X–H⋯Y bond angle to maximise the bond strength.

The presence of SSHBs can lead to a number of interesting and potentially useful phenomena, such as proton migration and proton order-disorder transitions. It is these properties of SSHBs that are of interest in this work.

## 1.2 Proton Migration

In certain compounds containing SSHBs, the proton has been seen to systematically and reversibly change its position in the hydrogen bond as a function of temperature; this is termed "proton migration". The extent of this migration depends on the specific system involved and has been observed in hydrogen bonds of the form O⋯H⋯O and N⋯H⋯O. The protons in the systems studied to date have been found to migrate from a position closer to the donor atom, at low temperatures, to either a more central position in the hydrogen bond, or to a position closer to the acceptor atom, at higher temperatures.

A number of reasons for the observation that a hydrogen bonded proton can be, on time-average, in different positions at different temperatures were considered.[7] These included the possibility of disorder, polymorphism and experimental error. However, it was concluded, based on early neutron diffraction studies, that gradual proton migration can occur, with the position of the proton dependent on temperature.[7] Factors which can, in principle, influence the presence or absence of this migration include various structural factors, such as hydrogen bond geometry and packing motifs, as well as

various chemical properties, such as acid-base properties of the donor and acceptor groups.

Temperature-dependent proton migration has the potential to be exploited in a wide range of applications, including ferroelectrics, electrochemical processes and crystal engineering.[10] However, this effect is not well-understood and has only been observed in a small number of compounds to date, a selection of which are discussed below.

### 1.2.1 Urea-Phosphoric Acid

Urea-phosphoric acid (UPA) is the most extensively studied hydrogen bonded system in which temperature-dependent proton migration has been observed. Urea and phosphoric acid co-crystallise in a 1:1 ratio in the orthorhombic space group *Pbca*, with eight dimer units in the unit cell. Many hydrogen bonds stabilise the complex layered structure but only one of these, a short strong intermolecular O–H···O bond with an O···O distance of 2.42 Å at 15 K, exhibits proton migration;[11] the proton in this short hydrogen bond has been found to migrate approximately 0.05 Å from an asymmetric position close to the donor urea oxygen at 15 K to a symmetric position in the centre of the hydrogen bond at 300 K.[11-13] The key hydrogen bond in UPA is shown in Figure 1.3.
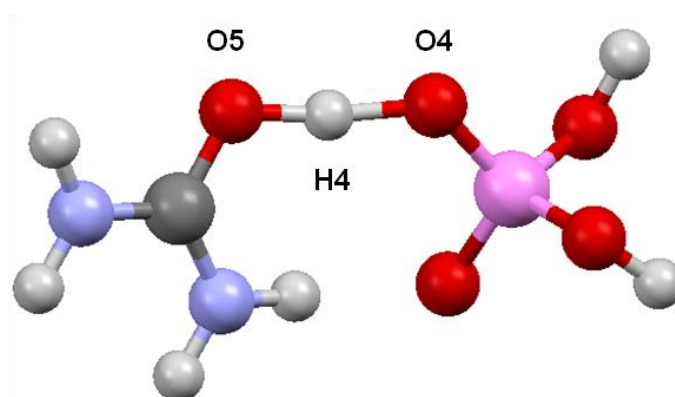


*Figure 1.3: One dimer unit of UPA with the key SSHB, O5···H4···O4, labelled,[14] where carbon is drawn in dark grey, nitrogen in blue, oxygen in red, hydrogen in light grey and phosphorous in pink.*

A number of X-ray and neutron diffraction studies have been carried out on this system[15, 16] since its structure was first reported by Sundera-Rao *et al.* in 1954.[17] These include studies at variable temperatures[12, 13, 18] and pressures,[19] and significant proton migration has been observed in each case. In order to fully understand proton behaviour in short hydrogen bonds such as this, however, information about the shape of the hydrogen bond potential is required. For this purpose, diffraction data are fairly limited and consequently computational methods have been employed.

Initial computational studies on this system were undertaken by Wilson *et al.*[11] who performed a series of *ab-initio* molecular orbital calculations on an isolated UPA dimer at 0 K. The results of even the highest level calculations did not correspond to the experimentally determined parameters, outputting a "short" O···O hydrogen bond distance of 2.61 Å that strongly disagrees with the experimentally determined distance of 2.42 Å at 15 K; the calculated O–H and H···O distances were also not in agreement with the experiment. In order to incorporate the effects of crystal packing the calculations were extended into a periodic environment using plane wave density functional theory (DFT) methods, again at 0 K, which output a much improved short O···O hydrogen bond distance of approximately 2.42 Å, in good agreement with that observed experimentally.

Following this work at 0 K a number of independent *ab-initio* molecular dynamics (MD) simulations were undertaken at a range of temperatures, with a view to understanding the proton migration observed experimentally in UPA. The first, by Morrison *et al.*[14], revealed the proton migration effect, albeit to a lesser extent than that measured experimentally, and calculated vibrational frequencies. A tentative conclusion, that the proton migration may be the result of a resonance between high frequency vibrations, was drawn. The second study, by Fontaine-Vive *et al.*,[4] showed low frequency lattice vibrations to be stabilising the crystal structure, at nonzero temperatures, in such a way that the minimum of the average potential is shifted towards the centre of the hydrogen bond. Although these separate MD simulations were similar, the conclusions have been the subject of some debate.

## 1.2.2  4-Methylpyridine-Pentachlorophenol

The crystal structures of 4-methylpyridine-pentachlorophenol (MP-PCP) determined from X-ray diffraction data at room temperature and 80 K were reported by Malarski *et al.* in 1987 and 1996, respectively;[20, 21] the first neutron work on this system was undertaken by Steiner *et al.* in 2001.[7] 4-methylpyridine and pentachlorophenol co-crystallise in a 1:1 ratio in the triclinic space group $P\bar{1}$, with two formula units in the unit cell, Figure 1.4.[20] The constituent molecules of this co-crystal form dimers linked by a very short intermolecular N–H···O bond with an N···O distance of 2.506 Å at 20 K.[7] Furthermore, the proton has been found to migrate across the bond, from an asymmetric position closer to the nitrogen atom of 4-methylpyridine at 20 K, to an asymmetric position closer to the oxygen atom of pentachlorophenol at room temperature. At 90 K the hydrogen bond is approximately geometrically centred, the structure is ordered at all temperatures, and no phase transitions have been observed.[7] Computationally, MD simulations have been performed on this system, but with little success; the N···O distance was overestimated by almost 0.1 Å at 20 K and, consequently, proton migration was not observed computationally. It was concluded that this is due to the dimeric nature of the co-crystal and, therefore, the absence of long range constraints caused by infinite networks of hydrogen bonds as observed, for example, in UPA. As a result, the hydrogen bond in MP-PCP has more freedom to lengthen in the initial geometry optimisation calculation.[5]
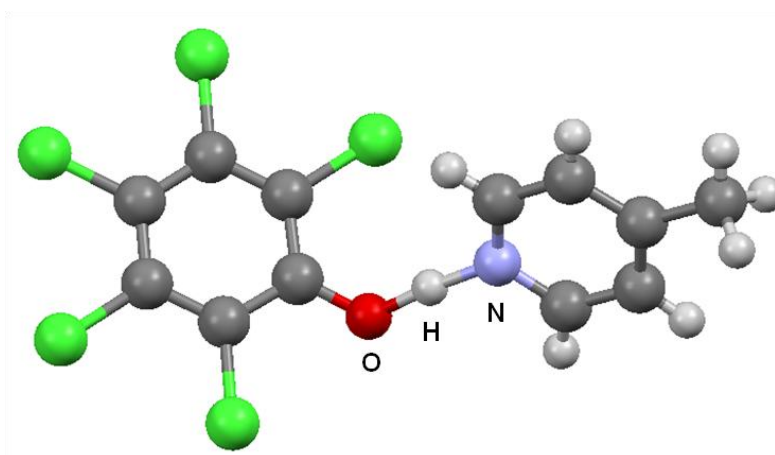


*Figure 1.4: The low temperature crystal structure of MP-PCP showing the short N···H···O bond (labelled).[5] (Carbon is drawn in dark grey, nitrogen in blue, oxygen in red, chlorine in green and hydrogen in light grey).*

## 1.2.3  Benzene-1,2,4,5-tetracarboxylic Acid-4,4'-Bipyridyl

The X-ray crystal structure of a 1:2 adduct of benzene-1,2,4,5-tetracarboxylic acid and 4,4'-bipyridyl (BTA-BPY), Figure 1.5, was reported by Lough *et al.* in 2000[22] and subsequent neutron diffraction studies were carried out by Cowan *et al.* at a range of temperatures between 20 and 296 K.[23, 24] Benzene-1,2,4,5-tetracarboxylic acid (BTA) and 4,4'-bipyridyl (BPY) co-crystallise in the triclinic space group $P\bar{1}$, forming infinite one-dimensional chains along the [012] direction which are stabilised by a number of short hydrogen bonds; the structure contains a short N⋯H–O hydrogen bond (N⋯O distance of approximately 2.610 Å at 20 K), in which the proton lies closer to an oxygen atom of BTA at all temperatures, and a very short N–H⋯O bond (N⋯O distance of 2.521 Å at 20 K), in which proton migration has been observed. The proton migrates approximately 0.1 Å, from a position closer to a nitrogen atom of BPY at 20 K to one closer to an oxygen atom of BTA at 296 K.[23, 24]

MD simulations have been performed on this system and, in contrast to MP-PCP, a temperature-dependent proton migration was successfully calculated. As a result of the characteristics and limitations of DFT methods, however, the calculated migration is smaller than that observed experimentally, as seen in UPA.[5]
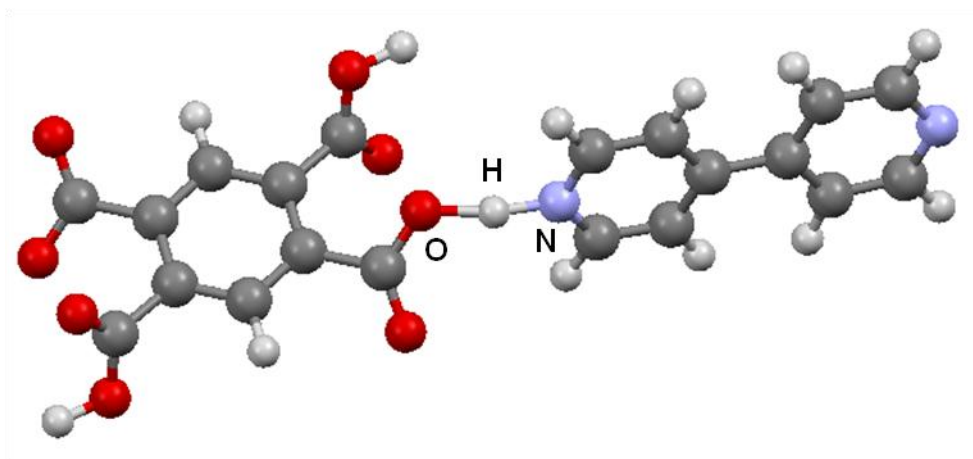


*Figure 1.5: The low temperature crystal structure of BTA-BPY, with the key SSHB, N⋯H⋯O, labelled.[5] (Carbon: dark grey, oxygen: red, nitrogen: blue and hydrogen: light grey).*

## 1.2.4  3,5-Pyridinedicarboxylic Acid

The crystal structure of 3,5-pyridinedicarboxylic acid (35PDCA) was first reported by Takusagawa *et al.* in 1973[25] with subsequent neutron and variable temperature studies undertaken by Cowan *et al.*[26] 35PDCA crystallises in the monoclinic space group $P2_1/c$, with four molecules in the unit cell.[25] The molecules form infinite two-dimensional planar sheets, perpendicular to the *c* axis, which are stabilised by a number of intermolecular hydrogen bonds. These include a "normal" medium-length O–H···O bond (2.57 Å at 15 K) and a very short strong N–H···O bond (2.52 Å at 15 K), which both occur between adjacent molecules within a sheet; no significant interactions exist between the sheets.[24] The low temperature crystal structure is shown in Figure 1.6.

The proton in the very short hydrogen bond has been found to migrate approximately 0.1 Å from an asymmetric position closer to the oxygen of the carboxyl group at 296 K to an asymmetric position closer to the pyridine nitrogen at 15 K.[26] At 15 K the internal geometry of the 35PDCA molecule corresponds to the zwitterionic form, with a protonated nitrogen and a deprotonated carboxyl oxygen, similar to the 23PDCA[27] and 34PDCA[28] isomers.
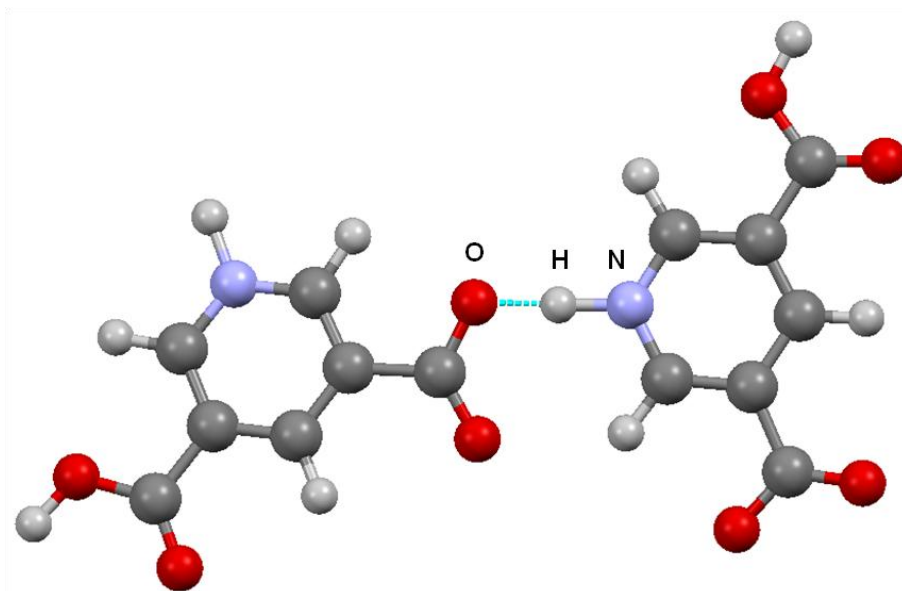


*Figure 1.6: The low temperature crystal structure of 35PDCA, with the SSHB (N–H···O) labelled .[5](Carbon: dark grey, oxygen: red, nitrogen: blue, hydrogen: light grey).*

The dynamics in 35PDCA have been investigated extensively in order to thoroughly understand the driving forces for proton migration.[5] MD simulations, analogous to those performed on UPA and BTA-BPY, allowed temperature-dependent effects to be investigated. Again, proton migration was found, albeit to a lesser extent than observed by neutron diffraction. Inelastic neutron scattering (INS) and phonon calculations were also performed, allowing the investigation of the molecular and hydrogen bond vibrations, and the assignment of the vibrational modes. INS was performed for a fully protonated and a partially deuterated sample of 35PDCA (in which the hydrogen bonds were deuterated and the pyridine ring was protonated); in contrast to UPA, which has a complex three-dimensional structure and large numbers of hydrogen bonds, selective deuteration of specific protons in 35PDCA is a relatively simple procedure. Deuteration of the hydrogen bonds allows certain vibrations to be highlighted, suppressing the modes relating to the atoms in the hydrogen bonds; the neutron scattering cross-section of hydrogen being approximately 20 times greater than that of deuterium. These studies led to a greater understanding of the low frequency dynamics of the system and to the conclusion that the low frequency lattice vibrations drive the proton transfer.

It is clear from the studies of Fontaine-Vive *et al.*[5] and Cowan *et al.*[26] that deuteration of 35PDCA does not affect the existence of a temperature-dependent proton migration. It does, however, cause subtle structural changes, shown in Table 1.2, which appear to affect the extent of proton migration; a larger migration has been found to occur in the deuterated form.

*Table 1.2: Protonated and deuterated unit cell parameters for 35PDCA at 15 and 296 K.*[26]

| | *a*/Å | *b*/Å | *c*/Å | *β*/° | *Volume*/Å³ |
|---|---|---|---|---|---|
| **Protonated at 15 K** | 9.7116(13) | 11.1347(17) | 6.4421(13) | 108.596(10) | 660.25(19) |
| **Deuterated at 15 K** | 9.7196(10) | 11.1396(11) | 6.4540(6) | 108.754(8) | 661.69(11) |
| **Protonated at 296 K** | 9.6986(7) | 11.1571(8) | 6.5891(6) | 107.804(5) | 678.85(9) |
| **Deuterated at 296 K** | 9.7614(10) | 11.2243(12) | 6.6430(8) | 108.304(2) | 691.02(13) |

In general, the cell parameters are seen to increase on deuteration. Whilst at 15 K the change is very small, at room temperature there is a much more significant, unexpected,

difference between the parameters. Additionally, at room temperature, the O4⋯N1 distance in the strong O4–H5⋯N1 hydrogen bond increases upon deuteration (from 2.525(3) to 2.564(3) Å), the O4–H5 distance decreases (from 1.218(6) to 1.108(4) Å) and the H5⋯N1 distance increases (from 1.308(6) to 1.457(4) Å).[26]

The room temperature results shown in Table 1.2 are unusual. Whilst the lattice parameters are expected to increase on deuteration as a result of the classical Ubbelohde effect (see Section 1.4),[29] this increase is expected to be very small (less than 0.05 Å). It is therefore likely that the observations made at 296 K are the result of more than this effect alone. No attempt was made in the existing literature to account for this effect.

Recent work by Delamore *et al.*[30] has involved the study of the compounds at a much larger number of temperatures using variable temperature powder XRD and neutron data. This latest work revealed an unexpected phase transition from powder X-ray and neutron diffraction between 150 and 200 K which has been explored further in this work (Chapter 3).

### 1.2.5 Isoniazid-4-Aminosalicylic Acid

Isoniazid (isonicotinic acid hydrazide) and 4-aminosalicylic acid have been found (using single crystal X-ray diffraction analysis only) to co-crystallise in a 1:1 ratio (INH-PAS) in the orthorhombic space group *Pna*2$_1$.[31] The structure is relatively complex, consisting of related pairs of INH-PAS, forming tetramers which then pack in infinite zigzag chains. The structure is stabilised by various N–H⋯O and O–H⋯N hydrogen bonds within and between the tetramers of a particular chain (no significant interactions exist between the chains); these hydrogen bonds are mostly medium in length, but a relatively short bond, with a donor-acceptor distance of 2.548(2) Å at 100 K, is present also. This short hydrogen bond forms between the nitrogen atom of the PAS pyridine ring and the oxygen atom of the INH carboxylic acid group. This bond is unusual as it is only short in one of the related pairs in the tetramer, with differences between these pairs resulting from their different intermolecular environments. In the pair containing the SSHB, temperature-dependent proton migration has been found to occur, from a position closer to the oxygen atom at 280 K (O–H of 1.11(7) Å) to an almost central position in the hydrogen bond at 100 K (O–H

of 1.25(5) Å).[31] This effect differs from that in the materials discussed previously in that the donor-acceptor distance also changes quite significantly, from 2.576(3) Å at 280 K to 2.548(2) Å at 100 K. The change in this O···N bond may also be causing the subtle changes in the O–H and H···N bonds.

### 1.2.6 Pyridinium 2,4-Dinitrobenzoate

The X-ray crystal structure of a 1:1 adduct of pyridine and 2,4-dinitrobenzoic acid, pyridinium 2,4-dinitrobenzoate (24PDNB), was first determined at 100 and 299 K.[32] Subsequent neutron diffraction work was then carried out by Majerz *et al.* at a range of temperatures between 30 and 300 K.[33] This compound crystallises in the triclinic space group *P*1̄ with the pyridine and 2,4-dinitrobenzoic acid components connected through relatively short, almost planar, N–H···O hydrogen bonds, of 2.568 Å at 300 K. This bond is longer than mentioned in previous sections, in which a large proton migration has been observed, and, while the N–H distance has been found to change systematically as a function of temperature (from 1.147(4) Å at 30 K to 1.171(9) Å at 300 K), no migration through the centre of the hydrogen bond occurs, *i.e.* an N–H bond is maintained at all temperatures.[33]

### 1.2.7 Organic Ferroelectrics

The relevance of SSHBs and proton migration reaches far beyond small organic molecules. For example, SSHBs are thought to play a key role in enzyme catalysis in certain enzymes, stabilising the intermediate state of the reaction.[34] Also, the components of some of the co-crystals mentioned above have important uses in medicine; for example, the components of the INH-PAS co-crystal (Section 1.2.5)[31] are known anti-tuberculosis (TB) drugs. The attempted co-crystallisation of such substances, which are already available for the treatment of TB, is of current research in the field of 'multiple-drug resistant organism' prevention. It seems that the unexpected presence of an SSHB in this compound leads to the modification of the structure through temperature-dependent proton migration, which in turn may lead to useful modifications of the physiochemical properties and potentially improved pharmacological action. Small organic molecules with SSHBs, such as those discussed here and throughout this thesis, are therefore interesting in their own right; however

they are also useful model systems for studies of complex biologically relevant interactions. Additionally it seems that, contrary to common opinion, the importance of temperature-dependent proton migration reaches beyond SSHB materials alone, being observed in a number of technologically important organic ferroelectric materials with medium-length hydrogen bonds.[35] These findings suggest that the presence of SSHBs is not a necessary condition for this type of behaviour and that other factors must also play a significant role.

Horiuchi *et al.*[35] have reported ferroelectric behaviour, with remarkably large spontaneous polarisation and high dielectric constant near room temperature, in co-crystals of phenazine with chloranilic acid, Phz-$H_2$ca, and its deuterated analogue. These $\pi$-molecular systems are linked by medium length hydrogen bonds, with a donor-acceptor distance of approximately 2.72 Å, which makes them fundamentally different to the systems described earlier in this chapter. The mechanism resulting in this ferroelectric behaviour has been researched extensively in recent years,[35-46] and has been found to involve proton migration. For the fully protonated form the molecule is in the paraelectric phase, centrosymmetric space group $P2_1/n$, at room temperature, and undergoes a phase transition to the ferroelectric phase, non-centrosymmetric space group $P2_1$, on cooling (with a phase transition temperature, $T_c$, of approximately 253 K), Figures 1.7a and 1.7b, respectively. The key structural difference between these phases is that, below 253 K, one of the protons has undergone a slight shift away from the oxygen donor towards the centre of the O–H$\cdots$N hydrogen bond, breaking the inversion symmetry. The nuclear density of the proton is modelled using a large elongated thermal ellipsoid.[38] This ferroelectric phase exists down to 146 K, below which the molecule transforms into a related incommensurate paraelectric phase. Furthermore, at 136 K, a transition to a second ferroelectric phase is observed, accompanied by a cell volume doubling. In this phase the proton is thought to be fully transferred to the nitrogen atom of the phenazine ring, with the compound existing in the monovalent ionic form, [H-Phz$^+$][Hxa$^-$].[44] In the fully deuterated form, a huge isotope effect is observed, with a ferroelectric phase transition above room temperature ($T_c$ of 304 K).[35] The iodo-, bromo- and fluoro-anilic acid-phenazine compounds have also been investigated;[35, 42, 44] with ferroelectricity in the bromo- analogue ($T_c$ of 138 K) well documented.[35]

<center>(a)                                        (b)</center>
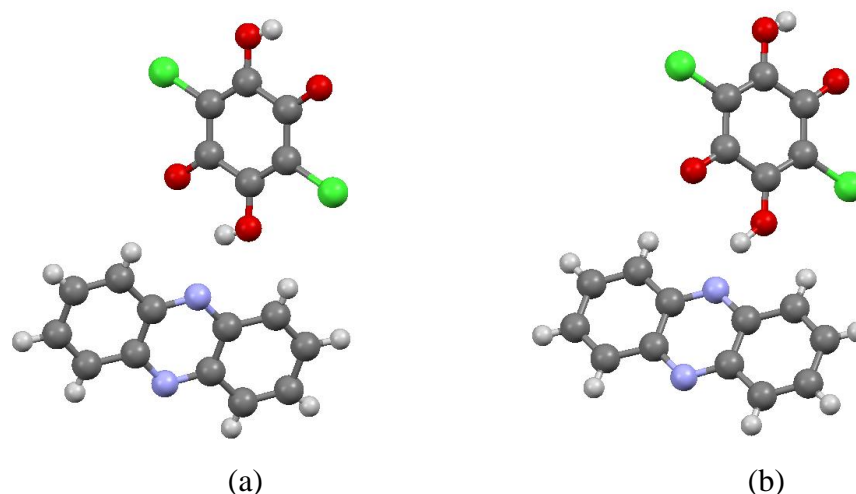
*Figure 1.7: The molecular structure of Phz-H$_2$ca at (a) 300 K and (b) 160 K. It can be seen that at 300 K, the hydrogen atom of the O–H⋯N bond is very close to the oxygen atom, whereas at 160 K, it has migrated towards the nitrogen atom slightly. (Hydrogen is drawn in light grey, carbon in dark grey, nitrogen in blue, oxygen in red and chlorine in green).*

## 1.3 Proton Order-Disorder Transitions

In many hydrogen-bonded compounds protons are seen to be disordered over two sites, one closer to the donor atom and another closer to the acceptor atom or the centre of the bond, with the relative occupancies of these sites changing with temperature. In some compounds, protons are found in such a disordered state at higher temperatures, gradually becoming more ordered on preferred sites as the temperature is lowered; this is observed in benzoic acid.[47]

Such proton order-disorder transitions have been found to play a significant role in the phase transitions responsible for ferroelectric behaviour in a number of SSHB materials, including potassium hydrogen phosphate, KH$_2$PO$_4$ (KDP).[48-50] The structure of this ferroelectric material consists of a network of PO$_4$ tetrahedra, joined by short O–H⋯O hydrogen bonds of approximately 2.50 Å. At high temperature KDP is in a paraelectric phase (space group $I\bar{4}2d$) in which the hydrogen atoms are equally distributed across two positions in the hydrogen bond. Below $T_c$ (approximately 123 K), however, the protons order, localising themselves onto one of these sites, leading to a ferroelectric

phase (space group *Fdd*2). A huge isotope effect is also observed in this compound on deuteration, with the deuterated form exhibiting a phase transition temperature, $T_c$, of around 229 K.[51]

An analogous mechanism has been found to result in ferroelectricity in other compounds,[52-54] most recently, a polymorph of 2-aminopyridine dihydrogen phosphate, *α*-2APP.[55] This compound undergoes a structural transition at 103 K, from nonpolar symmetry, space group *C2/c*, in the paraelectric phase, to polar symmetry, space group *Cc*, in the ferroelectric phase. At high temperature the asymmetric unit consists of one aminopyridinium cation and two dihydrogen phosphate anions, Figure 1.8a. These anions contain a short P–O bond, a long P–OH bond and two intermediate P–OH bonds. The hydrogen atoms of these intermediate bonds are located on inversion centres between two oxygen atoms of adjacent tetrahedra. Below $T_c$ these protons order on a single site, resulting in tetrahedra containing two short P–O bonds and two long P–OH bonds, a decrease in symmetry and induced polarity; the asymmetric unit of the low temperature structure contains two aminopyridinium cations and two dihydrogen phosphate anions, Figure 1.8b.[55]
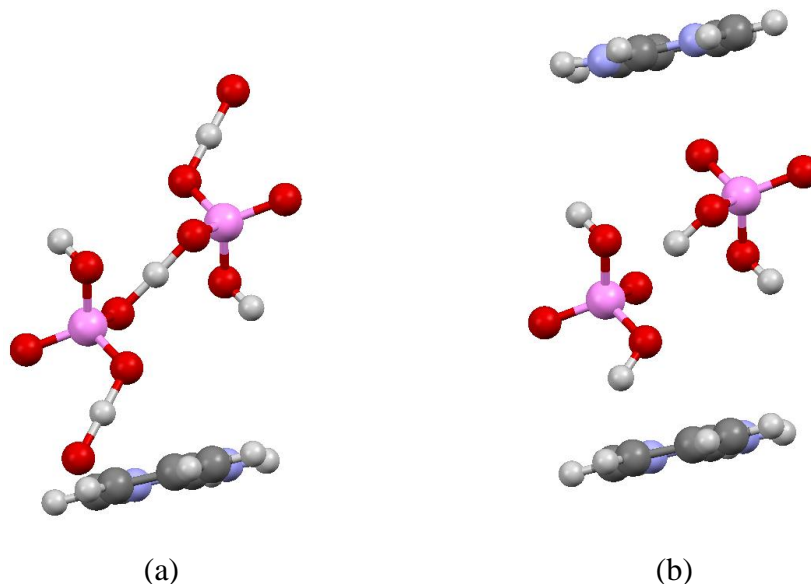


*Figure 1.8: The structure of α-2APP at a) 290 K and b) 30 K. (Carbon: dark grey, hydrogen: light grey, oxygen: red, nitrogen: blue and phosphorous: pink).*

Hybrid organic-inorganic ferroelectric materials, such as those described here, have received a great deal of attention in recent years due to their diverse areas of application in technology, including electronics, electro-optics and electromechanics.[56] However, owing to their flexibility, lightness and non-toxicity, as well as their demonstrable high spontaneous polarisation,[35] organic ferroelectrics are currently considered as preferable alternatives.[35, 36, 57, 58] Conventional organic ferroelectrics are, in general, of the proton order-disorder type,[52-54, 59] though exceptions to this exist, including the phenazine-anilic acids, described in Section 1.2.7, which are of the proton migration type.

## 1.4    The H/D Isotope Effect

The substitution of deuterium for hydrogen can provide valuable information about hydrogen-bond potentials and, consequently, is a useful technique for determining information about hydrogen bonds in crystals.[6, 60, 61] Isotope exchange has a number of interesting applications; for example, it has been used to locate hydrogen atoms in protein crystal structures, and distinguish *cis* and *trans* orientations of vicinal hydroxyl groups in 1,3-diols and monosaccharides, owing to the large differences between hydrogen and deuterium neutron scattering lengths and NMR chemical shifts, respectively.[62, 63] In addition, it is necessary to deuterate hydrogen-containing samples for powder neutron diffraction as a result of the large incoherent neutron scattering of hydrogen.

In general, such isotopic substitution has only a minor effect on the crystal structure, with the main change being a slight increase in hydrogen bond lengths on deuteration (the Ubbelohde effect).[29] It is thought that these increases are a result of the lower zero-point vibrational energy (ZPVE) of the X–D bond compared to the X–H bond (where X is any donor atom); as a result, the X–D bond is more stable, the deuterium is more difficult to abstract from the donor and the hydrogen bond is weaker. Consequently, slight increases in the lattice parameters are also common on deuteration. Such exchange can, however, occasionally lead to more severe structural changes; there are a number of well-studied examples of this and these are discussed below.

Mootz *et al.*[64] found an interesting structural change upon deuteration of trifluoroacetic acid tetrahydrate, $(H_5O_2)[(CF_3C–COO)_2H]\cdot6H_2O$. In the protonated form the structure is ionic with layers of hydrogen-bonded $(H_3O^+\cdot3H_2O)_n$ cations enclosing $F_3C\cdot COO^-$ anions. On deuteration, however, the structure becomes molecular with hydrogen-bonded $(D_2O)_n$ layers enclosing $F_3CCOOD$ molecules.

More recently, Malarski *et al.*[21] have found that isotopic substitution of hydrogen by deuterium in MP-PCP (discussed in Section 1.2.2) causes a drastic structural change. The protonated form of MP-PCP crystallises in the triclinic space group $P\bar{1}$ with two molecules in each unit cell. In contrast, the deuterated form crystallises in the monoclinic space group *Cc*, with four molecules in each unit cell. The most striking difference between these two isotopologues is that the fully protonated form possesses a SSHB as described in Section 1.2.2 whereas the fully deuterated form does not.

The most extensively studied system displaying large structural changes upon deuteration is $KH_2PO_4$ (KDP), Section 1.3.[48, 50] The protonated structure of KDP is tetragonal and paraelectric at room temperature, with a transition to an orthorhombic ferroelectric structure at 123 K.[65, 66] Partially deuterated KDP, *i.e.* $(K(D_xH_{1-x})_2PO_4$, is also paraelectric and tetragonal at room temperature. However, at deuteration levels greater than 98% the room temperature structure is monoclinic.[29, 67]

In 35PDCA the isotope effect manifests itself as a change in the variable temperature structural properties of the materials, as discussed previously (Section 1.2.4). It is this manifestation of the isotope effect which is one of the main focuses of this thesis.

## 1.5    Aims

Work presented in this thesis will extend the study of hydrogen bond compounds at a fundamental level, focussing on the structure and dynamic behaviour of the protons therein. Following recent studies, the structure and dynamics of the known proton migration material, 3,5-pyridinedicarboxylic acid (35PDCA), will be explored.[26] A number of isotopologues of 35PDCA, with systematically varying deuteration levels, will be used, in order to investigate the nature of the phase transition observed on full deuteration[30] and to determine whether the phase transition is dependent on the level of

deuteration alone, or whether it is affected by the position of the isotopic substitution. A combination of diffraction, spectroscopy, NMR and computational techniques will be employed in order to gain a full understanding of the mechanism of proton migration in this material.

In contrast to the simple interpretation of proton migration from diffraction,[26] previous AIMD simulations predict a two-site model; 35PDCA was found to be bistable, with the proton hopping between a position closer to the oxygen atom and a position closer to the nitrogen atom of the hydrogen bond, but avoiding any intermediate positions[5]. This computational prediction will be tested experimentally; spectroscopy will be used in order to determine the presence or absence of the two species resulting from such hopping (N–H···O and N···H–O). NMR will also be employed, in order to try to observe this proton transfer, and also test the proton hopping timescale predicted by these AIMD simulations.

Additionally, a number of further hydrogen bond compounds with the potential to exhibit interesting temperature-induced proton migration and disorder effects will be explored. Initially, a search for existing compounds containing short, intermolecular O–H···O and O–H···N hydrogen bonds, structurally similar to those in known proton migration materials, such as urea-phosphoric acid (UPA)[11] and 35PDCA, will be performed using the Cambridge Structural Database. The synthesis of any candidates resulting from these searches will then be attempted. Subsequently, the synthesis of a series of new co-crystals, with components based on those of the known SSHB and proton migration material, 4-methylpyridine-pentachlorophenol (MP-PCP),[7] will also be attempted. Successful candidates from all of this work will be characterised using a combination of variable temperature X-ray and neutron diffraction techniques, in order to determine both the length of the relevant hydrogen bonds and also to elucidate any interesting structural changes with temperature, particularly changes in the atomic positions of the hydrogen bond protons.

The presence of significant proton migration in some systems containing medium-length hydrogen bonds, such as phenazine-chloranilic acid (discussed earlier in this chapter)[35] and its absence in systems structurally similar to those in which it is known,[68] will be considered, in order to determine whether SSHBs are a necessary or

sufficient condition for this type of behaviour, or whether other factors are also involved.

## 1.6    References

1.    T. Steiner, *Angew. Chem. Int. Ed.*, 2002, **41**, 48.
2.    F. H. Allen, *Acta Crystallogr. Sect. B.*, 2002, **58**, 380.
3.    F. H. Allen and W. D. S. Motherwell, *Acta Crystallogr. Sect. B.*, 2002, **58**, 407.
4.    F. Fontaine-Vive, M. R. Johnson, G. J. Kearley, J. A. K. Howard and S. F. Parker, *J. Am. Chem. Soc.*, 2006, **128**, 2963.
5.    F. Fontaine-Vive, M. R. Johnson, G. J. Kearley, J. A. Cowan, J. A. K. Howard and S. F. Parker, *J. Chem. Phys.*, 2006, **124**, 234503.
6.    G. A. Jeffrey, *Introduction to Hydrogen Bonding*, Oxford University Press, 1997.
7.    T. Steiner, I. Majerz and C. C. Wilson, *Angew. Chem. Int. Ed.*, 2001, **40**, 2651.
8.    M. Schmidtmann and C. C. Wilson, *Crystengcomm*, 2008, **10**, 177.
9.    Z. Malarski, M. Rospenk, L. Sobczyk and E. Grech, *J. Phys. Chem.*, 1982, **86**, 401.
10.    P. Camilleri, C. A. Marby, B. Odell, H. S. Rzepa, R. N. Sheppard, J. J. P. Stewart and D. J. Williams, *Chem. Commun.*, 1989, 1722.
11.    C. C. Wilson and C. A. Morrison, *Chem. Phys. Lett.*, 2002, **362**, 85.
12.    C. C. Wilson, K. Shankland and N. Shankland, *Z. Kristall.*, 2001, **216**, 303.
13.    C. C. Wilson, *Acta Crystallogr., Sect. B*, 2001, **57**, 435.
14.    C. A. Morrison, M. M. Siddick, P. J. Camp and C. C. Wilson, *J. Am. Chem. Soc.*, 2005, **127**, 4042.
15.    D. Mootz and K. Albrand, *Acta Crystallogr., Sect. B*, 1972, **28**, 2459.
16.    B. L. Rodrigues, R. Tellgren and N. G. Fernandes, *Acta Crystallogr., Sect. B*, 2001, **57**, 353.
17.    R. V. G. Sundera-Rao, J. W. Turley and R. Pepinsky, *Acta Crystallogr.*, 1957, **10**, 435.
18.    A. Parkin, S. M. Harte, A. E. Goeta and C. C. Wilson, *New J. Chem.*, 2004, **28**, 718.
19.    C. C. Wilson and L. H. Thomas, *C. R. Chimie*, 2005, **8**, 1434.
20.    Z. Malarski, I. Majerz and T. Lis, *J. Mol. Struct.*, 1987, **158**, 369.
21.    Z. Malarski, I. Majerz and T. Lis, *J. Mol. Struct.*, 1996, **380**, 249.
22.    A. J. Lough, P. S. Wheatley, G. Ferguson and C. Glidewell, *Acta Crystallogr. Sect. B.*, 2000, **56**, 261.
23.    J. A. Cowan, J. A. K. Howard, G. J. McIntyre, S. M. F. Lo and I. D. Williams, *Acta Crystallogr., Sect. B*, 2003, **59**, 794.
24.    J. A. Cowan, *Ph.D. thesis*, University of Durham, 2002.
25.    F. Takusagawa, K. Hirotsu and A. Shimada, *Bull. Chem. Soc. Jpn.*, 1973, **46**, 2292.
26.    J. A. Cowan, J. A. K. Howard, G. J. McIntyre, S. M. F. Lo and I. D. Williams, *Acta Crystallogr., Sect. B*, 2005, **61**, 724.
27.    F. Takusagawa, K. Hirotsu and A. Shimada, *Bull. Chem. Soc. Jpn.*, 1973, **46**, 2372.
28.    F. Takusagawa, K. Hirotsu and A. Shimada, *Bull. Chem. Soc. Jpn.*, 1973, **46**, 2669.

29.    A. R. Ubbelohde and I. Woodward, *Nature*, 1939, **144**, 632.
30.    O. J. Delamore, *M.Chem.*, University of Durham, 2008.
31.    P. Grobelny, A. Mukherjee and G. R. Desiraju, *Crystengcomm*, 2011, **13**, 4358.
32.    L. Sobczyk, T. Lis, Z. Olejnik and I. Majerz, *J. Mol. Struct.*, 2000, **552**, 233.
33.    I. Majerz and M. J. Gutmann, *J. Phys. Chem. A*, 2008, **112**, 9801.
34.    W. W. Cleland and M. M. Kreevoy, *Science*, 1994, **264**, 1887.
35.    S. Horiuchi, R. Kumai and Y. Tokura, *J. Am. Chem. Soc.*, 2005, **127**, 5010.
36.    S. Horiuchi, R. Kumai, Y. Tokunaga and Y. Tokura, *J. Am. Chem. Soc.*, 2008, **130**, 13382.
37.    K. Saito, M. Amano, Y. Yamamura, T. Tojo and T. Atake, *J. Phys. Soc. Jpn.*, 2006, **75**, 033601.
38.    R. Kumai, S. Horiuchi, H. Sagayama, T. Arima, Y. Watanabe, Y. Noda and Y. Tokura, *J. Am. Chem. Soc.*, 2007, **129**, 12920.
39.    F. Ishii, N. Nagaosa, Y. Tokura and K. Terakura, *Phys. Rev. B*, 2006, **73**, 212105.
40.    K. Gotoh, T. Asaji and H. Ishida, *Acta Crystallogr. Sect. C.*, 2007, **63**, o17.
41.    H. Ishida and S. Kashino, *Acta Crystallogr. Sect. C.*, 1999, **55**, 1923.
42.    M. Amano, Y. Yamamura, M. Sumita, S. Yasazuka, H. Kawaji, T. Atake and K. Saito, *J. Chem. Phys.*, 2009, **130**, 034503.
43.    T. Asaji, K. Gotoh and Y. Watanabe, *J. Mol. Struct.*, 2006, **791**, 89.
44.    S. Horiuchi, R. Kumai and Y. Tokura, *J. Mater. Chem.*, 2009, **19**, 4421.
45.    T. Asaji, J. Seliger, V. Zagar, M. Sekiguchi, J. Watanabe, K. Gotoh, H. Ishida, S. Vrtnik and J. Dolinsek, *J. Phys. Condens. Matter.*, 2007, **19**, 226203.
46.    S. Horiuchi, R. Kumai and Y. Tokura, *Chem. Commun.*, 2007, **23**, 2321.
47.    C. C. Wilson, N. Shankland and A. J. Florence, *J. Chem. Soc. Faraday Trans.*, 1996, **92**, 5051.
48.    J. E. Tibballs, R. J. Nelmes and G. J. McIntyre, *J. Phys.*, 1982, **C15**, 37.
49.    R. Blinc and B. Zeks, *Adv. Phys.*, 1972, **21**, 693.
50.    Y. Noda, Y. Watanabe, H. Kasatani, H. Terauchi and K. Gesi, *J. Phys. Soc. Jpn.*, 1991, **60**, 1972.
51.    S. Koval, J. Kohanoff, J. Lasave, G. Colizzi and R. L. Migoni, *Phys. Rev. B: Condens. Matter*, 2005, **71**.
52.    G. F. Lipscomb, A. F. Garito and T. S. Wei, *Ferroelectrics*, 1980, **23**, 161.
53.    J. Kroupa, P. Vanek, R. Krupkova and Z. Zikmund, *Ferroelectrics*, 1997, **202**, 229.
54.    D. Bordeaux, J. Bornarel, A. Capiomont, J. Lajzerowicz-Bonneteau, J. Lajzerowicz and J. F. Legrand, *Phys. Rev. Lett.*, 1973, **31**, 314.
55.    I. R. Evans, J. A. K. Howard and J. S. O. Evans, *Cryst. Growth & Des.*, 2008, **8**, 1635.
56.    K. Uchino, *Ferroelectric Devices*, Marcel Dekker, New York, 2000.
57.    R. R. Choudhury and R. Chitra, *Crys. Res. Technol.*, 2006, **41**, 1045.
58.    S. Horiuchi, Y. Tokunaga, G. Giovannetti, S. Picozzi, H. Itoh, R. Shimano, R. Kumai and Y. Tokura, *Nature*, 2010, **463**, 789.
59.    Y. Kamishima, Y. Akishige and M. Hashimoto, *J. Phys. Soc. Jpn.*, 1991, **60**, 2147.
60.    J. M. Robertson and A. R. Ubbelohde, *Proc. R. Soc. London, Ser. A*, 1939, **170**, 222.
61.    T. R. Singh and J. L. Wood, *J. Chem. Phys.*, 1969, **50**, 3572.
62.    R. W. Harrison, A. Wlodawer and L. Sjolin, *Acta Crystallogr.*, 1988, **A44**, 309.
63.    J. Reuben, *J. Am. Chem. Soc.*, 1984, **106**, 6180.

64.  D. Mootz and M. Schilling, *J. Am. Chem. Soc.*, 1992, **114**, 7435.
65.  B. J. Isherwood and J. A. James, *J. Phys. C.*, 1972, **33**, 91.
66.  R. J. Nelmes, G. M. Meyer and J. E. Tibballs, *J. Phys. C.*, 1982, **15**, 59.
67.  G. Ravi, A. S. Haja Hameed and P. Ramasamy, *J. Cryst. Growth*, 1999, **207**, 319.
68.  I. R. Evans, J. A. K. Howard, J. S. O. Evans, S. R. Postlethwaite and M. R. Johnson, *Crystengcomm*, 2008, **10**, 1404.

# 2 Experimental and Computational Methods

The experimental and computational methods used in this work are described below. Hydrothermal synthesis and various solution methods were employed for crystal growth, and a general overview of these techniques is given. Both powder and single crystal X-ray diffraction, from laboratory sources, have been used extensively for the initial characterisation of products, with neutron diffraction being employed for accurate structure determination and the location of hydrogen atoms. A description of these methods, the general theory behind them and the instrumentation used to collect the diffraction data is given. In addition to these, a description of inelastic neutron scattering (INS), infra-red (IR) and Raman spectroscopy, which have been used to measure molecular vibrations, is given. Finally, the various computational techniques, used to complement and guide the experimental work, are described.

## 2.1 Synthetic Techniques

Crystal growth is often an unpredictable process; there are a large number of interconnected factors which affect the product, including temperature, pressure, the nature of the solvent, the concentration of the solute and the presence of contaminants. Optimising the reaction conditions to produce a crystal of high quality is a significant challenge. The most suitable method for a particular synthesis is dependent on the type of crystal required. For example, growth of large crystals suitable for neutron diffraction may require a vastly different method than that used to produce small crystals suitable for X-ray diffraction. Therefore, synthetic techniques must be optimised for the specific system and the required product.

All of the samples produced in this work have been grown using either hydrothermal synthesis or solution methods. The specific details of each synthesis are included in subsequent chapters; however, a general overview of each of these techniques is given here.

### 2.1.1  Hydrothermal Synthesis

Hydrothermal synthesis is commonly used for producing large, high quality crystals with a controlled composition, and as such has been used routinely throughout this work for the preparation of samples of a suitable size for neutron diffraction. The term 'hydrothermal synthesis' refers to the crystallisation of substances from aqueous solutions above temperatures of 373 K and pressures of 1 bar.[1] These conditions are analogous to those present in nature, and as such this technique is frequently used in the field of geological sciences for simulating natural mineral syntheses.

The reaction conditions of hydrothermal synthesis lead to a number of advantages of this method over other types of crystal growth. For example, reactants which are only sparingly soluble under ambient conditions, making solution methods unsuitable for crystal growth, may be dissolved. Also, crystalline phases which are unstable at their melting point, rendering growth from a melt an unsuitable method for crystal growth, may form.

In order to withstand the high temperatures and pressures involved over prolonged periods of time, hydrothermal syntheses usually take place in a reaction vessel inside a protective thick-walled steel autoclave. A variety of autoclaves exist to cover a wide range of pressures and temperatures, as well as varying vessel sizes. All of the syntheses described in this thesis were carried out using a 23 cm$^3$ lab scale Parr® General Purpose Acid Digestion Bomb, consisting of a Teflon reaction vessel inside a steel autoclave with a brass lid. These bombs are simple to use but have comparatively limited pressure-temperature capabilities (up to 80 bar and 523 K);[1] however, these limits were sufficient for this work.

### 2.1.2  Solution Methods

Solution methods are the most flexible and widely used techniques for crystal growth. A number of solution method variations exist, each involving crystallisation from one or more solvents in various ways. The main advantage of this method over other types of crystal growth is the presence of solvent which enables crystals to grow separately from each other. It is difficult to predict optimum conditions for a particular crystal growth

and therefore, in practice, favourable conditions are identified by screening; a very large batch of syntheses, varying in proportions and natures of solvents and reagents, can be set up and tested with ease. In general it is necessary to try numerous solution conditions before successfully crystallising a particular material.

Three common solution method variations have been used throughout this work and these are described in detail below.

### 2.1.2.1  The Cooling Method

The cooling method involves either preparing a hot saturated solution and slowly cooling it to room temperature, or making up a solution at room temperature and cooling it in the fridge or an ice bath. The method works due to the fact that, in general, solubility decreases with temperature; as the solution cools, the product should crystallise out of solution.

### 2.1.2.2  The Variable Concentration Method

The variable concentration method involves making up a solution using one or more volatile solvents. The solution volume will decrease over time as a result of solvent evaporation. During this time the concentration of the solute rises until it is able to crystallise. The rate of evaporation can be controlled in various ways. For example, it can be enhanced either by increasing the size of the aperture through which solvent evaporation takes place, or by heating the solution. Controlling the rate of evaporation in this way can also control the size of the crystals produced. In general, the more slowly the evaporation takes place, the larger the resulting crystals; a very rapid precipitation may even produce a polycrystalline material.

### 2.1.2.3  Seed Crystals

The method of seeding involves the addition of a small number of 'seed crystals' to the reaction. The term 'seed crystal' refers to a high quality crystal of the target material that cannot be used for structural analysis as a result of its significantly small size. If a small number of these are placed into a saturated solution of the starting materials, they

can act as nucleation points from which larger single crystals of the same material may grow.

## 2.2  Characterisation Methods

A range of techniques have been used to characterise the materials described in this work and these are discussed below. Diffraction (X-ray and neutron) has been used to determine structural details, whereas spectroscopy (INS, IR and Raman) has been used to measure molecular vibrations. In addition, nuclear magnetic resonance (NMR) and mass spectrometry (MS), which have been used for the quantification of deuteration levels in *d*-35PDCA, are briefly discussed.

### 2.2.1  Diffraction

The main method of characterisation for the systems studied in this work was diffraction. Diffraction is one of the most important techniques employed in the characterisation of crystalline materials, serving to determine very detailed features of a crystal structure. In this section the theory behind diffraction is given, alongside a description of the specific techniques used.

#### 2.2.1.1  Theory

A crystal is defined as a solid with a periodically repeating internal arrangement of atoms, and as such can be described in terms of its unit cell. The unit cell is the simplest unit in the crystal from which the entire structure can be determined through translational symmetry alone; it is defined by six lattice parameters, the lengths of the cell edges, *a*, *b* and *c*, and the angles between them, $\alpha$, $\beta$ and $\gamma$. The positions of the atoms in the unit cell are described by a set of fractional atomic coordinates, $(x_i, y_i, z_i)$, where $x_i = x/a$, $y_i = y/b$ and $z_i = z/c$ and *x*, *y* and *z* define the Cartesian coordinates. Further to this, a useful concept is to model a crystal as a discrete, theoretical set of parallel planes of atoms separated by a constant parameter, $d_{hkl}$. These planes are defined by Miller indices, *h*, *k* and *l*, where, by definition, the first plane of the (*hkl*) family from the origin will make intercepts at *a/h*, *b/k* and *c/l* on the unit cell axes.

Diffraction is an interference phenomenon that occurs when a wave interacts with a suitable diffraction grating, such as a solid or an aperture; it results in a change in the direction and intensity of the wave if its wavelength is approximately equal to the size of the object with which it interacts. As suggested by von Laue, X-rays can be produced with wavelengths of the same order of magnitude as the interatomic spacing in crystals and so are diffracted by them, with the atoms in the crystal behaving as a three dimensional diffraction grating. It was later found that neutrons could also be diffracted by crystalline materials in the same way, as a result of the wave-particle duality.[2] In von Laue's analysis, radiation interacts with the atoms of a crystal and is scattered (diffracted) by them in all directions. Figure 2.1 demonstrates this phenomenon in one dimension.

The resulting diffracted radiation then combines in one of two ways: destructively, in which case it cancels out, or constructively, in which case it produces intense peaks of radiation; when this radiation lands on a detector, a diffraction pattern (a set of discrete diffraction spots (peaks), each a wave with its own amplitude and relative phase) results.
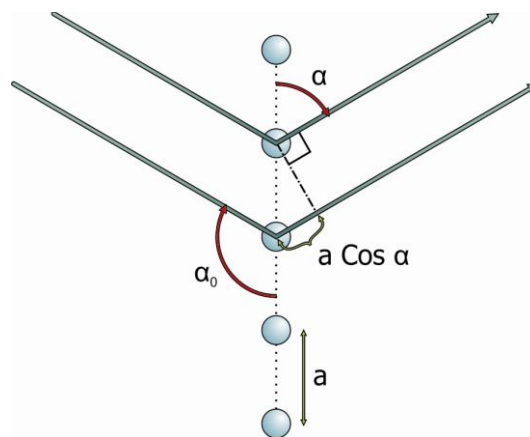


*Figure 2.1: Diffraction from a row of atoms with periodic spacing a, as envisaged by von Laue. The incident and diffracted beams are at angles $\alpha_0$ and $\alpha$ with respect to the row of atoms.*

It was found that for scattered radiation to interfere completely constructively in a one dimensional array of atoms, Equation 2.1 must be satisfied. Hence, for a peak to be

observed in the diffraction pattern the path lengths travelled by the beams of radiation scattered from different atoms in a row must differ by an integral number of wavelengths.

$$path \quad difference = a\cos\alpha - a\cos\alpha_0 = h\lambda \qquad \text{(Equation 2.1)}$$

where the path difference is the difference in the path lengths travelled by the beams of radiation scattered from different atoms in a row, $a$ is the interatomic spacing, $h$ is an integer, $\lambda$ is the wavelength, and $\alpha$ and $\alpha_0$ are the angles between the diffracted and incident beams with respect to the rows of atoms.

In reality a crystal has three dimensions and so there are in fact three equations, analogous to Equation 2.1, which must be satisfied simultaneously for constructive interference to occur; these are the Laue equations:

$$a(\cos\alpha - \cos\alpha_0) = h\lambda \qquad \text{(Equation 2.2)}$$

$$b(\cos\beta - \cos\beta_0) = k\lambda \qquad \text{(Equation 2.3)}$$

$$c(\cos\gamma - \cos\gamma_0) = l\lambda \qquad \text{(Equation 2.4)}$$

where $\lambda$ is the wavelength, $h$, $k$ and $l$ are integers, $a$, $b$ and $c$ are interatomic spacings and $\alpha$, $\beta$, $\gamma$, $\alpha_0$, $\beta_0$ and $\gamma_0$ are the angles between the diffracted and incident beams with respect to the rows of atoms. Hence, in von Laue's analysis a total of six angles, three interatomic spacings and three integers need to be determined; this is complex and impractical and so was later simplified by Bragg.

Bragg envisaged diffraction as the 'reflection' of the incident wave from the theoretical Miller planes within a crystal (see Figure 2.2), and although this is not physically correct it does give accurate peak positions.
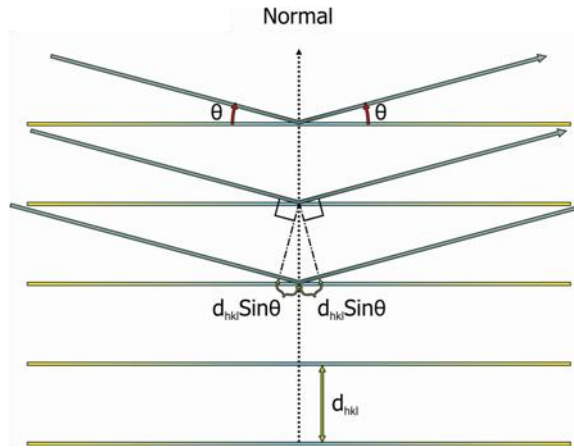
*Figure 2.2: Diffraction as envisaged by Bragg.*

Bragg found that for constructive interference to occur between two scattered waves, Bragg's law, as shown in Equation 2.5, must be satisfied. Hence a peak (or 'reflection') is observed in the diffraction pattern if the difference in the path length of the waves between successive Miller planes is an integer.

$$n\lambda = 2d_{hkl} \sin\theta$$ (Equation 2.5)

where *n* is any integer, $\lambda$ is the wavelength of the radiation used, $d_{hkl}$ is the perpendicular interplanar distance, $\theta$ is the angle of the incident X-ray beam with respect to the planes, and each diffracting plane is defined by three integers, *hkl*, which specify its orientation with respect to the unit cell edges.

The reflections in the diffraction pattern are each associated with a unique scattering vector. These vectors are in the same direction as the normal to the associated real space lattice planes and have a magnitude which is inversely proportional to the interplanar spacing, $d_{hkl}$. Collectively, the vectors form a set that can be used to describe the crystal; the end points of the vectors define a 'reciprocal lattice' with parameters, *a\*, b\*, c\*, α\*, β\** and *γ\**, which are inversely proportional to the real parameters, *a, b, c, α, β* and *γ* respectively. It is in fact this reciprocal lattice that is observed when radiation is diffracted by a crystalline material (hence there is a Fourier transform relationship between a crystal structure and its diffraction pattern), and it is computationally converted into the real space lattice during analysis.

The reciprocal lattice can be used to further define the diffraction condition, through the Ewald construction, as shown in Figure 2.3. Bragg's law is obeyed whenever a point in a reciprocal lattice, for reflecting planes *hkl*, lies on the surface of an Ewald sphere; this is a sphere of radius $1/\lambda$ (where $\lambda$ is the wavelength of incident radiation), which passes through the origin of the reciprocal lattice and contains the diffracting crystal at its centre. Hence, if the wavelength of the radiation changes, the radius of the Ewald sphere changes and different reflections are observed. If the incident beam is a white beam, as in the experiment on VIVALDI which is discussed in Section 2.3.1.2, there will be a range of radiation wavelengths and hence a range of Ewald spheres of varying radii. This allows a large number of reflections to be observed simultaneously. Similarly, if the crystal is rotated but the incident wavelength is kept constant, as in laboratory X-ray diffraction experiments, different *hkl* planes are brought into the diffraction position and therefore different reflections are observed.
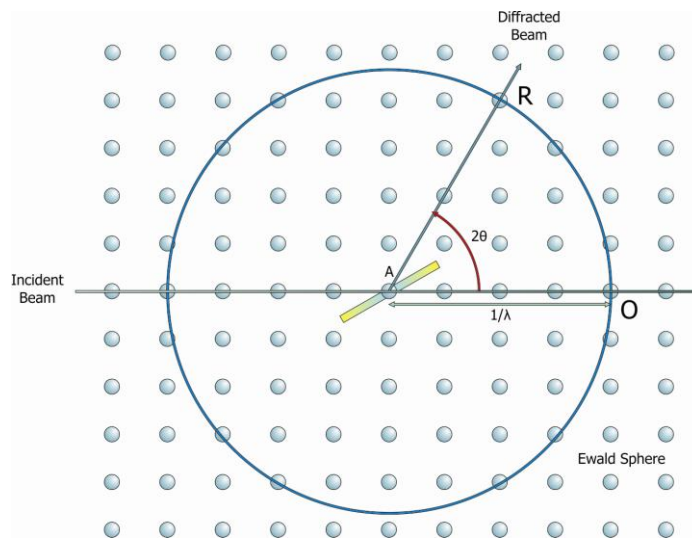


*Figure 2.3: The Ewald construction and the reciprocal lattice: O is the origin of the reciprocal lattice, A is the reflecting plane, hkl, of the crystal being studied, and R is a reciprocal lattice point that results in a peak in the diffraction pattern.*

Diffraction is an interference phenomenon and therefore the scattered beams of radiation have both an amplitude ($|F_{hkl}|$) and a phase ($\phi_{hkl}$). Whilst the amplitude can be measured quite easily using the experimentally observed intensity (each reflection in a diffraction pattern has a particular intensity, $I_{hkl}$, and this intensity is related to the amplitude, $|F_{hkl}|$, as shown in Equation 2.6), the phase is effectively un-measurable.

29

$$I_{hkl} \propto \left| F_{hkl} \right|^2 \qquad\qquad \text{(Equation 2.6)}$$

As previously mentioned, the diffraction pattern is the Fourier transform of the crystal structure and the mathematical relationship for this (the structure factor, $F_{hkl}$) is given by Equation 2.7.

$$F_{hkl} = \sum_{n=1}^{N} f_n \exp\left[ 2\pi i \left( hx_n + ky_n + lz_n \right) \right] \qquad\qquad \text{(Equation 2.7)}$$

where N is the number of atoms in the unit cell, $x_n$, $y_n$ and $z_n$ are the fractional atomic coordinates of the n$^{th}$ atom in the unit cell and $f_n$ is the form factor, describing the diffracting power of each element type as a function of Bragg angle (and dependent on the type of radiation being used).

If both the structure factor amplitude ($|F_{hkl}|$) and the relative phase ($\phi_{hkl}$) of each reflection are known, the continuous scattering density (electron density for X-ray scattering and nuclear density for neutron scattering) throughout the crystal structure could be computed using Equation 2.8.

$$\rho(xyz) = \frac{1}{V} \sum_{hkl} \left| F_{hkl} \right| \exp\left[ i\phi_{hkl} \right] \exp\left[ -2\pi i \left( hx + ky + lz \right) \right] \qquad\qquad \text{(Equation 2.8)}$$

where $\rho(xyz)$ is the scattering density, $V$ is the unit cell volume and the summation is over all observable reflections, *hkl*.

However, the information about the relative phases of the waves that compose each reflection is lost; this 'phase problem' is one of the central problems of crystallography, since this information is required in order to accurately determine the crystal structure. A number of structure solution procedures exist for attempting to solve this problem and recover the lost phase information. One such method, the Patterson method,[3, 4] derives the phases indirectly by proposing structural models and back-calculating the structure factors, and is particularly successful for structures with a single heavy atom amongst several light ones. However, this method is not very useful when a crystal structure,

such as those described in this thesis, consists of numerous similar atoms. Therefore, in this work, Direct Methods,[5] in which the phases are estimated directly from the measured intensities, and expanded using a triple-relation (a relation between the intensity and phase of one reflection with those of two further reflections), have been employed throughout.

The structure is then solved using an iterative process; the initial, approximate phases resulting from Direct Methods are used, along with the measured (observed) amplitudes, in a Fourier synthesis to yield an approximate atomic structure. From this structure, new amplitudes are calculated, allowing a new set of phases to be simulated. These improved phases are then reapplied to the original, observed amplitudes, resulting in an improved atomic structure. Additional Fourier syntheses may then be employed to better the model further. In addition, Fourier difference maps, which use the differences between the observed and calculated amplitudes together with the calculated phases, are often employed in order to locate any missing atoms in the structure; in particular, towards the end of structure determination, they are often used to locate hydrogen atoms. Eventually, when all atoms have been found, the atomic coordinates are refined by the method of Least Squares, an iterative procedure in which the atomic coordinates are adjusted in order to minimise the difference between the observed and calculated amplitudes. (Further details about Least Squares refinement can be found in Section 2.2.1.4).

### 2.2.1.2  X-rays and Neutrons

X-ray and neutron diffraction are of fundamental importance in the elucidation of crystal structures, giving important information about the positions of atoms in a structure; X-rays are scattered by the electrons in atoms in a crystal while neutrons are scattered by the atomic nuclei. Both of these methods have their various advantages and disadvantages in the analysis of crystal structures, and both have been used throughout this work for acquiring different levels of structural information. Similarly, both powder and single crystal diffraction techniques have been utilised throughout this work in order to extract various information about specific crystal structures and characteristics; all of these methods are detailed in the following sections.

X-ray and neutron beams, as previously mentioned, can be produced with wavelengths of orders of magnitude similar to the interplanar spacing in crystals and so are diffracted by them. Neutrons are uncharged spin-½ particles, whereas X-rays are a high energy form of electromagnetic radiation (with energies in the range 120 eV to 120 keV).

X-rays can be generated in the laboratory by accelerating electrons into a metal anode, such as molybdenum or copper, using an electric field. This causes the core electrons in the atoms of the anode to be excited into short-lived higher energy states. When these return to the ground state, energy is released in the form of X-rays; this process takes place inside the X-ray tube of a diffractometer. Molybdenum and copper produce X-rays with characteristic wavelengths of 0.711 Å and 1.542 Å respectively. Both types of radiation have been used to obtain the X-ray diffraction data presented in this thesis; single crystal data have been collected using molybdenum $K_\alpha$ radiation, whereas powder data have been collected using copper $K_\alpha$ radiation.

There are two methods of producing neutrons for diffraction; these are by spallation (at a spallation source) or by nuclear fission (at a reactor source). The neutrons produced at both sources have energies that are too high to be used for diffraction purposes; moderators must be employed to slow the neutrons down. Commonly used moderators include deuterium oxide/heavy water (the ILL), hydrogen and methane (ISIS). At a spallation source, such as ISIS in the UK, a pulse of high energy protons bombards a heavy metal tantalum target which releases energy by emitting neutrons. The neutron beam is therefore pulsed and neutrons of different wavelengths are differentiated by their time of arrival at a detector (their time-of-flight, TOF). At a reactor source, such as the ILL in France, the neutron beam is continuous and generated from highly enriched uranium in carefully controlled nuclear chain reactions. Choppers and monochromators are then used in order to differentiate neutrons of different wavelengths. Both types of neutron source have been used to obtain the neutron diffraction data presented in this thesis.

Neutron diffraction has a significant number of advantages over X-ray diffraction, particularly in the study of hydrogen-containing materials. The main advantage is that neutrons are scattered by the atomic nuclei whereas X-rays are scattered by the electron

density in a compound. There are a number of consequences of this occurrence as outlined below:

1) Neutron scattering powers vary erratically across the periodic table, often with large differences between adjacent elements; X-ray scattering power is proportional, to a first approximation, to the atomic number (Z) of an element and therefore increases smoothly across the periodic table. As a result, in neutron diffraction, heavier elements do not dominate lighter ones, and so light elements such as hydrogen can be observed in the presence of even the heaviest elements. Neutron diffraction also allows elements that are adjacent in the periodic table to be differentiated; this can be difficult with X-ray diffraction as adjacent elements will have nearly identical X-ray scattering powers. Finally, isotopes of the same element have different neutron scattering lengths and therefore isotopic substitution can be identified using neutron diffraction. However, as isotopes have the same number of electrons they cannot be distinguished using X-ray diffraction.

2) Neutron data do not suffer from aspherical effects and this is particularly important when trying to obtain accurate information about X-H covalent bonds lengths. In general, bond lengths deduced from X-ray diffraction are accurate for most atoms due to the similar positions of the electron density and the nuclei. However, hydrogen contains just a single electron and this is predominantly located in the centre of the covalent bond rather than centred upon the hydrogen nucleus. As a result, X-H covalent bond lengths deduced from X-ray diffraction are consistently shorter than those found by neutron diffraction.

Neutrons allow the possibility of studying magnetic structures in materials as they possess a magnetic dipole moment and are therefore sensitive to the magnetic fields generated by unpaired electrons in materials. Also, neutrons interact weakly with matter and so are capable of penetrating the bulk of a sample, whereas X-rays, which interact strongly, are absorbed by the sample and so can usually only obtain information about a layer close to the surface.

The main disadvantages of neutrons are that neutron beams are weak in intensity and they interact weakly with materials. Therefore larger samples are needed (which is not

always possible, especially for single crystals), data collection times are longer than those in X-ray diffraction (again as a result of low neutron fluxes) and they are only available at expensive central facilities. Furthermore, the study of hydrogen can still be problematic with neutron diffraction. As a result of its high incoherent scattering of neutrons, hydrogen produces a large incoherent background in powder diffraction making it difficult to study accurately. This incoherent background can be avoided by deuterating the powder sample, *i.e.* replacing all the hydrogen, $^1$H, isotopes with deuterium, $^2$H (D), which has a much lower incoherent neutron scattering cross-section. This can be time-consuming, expensive and difficult. Also, due to the H/D isotope effect, as discussed in Chapter 1, deuteration may alter the structure of the sample in such a way that the results may not be directly comparable with a fully protonated sample. Nevertheless, unlike X-ray diffraction, with the right sample and on the right instrument it is possible to study hydrogen accurately using neutron diffraction. (Further details of neutron scattering are given in Section 2.2.2.1).

### 2.2.1.3  Single Crystal Diffraction

Single crystal diffraction is the most powerful technique used for the determination of crystal structure. In a single crystal experiment, a good quality crystal is rotated on a goniometer head in a beam of X-rays or neutrons. This brings each crystal plane into position for diffraction, allowing the recording of diffracted intensity over a range of either $2\theta$ or a measurement of time whenever the Bragg condition is satisfied.

It is essential that the optimum crystal is selected for analysis by diffraction and so the first step in a single crystal experiment is to find crystals of good quality. The crystal chosen must be relatively small for X-ray diffraction in order to reduce absorption effects; smaller than $0.5 \times 0.5 \times 0.5$ mm$^3$ was found to be suitable for this work. However, crystals smaller than $0.1 \times 0.1 \times 0.1$ mm$^3$ seemed to diffract poorly, with a loss of high angle reflections. Conversely, for neutron diffraction crystals must be reasonably large. Crystals must also be single, with a clean appearance, *i.e.* lacking in cracks and other defects.

A useful tool in the evaluation of crystal quality is a polarising microscope. A perfect crystal polarises light and therefore when viewed between the two polarisers in such a

microscope will transmit polarised light.[1] If a crystal transmits polarised light, one of the polarisers can be rotated by 90°. In this orientation, no light may pass through and the crystal will become dark (extinguish). On continuing to rotate the polariser a further 90°, the crystal will become light again; this phenomenon will continue every 90°. Any crystal that does not extinguish completely and sharply is not appropriate and can be rejected immediately.

When a suitable crystal is found, it must be mounted on a goniometer head. In X-ray diffraction experiments it is attached to the goniometer head by a fibre on a metal pin; a glass fibre is used for larger crystals, whereas a hair is used for much smaller crystals. The crystal can be attached to the fibre in various ways; for low temperature experiments it is attached using inert perfluoropolyether oil which is then flash-frozen in a stream of cold nitrogen gas. However, for higher temperature work it is necessary to mount it in glue. As much of the work reported here involved comparing crystal structures at low temperature and just above room temperature (300 K), it was necessary to mount in glue for full data collections. Oil was used to mount crystals for rapid unit cell determinations for the purpose of determining the crystal quality at 120 K. In the neutron diffraction experiment on VIVALDI (see Section 2.3.1.2), crystals were wrapped in aluminium foil and then mounted on a vanadium pin using vacuum grease.

### 2.2.1.4 *Powder Diffraction and Rietveld Refinement*

In a powder diffraction experiment, instead of a single crystal, there is a collection of randomly oriented crystallites exposed to the beam. Powder diffraction suffers in comparison to single crystal diffraction because the random orientation of the crystallites scatters the beam over all possible angles simultaneously according to Bragg's law. The result is a cone of diffracted intensity for each lattice plane (which causes the three dimensional reciprocal space that is studied in single crystal diffraction to be projected onto a single dimension), and an overlap in a number of diffraction peaks.

---

[1] with the exception of black crystals, cubic crystals in all orientations and tetragonal and hexagonal crystals when viewed down the c axis

Despite its limitations, powder diffraction has become a powerful technique for phase identification and structural analysis where growth of a single crystal is not possible. This is largely as a result of the development of the Rietveld method (described further in this section) and real-space structure solution methodologies (such as simulated annealing and Monte Carlo). Both neutron and X-ray powder diffraction techniques have been used in this work, with the instruments and methods used described in following sections.

One of the key advances in materials chemistry stems from a technique devised by Hugo Rietveld in the 1960's for use in the characterisation of crystalline materials. A key feature of this technique is its ability to analyse the full diffraction pattern, rather than merely refining against individual Bragg peaks. Known as the Rietveld method, this is a least-squares fitting technique that effectively seeks to minimise the difference between observed and calculated powder diffraction patterns.[6, 7]

Powder diffraction data are presented as a plot of intensity of the diffracted beam as a function of the scattering angle, $2\theta$ (for X-ray and constant wavelength neutron diffraction) or a measure of time (for TOF neutron diffraction), with peaks in the pattern representing specific reflections. Each reflection has a position, an intensity and a peak shape profile. In Rietveld refinement, these intensities are considered as numerical values, $y_i$, at each of several thousand equally spaced steps, $i$. In a refinement, the quantity to be minimised is the residual, $S_y$, given in Equation 2.9.

$$S_y = \sum_i w_i (y_i - y_{ci})^2$$

(Equation 2.9)

where $w_i$ is $1/y_i$, $y_i$ is the observed intensity at the $i$th step, $y_{ci}$ is the calculated intensity of the $i$th step and the sum is over all data points.

The Rietveld method can be used as part of the structure solution process[8]; however, in general it is not a structure solution procedure but a structure refinement procedure. For this reason a reasonable starting model is required on which to base the refinement. The Rietveld refinement will adjust the refining parameters within the starting model, until the residual (Equation 2.9) is minimised. The best fit to the model data will depend on

whether an adequate starting model is used and whether a global minimum is reached in the refinement and not a local (false) minimum. Therefore, it is necessary to know detailed information about the crystal structure(s) of phases present in the powder sample, and also information about the diffractometer used, before a refinement is started. It is important to have some indicator after each least-squares cycle in order to judge whether a refinement is progressing satisfactorily. For this reason, a number of fit parameters are used to monitor least-square cycles as they progress. The most commonly quoted of these residual (*R*) factors, the *R*-pattern and the *R*-weighted pattern, are shown in Equations 2.10 and 2.11 below.

$$R_p = \frac{\sum |y_i(obs) - y_i(calc)|}{\sum y_i(obs)}$$

(Equation 2.10)

$$R_{wp} = \left[ \frac{\sum w_i (y_i(obs) - y_i(calc))^2}{\sum w_i (y_i(obs))^2} \right]^{1/2}$$

(Equation 2.11)

Mathematically, $R_{wp}$ is the most meaningful *R*-value as the numerator is $S_y$, the residual being minimised, and so this *R*-value best reflects the progress of the refinement. If the background in a diffraction pattern is high, however, the numerator of Equation 2.11 becomes large and, hence, $R_{wp}$ becomes artificially small. Therefore, another useful fitting parameter, the $R_{Bragg}$ (Equation 2.12), is also consulted. The $R_{Bragg}$ measures the fit to the individual Bragg peaks, with no intermediate (*i.e.* background) points taken into account, and is therefore nearly comparable to those *R*-values quoted for single crystal refinements.

$$R_{Bragg} = \frac{\sum |I_K('obs') - I_K(calc)|}{\sum I_K('obs')}$$

(Equation 2.12)

where $I_K$ is the intensity assigned to the *K*th Bragg reflection at the end of the refinement cycles. The 'obs' (of the observed $I_K$) is in quotations in this case due to the fact that $I_K$ is rarely observed directly, but is in fact deduced with the help of a model.

The $R_{exp}$, the expected $R$-value, Equation 2.13, can also be defined.

$$R_{\exp} = \left[ \frac{(N-P)}{\sum w_i y_{oi}^2} \right]^{\frac{1}{2}}$$  (Equation 2.13)

where $N$ is the number of observations, $P$ is the number of variables and $y_{oi}$ is the observed intensity.

This, in combination with the $R_{wp}$ (Equation 2.11), defines another useful numerical value, the 'Goodness-of-Fit' (GOF), $\chi$, Equation 2.14. The ideal situation at the end of a refinement procedure is to attain a value of 1 for the GOF.

$$GOF = \sqrt{\chi^2} = \frac{R_{wp}}{R_{\exp}}$$  (Equation 2.14)

The complete diffraction pattern is a mixture of a large number of factors which are influenced either by the instrument or the nature of the sample or both. Many of the instrument parameters are known and fixed, for example, the diffractometer geometry, X-ray wavelength and Lorentz polarisation factor. Instrument parameters that can be refined include the $2\theta$ zero error (or sample height), the background, and a contribution to the peak shape profile. A large number of refineable parameters provide information on the sample and these can be split into two types, structural parameters and profile parameters. The intensities of the peaks are determined by the structural parameters, for example the atomic coordinates, the temperature factors ($U_{ijs}$) and any preferred orientation effects. The profile parameters determine the position and shapes of the peaks; these include a further contribution to the peak shape profile, the unit cell parameters and crystallite size and strain. In addition, an overall scale factor can be refined.

In reality, the peaks in a diffraction pattern are broadened by a combination of instrumental and sample factors as mentioned in the previous paragraph. Peak shape profiles are used to describe the instrumental broadening effects and quantify the various sample effects. In an ideal X-ray diffraction pattern, the width of the reflection

profiles could be modelled by a Gaussian function, which gives a purely symmetrical and, therefore, physically unrealistic peak shape. The sample broadening effects are modelled by a Lorentzian expression. For all X-ray refinements in this work, a pseudo-Voigt (PV) peak shape function, as parameterised by Thomson, Cox and Hastings (TCHZ)[9] was used; this is a convolution of the Gaussian and Lorentzian functions. The peak shape profile in time-of-flight powder diffraction is markedly different and exhibits a characteristic asymmetry; this requires a more complex function. The leading edge of the peak is very sharp because the first neutrons to emerge are almost coincident with the high energy pulse hitting the target, while the trailing edge decays according to the moderator size and temperature. The peaks of a neutron diffraction pattern are therefore modelled as a convolution between a sharp edged exponential function, with two characteristic decays of known magnitude (determined by the moderator), and a Voigt function. The Voigt function is defined by a Gaussian and a Lorentzian term.

Significant preferred orientation was observed in the X-ray diffraction patterns of all of the samples produced in this work. Preferred orientation occurs if samples have a tendency to align themselves into layers within a flat sample holder. This is common when materials which grow in layers or as flat plates are packed into a flat sample holder. The result is that the randomness of the crystal orientation is reduced and this may give false intensity information; the reflections associated with planes along which the crystallites line up will have disproportionately high intensities, and so suppress all other intensities. Preferred orientation can be accounted for in a Rietveld refinement by applying a correction. The function used in this work was a spherical harmonic. In order to minimise the preferred orientation observed in X-ray diffraction, all diffraction slides were prepared by smearing a small amount of Vaseline® to the surface of a silicon slide and sieving a thin layer of the powdered sample onto it. The silicon slides used for this purpose are specially cut along the systematically absent (511) silicon plane resulting in a 'zero' background. In the neutron diffraction experiment on HRPD, the sample was placed into a cylindrical vanadium can which was then sealed. This prevented the powder from being aligned into layers.

## 2.2.2 Spectroscopy

A number of vibrational spectroscopy techniques have been used to study the vibrational modes of 3,5-pyridinedicarboxylic acid and its deuterated analogues (Chapter 4) and these are discussed here. While inelastic neutron scattering (INS) has many advantages, it will always be complementary to more common techniques, such as infrared (IR) and Raman spectroscopy, due to its high cost and low availability.

### 2.2.2.1  *Inelastic Neutron Scattering*

INS probes the atomic motion, allowing the experimental observation of the vibrational dynamics of a system; it is a type of vibrational spectroscopy which uses neutrons and has widespread applications in many areas of science. Neutrons are scattered by atomic nuclei either with or without a change in their energy, resulting in inelastic and elastic scattering, respectively. The scattered neutron waves may then also undergo interference. This may be interference with scattered waves of the same phase, resulting in coherent scattering. Alternatively the presence of natural isotopes and differing nuclear spins within a sample may destroy local order and consequently reduce the phase relationships between the scattered waves, resulting in incoherent scattering. While coherent elastic neutron scattering experiments (neutron diffraction, as described previously) yield information about the structure of a sample, incoherent inelastic neutron scattering probes uncorrelated, single particle dynamics and coherent inelastic neutron scattering experiments allow the determination of the phonon dispersion relation.

A neutron is characterised by its wave vector, $\boldsymbol{k}$, and its spin state, $\sigma$. From $\boldsymbol{k}$, the momentum, $\boldsymbol{p}$, velocity, $\boldsymbol{v}$, and the kinetic energy, $E$, can be calculated, given the neutron mass, $m$. (Equations 2.15 and 2.16).

$$\boldsymbol{p} = \hbar \boldsymbol{k} = m\boldsymbol{v} \qquad\qquad \text{(Equation 2.15)}$$

$$E = \frac{\boldsymbol{p}^2}{2m} = \frac{\hbar^2 \boldsymbol{k}^2}{2m} = \frac{m\boldsymbol{v}^2}{2} \qquad\qquad \text{(Equation 2.16)}$$

INS is a scattering process which involves an exchange of energy and momentum between neutrons and a sample. The aim of an INS experiment is to obtain the scattering function, $S(\mathbf{Q},\omega)$, as a function of energy, where the scattering vector, $\mathbf{Q}$, is the change in momentum (the difference between the incoming, $\mathbf{k}_i$, and outgoing wave vector, $\mathbf{k}_f$, of the neutron beam), and $\hbar\omega$ is the energy change experienced by the sample (Equations 2.17 and 2.18).

$$\mathbf{Q} = \mathbf{k}_i - \mathbf{k}_f \qquad \text{(Equation 2.17)}$$

$$\Delta E = \hbar\omega = E_i - E_f = \frac{\hbar^2}{2m}\left(\mathbf{k}_i^2 - \mathbf{k}_f^2\right) \qquad \text{(Equation 2.18)}$$

The observable in an INS experiment is the fraction of scattered neutrons with an energy, $E_f$, in a solid angle, $d\Omega$; this is the double differential scattering cross-section/ scattering intensity, $\dfrac{d^2\sigma}{dE_f\,d\Omega}$, and is related to the scattering function, $S(\mathbf{Q},\omega)$, by Equation 2.19.

$$S(\mathbf{Q},\omega) = \frac{4\pi}{\sigma}\frac{\mathbf{k}_i}{\mathbf{k}_f}\left(\frac{d^2\sigma}{dE_f\,d\Omega}\right) \qquad \text{(Equation 2.19)}$$

In terms of the actual sample under study, $S(\mathbf{Q},\omega)$ is given by Equation 2.20.

$$S(\mathbf{Q},\omega_i) = \sum_{i}\sum_{j=1}^{3N}\mathbf{Q}^2 \mathbf{u}_{ij}^2 \cdot \sigma_j \exp\left[-2W\right] \qquad \text{(Equation 2.20)}$$

where $i$ sums over all vibrational modes and $j$ over all atoms ($x,y,z$), $\mathbf{u}$ is the displacement vector (amplitude of vibrational motion), $\sigma$ is the total scattering power of the atoms and $W$ is a complex term involving $\mathbf{Q}$. Therefore it can be seen that while increasing the value of $\mathbf{Q}$ can increase $S(\mathbf{Q},\omega)$, at a certain point the exponential term (Debye-Waller factor) takes over and a larger value of $\mathbf{Q}$ actually reduces $S(\mathbf{Q},\omega)$. The experimental value of $\mathbf{Q}$ must, therefore, be a compromise between these two contributions.

INS has a number of advantages over other vibrational spectroscopy techniques such as IR and Raman, many of which are consequences of the neutron interaction with atomic nuclei.[10, 11] There are no selection rules in INS as a result of this interaction and therefore all vibrations are, in principle, measurable. Also, due to the erratically varying nature of neutron scattering cross-sections from element to element and isotope to isotope, light elements can be studied in the presence of heavy ones and isotopes can be distinguished; a consequence of this is that hydrogenous materials can be selectively deuterated in order to highlight the dynamics of specific hydrogen atoms of interest. As previously described (Section 2.2.1.2), unlike photons, one of the main advantages of neutron radiation is its penetrating nature. This allows the measurement of bulk sample properties, and also permits the use of low-cost aluminium for sample containers. INS spectrometers cover the whole molecular vibrational range of interest, with the lower energy range (below $400 \, cm^{-1}$) readily accessible; this region in particular is more difficult to obtain by IR and Raman techniques. However, the interaction of neutrons with matter is weak and therefore large samples, long experiment times and a neutron beam of sufficient intensity are required; the latter of these is only available at expensive central facilities making INS a costly and limited technique. IR and Raman spectroscopy, which are more widely available, are therefore considered to be valuable, complementary techniques.

### 2.2.2.2 Infrared and Raman Spectroscopy

IR and Raman spectroscopy are simple and reliable techniques that are widely used in chemistry. IR spectroscopy, in particular, has been used for investigating and characterising hydrogen bonding for decades. While Raman spectroscopy has been considered less useful for this purpose, largely due to the inherent weakness in scattering of groups engaged in hydrogen bonding,[12] it is still a valuable technique, yielding complementary information to IR. In general terms, both techniques are concerned with the interaction of electromagnetic radiation with matter, and both can be used to probe molecular vibrations; which in turn can be used in structure determination due to the fact that vibrational information is specific to chemical bonding and symmetry information.

In an IR experiment a beam of infrared light (typically mid-infrared light, with wavelengths of 3 to 25 μm) is passed through a sample. The alternating electrical field of the IR radiation interacts with fluctuations in the dipole moment of the molecule. Where the frequency of light matches the frequency of a vibrational mode in the sample, the light is absorbed, Figure 2.4 (left). The fraction of absorbed radiation at a particular energy is measured in order to produce a spectrum that is characteristic of the functional groups present in the sample. In order for a vibrational mode to be IR active it must cause changes in the dipole moment as the molecule vibrates.

In a Raman experiment a beam of monochromatic light (photons), usually from a laser, in the near-UV (200 to 400 nm), visible (390 to 750 nm) or near-IR (0.78 to 3 μm) range, is passed through a sample. The light interacts with the molecular vibrations (phonons in a solid), exciting the molecule to a virtual energy state. When the molecule relaxes the photons are then subsequently re-emitted; while most of the photons reflect from the sample without any change in energy (Rayleigh scattering), some photons are re-emitted with different frequencies due to exchange of energy between the photons and the phonons (Stokes and Anti-Stokes scattering), causing the molecule to return to a different vibrational state, Figure 2.4 (middle and right). The difference in frequency between the original monochromatic radiation and the re-emitted photons provides information about characteristic vibrational transitions in molecules. In order for a vibrational mode to be Raman active it must cause changes in the molecular polarisability.
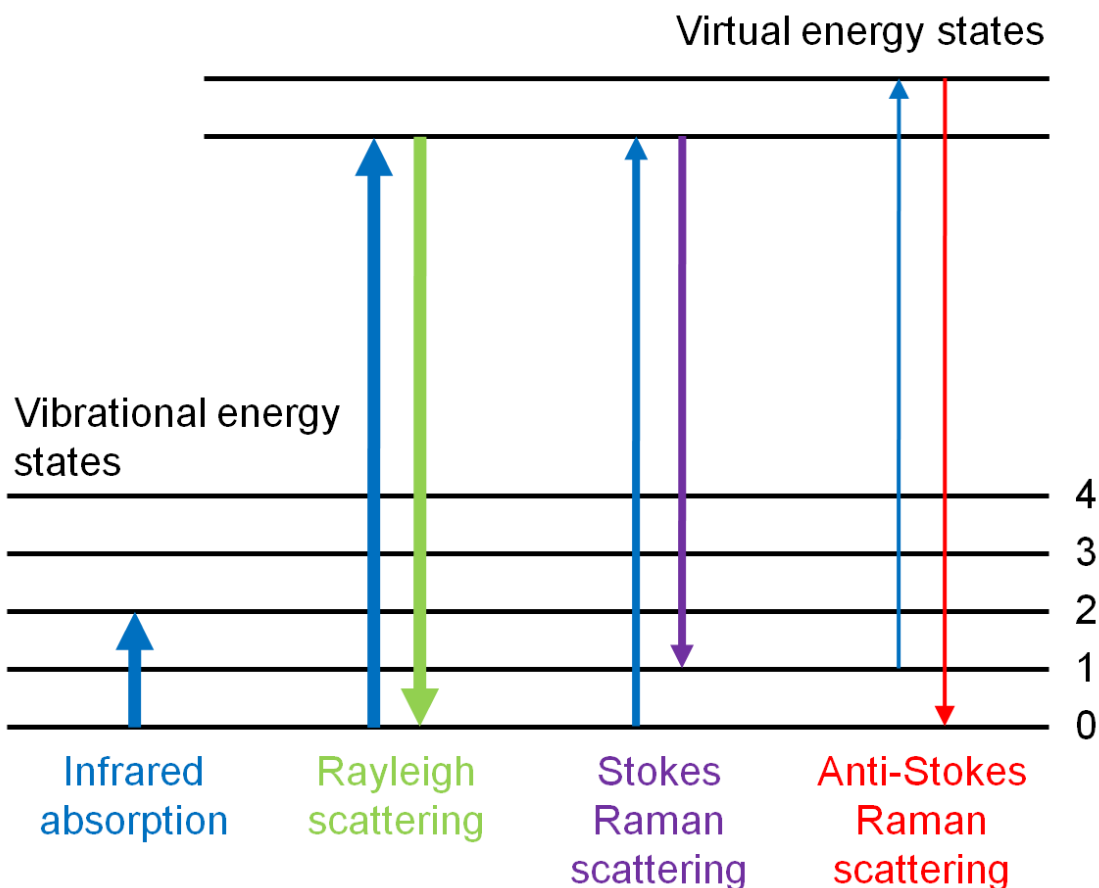
*Figure 2.4: An energy level diagram showing the states involved in IR and Raman spectroscopy; the line thickness represents the signal strength from the different transitions.*

## 2.3 Instrumentation

Various X-ray and neutron diffractometers were used for the data collections presented in this thesis. Sample quality was evaluated and variable temperature (VT) powder X-ray data were collected on a Bruker D8 ADVANCE diffractometer in Durham, and VT powder neutron data were collected on HRPD at ISIS. Single crystal X-ray and neutron data were collected on a Bruker SMART 1000 in Durham and on VIVALDI at the ILL, respectively. In addition, various spectrometers were used throughout this work. INS measurements were made using the instruments IN1 and IN8 at the ILL, while all of the IR and Raman work was undertaken at the Institute of Physical Chemistry in Warsaw, Poland, in the group of Jacek Waluk. All of these instruments are

described in the following section, alongside important details about special attachments.

### 2.3.1  Single Crystal Diffractometers

#### *2.3.1.1  Bruker SMART 1000*

All single crystal X-ray diffraction data were collected on a Bruker SMART 1000 diffractometer with a CCD (Charge Coupled Device) area detector, using a molybdenum X-ray source; MoK$_\alpha$ radiation ($\lambda = 0.711$ Å) is selected exclusively by diffraction from the (111) planes of a graphite monochromator. The temperature of the crystal can be controlled in different ways for different types of experiment. For routine tests of crystal quality at 120 K and data collections at low temperatures an Oxford Cryosystems Cryostream Plus,[13] which uses an open flow of nitrogen gas, was used to control the sample temperature; this is capable of reaching temperatures in the range of 80 to 500 K. For data collections at very low temperatures an Oxford Cryosystems HeliX device,[14] with its open flow of helium gas, was used. This is capable of reaching and sustaining temperatures down to 30 K.

The raw data are collected using the SMART software[15] and integrated using the SAINT suite of programmes;[16] this includes performing an absorption correction in SADABS[17] and reduction in XPREP.[15] The results are output from XPREP into two separate files, a **.**hkl file, which contains a list of the *hkl* reflections and their corresponding intensities, and a **.**ins file, which contains the general unit cell information, space group symmetry and unit cell contents. Finally, a calculated model is refined against the data. The programmes CRYSTALS and SHELXL were used for the single crystal X-ray refinements presented in this thesis.[18, 19]

#### *2.3.1.2  VIVALDI*

Variable temperature single crystal neutron diffraction data were collected on VIVALDI (the Very Intense Vertical Axis Laue Diffractometer) at the ILL[20] (see Figure 2.4). This diffractometer uses a white thermal-neutron beam and is equipped with a cylindrical image plate detector on a vertical axis. The vertical axis facilitates the use of heavy cryostats (enabling temperatures as low as 1.5 K to be produced), furnaces and pressure

cells. The cylindrical detector employs image plates of BaFBr doped with $Eu^{2+}$ ions, with added $Gd_2O_3$ offering high spatial resolution.[21]

During data collection on VIVALDI, the diffraction pattern for a single stationary crystal is recorded and stored. After each exposure the detector is rotated rapidly and a stimulating laser and photomultiplier detector are translated along the length of the cylinder reading out the stored diffraction pattern. The data are processed using the CCP4 Laue suite of programmes;[22] this involves indexing and processing reflection intensities in LAUEGEN,[23, 24] integrating in INTEGRATE+[25] and normalising reflections to a single incident wavelength in LAUENORM.[26] Finally, the SHELXTL package[19] is used for structure solution and refinement.
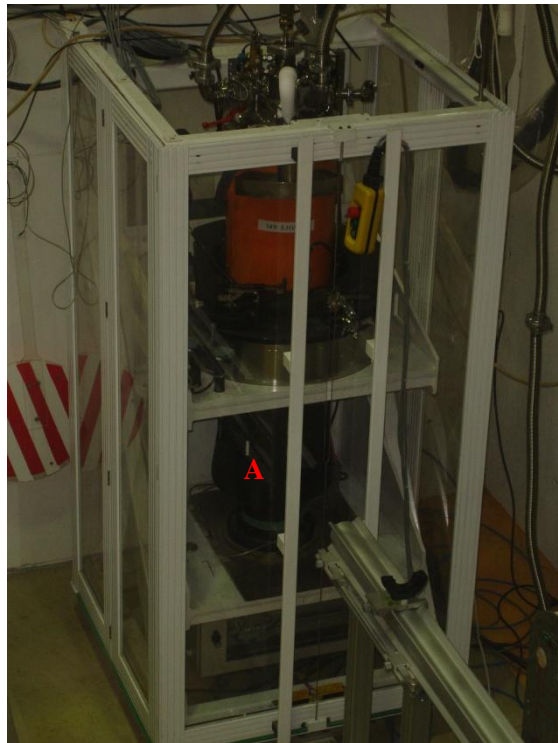


*Figure 2.5: Vivaldi at the ILL, where A is the cylindrical image-plate detector.*

### 2.3.1.3  SXD

At the ISIS spallation source, the neutron beam is pulsed and so neutrons of different wavelengths can be discriminated by their time of arrival at a detector. This is termed time-of-flight (TOF) neutron diffraction, and reflection intensities are obtained as a

function of their TOF at a fixed $2\theta$ angle. Using the standard equation of momentum (Equation 2.21) and the de Broglie relation (Equation 2.22), the wavelength can be written as a function of TOF (Equation 2.23).

$$\boldsymbol{p} = m\boldsymbol{v} = m\frac{d}{t} \qquad \text{(Equation 2.21)}$$

$$\boldsymbol{p} = \frac{h}{\lambda} \qquad \text{(Equation 2.22)}$$

$$\lambda = \frac{ht}{md} \qquad \text{(Equation 2.23)}$$

(where, $\boldsymbol{p}$ is the momentum, $m$ is the mass of a neutron, $\boldsymbol{v}$ is the velocity, $d$ is the neutron pathlength, $t$ is the TOF, $h$ is Planck's constant and $\lambda$ is the wavelength).

Variable pressure single crystal neutron diffraction data were collected on SXD at ISIS.[27] This diffractometer uses the TOF neutron diffraction technique. After leaving the heavy metal target, neutrons pass through an $H_2O$ moderator before reaching the sample, which is positioned at a predetermined angle. Diffracted neutrons are then detected by an array of 11 ZnS position-sensitive detectors, each of which contain a $64 \times 64$ square array of $3 \times 3$ mm pixels allowing large volume of reciprocal space to be explored. The sample may be rotated at intervals in order to collect as much information as possible. The raw data were acquired and analysed in the program SXD2001, and structural analysis was performed using SHELXL.[19, 27, 28]

Variable pressures were attained using a Paris-Edinburgh cell which has been optimised for use on SXD.[29-31] For these high pressure studies only six of the SXD detectors, those centred on the equatorial plane of the instrument (and covering the $2\theta$ ranges 15-60°, 65-115° and 120-160°, and a range of ±22° out of the equatorial plane) could be utilised due to the design of the pressure cell. In addition the sample could only be rotated about a single axis ($\omega$). A 4:1 mixture of deuterated methanol:ethanol was used as the pressure transmitting medium and a null scattering TiZr sample holder (gasket) was used.

## 2.3.2  Powder Diffractometers

### *2.3.2.1  Bruker D8 ADVANCE*

Powder X-ray diffraction data were collected on a Bruker D8 ADVANCE X-ray diffractometer in Durham. This technique was predominantly used throughout this work to obtain data for phase identification and Rietveld refinement. In addition, VT data (using the PheniX attachment as outlined below) were collected on this instrument in order to investigate any structural changes with temperature. All diffraction patterns obtained on the Bruker D8 have been given the labels, d9_xxxxx, where d9 is the local diffractometer code and xxxxx is a five digit reference number. These labels are referred to at relevant points in subsequent chapters.

The Bruker D8 ADVANCE diffractometer uses a copper anode target to generate X-rays with a current of 40 mA and a voltage of 40 kV; $CuK_{\alpha 1,2}$ radiation is provided and a nickel filter removes the $CuK_\beta$ radiation. The X-rays pass through a number of slits (namely a Soller slit and a divergence slit) before reaching the powder sample. A Lynx-Eye detector, containing 192 silicon strip detectors, collects the diffracted X-rays and outputs very high resolution data. The raw data are collected using the Bruker XRD Commander Software[32] and Rietveld refinements are carried out using TOPAS Academic.[33]

Low temperature and VT work was carried out on this instrument using an Oxford Cryosystems PheniX attachment which is capable of reaching and sustaining temperatures in the range of 12 to 310 K. The PheniX is a closed cycle cryostat which uses compressed helium gas provided by a water-cooled compressor. The diffraction slides for a VT PheniX experiment are prepared in the same way as described in Section 2.2.1.4, but with the addition of a small amount of heat conductive grease to the underside of the silicon slide to aid cooling. In order to cool the sample, the slide is fixed inside a chamber on the diffractometer. This is evacuated and then cooled by the conduction of heat between the sample and a coldhead.

In a PheniX experiment, temperatures are controlled and logged by the PheniX CryoPad software[34] and this is independent of the diffractometer software. During a VT

experiment the diffractometer Commander software is programmed to continuously collect patterns for a set amount of time over a set *2θ* range. At the same time the CryoPad software is independently programmed to cool the system at a particular rate and it records the exact system temperature every 60 seconds. The local FORTRAN routine, *phenixlogfile*[35] is then used to obtain the average temperature for each separate scan and multiple Rietveld refinements can be run sequentially using the local command, *multitopas*.[36] *Multitopas* performs sequential refinements on multiple datasets from a single TOPAS input file (*seed.inp*). When *multitopas* is run, an output file is produced for the first dataset (*seed.out*) which is then used as the input file for the next refinement. The results can be output as a **.**res file and imported into Microsoft Excel for further analysis.

### 2.3.2.2  HRPD

Variable temperature powder neutron diffraction data were collected on a time-of-flight neutron diffractometer, namely the High Resolution Powder Diffractometer (HRPD) at ISIS.[37] VT data in the range of 15 to 295 K were obtained in order to investigate structural changes with temperature.

HRPD is the highest resolution neutron diffractometer in the world and, on the pulsed ISIS neutron source, has three contributions to its resolution, $\Delta d/d$: the timing uncertainty, $\Delta t$, the angular uncertainty, $\Delta\theta$ and the neutron flight path uncertainties, $\Delta L$ (Equation 2.24).[38]

$$\frac{\Delta d}{d} = \left[ \left( \frac{\Delta t}{t} \right)^2 + \left( \Delta\theta \cot\theta \right)^2 + \left( \frac{\Delta L}{L} \right)^2 \right]^{\frac{1}{2}} \qquad \text{(Equation 2.24)}$$

The resolution on HRPD is maximised by using a very long neutron flight path, *L* which also increases *t* and hence minimises the $\Delta t/t$ and $\Delta L/L$ ratios. The diffracted neutrons are detected in three fixed *2θ* positions, at 168° (backscatter), 90° and 30° (low angle). The details of these detectors are shown in Table 2.1. The maximum resolution is obtained in backscattering geometry where the angular uncertainty term,

$\Delta d/d = \Delta\theta \cot \theta$, is minimised. It is, therefore, the data from this bank that have been used predominantly throughout this work.

*Table 2.1: Details of the detectors on HRPD.*

| Position | Backscattering | 90 ° | Low angle |
|---|---|---|---|
| Detector Type | ZnS scintillator | ZnS scintillator | 10 atm. $^3$He gas tube |
| $2\theta$ range | 160 - 176 ° | 80 - 100 ° | 28 - 32 ° |
| Resolution | ~ 4 x 10$^{-4}$ | ~ 2 x 10$^{-3}$ | ~ 2 x 10$^{-2}$ |

Data from HRPD are recorded using the Open GENIE programme and processed using Ariel.[39] Data is output as **.**gss and **.**asc files and the local command, *Splithrpdgsas2,*[40] is then used to convert these into **.**xye files for refinement. All refinements in this work were carried out using the local command, *multitopas_files*.[41] This runs Rietveld refinements like the *multitopas* command for PheniX data discussed previously, allowing a large number of individual diffraction patterns obtained at various temperatures to be refined sequentially.

### 2.3.2.3 D20

Variable pressure powder neutron diffraction data were collected on D20 at the ILL.[42] D20 is a high-flux, constant wavelength, 2-axis diffractometer which uses a thermal-neutron beam. It is equipped with a curved linear position-sensitive detector, containing 1536 detection cells covering a continuous $2\theta$ range of 153.6°, and various monochromators. Neutrons with a constant wavelength of 1.54 Å were selected exclusively for this work by reflection from the (113) plane of a germanium monochromator crystal; in addition a take-off angle of 90° was employed.

A Paris-Edinburgh press was used for studies at variable pressure. The pressure cell was linked to a gas pressure generator *via* a flexible high pressure capillary located several metres away from the beam, thus allowing the pressure to be adjusted continuously (from 0 to 40 kbar) while the sample remained in the beam. The pressure transmitting medium was a 4:1 mixture of deuterated methanol:ethanol and the sample holder (gasket) was a TiZr alloy in such a composition (2.08 Ti: 1 Zr) that its coherent scattering length was equal to zero.

The raw data were collected using the NOMAD software, data reduction was performed using LAMP and all structural refinements were carried out in TOPAS Academic.[43]

### 2.3.3 Spectrometers

#### 2.3.3.1 INS

Inelastic neutron scattering experiments were performed on the IN1-BeF and IN8 spectrometers at the ILL. IN1-BeF is a two-axis spectrometer which uses a hot beam of neutrons. It contains a monochromator unit consisting of three vertically focusing monochromators, all built from single crystals of copper in different reflecting planes (Cu(200), Cu(220) and Cu(331)). Incident neutron energies are then selected from the white neutron beam through Bragg reflections from one of these monochromators, *i.e.* the incident energy is varied as a function of the monochromator and its orientation. In this work the Cu(220) monochromator was used. The final neutron energy is then fixed using a liquid-nitrogen-cooled beryllium block between the sample and the detector. This beryllium block scatters the neutrons selectively, permitting only those with a specific energy through to the detector. In the case of this work the final neutron energy was 3.5 meV.

IN8 is a triple axis spectrometer which uses a thermal beam of neutrons. It is equipped with a double focusing monochromator consisting of three faces of differing crystals (PG(002), where PG is pyrolytic graphite, Cu(200) or bent perfect Si(111)). The incident energies are selected through Bragg reflections from one of these faces. The scattered neutrons are then further diffracted by an analyser (PG(002), Si(111) or Cu(111)) which focuses the neutrons onto a single, vertically mounted, $^3$He detector. In this work the Si(111) monochromator and the PG(002) analyser were used and the value of $Q$ was kept constant by rotating the crystal.

Both INS spectrometers were equipped with cryostats allowing data collection as a function of temperature from ambient down to 10 K.

### 2.3.3.2 IR

Fourier-transform infrared (FTIR) spectra were measured using a Nicolet Magna 560 FTIR spectrometer with a MCT/B liquid-nitrogen-cooled detector. Spectra were collected in the range 400 to 4000 cm$^{-1}$ with a spectral resolution of 0.5 cm$^{-1}$. In addition, the spectrometer was equipped with a closed-cycle helium cryostat (CSW-202 N, Advanced Research Systems), allowing measurements as a function of temperature in the range 10 to 323 K.

### 2.3.3.3 Raman

Raman spectra were recorded using an InVia Renishaw Raman spectrometer based on a Leica microscope equipped with objectives with 5× magnification, a 1200 grooves/mm grating, and a thermoelectrically cooled CCD array detector. A 785 nm HPNIR785 laser was used to excite the single crystal sample, though the laser power on the sample was 30 mW or less. A resolution of 5 cm$^{-1}$ and a wavenumber accuracy of ±2 cm$^{-1}$, were used, and both were calibrated with the Rayleigh line and the 520.6 cm$^{-1}$ line of silicon. Samples were carefully checked for possible thermal decomposition, and, whenever necessary, this was avoided by defocusing or lowering the laser power. The Raman spectra were measured as a function of temperature in the range of 79-373 K with the use of a Linkam 650 heat/cool cell.

## 2.4 Auxiliary Characterisation Methods

Nuclear Magnetic Resonance spectroscopy (NMR) and Mass Spectrometry (MS) were used for the quantification of the deuteration levels in various samples of deuterated 3,5-pyridinedicarboxylic acid (as described in Chapter 3).

Solution-state NMR spectroscopy, the most commonly used analytical technique in the characterisation of organic compounds, exploits the magnetic properties of certain nuclei. $^2$D NMR spectra were acquired for this work using a Varian UNITY INOVA 500, a high-resolution FT-NMR spectrometer. As NMR spectroscopy was used for the purpose of accurately determining the deuterium occupancy at each site in a fully deuterated sample of 3,5-pyridinedicarboxylic acid, it was essential that the NMR sample was prepared precisely; it was necessary to ensure that the concentration of

deuterium at the D(2) position (the deuterium position 'para' to the pyridine nitrogen, Chapter 3) was approximately equal to that of the natural abundance of $^2$D in the standard used. The standard used was dimethylsulphoxide (DMSO) and it was found that $0.7\,cm^3$ of DMSO standard and $0.00152\,g$ of the sample were appropriate. However, due to the rapid exchange of a number of labile deuterium atoms for the protons of the DMSO standard, this method was only suitable for determining the deuterium content of the pyridine ring and therefore was not suitable for all samples required throughout this work.

Mass spectrometry, on the other hand, was more useful for a quick check of deuteration. Electron Impact (EI) mass spectrometry was conducted on a Thermo-Finnegan DSQ instrument with a solids probe inlet. EI spectrometry is conducted at low pressure and involves sample ionisation, bombardment with electrons from a heated filament, acceleration by a magnetic field and detection of resulting ion fragments. It is of relatively low resolution compared to other forms of mass spectrometry, but this was sufficient for the work required. The level of deuteration was determined based on the mass/charge ratio of the peak in the spectra with 100 % abundance: for the fully deuterated sample this was 172, for two partially deuterated forms, one in which the pyridine ring was deuterated with the hydrogen bonds remaining protonated and one in which the hydrogen bonds only were deuterated, this was 170 and 169, respectively.

## 2.5 Computational Theory and Tools

A range of computational methods have been used throughout this work in order to calculate various physical and chemical properties of the systems studied; including equilibrium structures, total energies, thermodynamic properties and vibrational frequencies. The results of such calculations have been used to guide and complement experimental work, and hence help to support and enhance conclusions.

There are two computational approaches that can be adopted for the calculation of such properties. These are classified as molecular mechanics (empirical) methods, where electronic structure is not accounted for directly, and quantum mechanics (*ab-initio*) methods, where the electrons are described in detail. These methods range in their accuracy, though the most accurate methods are only feasible for small systems. The

nature of the work undertaken for this thesis required the *ab-initio* approach, and consequently, the fundamentals of this method, for the calculation of energy and forces, are described in the subsequent section. This is followed by a description of the methods used for determining the various physical and chemical properties of interest, and the specific tools used for these purposes.

## 2.5.1  Calculating Energy and Forces

*Ab-initio* calculations deal with solving the time-independent Schrödinger equation, Equation 2.25, for a given system in order to determine the energy levels, and other properties, such as vibrational frequencies, of atoms and molecules.[44]

$$\hat{H}\psi = E\psi \qquad\qquad \text{(Equation 2.25)}$$

where $E$ is the total energy of the system, $\psi$ is the nuclear-electronic wavefunction (which depends on the coordinates of all electrons and all nuclei in the system), and $\hat{H}$ is the Hamiltonian operator. The Hamiltonian operator, Equation 2.26, comprises the kinetic and potential energy terms of a system containing $N$ electrons and $M$ nuclei.

$$\hat{H} = \hat{T} + \hat{V}$$

$$= \hat{T}_e + \hat{T}_n + \hat{V}_{en} + \hat{V}_{ee} + \hat{V}_{nn}$$

$$= -\sum_i^N \frac{\hbar^2}{2m_e}\nabla_i^2 - \sum_A^M \frac{\hbar^2}{2m_A}\nabla_A^2 - \sum_{Ai}\frac{Z_A e}{4\pi\varepsilon_0 r_{Ai}} + \sum_{i<j}\frac{e^2}{4\pi\varepsilon_0 r_{ij}} + \sum_{A<B}\frac{Z_A Z_B}{4\pi\varepsilon_0 r_{AB}}$$

$$\text{(Equation 2.26)}$$

where $\hat{T}$ and $\hat{V}$ are the kinetic and potential energy of the electrons (*e*) and nuclei (*n*), *i* and *j* run over all electrons and *A* and *B* over all nuclei. The terms $m_A$ and $Z_A$ are the mass and charge of nucleus *A*, and $m_e$ and *e* are the electronic mass and charge. $r_{Ai}$ is the distance between nucleus *A* and electron *i*, $r_{ij}$ is the distance between electrons *i* and *j* and $r_{AB}$ is the distance between nuclei *A* and *B*. Finally, $\nabla^2$ is the Laplacian operator, which describes the curvature of the wavefunction.

Solving the Schrödinger equation requires calculating the value of the total energy, *E,* for the system. For 'many-body' systems this leads to equations too complicated to be solvable, and a number of approximations are therefore required. One such approximation is the Born Oppenheimer approximation, which is centred on the fact that electrons are very light compared to nuclei.[45] For each nuclear configuration, nuclei are therefore regarded as being clamped in space with the electrons moving around within this fixed nuclear framework. In basic terms this approximation allows the electronic and nuclear components of the wavefunction to be treated independently. It also causes the nuclear kinetic energy to become zero, and the nuclear potential energy to become a constant, for a particular nuclear configuration, reducing the Schrödinger equation and Hamiltonian operator to their electronic forms, Equations 2.27 and 2.28.

$$\hat{H}_e \psi_e = E_e \psi_e \tag{Equation 2.27}$$

$$\hat{H}_e = -\sum_i^N \frac{\hbar^2}{2m_e} \nabla_i^2 - \sum_{Ai} \frac{Z_A e}{4\pi\varepsilon_0 r_{Ai}} + \sum_{i<j} \frac{e^2}{4\pi\varepsilon_0 r_{ij}} + \sum_{A<B} \frac{Z_A Z_B}{4\pi\varepsilon_0 r_{AB}} \tag{Equation 2.28}$$

where $\psi_e$ is the electronic wavefunction which depends on the coordinates of all the electrons and $E_e$ is the electronic energy, for a given arrangement of nuclei. If the nuclear coordinates are varied, both $\psi_e$ and $E_e$ change; the change in $E_e$ as a function of the nuclear coordinates defines the potential energy surface (PES).

Equation 2.28, while significantly simplified, still contains a fundamental problem in that only one-electron systems can be solved by it exactly. This is due to the difficulty in obtaining the electron interaction term (the 3rd term of the electronic Hamiltonian, Equation 2.28). In this term two separate electron behaviours have to be described, namely, correlation and exchange effects. Correlation takes account of the fact that electrons are coupled; electrons repel each other and the movement of one electron has an instantaneous effect on all others. Exchange takes account of the fact that electrons with the same quantum numbers *n, l* and $m_l$ but opposite spins are able to pair up, while those with like spins avoid each other. A number of very different approaches have been used to develop methods which attempt to deal with these effects and find approximate

solutions to the Schrödinger equation. It is the method of density functional theory (DFT) that has been used throughout this work and therefore this is described below.

The key idea in DFT is that the complex many-body electronic wavefunction, $\psi_e$, can be replaced by the much simpler one-electron density, $\rho(\boldsymbol{r})$, which depends only on the atomic coordinates, *x*, *y* and *z*.

In 1964, Hohenburg and Sham[46] proved that $E_e$ could be rigorously expressed in terms of $\rho(\boldsymbol{r})$ due to the fact that the external potential of the nuclei (the 2nd term in Equation 2.28) uniquely determines the electron density. The density can then be used to determine the number of electrons, *N*, through Equation 2.29. (Note also that the 1st and 3rd terms of Equation 2.28 are completely determined by the number of electrons, *N*, while the 4th term is a constant for a particular nuclear configuration).

$$\int \rho(\boldsymbol{r}_1)d\boldsymbol{r}_1 = N \qquad\qquad \text{(Equation 2.29)}$$

As a result of this, the density uniquely determines the Hamiltonian, $\hat{H}$, which, in turn, determines the wavefunction and all properties (such as energy) *via* the Schrödinger equation. $E_e$ can, therefore, be written as shown in Equation 2.30, omitting the nuclear-nuclear repulsion constant for clarity.

$$E_e = E_e[\rho] = T[p] + V_{en}[p] + V_{ee}[p] \qquad\qquad \text{(Equation 2.30)}$$

The problem with this equation is that *T[ρ]* is very large and difficult to express in terms of *ρ*, and so, in 1965, Kohn and Sham[47] rearranged this expression to give Equation 2.31.

$$E_e = T_s[p] + V_{en}[p] + J[p] + \left(T[p] - T_s[p] + V_{ee}[p] - J[p]\right) \qquad \text{(Equation 2.31)}$$

where $T_s$ is the kinetic energy of a non-interacting system with the same density as the true system. The final term (in round brackets) is the exchange-correlation energy, $E_{xc}[\rho]$, which contains the difference between the exact electron-electron repulsion and the Coulomb energy together with a small kinetic energy term.

The main problem with DFT is that the exchange-correlation term, $E_{xc}[\rho]$, is not known and must, therefore, be approximated. A number of functionals exist for this reason, including PBE, PW91 and BLYP.[48-52] These functionals are based on a number of classes of approximations; two widely used approximations are local density approximations (LDA) and generalised gradient approximations (GGA). LDAs depend only on the local density at each point in space, whereas GGAs introduce additional information regarding the gradient of the density. The GGA method is the most suitable for calculating the physical properties of hydrogen-bonded systems,[53, 54] due to the delocalised nature of the electron density in hydrogen bonds and, as such, has been the method of choice throughout this work, with the Perdew, Burke and Ernzerhof (PBE) functional being employed.[48]

From Equation 2.31, it follows that the exact density is given by Equation 2.32, where $\varphi_i$ are a set of orbitals known as the Kohn-Sham orbitals obtained from a set of one-electron equations known as the Kohn-Sham equations, Equation 2.33.

$$\rho(\boldsymbol{r}) = \sum_i \varphi_i^2(\boldsymbol{r}) \qquad \text{(Equation 2.32)}$$

$$\hat{F}^{KS}\varphi_i(\boldsymbol{r}) = \varepsilon_i\varphi_i(\boldsymbol{r}_1) \qquad \text{(Equation 2.33)}$$

where $\hat{F}^{KS}$ contains the kinetic energy operator, the external potential due to the nuclei, the coulomb potential and an exchange term.

In practice, solving the Schrödinger equation using DFT is a self-consistent procedure and requires finding the solutions to the Kohn-Sham equations, *i.e.* the one-electron molecular orbitals, $\varphi_i$, and the orbital energies, $\varepsilon_i$. This involves expanding these molecular orbitals linearly in terms of a set of mathematical functions (a basis set), $\eta_\beta$, Equation 2.34; commonly these basis sets are atomic orbitals (AO) or plane waves (PW).

$$\varphi_i(r) = \sum_\beta c_{\beta i}\eta_\beta(\boldsymbol{r}) \qquad \text{(Equation 2.34)}$$

where $c_{\beta i}$ is the expansion coefficient.

In the atomic orbital approach the basis set is composed of a finite number of atomic orbitals centred at each atomic nucleus within the molecule. In the plane wave approach the basis set is composed of sets of plane waves which are uncoupled from the atomic nuclei, Equation 2.35. Due to the fact that such a large quantity of plane waves would be required to describe the high electron densities near the nuclei, core pseudopotentials or projector-augmented wave (PAW) potentials are also commonly employed in this approach; these are smooth potentials used to account for the core electrons, *i.e.* the electrons less involved in the determination of the physical properties of the molecules, reducing the number of plane waves required.

$$\varphi_i(\boldsymbol{r}) = \sum_k c_{ik} \exp(i\boldsymbol{k}.\boldsymbol{r}) \qquad \text{(Equation 2.35)}$$

where $\boldsymbol{k}$ is the wavevector of the plane wave, defined as the vector parallel to the direction of propagation of the wave.

DFT allows generally accurate calculations to be performed, and, due to its treatment of electrons, proton migration behaviour can be accounted for. The main disadvantage of the method is a result of the approximations of $E_{xc}[\rho]$; as these approximations are all over a local range, non-local effects, such as dispersion (van der Waals), are not taken into account. In addition, quantum mechanical techniques in general are relatively slow, in comparison to empirical methods, with computational cost scaling as $N^3$ for simple DFT calculations (this is worse for more complex calculations). For this reason, only relatively small systems (up to a few hundred atoms) and short timescales (up to 100 ps) can feasibly be studied; quantum methods are not really possible for very large systems, such as proteins and polymers.

Once the spatial distribution of the electrons has been determined, by solving the Schrödinger equation, the forces acting on each of the atoms can be calculated. In *ab-initio* calculations, the forces acting on an atom are calculated as the negative of the derivative of the total energy with respect to the nuclear positions. In addition, the Hellman-Feynman theorem relates the derivative of the total energy with respect to the

nuclear positions, to the expectation value of the derivative of the Hamiltonian with respect to the nuclear positions, Equation 2.36.

$$\boldsymbol{F} = -\frac{dE_e}{dx} = -\left\langle \psi \left| \frac{d\hat{H}_e}{dx} \right| \psi \right\rangle$$

(Equation 2.36)

### 2.5.2 Using Energy and Forces

It must be pointed out that, for all of the calculations reported in this thesis, periodic boundary conditions have been employed. These allow the simulation of a large system by modelling a small building block that is representative of the whole system; the unit cell is usually used for this purpose. Then, during a calculation, when part of one particle passes through a face of the unit cell, its periodic image enters the opposite face (the equivalent position) with the same velocity. Periodic boundary conditions are employed alongside the minimum image convention, where a particle in the simulation interacts with the nearest image of the remaining, surrounding particles in the system, regardless of which unit cell the nearest particle is in.

#### 2.5.2.1 Single-Point Energy Calculations

A single point energy calculation calculates the wavefunction and charge density, and hence the total energy, for a particular arrangement of nuclei, independent of time (as described in Section 2.5.1).

#### 2.5.2.2 Geometry Optimisation

A common task in molecular simulations is the optimisation, or minimisation with respect to potential energy, of the geometry of a given molecule or crystal structure, in order to attain a stable state with the forces acting on the atoms as close to zero as possible, as would be found at 0 K. This optimisation is a two-stage process. Initially the energy of a system needs to be evaluated for a given conformation, which is achieved by a single-point energy calculation. Following this the coordinates of the atoms (and possibly the cell parameters) are adjusted in order to minimise the total energy of the system; this is an iterative process, with the two-stage cycle being repeated until the equilibrium structure is reached. A number of algorithms exist for

performing these geometry optimisation calculations, varying in their accuracy and computational cost. The total number of iterations required to minimise the energy of the system depends on the nature of this algorithm as well as the number of atoms present in the structure. Overall, the efficiency of the process can be judged by the computational time required to evaluate the energy and the number of iterations required for convergence. Owing to the large amount of computational time required for such calculations, it is imperative that a sensible starting model is used; the time spent optimising the geometry of a crystal structure would be in vain if the atoms were incorrectly placed within the unit cell or the initial lattice parameters were far from expected.

### 2.5.2.3  Molecular Dynamics

Molecular dynamics (MD) simulations provide the possibility to study the physical evolution of a system over time and are based on solving Newton's law of motion, Equation 2.37.

$$\boldsymbol{F}_i = m_i\boldsymbol{a}_i = m_i\frac{d^2\boldsymbol{r}_i}{dt^2} \qquad\qquad \text{(Equation 2.37)}$$

where $\boldsymbol{F}_i$, $m_i$, $\boldsymbol{a}_i$ and $\boldsymbol{r}_i$ are the force, mass, acceleration and position of atom $i$ at time $t$.

Such simulations result in a trajectory, a set of atomic coordinates and velocities for the structures generated at a sequence of timesteps, at finite temperature. In general, the starting structure for MD calculations is the equilibrium structure, obtained by a geometry optimisation calculation. This system is then displaced from equilibrium by an initial impulse, corresponding to the temperature *via* the kinetic energy of the atoms, generating an initial set of atomic coordinates and velocities for the MD calculation. The forces acting on the atoms of this initial structure are computed from an expression of the total energy of the system as the derivatives with respect to the appropriate atomic coordinates, Equation 2.36. Consequently, the accelerations acting on each atom can be calculated, Equation 2.37, and, hence, the coordinates and velocities at a later time can be determined, Equations 2.38 and 2.39 respectively;[55] each subsequent structure in the trajectory is calculated from the previous structure in this way.

$$r(t + dt) = r(t) + v(t)dt + \frac{a}{2}dt^2 ...$$ (Equation 2.38)

$$v(t + dt) = v(t) + a(t)dt...$$ (Equation 2.39)

When simulating in the bulk it is usually necessary to conserve certain quantities. These conserved quantities define the ensemble that is used. In this work the microcanonical (*NVE*) and canonical (*NVT*) ensembles have been used; in the *NVE* ensemble, the number of particles (*N*), the volume (*V*) and the total free energy (*E*) are kept constant, whereas in the *NVT* ensemble the temperature (rather than the free energy) is kept constant.

A number of INS observables, such as the scattering function, $S(Q,\omega)$, can be extracted from the MD trajectory *via* time-dependent correlation functions.[55]

### 2.5.2.4  Lattice Dynamics

Lattice dynamics (LD) calculations provide the possibility to study the vibrations of atoms in crystals, and allow the determination of various thermodynamic properties, such as free energy. As with MD, forces are central to this method, and the starting point for the calculation is the equilibrium (geometry optimised) structure.

In the study of lattice dynamics, the potential energy surface is harmonically approximated, and this is sufficiently accurate to describe the effects of interest in this work. In addition, atomic motions are frequently found to be adequately described as travelling waves, characterised in terms of a wavevector, *k*, angular frequency, $\omega$, an amplitude and a direction of travel; where *k* is normalised such that $|k| = 2\pi/\lambda$, $\omega$ is calculated as $\sqrt{k/m}$ (where *k* is the force constant and *m* is the mass) and is a function of both *k* and the inter-atomic forces, and the amplitude is a function of $\omega$ and temperature. (The dependence of $\omega$ on *k* is dispersion). Such a wave, travelling through a crystal, displaces an atom, with a mass, *m*, at a position, *r*, by a certain amplitude. This displacement induces inter-atomic forces on all the atoms of the system, calculated by $F = ma = -kx$.

In order to describe/calculate these waves interatomic forces are, therefore, required. A complete set of interatomic forces are obtained by individually displacing all the atoms of the crystal along each of the Cartesian directions. These forces are then used to construct the dynamical matrix (DM), Equation 2.40, which is an expression of all of the atomic interactions in the system. Diagonalising the DM results in a set of normal modes (NM), each one having a characteristic frequency (obtained from the eigenvalues) and a displacement vector (obtained from the eigenvectors) describing the relative motion of all of the atoms in that mode.

$$\boldsymbol{D}_{ij}(\boldsymbol{k}) = \frac{1}{\sqrt{m_i m_j}} \sum_{i,j} k_{ij} \exp\left(i\boldsymbol{k} \cdot \left(\boldsymbol{r}_i - \boldsymbol{r}_j\right)\right)$$
(Equation 2.40)

where the indices, $i$ and $j$, run over all atoms, and $m$ and $\boldsymbol{r}$ are the masses and positions of the atoms present, respectively. The matrix $k_{ij}$ is the Hessian matrix (a matrix of force constants resulting from DFT).

Again, a number of INS observables, such as the scattering function, $S(\boldsymbol{Q},\omega)$, described previously, can be constructed, in this case from the set of NM. The free energy is calculated from the eigenvalues.

## 2.5.3  Tools

A range of *ab-initio* calculations have been performed throughout this work using the CASTEP, DMol[3] and VASP DFT codes.[56-60] Whilst the specific parameters used for each calculation are given in relevant places in the following chapters, a general overview of these codes, their use in this work, and a description of their important parameters is given here.

CASTEP is a software package[56] which uses DFT with a PW basis set to calculate the electronic properties of a variety of materials. In this work it has been employed for a range of geometry optimisation calculations, in which the default minimisation method, BFGS, was used, as well as various molecular dynamics calculations.

DMol$^3$ is a software package[57, 58] which uses DFT with a localised atomic orbital (AO) basis set to calculate the properties of materials rapidly and accurately. In this work it has been employed for the calculation of vibrational frequencies, allowing properties such as the partial densities of states to be obtained, and various single-point energy calculations. Both CASTEP and DMol$^3$ have been used in the Materials Studio$^®$ software environment.

VASP is a package[59, 60] for performing *ab-initio* MD using DFT with the PAW method[61] and a PW basis set. In this work it has been predominantly used for geometry optimisation and MD simulations.

These three different codes have been used throughout this work simultaneously for various reasons. Initial work[62] on 35PDCA (a large focus of this thesis, see later) was performed in VASP, and therefore this code was used in order to continue and expand this previous work. CASTEP was readily available in Materials Studio$^®$ and therefore allowed quick and easy comparisons with the VASP data. In contrast to these codes, which use a PW basis set, DMol$^3$ uses a basis set of localised atomic orbitals. With this code the high temperature form of 35PDCA could be stabilised (see Chapters 3 and 5) allowing a range of calculations to be performed which were not possible with the PW codes.

## 2.6  References

1. A. Rabenau, *Angew. Chem. Int. Ed. Engl.*, 1985, **24**, 1026.
2. C. G. Shull and E. O. Wollan, *Science*, 1948, **108**, 69.
3. A. L. Patterson, *Phys. Rev.*, 1934, **46**, 372.
4. A. L. Patterson, *Z. Kristallogr. Kristallgeom. Kristallphys. Kristallchem.*, 1935, **90**, 517.
5. D. Harker and J. S. Kasper, *J. Chem. Phys.*, 1947, **15**, 882.
6. H. M. Rietveld, *J. Appl. Crystallogr.*, 1969, **2**, 65.
7. R. A. Young, ed., *The Rietveld Method*, Oxford University Press, 1993.
8. I. R. Evans, J. A. K. Howard and J. S. O. Evans, *J. Mater. Chem.*, 2003, **13**, 2098.
9. P. Thompson, D. E. Cox and J. M. Hastings, *J. Appl. Crystallogr.*, 1987, **20**, 79.
10. G. J. Kearley and M. R. Johnson, *Vib. Spectrosc.*, 2010, **53**, 54.
11. B. S. Hudson, *Vib. Spectrosc.*, 2006, **42**, 25.
12. P. Schuster, G. Zundel and C. Sardorfy, eds., *The Hydrogen Bond*, North-Holland, 1976.
13. J. Cosier and A. M. Glazer, *J. Appl. Crystallogr.*, 1986, **19**, 105.

14.     *Oxford Cryosystems Newsletter*, February 2004.
15.     *Bruker SMART v5.629*, Bruker AXS Inc., Madison, WI, USA, 2000.
16.     *Bruker SAINT+ v6.45*, Bruker AXS Inc., Madison, WI, USA, 2003.
17.     G. M. Sheldrick, *SADABS*, University of Gottingen, Germany, 1996.
18.     P. W. Betteridge, J. R. Carruthers, R. I. Cooper, K. Prout and D. J. Watkin, *J. Appl. Crystallogr.*, 2003, **36**, 1487.
19.     G. M. Sheldrick, *SHELXL* Bruker AXS Inc., University of Gottingen, Germany, 2000.
20.     C. J. Wilkinson, J. A. Cowan, D. A. A. Myles, F. Cipriani and G. J. McIntyre, *Neutron News*, 2002, **13**, 37.
21.     G. J. McIntyre, M.-H. Lemee-Cailleau and C. J. Wilkinson, *Physica B*, 2006, **385-386**, 1055.
22.     J. R. Helliwell, J. Habash, D. W. J. Cruickshank, M. M. Harding, T. J. Greenhough, J. W. Campbell, I. J. Clifton, M. Elder, P. A. Machin, M. Z. Papiz and S. Zurek, *J. Appl. Crystallogr.*, 1989, **22**, 483.
23.     J. W. Campbell, *J. Appl. Crystallogr.*, 1995, **28**, 228.
24.     J. W. Campbell, Q. Hao, M. M. Harding, N. D. Nguti and C. J. Wilkinson, *J. Appl. Crystallogr.*, 1998, **31**, 23.
25.     C. J. Wilkinson, H. W. Khamis, R. F. D. Stansfield and G. J. McIntyre, *J. Appl. Crystallogr.*, 1988, **21**, 471.
26.     J. W. Campbell, J. Habash, J. R. Helliwell and K. Moffat, *Information Quarterly for Protein Crystallography, No. 18*, SERC, Daresbury Laboratory, Warrington, England, 1986.
27.     D. A. Keen, M. J. Gutmann and C. C. Wilson, *J. Appl. Crystallogr.*, 2006, **39**, 714.
28.     G. M. Sheldrick, *Acta Crystallogr., Sect. A*, 2008, **64**, 112.
29.     S. Klotz, G. Hamel and J. Frelat, *High Press. Res.*, 2004, **24**, 219.
30.     C. L. Bull, M. Guthrie, R. J. Nelmes, J. S. Loveday, H. Hamidov and M. J. Gutmann, *High Press. Res.*, 2009, **29**, 644.
31.     C. L. Bull, M. Guthrie, R. J. Nelmes, J. S. Loveday, K. Komatsu, H. Hamidov and M. J. Gutmann, *High Press. Res.*, 2009, **29**, 780.
32.     *Diffrac+ XRD Commander v2.3: Software for Controlling Bruker Diffractometers*, Bruker AXS, Karlsruhe, 2000.
33.     A. A. Coehlo, *TOPAS Academic: General profile and structure analysis software for powder diffraction data*, Bruker AXS, Karlsruhe, 2000.
34.     *Cryopad v1.484*, Oxford Cryosytems, 2007.
35.     J. S. O. Evans, *phenixlogfile*, Fortran 77 program, Durham, 1999.
36.     J. S. O. Evans, *Multitopas*, Fortran 77 Routine, University of Durham, 1999.
37.     R. Ibberson, W. I. F. David and K. S. Knight, *A User Guide, ISIS Crystallography*, 1992.
38.     T. G. Worlton, J. D. Jorgensen, R. A. Beyerlein and D. L. Decker, *Nuclear Instruments & Methods*, 1976, **137**, 331.
39.     P. G. Radaelli, T. Proffen and L. C. Chapon, *Ariel 4.0*, ISIS Facility, Oxford, UK, 2008.
40.     J. S. O. Evans, *Splithrpdgsas2*, Fortran 77 routine, Durham, 2007.
41.     J. S. O. Evans, *Multitopas_files*, Fortran 77 routine, Durham, 1999.
42.     T. C. Hansen, P. F. Henry, H. E. Fischer, J. Torregrossa and P. Convert, *Meas. Sci. Technol.*, 2008, **19**, 034001.
43.     A. A. Coehlo, *TOPAS Academic: General profile and structure analysis software for powder diffraction data*, Bruker AXS, Karlsruhe, 2005.

44. E. Shrodinger, *Ann. Phys.*, 1926, **79**, 489.
45. M. Born and R. Oppenheimer, *Ann. Phys.*, 1927, **84**, 457.
46. P. Hohenberg and L. J. Sham, *Phys. Rev. B*, 1964, **136**, 864.
47. W. Kohn and L. J. Sham, *Phys. Rev. A*, 1965, **140**, 1133.
48. J. P. Perdew, K. Burke and M. Ernzerhof, *Phys. Rev. Lett.*, 1997, **78**, 1396.
49. J. P. Perdew, J. A. Chevary, S. H. Vosko, K. A. Jackson, D. J. Singh and C. Fiolhais, *Phys. Rev. B*, 1992, **46**, 6671.
50. A. D. Becke, *Phys. Rev. A*, 1988, **38**, 3098.
51. C. Lee, W. Yang and R. G. Parr, *Phys. Rev. B*, 1988, **37**, 785.
52. B. Miehlich, A. Savin, H. Stoll and H. Preuss, *Chem. Phys. Lett.*, 1989, **157**, 200.
53. J. P. Perdew, K. Burke and M. Ernzerhof, *Phys. Rev. Lett.*, 1996, **77**, 3865.
54. D. C. Patton, D. V. Porezag and M. R. Pederson, *Phys. Rev. B*, 1997, **55**, 7454.
55. M. R. Johnson, M. Zbiri, M. A. Gonzalez, E. Pellegrini, P. Calligari, L. Capogna, E. Farhi, A. Filhol, R. Ghosh and D. Richard, *Collection SFN*, 2010, **10**, 427.
56. S. J. Clark, M. D. Segall, C. J. Pickard, P. J. Hasnip, M. J. Probert, K. Refson and M. C. Payne, *Z. Kristall.*, 2005, **220**, 567.
57. B. Delley, *J. Chem. Phys.*, 1990, **92**, 508.
58. B. Delley, *J. Chem. Phys.*, 2000, **113**, 7756.
59. G. Kresse and J. Hafner, *Phys. Rev. B*, 1993, **47**, 558.
60. G. Kresse and J. Furthmuller, *Phys. Rev. B*, 1996, **54**, 11169.
61. P. E. Blochl, *Phys. Rev. B*, 1994, **50**, 17953.
62. F. Fontaine-Vive, M. R. Johnson, G. J. Kearley, J. A. Cowan, J. A. K. Howard and S. F. Parker, *J. Chem. Phys.*, 2006, **124**, 234503.

# 3  3,5-Pyridinedicarboxylic Acid: the Isotope Effect and the Structural Origin of H/D Migration

The crystal structure of fully protonated 3,5-pyridinedicarboxylic acid (*h*-35PDCA) was first solved by Takusagawa *et al.*[1] in the monoclinic space group $P2_1/c$. It crystallises with four molecules in the unit cell (one in the asymmetric unit) arranged in infinite two-dimensional planar sheets perpendicular to the *c* axis, Figure 3.1a.
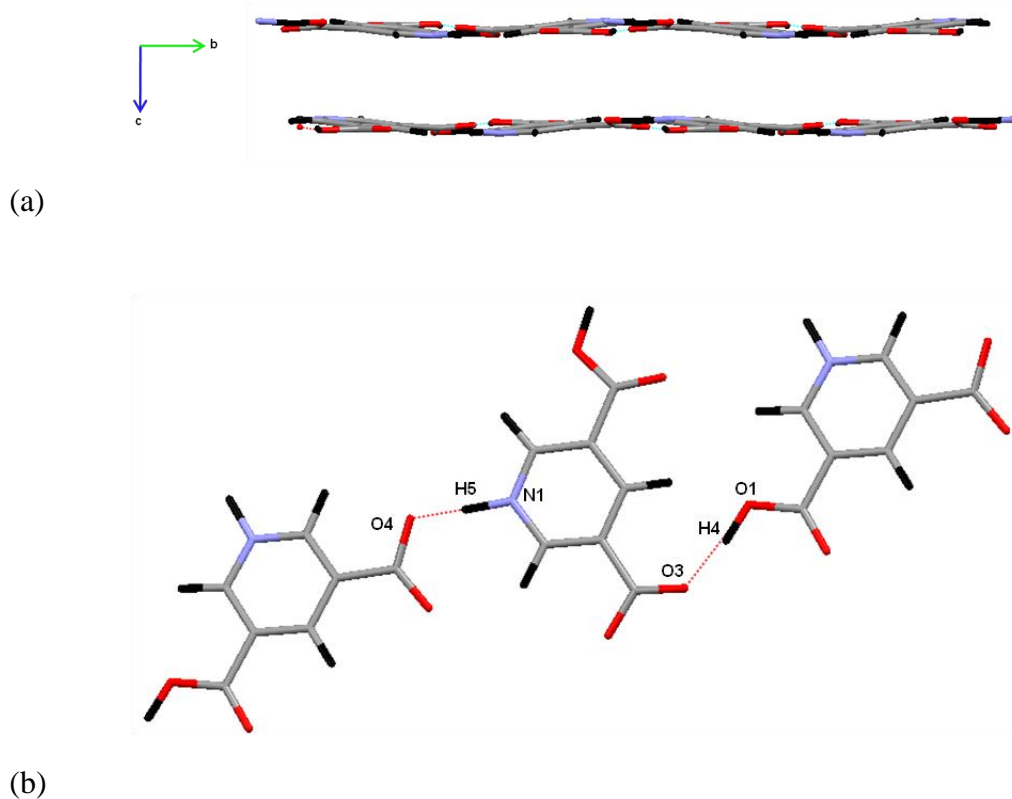


(a)



(b)

*Figure 3.1: (a) The packing of 35PDCA as viewed down the a axis. (b) The structure of 35PDCA in the ab plane, highlighting the SSHB (N1–H5···O4), at 15 K.*

The two dimensional structure is stabilised by a number of intermolecular hydrogen bonds in the layers, including an N–H···O bond with a donor-acceptor separation of 2.52 Å at 15 K, Figure 3.1a;[2] this is one of the shortest N···H···O bonds reported in the literature, as demonstrated by Figure 1.1b in Chapter 1. It also contains a further, 'normal' medium-length O···H···O hydrogen bond with an O···O separation of 2.57 Å at

66

15 K; no significant interactions exist along the *c* axis due to the staggered nature of the pyridine rings preventing any π-π overlap, and the large distance of 2.89 Å between the sheets preventing any interactions stronger than van der Waals forces.

A two temperature single crystal neutron diffraction study on the fully protonated compound has shown that a reversible, temperature-dependent, proton migration occurs in the short N···H···O hydrogen bond. At 15 K the proton lies closer to the pyridyl nitrogen atom, with an N–H distance of 1.213 Å and an O···H distance of 1.311 Å. At 296 K, however, it lies closer to the oxygen atom of a carboxylic acid group in an adjacent molecule, with an N···H distance of 1.308 Å and an O–H distance of 1.218 Å.[2]

A deuterated form of 35PDCA (*d*-35PDCA, in which all hydrogen atoms have been replaced by deuterium) has also been studied by single crystal neutron diffraction. This was found to be isomorphous with the protonated material and to exhibit deuteron migration. An inspection of certain structural parameters determined for this sample, however, reveals two unusual features. Firstly, while the unit cell volumes are very similar at 15 K (660.2(2) Å$^3$ and 661.7(2) Å$^3$ for *h*-35PDCA and *d*-35PDCA, respectively), they differ by approximately 12 Å$^3$ at 296 K (678.85(9) Å$^3$ and 691.0(1) Å$^3$). Secondly, the magnitude of migration in the two forms is dramatically different: the proton in *h*-35PDCA moves away from the nitrogen donor (N1) and towards the centre of the hydrogen bond by 0.095(7) Å between 15 and 296 K, whereas the deuteron shift in the same region is considerably larger at 0.306(5) Å.[2]

The deuteron migration in *d*-35PDCA is significantly larger than any proton displacement found in any other systems thus far, the magnitude of which is typically around 0.1 Å (0.08(1) Å in MP-PCP and 0.095(5) Å in BTA-BPY).[3, 4] These large differences are surprising in light of the small perturbations expected, and generally found, on isotopic substitution.[5] The relative magnitudes of the proton and deuteron shifts in 35PDCA are also unusual given the smaller zero-point motion of deuterium, which might be expected to localise it near the donor atom and preclude its migration. INS experiments and *ab-initio* MD studies have also been reported for *h*-35PDCA and a partially deuterated form (*acid-d*-35PDCA, in which the ring hydrogen atoms remain protonated but those in the hydrogen bonds are deuterated). The experiments and simulations provide compelling evidence that low-frequency lattice phonon modes,

which change little on deuteration in terms of frequency and character, have an important role in driving the proton and deuteron migration in the two forms of this material.[6] This conclusion, however, again points to the open question of the origin of the unusual differences in the proton and deuteron shifts observed by diffraction.

Recent variable temperature powder diffraction work on *d*-35PDCA revealed an unexpected phase transition from powder X-ray and neutron diffraction between 150 and 200 K, Figure 3.2.[7]
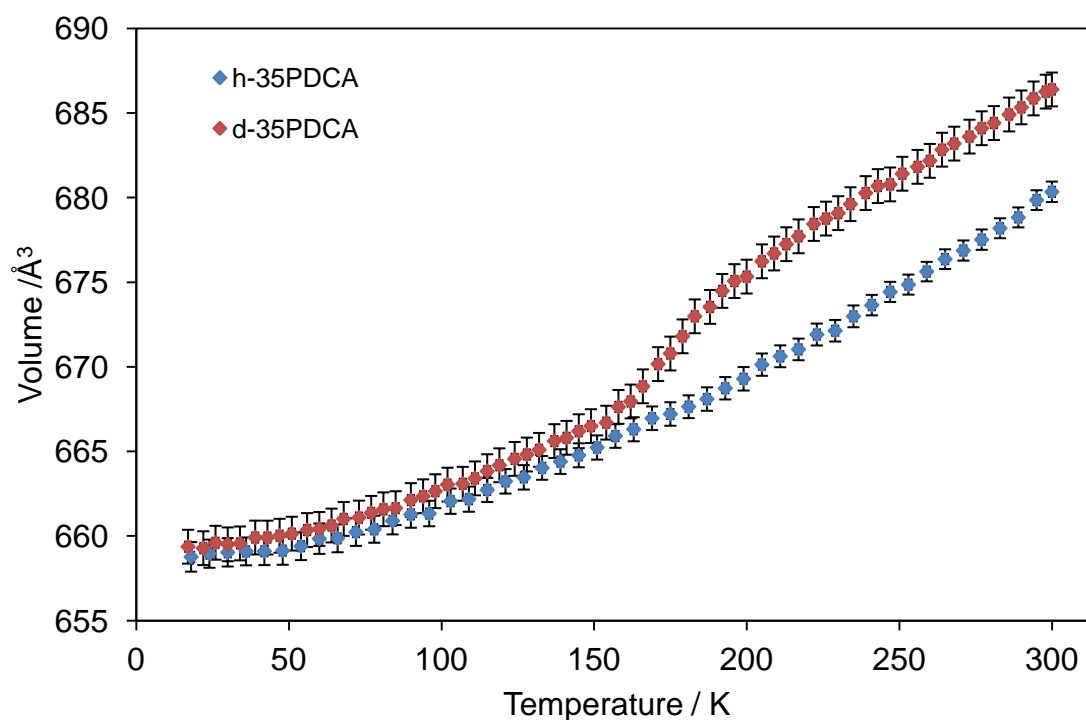


*Figure 3.2: The dependence of the unit cell volume on temperature for h-35PDCA and d-35PDCA. Different behaviour in the unit cell volume as a function of temperature is clearly visible.*

The aim of this work was to investigate the nature of this phase transition, to determine any role it may have in the remarkably large deuteron migration in *d*-35PDCA, and to gain further insight into the isotope effect in this material. For this purpose, four isotopologues of the material will be prepared. These isotopologues are shown in Figure 3.3, and vary by deuteration of the hydrogen bonds and the ring protons. Those shown include fully deuterated *d*-35PDCA, fully protonated *h*-35PDCA and two

partially deuterated forms: *ring-d*-35PDCA, in which the ring is deuterated and the hydrogen bonds remain protonated, and *acid-d*-35PDCA, in which the ring remains protonated and the hydrogen bonds are deuterated. In order to address the issues stated above, a combination of experimental and computational methods will be used: both variable temperature powder and single crystal neutron diffraction will be used to study changes in the structure of the isotopologues with temperature, and free energy calculations will be used to clarify the observed isotope effects and the role of vibrations in driving the phase transition.



|  |  |  |  |
|---|---|---|---|
| *d*-35PDCA | *ring-d*-35PDCA | *acid-d*-35PDCA | *h*-35PDCA |
| (a) | (b) | (c) | (d) |
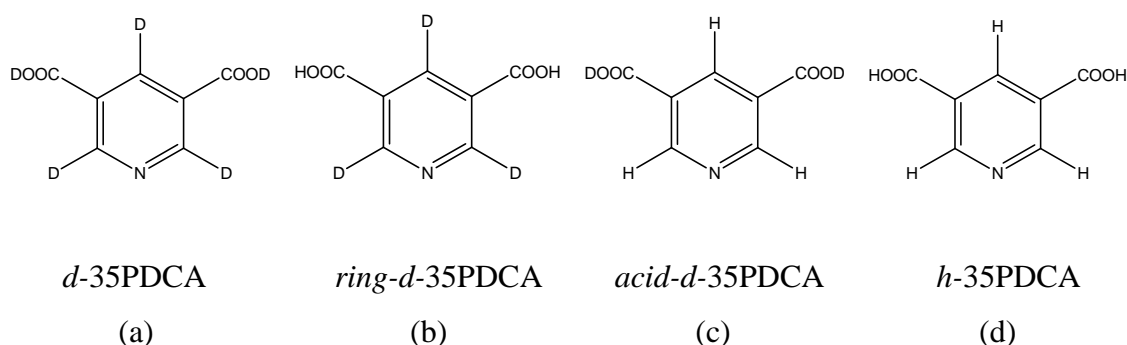
*Figure 3.3: The four isotopologues of 35PDCA studied in this work: a) d-35PDCA, b) ring-d-35PDCA, c) acid-d-35PDCA and d) h-35PDCA.*

## 3.1 Experimental Details

All reagents for synthesis, 3,5-pyridinedicarboxylic acid (Sigma-Aldrich, 98 %), $D_2O$ (Apollo Scientific, 99.9 %) and sodium metal (Alfa-Aesar, 99 %) were used as received without further purification. The solution of NaOD (5 M) for base-catalysed solvothermal deuteration was prepared by the addition of 1.15 g of sodium metal to 10 ml of $D_2O$ under nitrogen. The experimental setup for this reaction is shown in Figure 3.4.
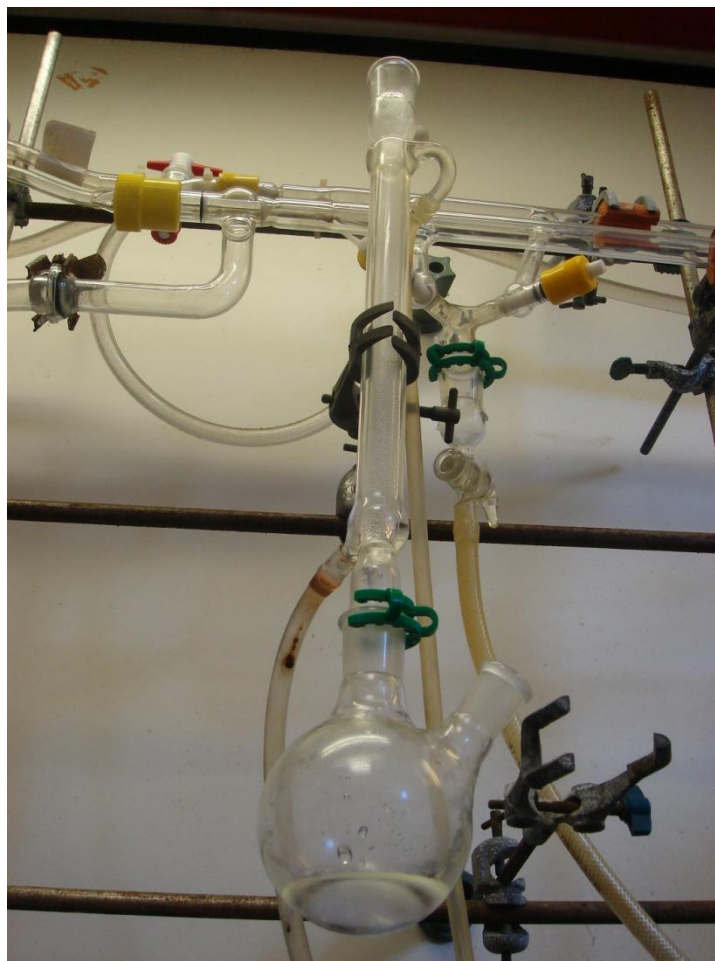
*Figure 3.4: The experimental set-up for the synthesis of NaOD.*

The fully deuterated compound (*d*-35PDCA) was prepared by H-D exchange in solution using a process developed by Delamore.[7] The reaction was carried out under hydrothermal conditions using a 23 ml Parr® General Purpose Acid Digestion Bomb P/N 4749 from Scientific & Medical Products Ltd, consisting of a Teflon reaction vessel inside a steel autoclave with a brass lid. Commercial *h*-35PDCA (0.5 g) and the pre-prepared NaOD (5 ml, 5 M) were reacted at 503 K for 12 hours under autogenous pressure in the autoclave. After cooling, the reaction mixture was neutralised with concentrated HCl (5 M) and centrifuged; the resulting white precipitate was filtered and dried. This was then reacted further with 7.5 ml of $D_2O$ at 473 K for 2 hours, again under pressure in the autoclave. The level of deuteration was determined using mass spectrometry and later confirmed by single crystal neutron diffraction. Dark yellow rod-shaped crystals of *d*-35PDCA (typical dimensions $0.5 \times 0.5 \times 2$ mm$^3$) were obtained

*via* this process when the reaction mixture was cooled to room temperature at a rate of 0.2° per minute.

A sample in which the pyridine ring was deuterated and the hydrogen bonds were protonated (*ring-d*-35PDCA) was prepared in the same way as the fully deuterated sample except that the final product was then allowed to stand in $H_2O$ overnight, which led to the D/H exchange on the carboxyl group positions. The cream-coloured product obtained was then filtered and dried and the deuteration level was confirmed using mass spectrometry.

The sample in which the pyridine ring was protonated and the hydrogen bonds were deuterated (*acid-d*-35PDCA) was prepared by hydrothermal treatment of 0.5 g of 35PDCA in 7.5 ml of $D_2O$. The oven was programmed to heat to 448 K at 5° per minute, dwell for 2 hours and then cool to room temperature at 0.2° per minute. The deuteration level of the cream-coloured product was confirmed using mass spectrometry.

Large cream-coloured crystals of the fully protonated material (*h*-35PDCA) were obtained after heating commercial 35PDCA (0.5 g) in 7.5 ml of $H_2O$ for 2 hours at 473 K under pressure in the autoclave.

Variable temperature powder X-ray diffraction data were collected for all isotopologues on the Bruker D8 ADVANCE diffractometer from 5 to 60° $2\theta$ with a step size of 0.014° $2\theta$. Simultaneously, the sample was cooled from 300 to 12 K at a rate of 15 K per hour. Data processing and analysis were carried out using the TOPAS Academic software.[8]

A column-shaped single crystal of *d*-35PDCA, measuring $0.14 \times 0.14 \times 0.22$ mm$^3$ was selected for single crystal X-ray analysis. Data were collected at 100, 150, 175, 200, 250 and 300 K on the Bruker SMART 1000 diffractometer. A full sphere of data was collected at each temperature by a series of $\omega$ scans, using a frame width of 0.3° in $\omega$ and an exposure time of 20 seconds per step. The raw data were collected using the SMART software and integrated using the SAINT suite of programmes;[9-11] Structure

refinement on $F^2$ was carried out using CRYSTALS.[12] All non-hydrogen atoms were refined anisotropically. Hydrogen atoms were located using Fourier difference maps and refined isotropically; a three parameter Chebyshev weighting scheme was also used.

Variable temperature neutron powder diffraction data for *d*-35PDCA were collected on the high-resolution powder diffractometer (HRPD) at the ISIS pulsed neutron source.[13] The sample was finely ground and packed into a 15 mm diameter cylindrical vanadium can. Neutron time-of-flight data were recorded over a time-of-flight range of 30 to 130 ms. Three-hour diffraction patterns were recorded at both 15 and 295 K in addition to recording large numbers of patterns on both cooling and warming over a range of temperatures; on cooling, one-minute patterns were recorded every 3 K between 290 and 8.5 K and on warming, 26-minute patterns were recorded every 10 K between 15 and 295 K. Rietveld refinements and parametric analyses were performed using the programme TOPAS Academic.[8, 14]

Variable temperature single crystal neutron diffraction data on *d*-35PDCA were collected on VIVALDI at the ILL.[15] A dark yellow rod-shaped crystal, measuring $1.5 \times 0.4 \times 0.4$ mm$^3$, was mounted on a vanadium pin in vacuum grease. Data were collected at 300, 250, 200, 175, 150, 100, 50 and 15 K; ten diffraction patterns, each accumulated over two hours, were collected at each temperature with successive patterns distinguished by a rotation of 20° of the crystal perpendicular to the incident beam. The data were processed using the CCP4 Laue suite of programmes.[16-18] Structure refinement on $F^2$ was carried out using SHELXL.[19] Atomic coordinates and anisotropic displacement parameters were refined for all atoms. Following an initial free refinement of the D atoms fractional occupancies, which showed an almost complete and equal deuteration level on these sites, the occupancies of sites D1-D5 were fixed. The overall deuteration level obtained for the sample from the single crystal neutron diffraction was 94(1) %.

Variable pressure diffraction data were collected on *d*-35PDCA. An initial single crystal X-ray diffraction experiment was undertaken, using a diamond anvil cell at room temperature. A thin metal gasket was firmly placed on top of the lower part of a diamond anvil cell and coated in paraffin oil, which acted as the pressure-transmitting

medium in this case. A crystal, measuring $0.11 \times 0.25 \times 0.27$ mm$^3$, was then fixed to the surface of the diamond of the upper diamond anvil using vacuum grease. A small ruby crystal, used as the pressure standard in this experiment, was added alongside the *d*-35PDCA crystal. The upper diamond anvil, containing the crystals, was then screwed onto the lower anvil (and gasket). Pressures of 0, 5, 15 and 25 kbar were obtained by simply tightening the screws of the pressure cell. At each pressure rapid data collections were performed on a XIPHOSII diffractometer (a combined Bruker, Incoatec and Huber instrument)[20] and the raw data were indexed using the Bruker SMART software.[9]

Variable pressure single crystal diffraction work was subsequently undertaken on SXD at ISIS[21], with a modified Paris-Edinburgh press which had been optimised for use on this instrument.[22, 23] A crystal, measuring $0.9 \times 1.0 \times 1.7$ mm$^3$ was glued to the centre of the sample holder, using a cyanoacrylate adhesive, such that the *ab* crystal plane was perpendicular to the direction of the neutron beam. A 4:1 methanol:ethanol deuterated mixture (the pressure-transmitting medium) and a piece of glass wool were added to the sample holder and the press was sealed with a load of 5 tonnes.[24] All data collections were obtained at room temperature, and three different pressures were attempted: ambient pressure, 5 kbar and 10 kbar. For each pressure, data were collected in three sample orientations at 8 hours per orientation; a total of 24 hours. Data integration was carried out using the ISIS SXD2001 software suite[21] and structure refinement on $F^2$ was carried out using SHELXL.[19]

Variable pressure powder neutron diffraction data were then obtained, on D20 at the ILL[25] ($\lambda = 1.54$ Å), using a Paris-Edinburgh press. A sample of *d*-35PDCA (0.13 g) was finely ground with 10 % NaCl (for pressure calibration), and then a small amount of this mixture was loaded onto the sample holder (a TiZr gasket). A 4:1 methanol:ethanol deuterated mixture (the pressure-transmitting medium) was added to the powder and the press was sealed. All data collections were obtained at room temperature, at pressures of approximately 0, 2, 5, 10, 15, 20 and 40 kbar. At each pressure, data were acquired over 2-3 hours (6-9 repetitions of 50 acquisitions, at 24 seconds per acquisition) depending on data quality, with the longer data collection time being required at higher pressures (above 10 kbar). The raw data were collected using the program NOMAD, data reduction was achieved using LAMP and structural refinements were performed in TOPAS Academic.[8]

## 3.2 Results and Discussion

### 3.2.1 Powder X-ray Diffraction: Evidence for Structural Phase Transitions

Batches of all four 35PDCA isotopologues were prepared and studied by VT powder XRD. For each sample data were collected between 12 and 300 K and analysed by sequential single-phase Rietveld fitting. For each isotopologue the high temperature, N···H/D–O, literature structure[2] was used as the starting model for the refinement and the diffraction patterns were analysed starting from the 300 K pattern. A total of 78 parameters were refined in each analysis, including 10 coefficients of a Chebyshev polynomial to model the background, a term to correct for changes in the sample height on cooling, 4 lattice parameters, the fractional atomic coordinates for each atom, 1 parameter to describe the isotropic thermal displacement of all of the atoms, 4 parameters to define the TCHZ peak shape and a scale factor; a 4th order spherical harmonic function was also required to correct for preferred orientation and an additional Gaussian peak was used to model the amorphous humps found between 18 and 20° *2θ*.
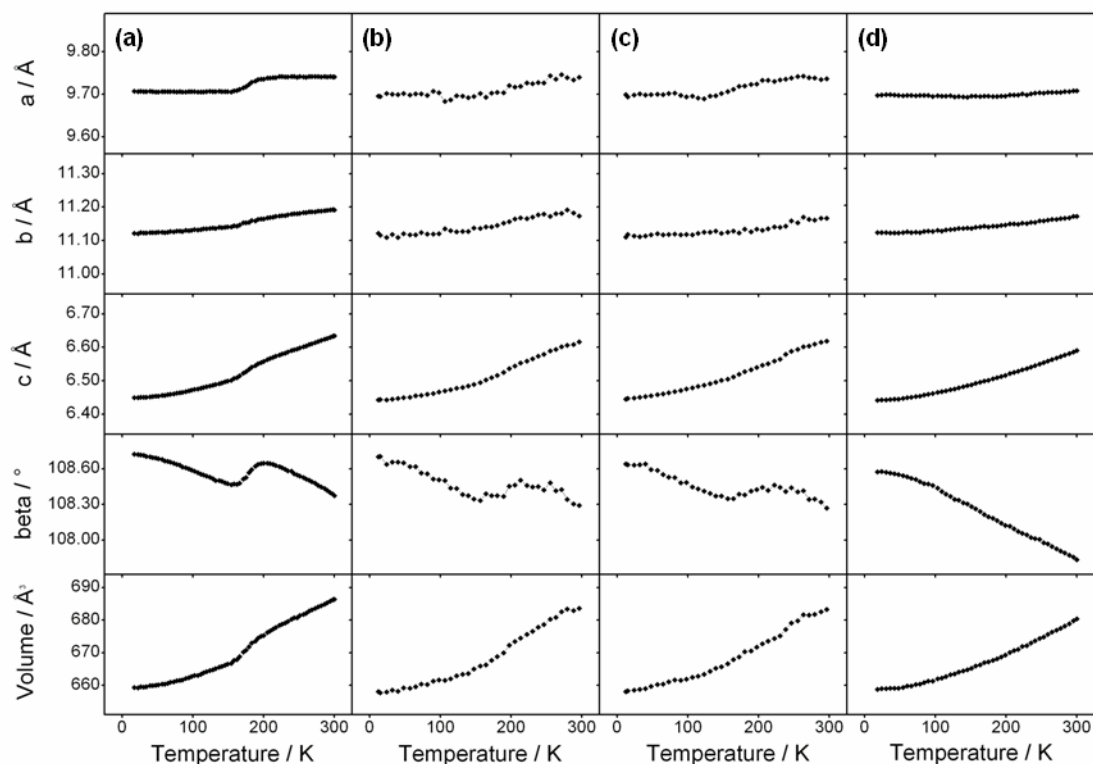


*Figure 3.5: Temperature dependence of the unit cell parameters of the four 35PDCA isotopologues obtained from variable temperature XRD data by sequential single-phase*

*Rietveld refinements: a) d-35PDCA, b) ring-d-35PDCA, c) acid-d-35PDCA and d) h-35PDCA. The unit cell parameters a, b and c are plotted on the same % scale for direct comparison.*

The temperature dependence of the unit cell parameters of *d*-35PDCA extracted from this data analysis shows features suggesting that a phase transition in this material occurs between 150 and 200 K, in agreement with previous powder X-ray and neutron diffraction results. This is in contrast to the smooth temperature dependence trends observed for the cell parameters of *h*-35PDCA, consistent with normal thermal expansion effects (Figure 3.5d). Variable temperature diffraction data collected on the two partially deuterated isotopologues, *ring-d*-35PDCA and *acid-d*-35PDCA, show that they behave similarly to the fully deuterated form, possibly also exhibiting a structural phase transition (Figures 3.5b and c), though with higher phase-transition temperatures.
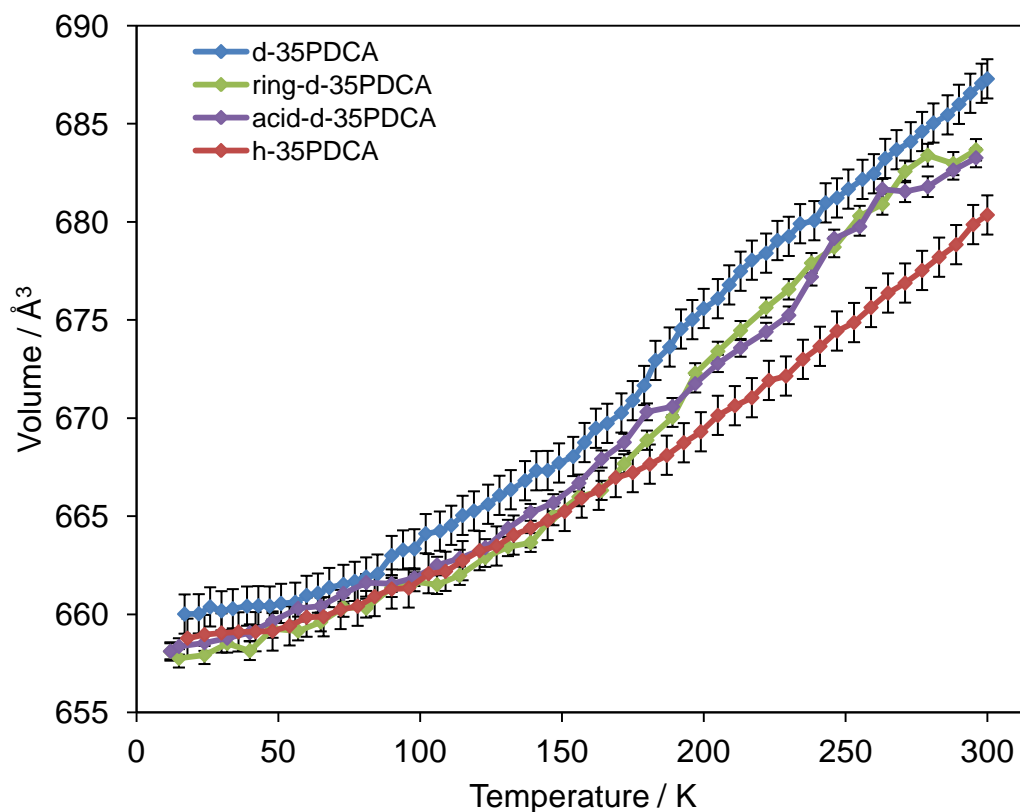


*Figure 3.6: The temperature dependence of the unit cell volumes of the four 35PDCA isotopologues, plotted together for comparison.*

The unit cell volumes of all four isotopologues are plotted together in Figure 3.6, for comparison. The temperature dependence of the unit cell volume of *h*-35PDCA is completely smooth; in *d*-35PDCA the discontinuity, highlighting the phase transition, is very pronounced, with the unit cell volume increasing by approximately 10 $\text{Å}^3$ between 150 and 200 K. The partially deuterated samples, *ring-d*-35PDCA and *acid-d*-35PDCA, show very similar volume trends which lie between those of the other isotopologues. They also seem to exhibit a phase transition, albeit less pronounced than that in *d*-35PDCA. The observed trends suggest that molecular mass is a key factor determining the phase transition, rather than the location of selective deuteration, suggesting that phonons play a key role in the transition.

### 3.2.2 Powder Neutron Diffraction: Nature of the Phase Transition in *d*-35PDCA

Figures 3.5 and 3.6 show the temperature dependence of the lattice parameters in *d*-35PDCA. Those data suggest, at a first glance, that a continuous phase transition occurs within this compound between 150 and 200 K. There is, however, experimental evidence (in both X-ray and neutron powder diffraction) to suggest that the low (N–D⋯O) and high (N⋯D–O) temperature phases co-exist within this temperature region. Whilst X-ray data at 90 K (Figure 3.7) show a single peak at approximately 21.70° 2$\theta$, which is shifted to 21.55° 2$\theta$ at 230 K, the data collected at 175 K clearly show the presence of two peaks in this region; the single peak at 90 K corresponds to the N–D⋯O species, whilst that at 230 K corresponds to the N⋯D–O species. The appearance of two peaks at 175 K clearly indicates the co-existence of both the N–D⋯O and N⋯D–O species.
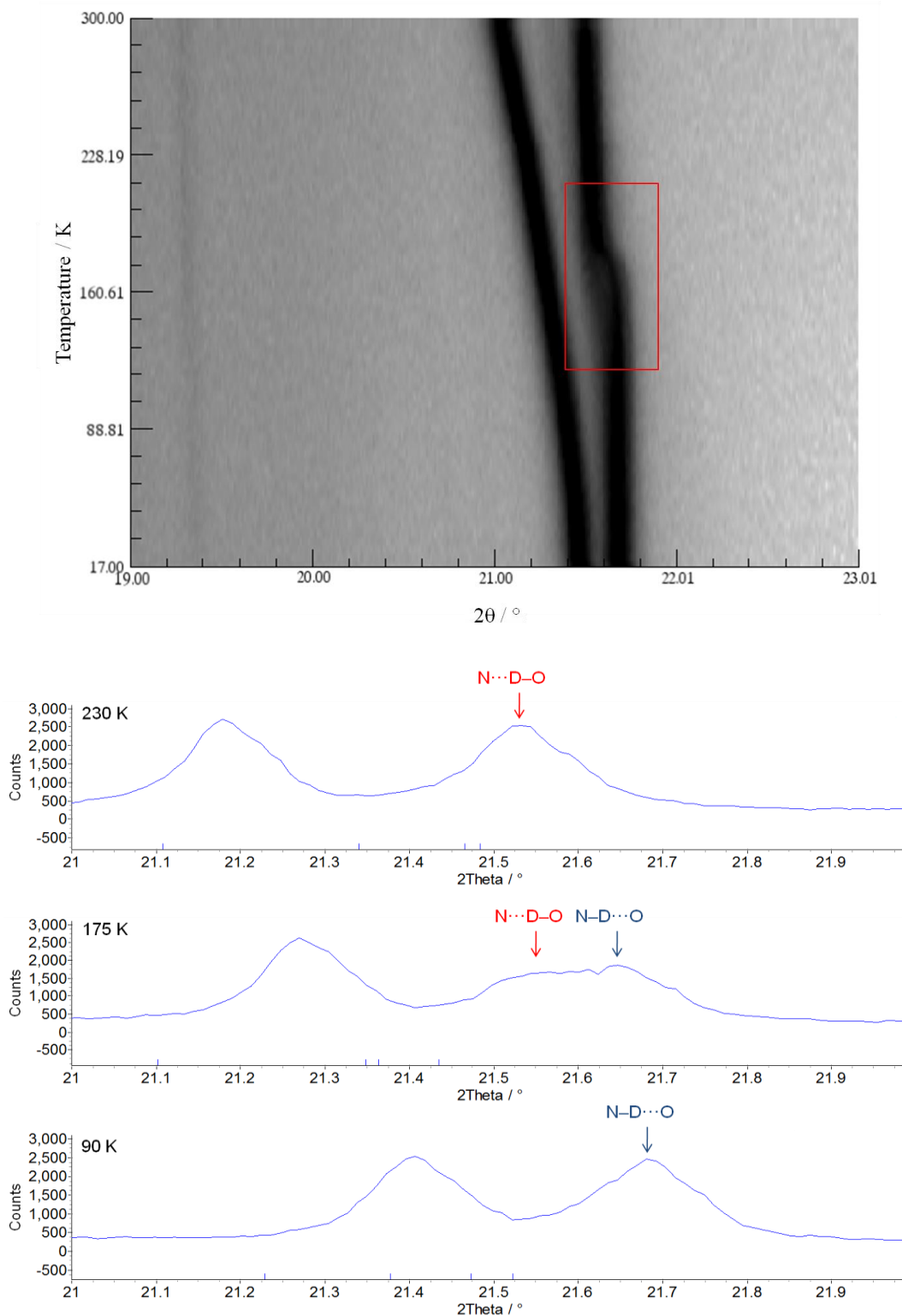
*Figure 3.7: (top) A film plot of a segment of powder XRD data: the highlighted feature illustrates phase co-existence in the phase transition temperature region (between 150 and 200 K); (bottom) The observed powder X-ray diffraction data representative of the high- and low-temperature single-phase regions and the intermediate phase co-existence.*

The same effect is observed in the neutron data collected on HRPD. These data at 15 and 285 K (Figure 3.8) show a single peak at approximately 92.25 ms, which is shifted to 92.75 ms at 285 K, whilst the data collected at 155 K clearly show the presence of two peaks in this region; the single peak at 15 K corresponds to the N–D···O species, whilst that at 285 K corresponds to the N···D–O species. The appearance of two peaks at 155 K clearly indicates the co-existence of both the N–D···O and N···D–O species.

This co-existence is in agreement with the bimodal distribution of proton positions within the hydrogen bond obtained in previous theoretical studies, DFT molecular simulations; although a phase transition was not predicted in this work.[6] These studies showed that protons within the hydrogen bond spend very little time centred between the O and N atoms, and more time lying in stable positions closer to either atom. It is therefore logical to conclude that both the N–D···O and N···D–O forms of *d*-35PDCA may co-exist under certain conditions.

No clear evidence for a change in space group has been observed by powder diffraction, with data modelled well in $P2_1/c$ at all temperatures, as demonstrated by Rietveld fits of the powder neutron diffraction data, Figure 3.9. (In these refinements a total of 78 parameters were refined, including 12 coefficients of a Chebyshev polynomial to model the background, 4 lattice parameters, the fractional atomic coordinates for each atom, 1 parameter to describe the isotropic thermal displacement of all the non-deuterium atoms, 6 parameters to describe the anisotropic thermal displacement of D5 and 1 parameter to describe the isotropic thermal displacement of the remaining deuterium atoms). This, by definition, is an isosymmetric ('Type 0') structural phase transition[26] and was confirmed by single crystal neutron diffraction work (see Section 3.2.3).
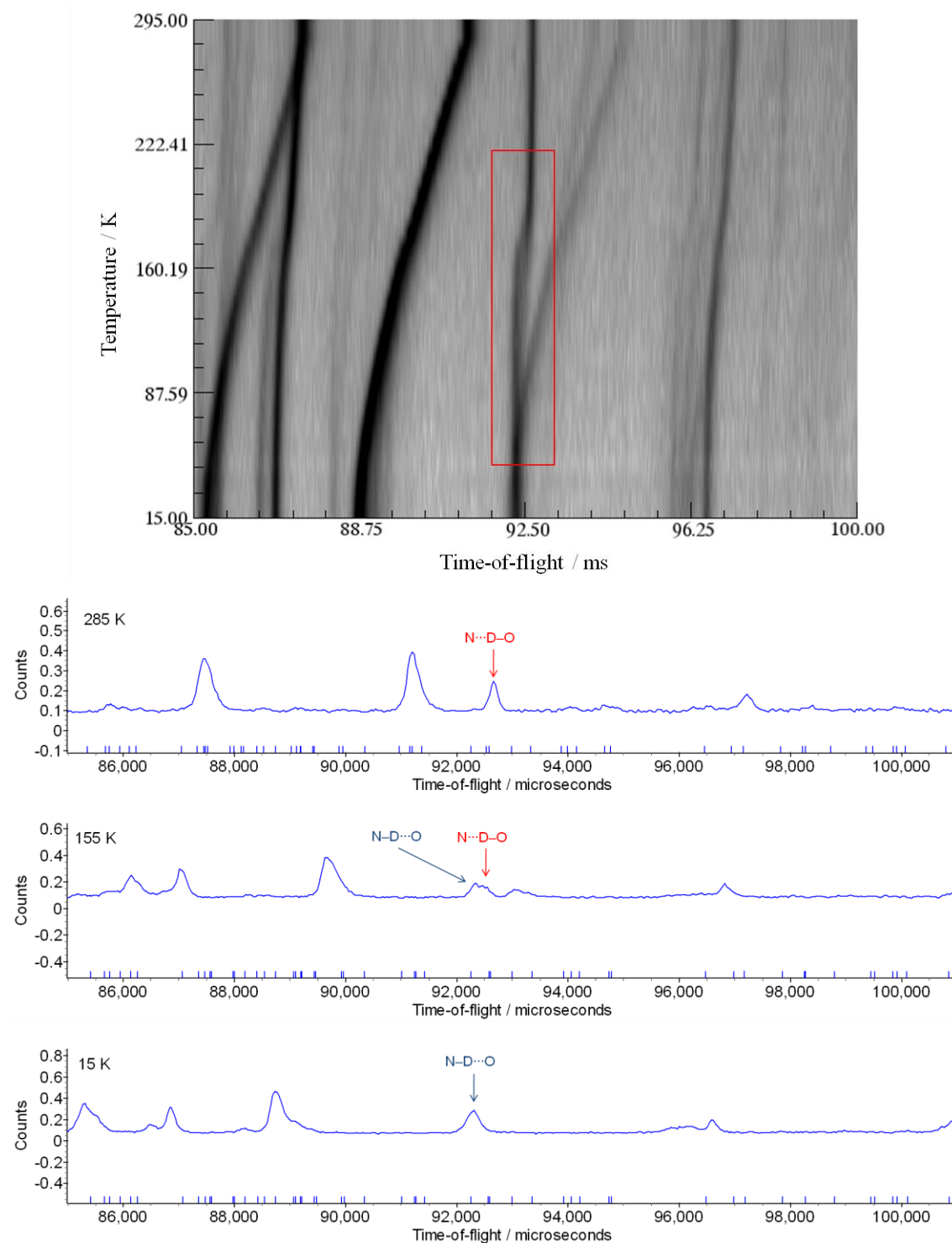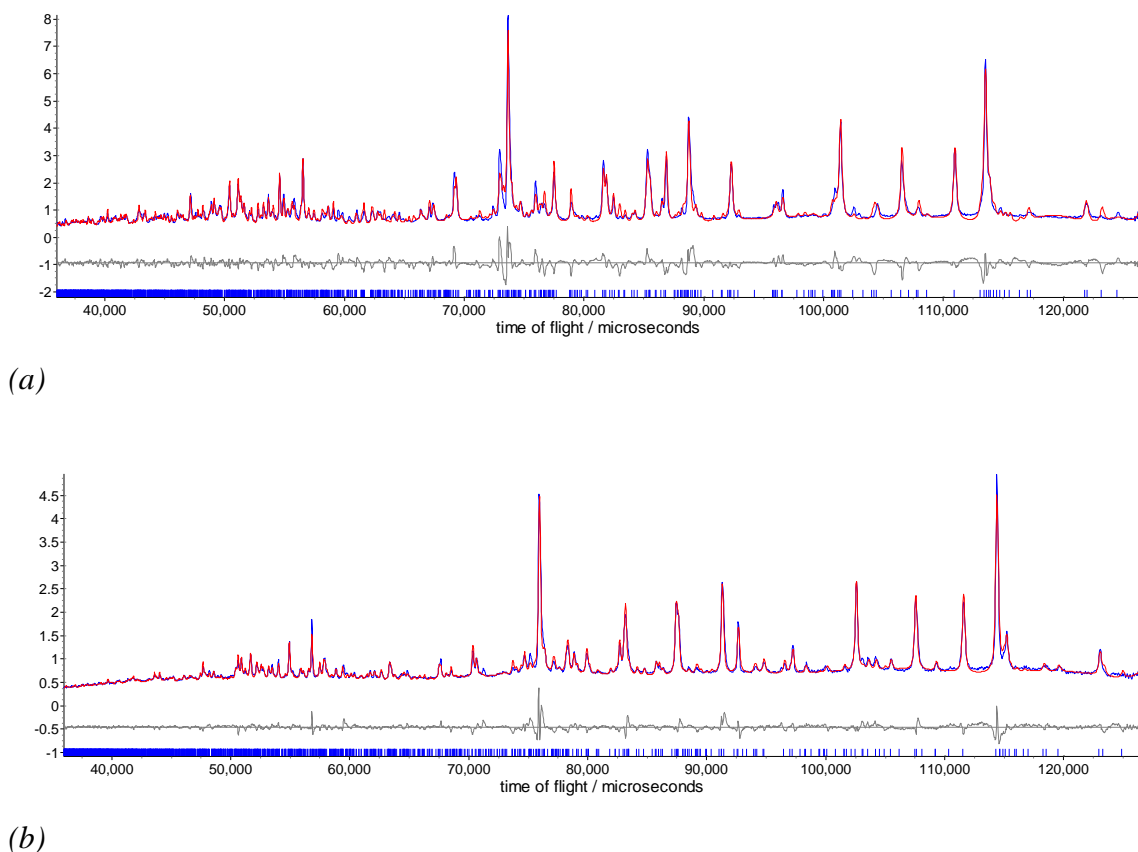
*Figure 3.8: (top) A film plot of a segment of powder neutron data: the highlighted feature illustrates phase co-existence in the phase transition temperature region (between 150 and 200 K); (bottom) The observed powder neutron diffraction data representative of the high- and low-temperature single-phase regions and the intermediate phase co-existence.*

*(a)*



*(b)*

*Figure 3.9: The Rietveld fit of d-35PDCA in the P2₁/c space group at (a) 15 K and (b) 295 K obtained by powder neutron diffraction; observed pattern in blue, calculated pattern in red and a difference plot (showing the difference between the observed and calculated patterns) in grey.*

The phase co-existence and apparent peak broadening observed in the powder diffraction data, and described above, was investigated quantitatively using parametric Rietveld refinement. Detailed analysis of the temperature dependence of cell parameters close to the phase transition, by standard Rietveld refinement, is complicated partly by the relatively low quality of the variable temperature powder diffraction data but more fundamentally by the difficulty of modelling two structurally very similar materials potentially co-existing close to the phase-transition temperature, $T_c$. For situations such as this a parametric approach to Rietveld refinement, in which all the diffraction patterns are fitted simultaneously to a single evolving structural model, can have significant advantages – essentially well-defined regions of the diffraction surface help constrain behaviour close to $T_c$.[14] Parametric fitting of all 28 data sets collected on cooling, using a two-phase model to describe contributions from the low- (N–D···O) and

80

high-temperature (N⋯D–O) structures, was performed by John Evans. The results are briefly summarized here for completeness and for the discussion of the single crystal neutron diffraction results (Section 3.2.3).

Results from parametric surface fitting are shown in Figure 3.10. Figure 3.10a shows the temperature dependence of the phase fractions from this model and Figures 3.10b and 3.10c show the evolution of the *β*-angles and cell volumes. In these latter figures the open points show the parameterised values extracted from all data for each individual phase whilst the filled data points are a phase-fraction-weighted average. This gradual temperature dependence of the averaged plots can be compared to the refinements shown in Figure 3.5a. The apparent continuous nature of the transition with the single-phase model is a result of averaging over two peaks from each phase present near $T_c$.
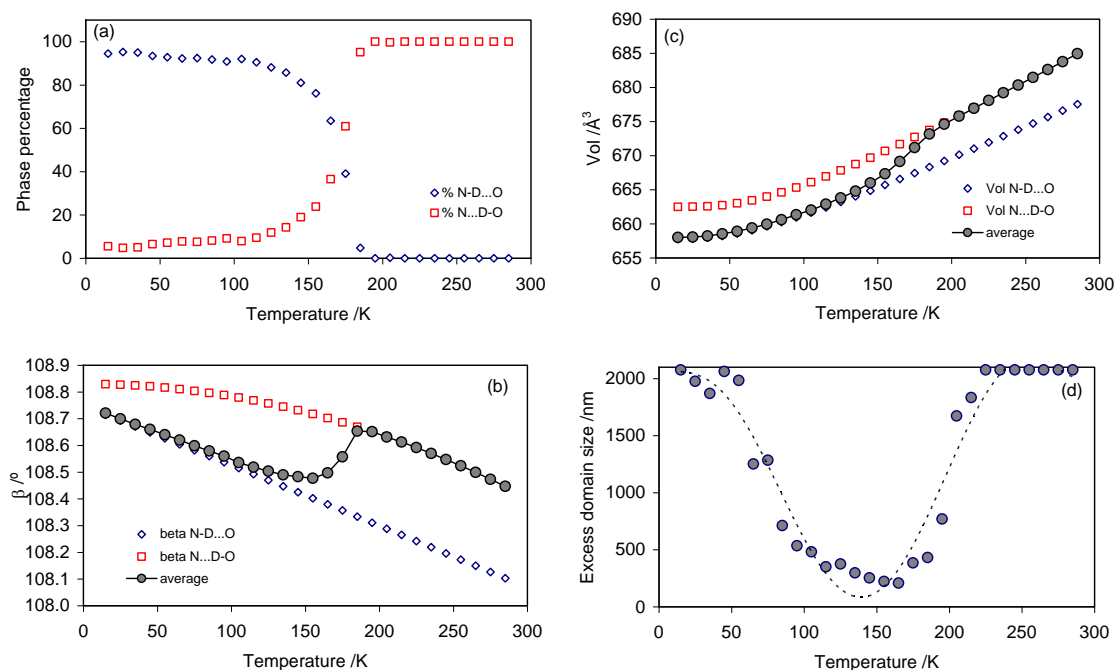


*Figure 3.10: Temperature dependence of the parameters of d-35PDCA extracted from variable temperature powder neutron diffraction data by parametric Rietveld refinement: (a) N–D⋯O and N⋯D–O phase fractions; (b) the monoclinic β-angle; (c) the unit cell volume; and (d) excess domain-size peak broadening. Open symbols represent parametric fits for each phase and closed symbols a phase-fraction-weighted average. All of these graphs are courtesy of John Evans.*[27]

The temperature-dependent behaviour of $d$-35PDCA observed by powder neutron diffraction, modelled by parametric Rietveld refinement, and associated with giant deuteron migration, can be interpreted as nonclassical phase transition behaviour. This was initially described by Ubbelohde[28-30] by the existence of "hybrid crystals" in which domains of the two forms of a material, with very similar structures, co-exist around $T_c$. These hybrid crystals can be viewed as domains of one phase grown within the other.

Our diffraction data and parametric analysis suggest that when the $d$-35PDCA is cooled from room temperature, where it exists in the pure N···D–O form, domains of the pure N–D···O form start to nucleate and grow within the original material. Whilst the structures of the two forms are very similar, their unit cell volumes differ significantly. Therefore it was possible to model the size of these domains as a function of peak broadening, as shown in Figure 3.10d, brought about by strain experienced by the crystal at the interfaces between them. These results clearly show that the domain sizes of the two forms change during the transition, with smaller domains existing around the critical temperature $T_c$ relative to domain sizes at temperatures far from the transition.

### 3.2.3  Single Crystal Diffraction Studies: Deuteron Migration

Variable temperature X-ray diffraction data were collected on a single crystal of $d$-35PDCA, at 35, 100, 150, 175, 200, 250 and 300 K in order to gain preliminary insight into any temperature-dependent changes in the D5 deuteron position relative to the N1 and O4 atoms.

Structure refinement on $F^2$ was carried out at each temperature using CRYSTALS. Atomic coordinates and anisotropic displacement parameters were refined for all non-hydrogen atoms, with atomic coordinates and isotropic displacement parameters refined for all hydrogen atoms; a three parameter optimal weighting scheme was also used. No change in space group was observed over the temperature range studied, with data modelled well in $P2_1/c$ at all temperatures. A summary of the crystallographic data is given in Table 3.1.

*Table 3.1: Crystallographic data for the XRD structure of d-3,5PDCA at various temperatures.*

| Temperature/K | 35 | 100 | 150 | 175 | 200 | 250 | 300 |
|---|---|---|---|---|---|---|---|
| Chemical formula | $C_7D_5NO_4$ | $C_7D_5NO_4$ | $C_7D_5NO_4$ | $C_7D_5NO_4$ | $C_7D_5NO_4$ | $C_7D_5NO_4$ | $C_7D_5NO_4$ |
| $M_r$ | 172.15 | 172.15 | 172.15 | 172.15 | 172.15 | 172.15 | 172.15 |
| Crystal system, space group | Monoclinic, $P12_1/c1$ | Monoclinic, $P12_1/c1$ | Monoclinic, $P12_1/c1$ | Monoclinic, $P12_1/c1$ | Monoclinic, $P12_1/c1$ | Monoclinic, $P12_1/c1$ | Monoclinic, $P12_1/c1$ |
| $a$/Å | 9.7239(14) | 9.7376(7) | 9.7446(7) | 9.7539(8) | 9.7566(7) | 9.7583(8) | 9.759(2) |
| $b$/Å | 11.1395(16) | 11.1417(8) | 11.1542(8) | 11.1647(9) | 11.1722(8) | 11.1866(9) | 11.203(2) |
| $c$/Å | 6.4578(9) | 6.4958(5) | 6.5300(5) | 6.5529(5) | 6.5758(5) | 6.6137(5) | 6.6390(14) |
| $\beta$/° | 108.706(2) | 108.5450(10) | 108.5510(10) | 108.5900(10) | 108.5970(10) | 108.4960(10) | 108.330(3) |
| $V$/Å$^3$ | 662.55(16) | 668.04(9) | 672.89(9) | 676.37(9) | 679.35(9) | 684.67(9) | 689.0(3) |
| $Z$ | 4 | 4 | 4 | 4 | 4 | 4 | 4 |
| $\mu$ /mm$^{-1}$ | 0.14 | 0.14 | 0.14 | 0.14 | 0.14 | 0.14 | 0.14 |
| Data collection method | $\omega/2\theta$ | $\omega/2\theta$ | $\omega/2\theta$ | $\omega/2\theta$ | $\omega/2\theta$ | $\omega/2\theta$ | $\omega/2\theta$ |
| Criterion for observed reflections | $I > 2.0\sigma(I)$ | $I > 2.0\sigma(I)$ | $I > 2.0\sigma(I)$ | $I > 2.0\sigma(I)$ | $I > 2.0\sigma(I)$ | $I > 2.0\sigma(I)$ | $I > 2.0\sigma(I)$ |
| $\theta_{max}$ /° | 27.7 | 30 | 30 | 30 | 30 | 30 | 28 |
| Refinement on | $F^2$ | $F^2$ | $F^2$ | $F^2$ | $F^2$ | $F^2$ | $F^2$ |
| $R[F^2 > 2s(F^2)]$, $wR(F^2)$ | 0.046, 0.105, | 0.056, 0.103 | 0.061, 0.109 | 0.053, 0.096 | 0.052, 0.094 | 0.051, 0.091 | 0.052, 0.115 |
| No. of reflections | 1866 | 2805 | 2682 | 2577 | 2477 | 2320 | 1339 |
| No. of parameters | 129 | 129 | 129 | 129 | 129 | 129 | 129 |

Due to the problems surrounding the retrieval of hydrogen atom positions and hence hydrogen bond information from XRD data, the temperature dependence of the length of the C8–O4 single bond is used as an indirect probe of information about changes in the hydrogen bond of interest. This C8–O4 bond is adjacent to the hydrogen bond and therefore affected by subtle changes therein. Also, as a result of the greater electron density of both carbon and oxygen, the C–O bond lengths obtained from XRD do not suffer from the same aspherical effects as hydrogen and are therefore more reliable. Three different C–O bond lengths are plotted in Figure 3.11a for comparison: the C8–O4 single bond (involving the oxygen atom in the short N1–D5···O4 hydrogen bond), the C7=O2 double bond and the C7–O1 single bond (neither of which contain atoms involved in the short N1–D5···O4 hydrogen bond and therefore would not be expected to change significantly with temperature). The bond lengths C7=O2 and C7–O1 clearly fall within the distribution maxima corresponding to double and single bonds, respectively, as evidenced by a histogram of carboxyl C–O bond lengths based on a search of organic structures in the Cambridge Structural Database (CSD), Figure 3.11b.[31, 32] These two bonds do not change very much with temperature; least-squares fitting of the data points gives lines with gradients of just -0.00003(1) for C7=O2 and -0.00001(1) for C7–O1, suggesting that the double- and single-bond character of these bonds, respectively, is retained.



(a)                                                        (b)
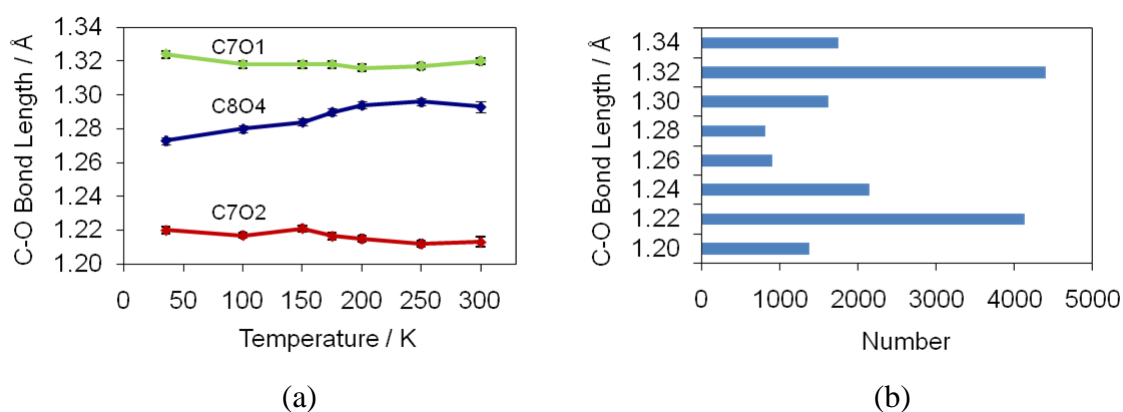
*Figure 3.11: (a) The temperature dependence of the relevant C–O bond lengths in d-35PDCA obtained from single crystal XRD data. (b) A histogram of carboxyl C-O bond lengths as derived from the CSD.*

By contrast, the C8–O4 single bond becomes progressively shorter with decreasing temperature, suggesting a shift towards double-bond character. This variation in the

C8–O4 bond length suggests that the D5 deuteron migrates away from the O4 atom and closer to N1 at lower temperatures, altering the character of the bonding to the carboxyl group carbon C8 (Figure 3.12); *i.e.* as the D5 atom moves away from the O4 atom it is stabilised by the delocalisation of electron density from the C8=O3 double bond, and hence itself becomes more double bond-like in nature.
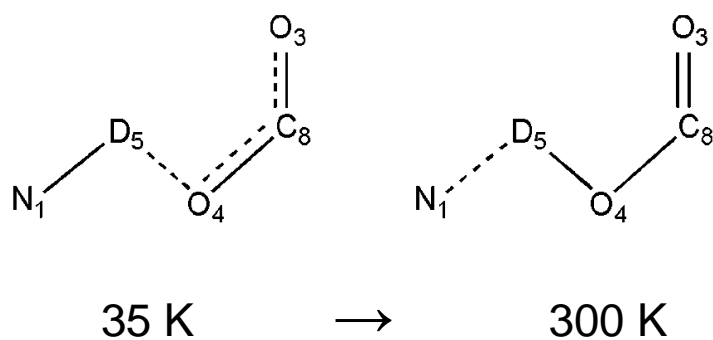


*Figure 3.12: The relevant fragment of the d-35PDCA structure, indicating the shift of C8–O4 towards a double bond at lower temperatures as an N1–D5 bond forms.*

In order to determine accurately the extent of this deuteron migration, variable temperature single crystal neutron diffraction data were collected on *d*-35PDCA and structure refinement on $F^2$ was carried out using the SHELXTL package. For this, no $I/\sigma$ cutoff was used, and atomic coordinates and anisotropic displacement parameters were refined for all atoms. Following an initial free refinement of the D atoms fractional occupancies, which led to a consistent value of 0.94(2) for each, the occupancies of sites D1-D5 were fixed. A summary of the crystallographic data is given in Table 3.2 and the evolution of the *d*-35PDCA structure is depicted in Figure 3.13. It should be noted that since only ratios between unit cell dimensions can be determined in the white-beam Laue technique, the unit cell dimensions output from VIVALDI are not accurate. It is therefore necessary to use cell dimensions found by some other means in the refinement of a calculated model against the data obtained from this particular instrument. The cell parameters found from the HRPD data have been used in this case.

*Table 3.2: Crystallographic data for the ND structure of dd-3,5PDCA at various temperatures.*

| Temperature/K | 15 | 50 | 150 | 175 | 200 | 250 | 300 |
|---|---|---|---|---|---|---|---|
| Chemical formula | $C_7D_5NO_4$ | $C_7D_5NO_4$ | $C_7D_5NO_4$ | $C_7D_5NO_4$ | $C_7D_5NO_4$ | $C_7D_5NO_4$ | $C_7D_5NO_4$ |
| $M_r$ | 167 | 167 | 167 | 167 | 167 | 167 | 167 |
| Crystal system, space group | Monoclinic, $P12_1/c1$ | Monoclinic, $P12_1/c1$ | Monoclinic, $P12_1/c1$ | Monoclinic, $P12_1/c1$ | Monoclinic, $P12_1/c1$ | Monoclinic, $P12_1/c1$ | Monoclinic, $P12_1/c1$ |
| $a$/Å | 9.7043 (13) | 9.7030 (13) | 9.7081 (13) | 9.7262 (13) | 9.7372 (13) | 9.7415(13) | 9.7433(13) |
| $b$/Å | 11.1106 (17) | 11.1120 (17) | 11.1342 (17) | 11.1511 (17) | 11.1638 (17) | 11.1779(17) | 11.1897(17) |
| $c$/Å | 6.4402 (13) | 6.4445 (13) | 6.4954 (13) | 6.5269 (13) | 6.5546 (13) | 6.5953(13) | 6.6307(13) |
| $\beta$/° | 108.690 (10) | 108.656 (10) | 108.412(10) | 108.555 (10) | 108.634(10) | 108.532(10) | 108.392(10) |
| $V$/Å³ | 657.77 (19) | 658.33 (19) | 666.16 (19) | 671.09 (19) | 675.16 (19) | 680.920 (19) | 685.982(19) |
| $Z$ | 4 | 4 | 4 | 4 | 4 | 4 | 4 |
| No. measured and independent reflections | 6154, 1425 | 6319, 1431 | 6476, 1428 | 6742, 1753 | 6806, 1775 | 6303, 1469 | 6243, 1439 |
| $R_{int}$ | 0.369 | 0.368 | 0.272 | 0.261 | 0.241 | 0.255 | 0.220 |
| Data collection method | Laue | Laue | Laue | Laue | Laue | Laue | Laue |
| $\theta_{max}$ (°) | 29.8 | 29.7 | 29.6 | 34.9 | 34.9 | 30.4 | 30 |
| Refinement on | $F^2$ | $F^2$ | $F^2$ | $F^2$ | $F^2$ | $F^2$ | $F^2$ |
| $R[F^2 > 2s(F^2)]$, $wR(F^2)$ | 0.157, 0.280 | 0.164, 0.285 | 0.138, 0.236 | 0.154, 0.240 | 0.127, 0.215 | 0.132, 0.213 | 0.118, 0.191 |
| No. of parameters | 156 | 156 | 156 | 156 | 156 | 156 | 156 |
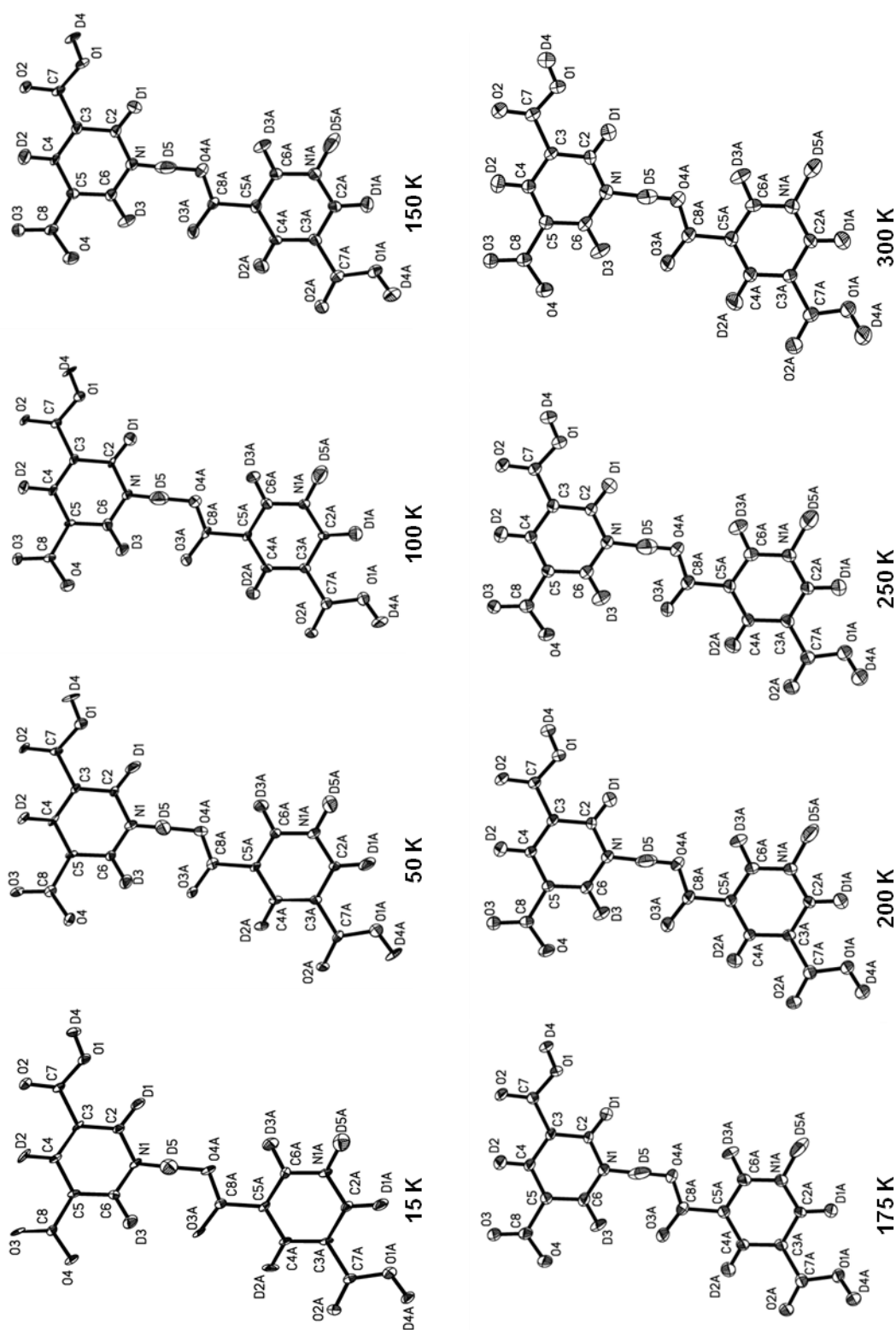
*Figure 3.13: The evolution of the d-35PDCA structure with temperature. Atomic displacement parameters are drawn at the 50 % probability level.*

A reversible, temperature-dependent diffraction spot profile degradation was observed in the low temperature diffraction patterns. An example of a diffraction plate demonstrating this at 15 K is shown in Figure 3.14a alongside the equivalent plate at 300 K for comparison, Figure 3.14b. In addition a number of spots, at varying positions on the diffraction plates, are shown in Figure 3.15 to demonstrate the evolution of the spot profiles with temperature. It must be noted, however, that the same reversible degradation was also observed in another crystal during preliminary testing and therefore this phenomenon was not simply a result of a fault in the crystal used. In the laboratory X-ray diffraction work, using Mo $K_\alpha$ radiation (0.71073 Å) and a much smaller crystal (0.004 mm$^3$ in volume compared to that of 0.24 mm$^3$ used in the neutron Laue diffraction work), such changes in diffraction spot profiles with varying temperature were not observed. In light of conclusions based on the neutron powder diffraction data modelling, this behaviour is ascribed to a reversible domain structure development in the single crystal.
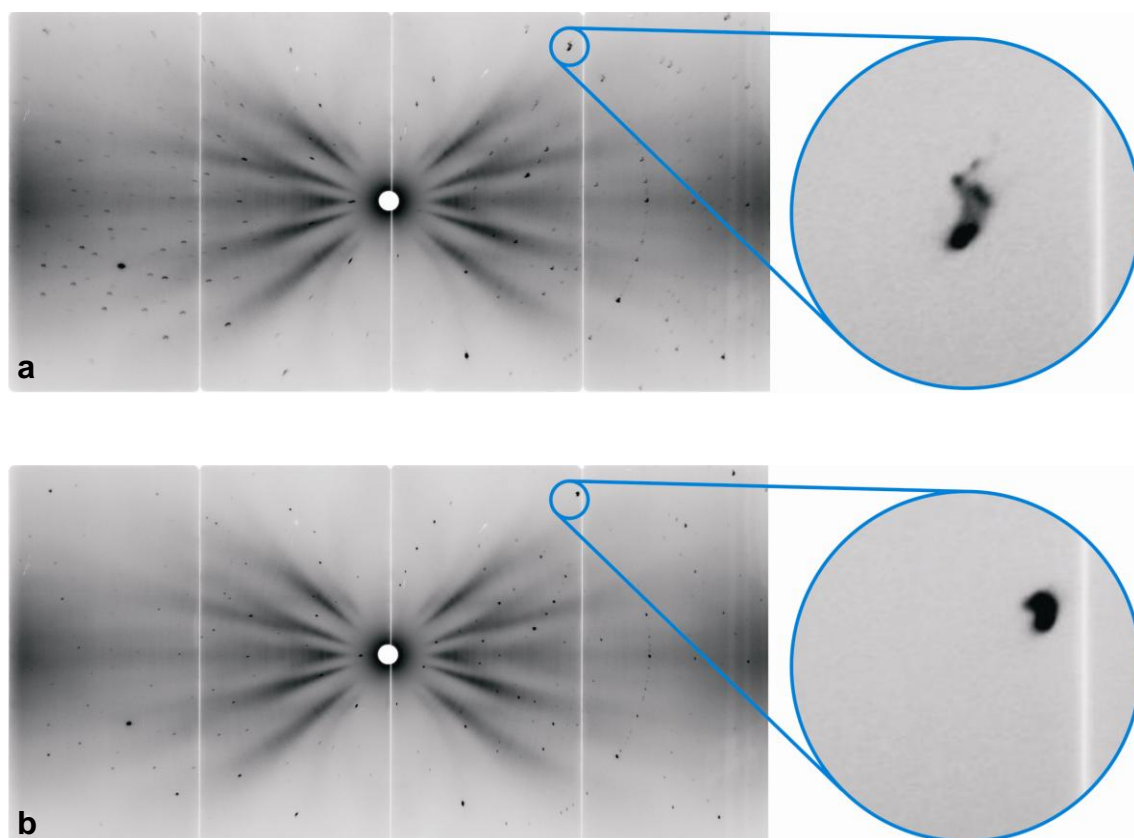


*Figure 3.14: Examples of corresponding diffraction patterns at (a) 15 K and (b) 300 K, with an equivalent spot in each pattern highlighted.*
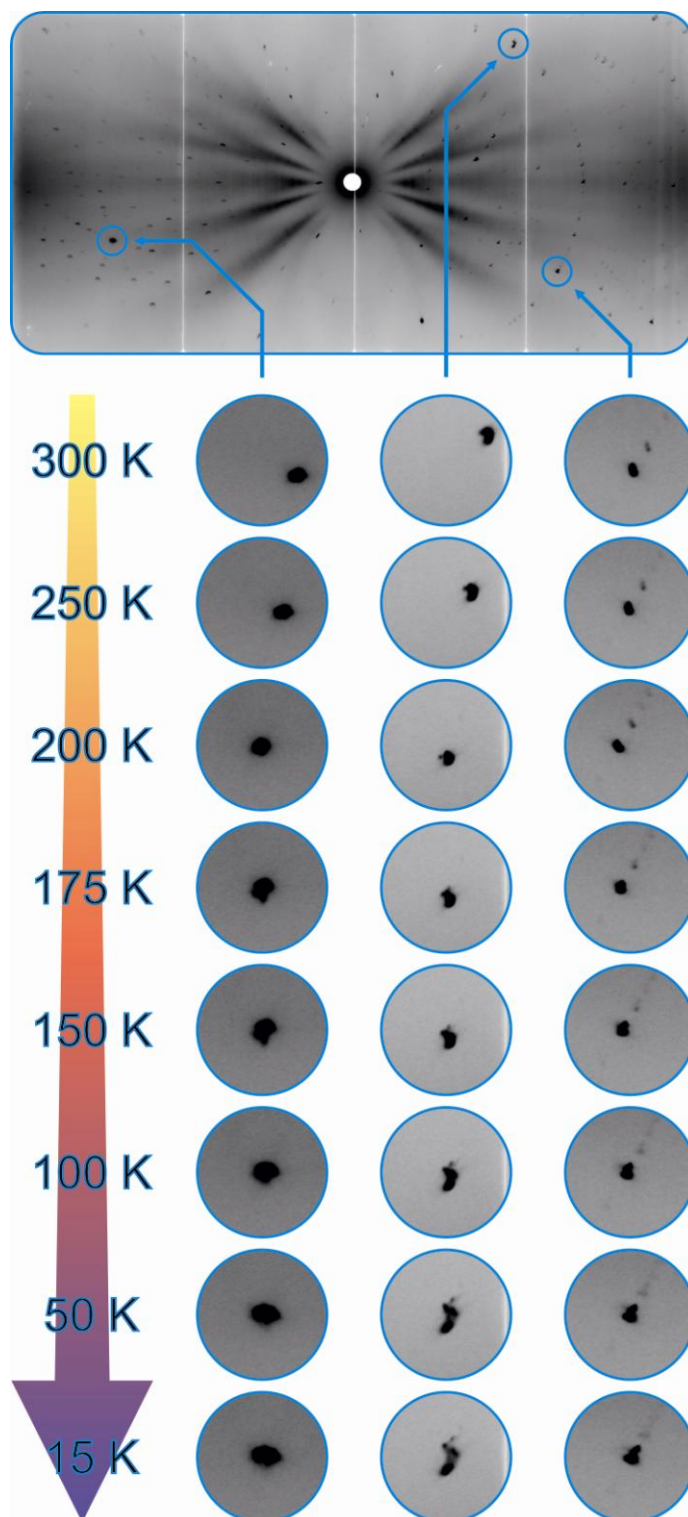
*Figure 3.15: The evolution of various spot profiles over the temperature range studied*

Figure 3.16 shows the effect of temperature on the D5–N1 and D5–O4 bond lengths in *d*-35PDCA. The data show that as the D5···N1 distance increases with increasing temperature, the O4···N1 distance decreases; the changes observed are from 1.159(8) Å

at 15 K to 1.478(6) Å at 300 K for D5···N1, and from 1.374(10) Å at 15 K to 1.092(7) Å at 300 K for O4···N1. These results reveal the migration of the deuteron away from the donor atom N across the centre of the hydrogen bond between these temperatures; the overall distance of the migration is 0.32(1) Å. Whilst these data reveal an apparent gradual migration of the deuteron between these temperatures, the evidence for the co-existence of the low- and high-temperature forms of *d*-35PDCA, and the unusual behaviour of the crystals on cooling and heating, suggest that in the temperature region of 150 to 200 K, the derived distances represent an average of the N–D···O and N···D–O species. In addition, Figure 3.16 shows the temperature dependence of the equivalent distances, H5–N1 and H5–O4, in *h*-35PDCA. These results also give evidence for proton migration; however, this is much smaller in magnitude and centring of the proton in the hydrogen bond occurs approximately 50 K higher than in *d*-35PDCA.
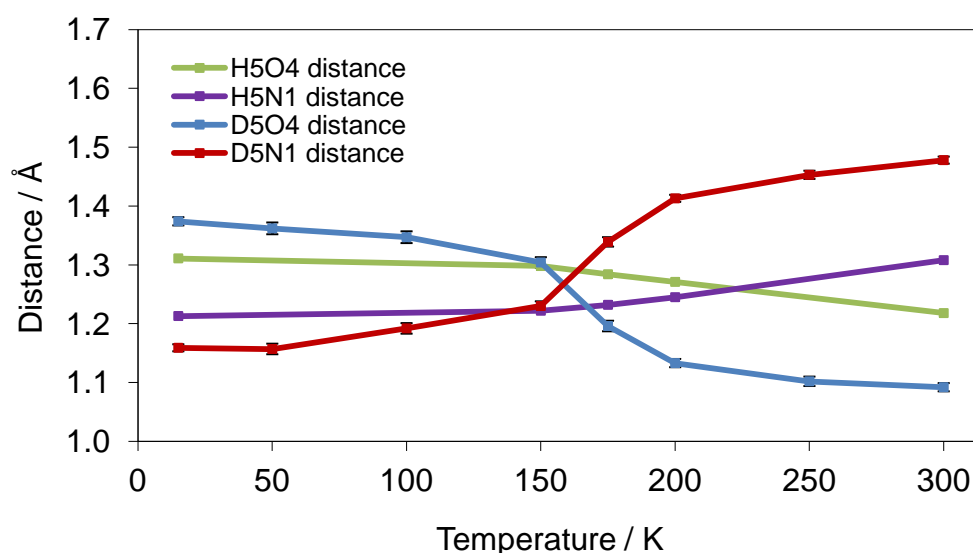


*Figure 3.16: The temperature dependence of the D5–O4 and D5–N1 bond lengths in d-35PDCA (red and blue curve) and the H5–O4 and H5–N1 in h-35PDCA (green and purple) obtained from single crystal neutron diffraction (with the literature values used for h-35PDCA at 15 and 300 K).[2] Where not obvious, esd bars on bond lengths are smaller than the symbols plotted.*

### 3.2.4 Variable Pressure Studies

The *d*-35PDCA compound was studied as a function of pressure in order to further understand the proton migration phenomenon, by separating lattice expansion effects

from the effects caused by the activation of phonons. Preliminary variable pressure single crystal X-ray diffraction data were obtained at room temperature using a diamond anvil cell. The aim of this experiment was to obtain a rough set of lattice parameters as a function of pressure, for use in a forthcoming variable pressure single crystal neutron diffraction experiment at ISIS. Lattice parameters were successfully obtained at 0, 5 and 15 kbar; however at 25 kbar the crystal mosaicity had increased so much, possibly as a result of crystal shattering, that it was not possible to index the unit cell.

Following this, a variable pressure single crystal neutron diffraction study was undertaken on SXD at ISIS using a modified Paris-Edinburgh pressure cell. The aim of this experiment was to determine any structural changes, particularly in the position of the D5 atom (that of the SSHB), as a function of pressure. However, a number of problems were encountered during the course of this experiment, predominantly due to the inability to obtain sufficient numbers of reflections; it was only possible to use 6 out of 11 of the instrument's detectors with the pressure cell in place, as a result of its design, therefore many reflections may have been lost. Furthermore, the crystal quality deteriorated significantly with the application of pressure. This lack of reflections meant that structural analysis, even with the lattice parameters from single crystal XRD (described above) and constant wavelength neutron data (see below), was not possible. An additional problem encountered during this experiment involved the inability to reliably determine the pressures being achieved. The pressure calibration method on this instrument relied on a pre-determined set of lattice parameters from single crystal XRD, described above. These lattice parameters were then used to determine a relationship between lattice contraction and pressure, to be used with the newly determined lattice parameters from SXD. However, a combination of the lack of reflections produced by the sample in this case (for the reasons described above), and the fact that only lattice parameter ratios can be determined using the white-beam Laue technique, meant that it was not possible to reliably index the unit cell at any nominal pressure and consequently the actual pressure achieved could not be determined.

Further work, using powder neutron diffraction on D20 at the ILL, was therefore undertaken. The aim of this work was to obtain a reliable set of lattice parameters as a function of pressure in order to determine the presence of any potential phase transitions occurring with increasing pressure. The *d*-35PDCA sample was studied at room

temperature, at pressures in the range of 0 to 43 kbar. All of the raw data obtained are given in Figure 3.17.
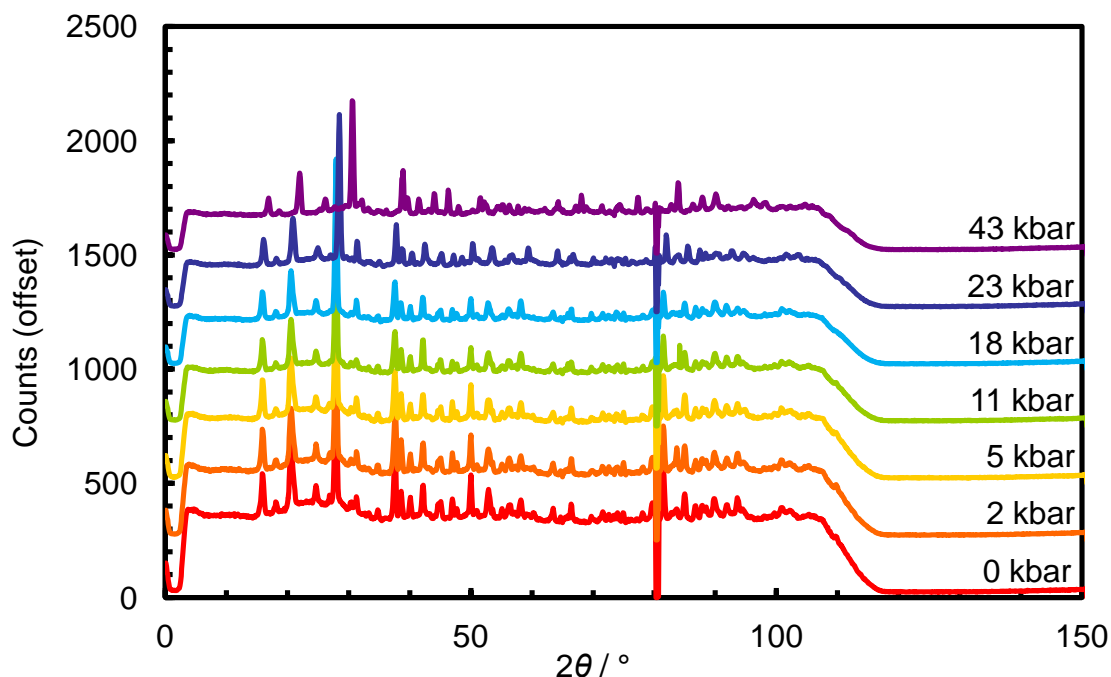


*Figure 3.17: The variable pressure data collected for d-35PDCA. An electrical fault on the instrument resulted in the spike at 80° 2θ; this region was excluded in the Rietveld analysis. In addition, these peaks include those resulting from the NaCl pressure calibration material.*

For each pressure the high temperature, N···D–O, structure, obtained from single crystal neutron diffraction, was used as the starting model for the Rietveld refinement. A model for NaCl (the pressure calibration material) was also included in the refinement. A total of 86 parameters were refined in each analysis, including 15 coefficients of a Chebyshev polynomial to model the background, 4 lattice parameters for *d*-35PDCA and 1 for NaCl, 4 parameters to define the TCHZ peak shape for both phases, and a scale factor. In addition, for each refinement, bond distances and angles within the *d*-35PDCA molecule were restrained relative to those at ambient pressure; torsion angles were also restrained in order to describe the molecules as approximately planar. Anisotropic displacement parameters were refined for the D5 atom of *d*-35PDCA only, with isotropic thermal displacement parameters refined for all of the other atoms. Whilst these refinements modelled peak positions well, and hence sensible lattice parameters

could be extracted, peak intensities were not modelled so well, and hence atomic parameters and thermal displacement parameters were not as reliable. Therefore in the final refinements, the changing position of the D5 atom as a function of pressure was not analysed. A rigid-body approach was also attempted, where the 35PDCA molecule was forced to be rigid, in an effort to better the structural model; however the outcome of the refinement was not improved.

It seems from Figure 3.17 that the main change upon increasing pressure is a shift of the peaks to higher $2\theta$ values, reflecting a decrease in the lattice parameters as expected. No significant peak appearances or losses, indicative of a possible change in symmetry, are apparent.

Figure 3.18 shows that, in the pressure range studied (0 to 43 kbar), the *a*, *b* and *c* parameters decreased by 2, 3 and 8 %, respectively, while the $\beta$ angle increased by 1 %, resulting in an overall decrease in the volume of 13 %. As expected, the largest change in the lattice parameters is in the *c*-axis, the axis perpendicular to the layers, in which only very weak intermolecular interactions exist. In addition, it seems that a potential phase transition is present, occurring above 18 kbar, with very few changes occurring as a function of pressure below this. These results are comparable to those obtained from variable temperature experiments; the transition observed from the variable pressure experiment appears to be similar to that observed at 150 K on changing temperature. Similarly, the largest change in unit cell parameters observed in both experiments is in the *c*-axis. Overall, the magnitude of the change in lattice parameters determined from the variable pressure data is much greater than that observed over the temperature range studied. These comparisons suggest that similar proton migration behaviour is occurring on increasing pressure, from the oxygen atom in a larger unit cell to the nitrogen atom in a smaller unit cell, as observed on decreasing temperature.
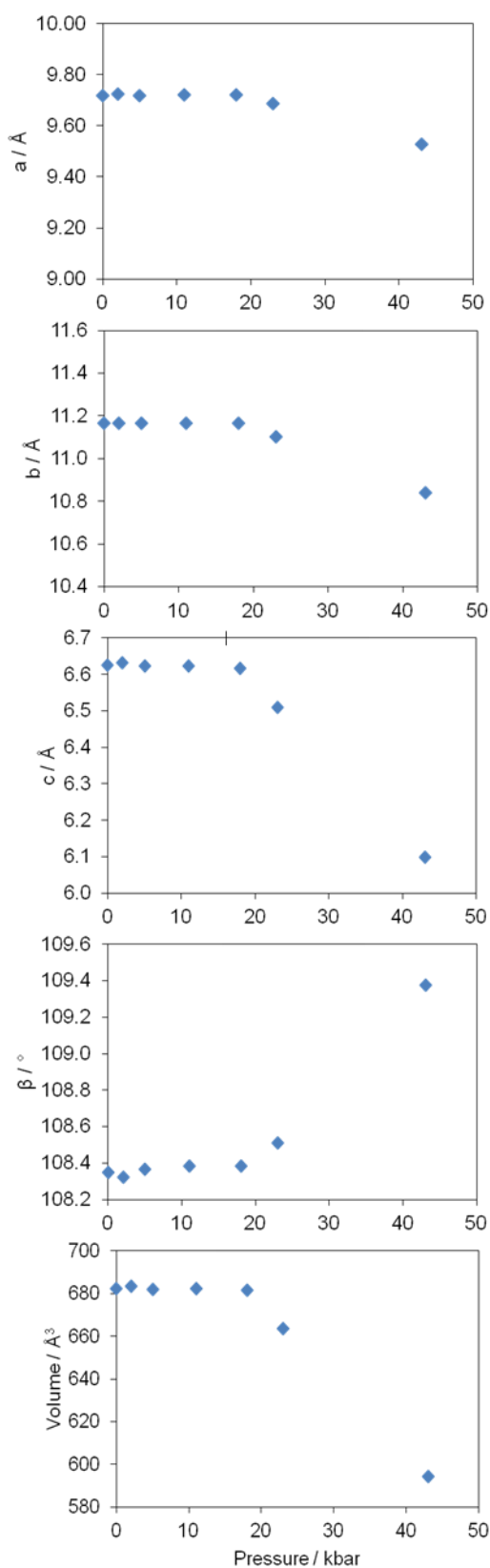
*Figure 3.18: Pressure dependence of the unit cell parameters of d-35PDCA from powder neutron diffraction, obtained by Rietveld analysis. The unit cell parameters a, b*

*and c are plotted on the same % scale for direct comparison. Where not observed, esd bars are smaller than the symbols plotted.*

In order to investigate the structural changes observed with the application of pressure, a geometry optimisation calculation was performed in DMol$^3$. The starting structure used was based on that obtained from single crystal neutron diffraction at 300 K, but with the unit cell parameters obtained from powder neutron diffraction at 43 kbar. This calculation resulted in the proton-transferred N1–D5···O4 species, as suggested from comparison with the variable temperature data.

The suggestion of a phase transition in the variable pressure data, analogous to that from variable temperature studies, combined with the observation of the proton-transferred structure from theoretical studies, using the lattice parameters determined at 43 kbar, merits further study of this material as a function of pressure. In order to obtain reliable hydrogen bond distances, and so determine whether proton migration, analogous to that observed on decreasing temperature, is in fact occurring on increasing pressure, a further variable pressure single crystal neutron diffraction experiment should be performed.

### 3.2.5 The Role of Molecular Vibrations

In order to determine the driving force of the experimentally observed phase transitions and understand the isotope effect, a DFT computational study of the 35PDCA isotopologues was undertaken. The Helmholtz free energy of a crystal $G(T,V)$ as a function of temperature $T$ and structure (expressed here by the unit cell volume, $V$, and isotopic composition, $H/D$) is given by Equation 3.1:[33, 34]

$$G(T,V,H/D) = E(V) + F(T,V,H/D) - TS(T,V,H/D) \qquad \text{(Equation 3.1)}$$

where $E(V)$ is the enthalpy of the crystal. $F(T,V)$ is the internal vibrational energy which, for a given $V$ and $H/D$, increases with temperature. The vibrational entropy, $S(T,V,H/D)$, also increases with temperature for a given $V$ and $H/D$. The last two terms in the equation constitute the vibrational free energy $G_{vib}$ which decreases with increasing temperature since the entropy term dominates. $G_{vib}$ depends on isotopic

composition through the masses of the atoms and takes into account the quantum zero-point energy of protons and deuterons *via* the $F$ term in Equation 3.1. In principle a *pressure × volume* term should be added to the Helmholtz free energy, giving the Gibbs' free energy. However, for crystals close to ambient pressure, the *pressure × volume* term is negligible.[34]

The equilibrium structure ($V$) at a given temperature ($T$) corresponds to the free energy $G(T,V,H/D)$ minimum. At $T = 0$ K, the vibrational entropy is zero, so the stable structure ($V_0$) is determined by enthalpy and zero-point internal vibrational energy. For a system which has undergone thermal expansion to unit cell volume $V_1$, $E(V_1) > E(V_0)$. The temperature at which the expanded structure becomes the equilibrium structure depends on the enthalpy difference $E(V_1) - E(V_0)$, and how much more steeply $G_{vib}$ for the structure with cell volume $V_1$ decreases with increasing temperature, compared to the structure with cell volume $V_0$.

$G_{vib}$ can be calculated with good accuracy, within the harmonic approximation, using density functional theory methods to determine the normal modes of vibration of the crystal. The accuracy of such normal-mode calculations has been demonstrated for 35PDCA.[6] $G_{vib}$ for a given structure ($V$) is then given by Equation 3.2.

$$G_{vib}(T,V,H/D) = k_B T \sum_0^{\omega_{max}} g(\omega) \ln \left[ 2 \sinh \left( \frac{\hbar\omega}{2k_B T} \right) \right] \qquad \text{(Equation 3.2)}$$

where $\hbar\omega$ is the vibrational eigen-energy and the sum runs over all modes. In principle, DFT methods would also give a reliable estimate of the enthalpy difference $E(V_1) - E(V_0)$, but, in the case of molecular crystals, the absence of dispersive interactions means that the enthalpy difference is not determined with sufficient accuracy. This fact also means that normal-mode calculations to determine $G_{vib}$ are best performed using experimental unit cell parameters rather than those obtained from structure optimisation.

The following discussion is based on calculations of normal modes and $G_{vib}$ for *d*-35PDCA in three different structural models: firstly, using the 15 K unit cell

parameters and the low-temperature N–D···O structure (N–D···O in $V_0$); secondly, using the 300 K cell parameters and the N–D···O structure (N–D···O in $V_1$); and thirdly, using the 300 K cell parameters and the high-temperature deuteron-transferred N···D–O structure (N···D–O in $V_1$). In this way, the effect of lattice thermal expansion can be separated from that of deuteron migration. All calculations performed here were performed with the DMol$^3$ code,[35] which allowed the high temperature structure with the proton migrated to the oxygen to be most accurately reproduced. Dispersion-corrected DFT based on empirical potentials was tested with DMol$^3$, but the agreement between the DFT-optimised and the experimentally determined structures was not improved and the energy differences between the three structural models were not more realistic.

The normal-mode calculations have been performed with DMol$^3$ in the Materials Studio software suite (version 5.0).[35] The GGA-PBE functional was used to describe the exchange and correlation energy, the *k*-point mesh (0,0,0) and the DND basis set were used to describe the expansion of atomic orbitals.

Figure 3.19 shows $G_{vib}$ curves for the N–D···O crystal structure in the small unit cell (N–D···O in $V_0$, curve A), the N–D···O crystal structure in the large unit cell (N–D···O in $V_1$, curve B) and the deuteron-transferred N···D–O structure in the large unit cell (N···D–O in $V_1$, curve C). As expected, all curves show a decrease in $G_{vib}$ with increasing temperature.
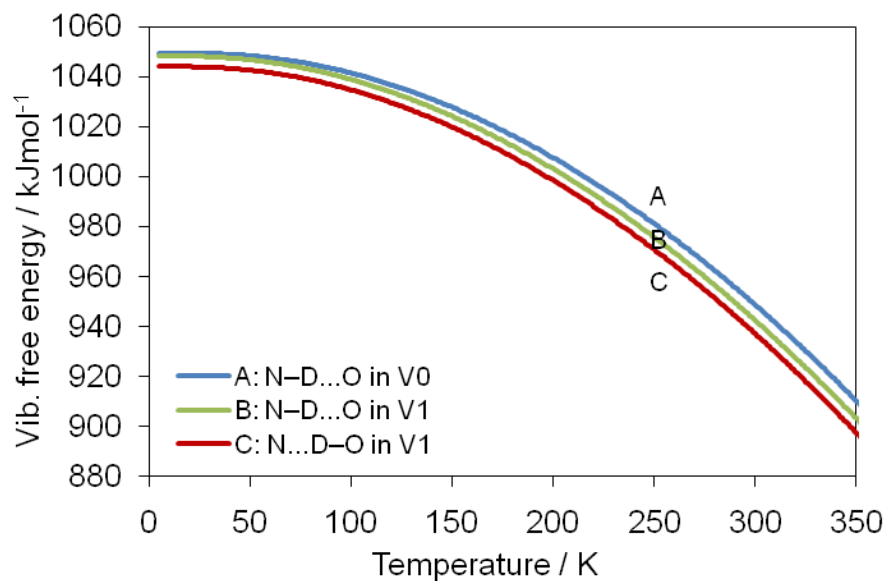
*Figure 3.19: $G_{vib}$ vs. temperature curves calculated for d-35PDCA: the N–D···O structure in the small unit cell (N–D···O in $V_0$, curve A), the N-D···O structure in the large unit cell (N–D···O in $V_1$, curve B) and the deuteron-transferred N···D–O structure in the large unit cell (N···D–O in $V_1$, curve C).*

It is the differences between these curves that are most meaningful and are shown in Figure 3.20. Note the sign in the plot is such that a larger positive magnitude means increased stability. Curve A-B shows the stabilising effect of lattice expansion over the whole temperature range. As expected, the larger volume structure becomes increasingly stabilised by $G_{vib}$ as temperature increases. Curve B-C shows the variation in $G_{vib}$ due to deuteron migration. Below 137 K, the structure without deuteron migration is favoured by $G_{vib}$ (*i.e.* if the deuteron moves, the $G_{vib}$ stabilisation is reduced relative to its 0 K value). The structure with deuteron migration is favoured at higher temperatures, as observed experimentally. The magnitude of the change in $G_{vib}$ stabilisation due to thermal expansion over this temperature range is around four times that due to deuteron migration. However, in reality we know that the two contributions are coupled as illustrated by the change in cell volume at the phase transition (see Figure 3.6), and the total change in $G_{vib}$ at room temperature relative to that at 0 K is about 6 kJmol$^{-1}$ (750 K).
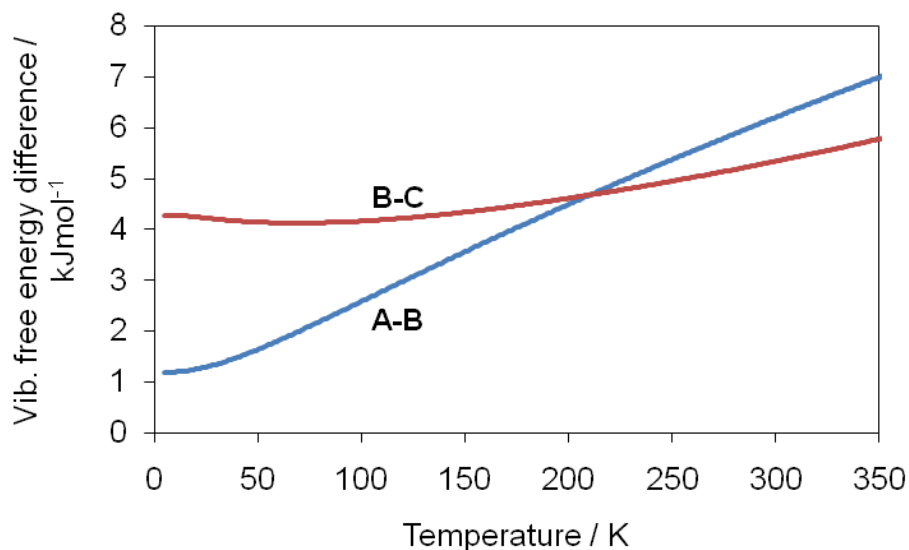
*Figure 3.20: $G_{vib}$ differences showing the contribution of lattice expansion (curve A-B) and deuteron migration (curve B-C) to free energy stabilisation in d-35PDCA.*

The same $G_{vib}$ calculations were performed for the other three 35PDCA isotopologues. For each isotopologue, the effect of isotopic composition on $G_{vib}$ is shown in Figure 3.21 for the small unit cell structures with *H/D* bonded to the N atom (curve A, solid) and for the large unit cell structures with *H/D* migrated towards the O atom (curve C, dashed). Note the DD pair of curves is equivalent to curves A and C in Figure 3.19. Deuteration, which causes a red shift of some of the modes due to the increased mass, reduces $G_{vib}$, and the relative offset between the various pairs of curves is proportional to the number of deuterons: 0 for *h*-35PDCA (HH), 2 for *acid-d*-35PDCA (HD), 3 for *ring-d*-35PDCA (DH) and 5 for *d*-35PDCA (DD).
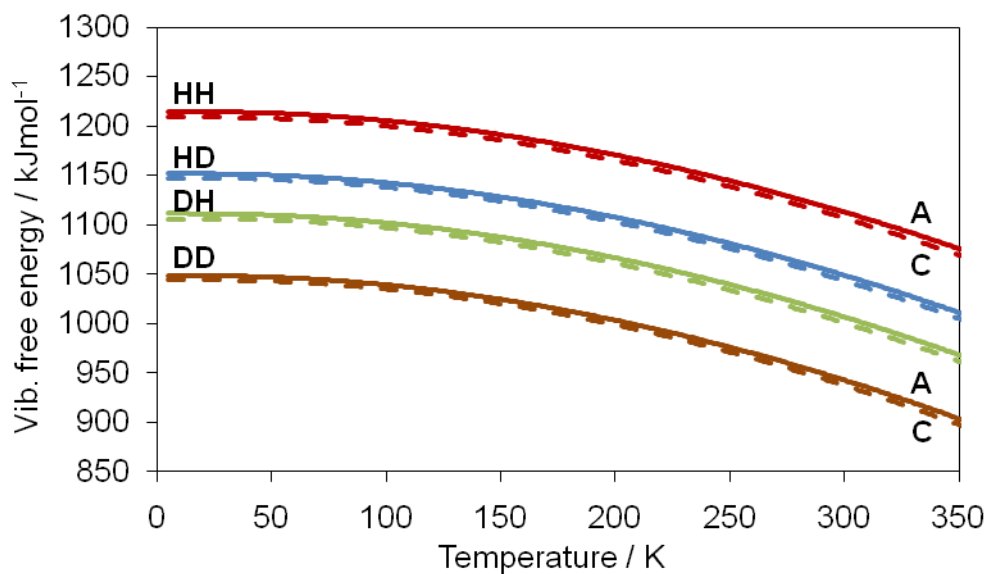
*Figure 3.21: Comparative plots of $G_{vib}$ vs. temperature for the four isotoplogues of 35PDCA: h-35PDCA (HH), acid-d-35PDCA (HD), ring-d-35PDCA (DH) and d-35PDCA (DD). For each isotopic composition, two curves are shown: one for the small unit cell structure with H/D bonded to the N atom (curve A, solid) and one for the large unit cell structure with H/D migrated towards the O atom (curve C, dashed).*

Again the free energy differences (A-C), which represent both thermal expansion and proton migration effects, are most meaningful and these are shown in Figure 3.22 for the *h*-35PDCA (HH) and *d*-35PDCA (DD) systems. The two curves evolve similarly with temperature. Assuming an enthalpy and zero-point vibrational energy difference of 8.4 kJmol$^{-1}$ between the low- and high-temperature structures (consistent with the value obtained from DFT calculations), then the curves A and C will all cross (A-C = 0) at approximately $170 \pm 10$ K. This result is consistent with the experimental observation that the changes in the cell parameters occur at a similar temperature for the partially and fully deuterated systems.
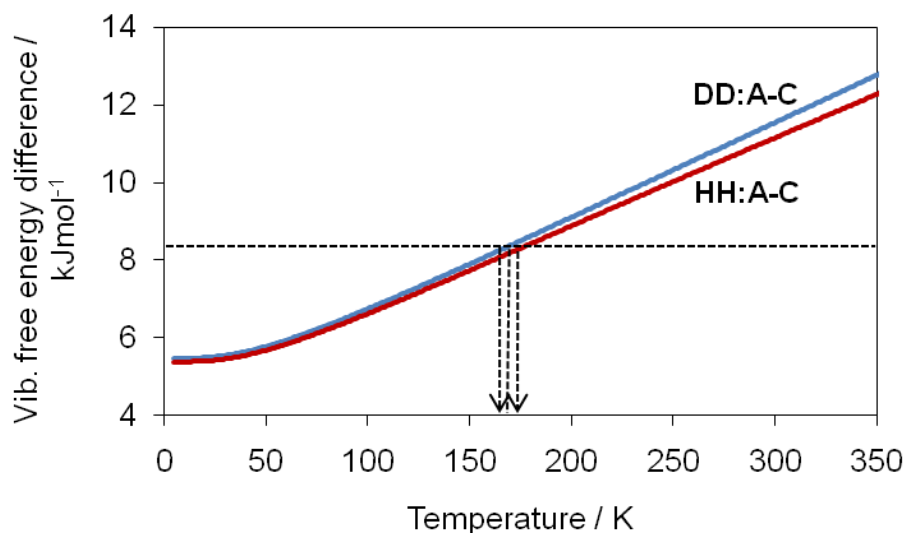
*Figure 3.22. $G_{vib}$ stabilisation (A-C) due to both proton/deuteron migration and thermal expansion as a function of temperature, for h-35PDCA (HH) and d-35PDCA (DD). The horizontal and vertical dashed lines indicate a transition temperature of 170 K if the enthalpy difference between low- and high-temperature structures is 8.4 kJmol$^{-1}$.*

Finally, the reason why no evidence of a distinct first-order phase transition is observed for the fully protonated material can be investigated in terms of the $G_{vib}$ changes for the *h*-35PDCA (HH) and *d*-35PDCA (DD) isotopologues, calculated in the two sets of unit cells determined experimentally at 15 and 300 K (Figure 3.23). There are four combinations which show that the changes in $G_{vib}$ as a function of temperature, here set to zero at 0 K, are always bigger for the *d*-35PDCA (DD) molecule in the same lattice (the blue curves are above the red curves in each solid-dashed line pair) by 0.42 to 0.84 kJmol$^{-1}$ (50 to 100 K) at 300 K. However, as stated above, the proton/deuteron migration is associated with a pronounced expansion of the lattice. Taking into account both effects reveals a much stronger $G_{vib}$ stabilisation upon proton/deuteron migration (4.18 kJmol$^{-1}$ or 500 K, the difference between the upper and lower solid curves in Figure 3.21) at 300 K in favour of the *d*-35PDCA form compared to the *h*-35PDCA phase.
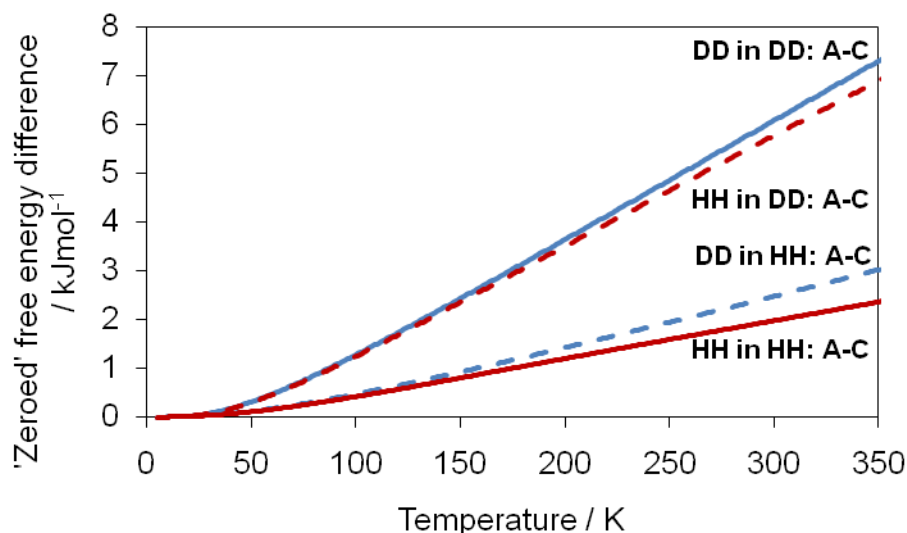
*Figure 3.23: $G_{vib}$ stabilisation due to both proton/deuteron migration and thermal expansion (A-C), set to zero at 0 K, for h-35PDCA (HH) and d-35PDCA (DD), calculated using the unit cell parameters determined experimentally for the two isotopologues at 15 and 300 K. The upper and lower pairs each show the effect of isotopic substitution without change in lattice parameters. Comparing upper and lower solid curves shows the effect of isotopic change and unit cell volume variation.*

## 3.3  Conclusions

It has been demonstrated, using variable temperature powder and single crystal neutron diffraction, that the giant deuteron migration in *d*-35PDCA is driven by a first-order isosymmetric phase transition. Between 15 and 300 K, the deuteron involved in a short strong hydrogen bond moves by 0.32(1) Å, and the structure changes from the low temperature N–D···O form to the high-temperature N···D–O form; the magnitude of deuteron migration observed is unprecedented in this class of compounds. Powder neutron diffraction data show that this is a nonclassical phase transition, which occurs *via* growth of the daughter phase in the parent phase matrix, and is accompanied by more marked changes in the cell parameters close to the transition critical temperature $T_c$, estimated as approximately 175 K; this was modelled by parametric Rietveld refinement as domain-size-dependent excess peak broadening. Similar phase transitions are observed by powder diffraction in two partially deuterated forms of 35PDCA, *ring-d*-35PDCA and *acid-d*-35PDCA.

A variable pressure powder neutron diffraction experiment was successfully performed at room temperature, with the aim of separating the effects of lattice expansion from the effects caused by the activation of phonons. The results of this work suggest that a possible phase transition occurs above 18 kbar, comparable with that observed at 150 K from variable temperature data, implying that possible proton migration is occurring on increasing pressure. This is also suggested by theoretical studies on *d*-35PDCA, which predict that the proton-transferred (N–H⋯O) structure is the lowest energy configuration for the unit cell determined at 43 kbar. A further variable pressure single crystal neutron diffraction experiment should be undertaken, using a different type of pressure cell, in order to confirm and reliably quantify these findings.

DFT calculations show that deuteron migration in *d*-35PDCA results in a decrease in vibrational free energy $G_{\text{vib}}$ with increasing temperature which is about 25% of the decrease in $G_{\text{vib}}$ due to lattice thermal expansion. Vibrational free energy changes, which are estimated to be equivalent to 6 kJmol⁻¹ for *d*-35PDCA at room temperature, can therefore be identified as the driving force for the observed structural phase transition. The calculations predict that the critical temperature $T_{\text{c}}$ should be similar for all isotopologues which display the phase transition, in agreement with our experimental observations. Finally, the DFT calculations also demonstrate that the vibrational free energy stabilisation is the most pronounced for the fully deuterated material and proportional to the level of deuteration, *i.e.* the mass of the molecule. This is again consistent with the experimental structural work, where distinct crystallographic first-order phase transitions were clearly observed for the three deuterated systems but not observed for the fully protonated *h*-35PDCA.

The analysis in terms of vibrational free energy extends the original analysis based on molecular dynamics simulations,[6] which highlighted the role of low frequency lattice modes, to include the role of all vibrations, weighted by the Boltzmann population factor, including higher frequency modes that are more sensitive to isotopic substitution.

## 3.4 References

1.    F. Takusagawa, K. Hirotsu and A. Shimada, *Bull. Chem. Soc. Jpn.*, 1973, **46**, 2292.
2.    J. A. Cowan, J. A. K. Howard, G. J. McIntyre, S. M. F. Lo and I. D. Williams, *Acta Crystallogr., Sect. B*, 2005, **61**, 724.
3.    T. Steiner, I. Majerz and C. C. Wilson, *Angew. Chem. Int. Ed.*, 2001, **40**, 2651.
4.    J. A. Cowan, J. A. K. Howard, S. A. Mason, G. J. McIntyre, S. M. F. Lo, T. Mak, S. S. Y. Chui, J. W. Cai, J. A. Cha and I. D. Williams, *Acta Crystallogr. Sect. C*, 2006, **62**, O157.
5.    J. Zhou, Y. S. Kye and G. S. Harbison, *J. Am. Chem. Soc.*, 2004, **126**, 8392.
6.    F. Fontaine-Vive, M. R. Johnson, G. J. Kearley, J. A. Cowan, J. A. K. Howard and S. F. Parker, *J. Chem. Phys.*, 2006, **124**, 234503.
7.    O. J. Delamore, *M.Chem.*, University of Durham, 2008.
8.    A. A. Coehlo, *TOPAS Academic: General profile and structure analysis software for powder diffraction data*, Bruker AXS, Karlsruhe, 2005.
9.    *Bruker SMART v5.629*, Bruker AXS Inc., Madison, WI, USA, 2000.
10.   *Bruker SAINT+ v6.45*, Bruker AXS Inc., Madison, WI, USA, 2003.
11.   G. M. Sheldrick, *SADABS*, University of Gottingen, Germany, 1996.
12.   P. W. Betteridge, J. R. Carruthers, R. I. Cooper, K. Prout and D. J. Watkin, *J. Appl. Crystallogr.*, 2003, **36**, 1487.
13.   R. Ibberson, W. I. F. David and K. S. Knight, *A User Guide, ISIS Crystallography*, 1992.
14.   G. W. Stinton and J. S. O. Evans, *J. Appl. Crystallogr.*, 2007, **40**, 87.
15.   G. J. McIntyre, M.-H. Lemee-Cailleau and C. J. Wilkinson, *Physica B*, 2006, **385-386**, 1055.
16.   J. W. Campbell, J. Habash, J. R. Helliwell and K. Moffat, *Information Quarterly for Protein Crystallography, No. 18*, SERC, Daresbury Laboratory, Warrington, England, 1986.
17.   J. W. Campbell, Q. Hao, M. M. Harding, N. D. Nguti and C. J. Wilkinson, *J. Appl. Crystallogr.*, 1998, **31**, 23.
18.   C. J. Wilkinson, H. W. Khamis, R. F. D. Stansfield and G. J. McIntyre, *J. Appl. Crystallogr.*, 1988, **21**, 471.
19.   G. M. Sheldrick, *SHELXL* Bruker AXS Inc., University of Gottingen, Germany, 2000.
20.   M. R. Probert, C. M. Robertson, J. A. Coome, J. A. K. Howard, B. C. Michell and A. E. Goeta, *J. Appl. Crystallogr.*, 2010, **43**, 1415.
21.   D. A. Keen, M. J. Gutmann and C. C. Wilson, *J. Appl. Crystallogr.*, 2006, **39**, 714.
22.   S. Klotz, G. Hamel and J. Frelat, *High Press. Res.*, 2004, **24**, 219.
23.   C. L. Bull, M. Guthrie, R. J. Nelmes, J. S. Loveday, H. Hamidov and M. J. Gutmann, *High Press. Res.*, 2009, **29**, 644.
24.   C. L. Bull, M. Guthrie, R. J. Nelmes, J. S. Loveday, K. Komatsu, H. Hamidov and M. J. Gutmann, *High Press. Res.*, 2009, **29**, 780.
25.   T. C. Hansen, P. F. Henry, H. E. Fischer, J. Torregrossa and P. Convert, *Meas. Sci. Technol.*, 2008, **19**, 034001.
26.   A. G. Christy, *Acta Crystallogr. Sect. B.*, 1995, **51**, 753.
27.   S. J. Ford, O. J. Delamore, J. S. O. Evans, G. J. McIntyre, M. R. Johnson and I. R. Evans, *Chem. Eur. J.*, 2011, **in press**.

28.    A. R. Ubbelohde, *Nature*, 1966, **212**, 70.
29.    A. R. Ubbelohde, *J. Chim. Phys. Phys.- Chim. Biol.*, 1966, **63**, 33.
30.    A. R. Ubbelohde, *Acta Crystallogr., Sect. A*, 1963, **16**, 183.
31.    F. H. Allen, *Acta Crystallogr. Sect. B.*, 2002, **58**, 380.
32.    F. H. Allen and W. D. S. Motherwell, *Acta Crystallogr. Sect. B.*, 2002, **58**, 407.
33.    M. Sternik and K. Parlinski, *J. Chem. Phys.*, 2005, **123**, 204708.
34.    Z. Lodziana and K. Parlinski, *Phys. Rev. B*, 2003, **67**, 174106.
35.    B. Delley, *J. Chem. Phys.*, 2000, **113**, 7756.

# 4 3,5-Pyridinedicarboxylic Acid: Evidence for the Vibrational Modes Involved in Proton Migration

The diffraction work, reported in Chapter 3, shows a structural phase transition associated with a switchover in the populations of the two hydrogen bond sites for the fully deuterated, *d*-35PDCA, sample. For the protonated material, *h*-35PDCA, the change with increasing temperature appears more progressive; in the range 20 to 200 K the N1–H5 distance increases steadily from approximately 1.2 Å to approximately 1.3 Å whereupon the hydrogen atom, H5, is more closely associated with the oxygen atom, O4. The phase transition in *d*-35PDCA has been found to occur *via* growth of the daughter phase (N···D–O) in the parent phase matrix (N–D···O) on increasing temperature. In diffraction, however, instantaneous effects caused by changes in the atomic positions are averaged over time and space, and therefore certain short-range effects may be missed. Vibrational spectroscopy probes specific molecular vibrations, sensitive to a 1 nm length scale, and therefore provides information about the local bonding environment. Thus the combined use of diffraction and vibrational spectroscopy can provide a more complete view of the mechanism of migration.

The diffraction work was consequently followed up by a vibrational spectroscopy study, reported in this chapter. Variable temperature inelastic neutron scattering (on IN1 at ILL), infrared (IR) and Raman spectroscopy were used to investigate the changes in the vibrational spectra of various isotopologues of 35PDCA, as a function of temperature. The aim of this work was to provide evidence for the existence of the two or more molecular species, caused by proton hopping, and also to study any differences between the various 35PDCA samples, providing further information about the isotope effect on proton migration in this compound.

The three methods used result in different spectra due to the different ways that they interact with a sample. All spectroscopic techniques offer an indirect method of obtaining structural information since it is the vibrational modes, that are characteristic of the molecular structure, that are studied. For IR spectroscopy photons of light interact with fluctuations of the dipole moment of a molecule and in Raman scattering there must be a change in the molecular polarisability in order for a specific vibration to be

observed. Neutron vibrational spectroscopy (INS) is another variant on this theme, but due to the absence of selection rules, all vibrations should, in principle, be observable. The observed intensity in INS, given by Equation 4.1 and described in detail in Chapter 2, is a function of the magnitude of transferred momentum, $Q$ (determined only by the spectrometer used), the total scattering power of the atoms, $\sigma$ (non-zero for all atoms) and the amplitude of the atomic displacements, $u$ (determined by the forces and masses in the molecule under study). As all atoms undergo motion, they all contribute to the INS intensity, *i.e.* there are no selection rules.

$$S(\boldsymbol{Q}, \omega_i) = \sum_i \sum_{j=1}^{3N} \boldsymbol{Q}^2 \boldsymbol{u}_{ij}^2 \cdot \sigma_j \exp\left[-2W\right] \qquad \text{(Equation 4.1)}$$

where $i$ sums over all vibrational modes and $j$ over all atoms in all directions ($x,y,z$), and $W$ is a complex term involving $\boldsymbol{Q}$.

In reality, however, not all vibrations are seen as individual peaks due to the lower resolution of INS (in comparison with IR and Raman), the low scattering power of certain atoms and the intensity fall off at higher energies due to the Debye-Waller factor (the exponential term in Equation 4.1).

In this work three of the isotopologues, *h*-35PDCA, *ring-d*-35PDCA and *d*-35PDCA, have been used. The *ring-d*-35PDCA sample was studied using inelastic neutron scattering (INS). As the ring is deuterated in this sample, the scattering signal from hydrogen atoms not involved in hydrogen bonding is effectively suppressed (deuterium has a much lower total neutron scattering power than hydrogen due to its much lower incoherent scattering length). Raman and IR spectroscopy studies were also used to complement this work; their ability to study both the *h*-35PDCA and *d*-35PDCA isotopologues, which are less suitable for study by INS as the ring hydrogen/deuterium cannot be differentiated from those of the hydrogen bonds, allows for an effective comparison with diffraction in order to determine whether spectral changes are coincident with diffraction observations.

Finally, previous work found that low frequency lattice vibrations drive the proton migration observed in this compound. Fourier transform of the time-dependent N1–H5

bond length variation at 300 K revealed two well-defined peaks at 115 and 145 cm$^{-1}$ (14 and 18 meV) whilst phonon calculations found that these peaks correspond to vibrations in the plane of the molecular sheets which modulate the geometry of the hydrogen bond.[1] In the current work INS (on IN8 at the ILL) was further used to look for the experimental temperature dependence of the low frequency phonons that are regarded as driving the proton migration in 35PDCA.

## 4.1 Experimental

### 4.1.1 Synthesis

A range of 3,5-pyridinedicarboxylic acid isotopologues were prepared, Figure 4.1. The synthesis of these samples is described in detail in Section 3.1 of Chapter 3.



|           |                  |            |
|-----------|------------------|------------|
| *h*-35PDCA | *ring-d*-35PDCA | *d*-35PDCA |
| (a)       | (b)              | (c)        |
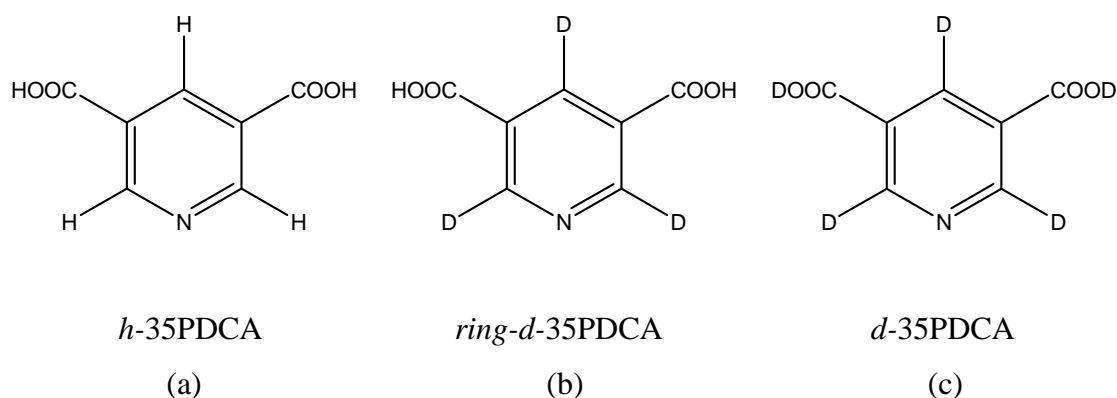
*Figure 4.1: The three isotopologues of 35PDCA studied in this work: a) fully protonated 35PDCA, b) partially deuterated 35PDCA and c) fully deuterated 35PDCA.*

### 4.1.2 Spectroscopy

#### 4.1.2.1 IN8

A cuboid-shaped single crystal of *h*-35PDCA, measuring approximately $1.9 \times 3.2 \times 3.6$ mm$^3$, was studied on IN8. A crystal of suitable quality was identified under a microscope and aligned using Orient Express; it was necessary to align the crystal with the *ab* plane as the scattering plane. Once the correct plane was found, the crystal was then transferred to IN8 where the alignment was refined on several Bragg

peaks. The Si(111) monochromator and the PG(002) analyser were used throughout this work.

Data were collected at two orientations, one parallel to the *b* axis (and therefore the short N1–H5···O4 hydrogen bond) and one parallel to the *a* axis (the normal medium-length O3–H4···O1 hydrogen bond), at Brillouin zones centred at 070 and 600 respectively, in the temperature range 10 to 300 K. *Q* values of 3.94 and 3.87 Å$^{-1}$ (for the Brillouin zones centred at 070 and 600, respectively) were kept constant by rotating the crystal.

### 4.1.2.2 IN1

The *ring-d*-35PDCA sample was measured on IN1 (BeF) in order to study the vibrations of the hydrogen bond protons at a range of temperatures from 10 to 320 K. A flat, powdered sample (200 mg), measuring $0.1 \times 2 \times 3$ cm$^3$, was wrapped securely in aluminium foil and measured. Initial scans were run at 11, 190 and 300 K over an energy range of 40 to 140 meV (323 to 1129 cm$^{-1}$) and using a monitor of $5 \times 10^5$ counts. A region of interest, spectral range 60 to 90 meV (484 to 726 cm$^{-1}$), was then identified and additional measurements were made in this range at temperatures of 100, 160, 175, 210, 250, 280, 300 and 320 K using a monitor of $1 \times 10^6$ counts.

### 4.1.2.3 IR Spectroscopy

The three isotopologue samples, *h*-35PDCA, *ring-d*-35PDCA and *d*-35PDCA were studied by IR. Powdered samples, pressed into pellets with KBr, were required for IR analysis; a small amount of each 35PDCA sample was finely ground with 200 mg of oven-dried, spectroscopic grade KBr and pressed into transparent pellets. Fourier-transform infrared (FTIR) spectra were measured using a Nicolet Magna 560 FTIR spectrometer with a MCT/B liquid-nitrogen-cooled detector. Spectra were collected, with a spectral resolution of 0.5 cm$^{-1}$, in the range 400 to 4000 cm$^{-1}$ (50 to 496 meV). In addition, measurements were recorded as a function of temperature in the range 10 to 323 K.

### *4.1.2.4  Raman Spectroscopy*

The three isotopologues were also studied by Raman spectroscopy. Small single crystals (less than $1\,mm^3$ in size) of each isotopologue were used for these measurements. Spectra were recorded, with an InVia Renishaw Raman spectrometer, in the range 250 to $4000\,cm^{-1}$ (31 to 496 meV). A 785 nm HPNIR785 laser was used to excite the sample and laser power on the sample was 30 mW or less. A resolution of $5\,cm^{-1}$ and a wavenumber accuracy of $\pm 2\,cm^{-1}$ were employed, both calibrated with the Rayleigh line and the $520.6\,cm^{-1}$ line of silicon. Samples were carefully checked for possible thermal decomposition, and, whenever necessary, this was avoided by defocusing or lowering the laser power. The Raman spectra were measured as a function of temperature in the range of 79 to 373 K.

By convention, in an INS experiment, energy/frequency is reported in meV, whereas in IR and Raman it is reported in $cm^{-1}$. The results in this chapter follow this convention; however, where possible, conversions are also given (1 meV = $8.066\,cm^{-1}$).

### 4.1.3  Computational Methods

Computational studies were used throughout this work in order to complement all of the experimental observations. Normal-mode calculations have been performed with DMol$^3$ in the Materials Studio software suite (version 5.0).[2, 3] The GGA-PBE functional was used to describe the exchange and correlation energy and the DND basis set was used to describe the expansion of atomic orbitals.[4-6] In addition the calculations were performed at the gamma point with an energy cut-off of 300 eV.

The input structures for the normal-mode analyses were the fully deuterated isotopologue (*d*-35PDCA), obtained from single crystal neutron diffraction data collected at 15 and 300 K, with their unit cell parameters determined by powder neutron diffraction ($a$ = 9.7043 Å, $b$ = 11.1106 Å, $c$ = 6.4402 Å and $\beta$ = 108.690° for the low temperature structure and $a$ = 9.7433 Å, $b$ = 11.1897 Å, $c$ = 6.6307 Å and $\beta$ = 108.392° for the high temperature structure, see Chapter 3).[7] Following geometry optimisation, a single-point energy calculation was performed with the 'frequency analysis' function enabled, allowing calculation of the vibrational mode frequencies. The resulting output

(eigenvectors) did not take the deuteration into consideration and so, in order to study the deuterated isotopologues, a routine was written to manipulate the output; in this routine the dynamical matrix was constructed for each deuterated isotopologue using the Hessian matrix (a matrix of inter-atomic force constants) resulting from the initial (effectively fully protonated) frequency analysis. The correct masses for each isotopologue were then introduced into the dynamical matrix according to Equation 2.40 (Chapter 2) and this matrix was diagonalised to obtain the correct (mass-weighted) eigenvalues and eigenvectors.

In order to calculate the partial density of states (DOS) for specific atoms as required, a local routine was again used. In this routine the eigenvector components (*x*, *y* and *z*) for each atom required, at each frequency, were summed. The resulting DOS was then output as a function of the vibrational mode frequencies.

## 4.2 Results and Discussion

### 4.2.1 Evidence for the Co-existence of Molecular Species

#### 4.2.1.1 INS: Experimental Results and Discussion

The partially deuterated sample, *ring-d*-35PDCA, was measured on IN1 in order to study the changes in the vibrational spectrum as a function of temperature, with the aim of providing evidence for the existence of the two molecular species, the low-temperature (LT) N–H···O form and the high-temperature (HT) N···H–O form, caused by proton hopping. This sample is ideal for study by inelastic neutron scattering due to the fact that, as a result of the large incoherent scattering cross-section of hydrogen, and comparatively low incoherent scattering cross-section of deuterium, the signals from the ring protons are effectively suppressed, leaving only the signal of the hydrogen atoms of interest. (It should be noted that the coherent scattering cross-sections for both isotopes are much weaker than their incoherent scattering cross-sections and therefore do not contribute greatly to their total scattering powers). The preliminary dataset obtained on the *ring-d*-35PDCA isotopologue at 11 K is given in Figure 4.2a alongside previous INS data (Figures 4.2b and 4.2c), also obtained at low temperature but on a number of the other isotopologues (*acid-d*-35PDCA and *h*-35PDCA), in order to demonstrate the effects of selective deuteration; these additional

data were obtained on the instrument TOSCA at ISIS and have been described in detail by Fontaine-Vive *et al.*[1]
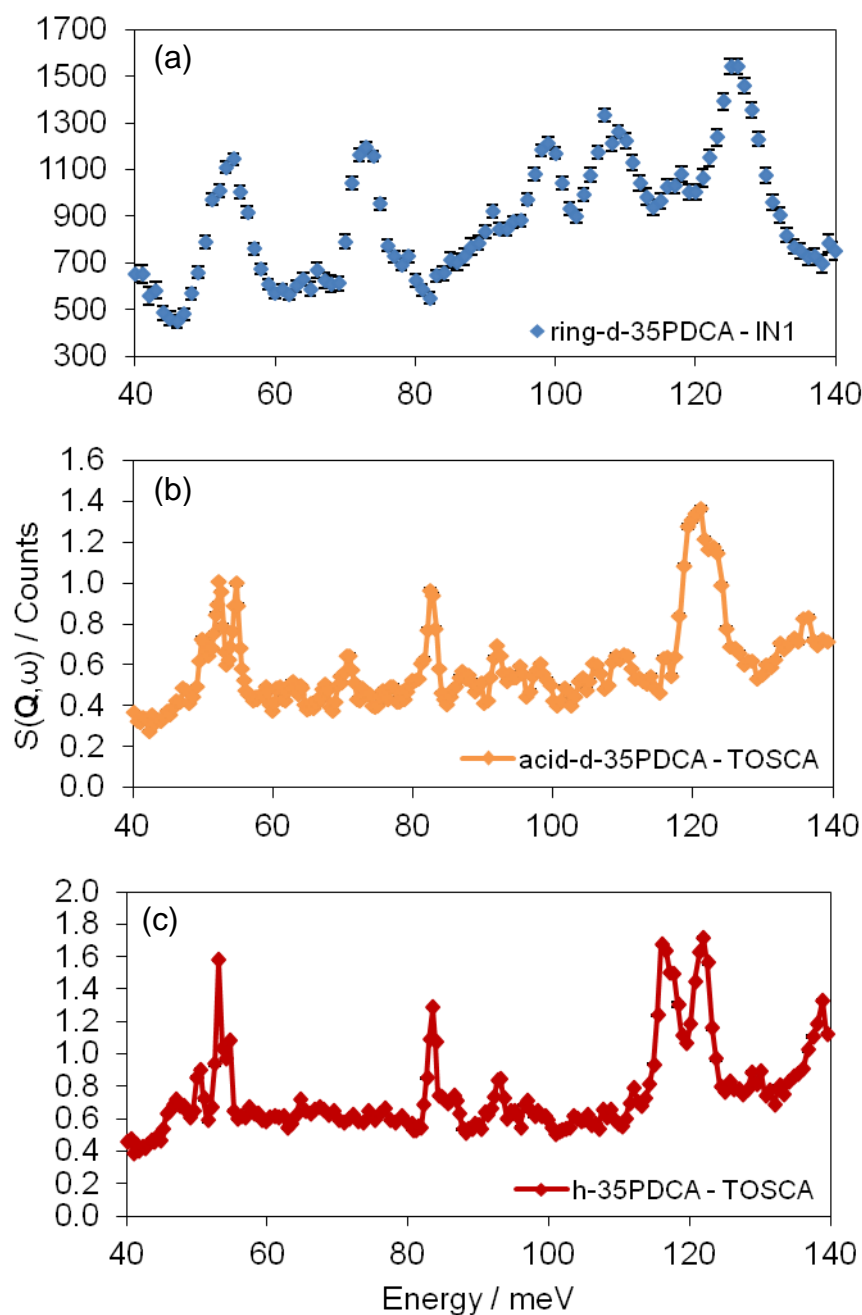


*Figure 4.2: Plots of scattering intensity as a function of energy obtained on various 35PDCA isotopologues at low temperature: a) ring-d-35PDCA from IN1, b) acid-d-35PDCA from TOSCA and c) h-35PDCA from TOSCA.*

Figure 4.2 clearly shows a number of differences between the INS results for the varying isotopologues, particularly between the *h*-35PDCA and *ring-d*-35PDCA forms,

demonstrating the large effect that selective deuteration has on the INS spectra; the differing neutron scattering cross-sections of hydrogen and deuterium, as well as the mass changes, affect the whole vibrational spectrum. The close similarities between the INS spectra of the *acid-d*-35PDCA and *h*-35PDCA isotopologues are reproduced well by VASP calculations.[1] The mode of interest in the current work (that at 75 meV (605 cm$^{-1}$), see later) is clearly defined for the *ring-d*-35PDCA showing the suitability of this sample for the present studies.

The preliminary IN1 data, obtained at 11 K, are also given alongside the remaining preliminary INS data measured for this isotopologue at 190 and 300 K, in order to demonstrate the effects of temperature change on this sample (Figure 4.3). These results show a single peak in the range 70 to 90 meV (565 to 726 cm$^{-1}$), corresponding to the LT species, at 11 K. However, on increasing the temperature from 11 to 190 K, an additional peak appears at 80 meV (645 cm$^{-1}$), existing alongside the previous peak, corresponding to the HT species. The exact temperature range of co-existence is not clear from these results and therefore further study, at a number of intermediate temperatures, was undertaken.

At 300 K it is no longer possible to distinguish the two peaks resulting from the co-existence of the LT and HT species. However, it is clear that the system has not shifted towards a fully HT species, as suggested by diffraction studies (Chapter 3). It seems that one of two situations could be occurring at this temperature; either all peak resolution has been lost, possibly due to the increased vibrational motion at this temperature preventing such subtle proton effects from being observed, or, the large number of peaks observed are a true reflection of a disordered structure at this temperature. It was necessary to repeat this study in the energy range of interest, allowing a longer collection time for each data point and a higher density of points, in order to explain this.
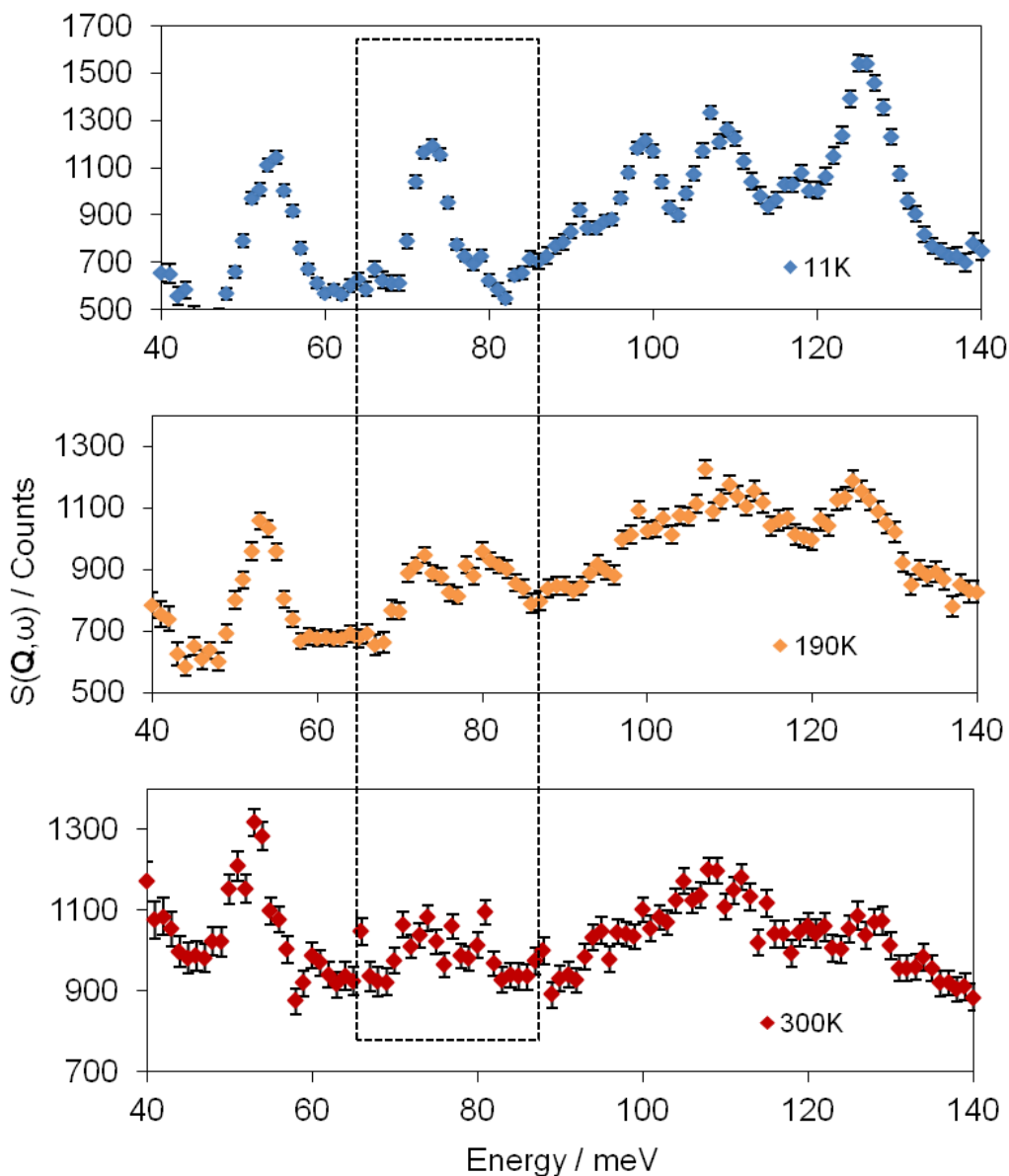
*Figure 4.3: The preliminary IN1 data, with the dotted rectangle highlighting the onset of phase co-existence as the temperature is increased.*

These further studies were undertaken with specific focus on the energy range of interest, 60 to 90 meV (484 to 726 cm$^{-1}$). Some of the results of the study at intermediate temperatures are shown in Figure 4.4 alongside the preliminary data, for comparison.
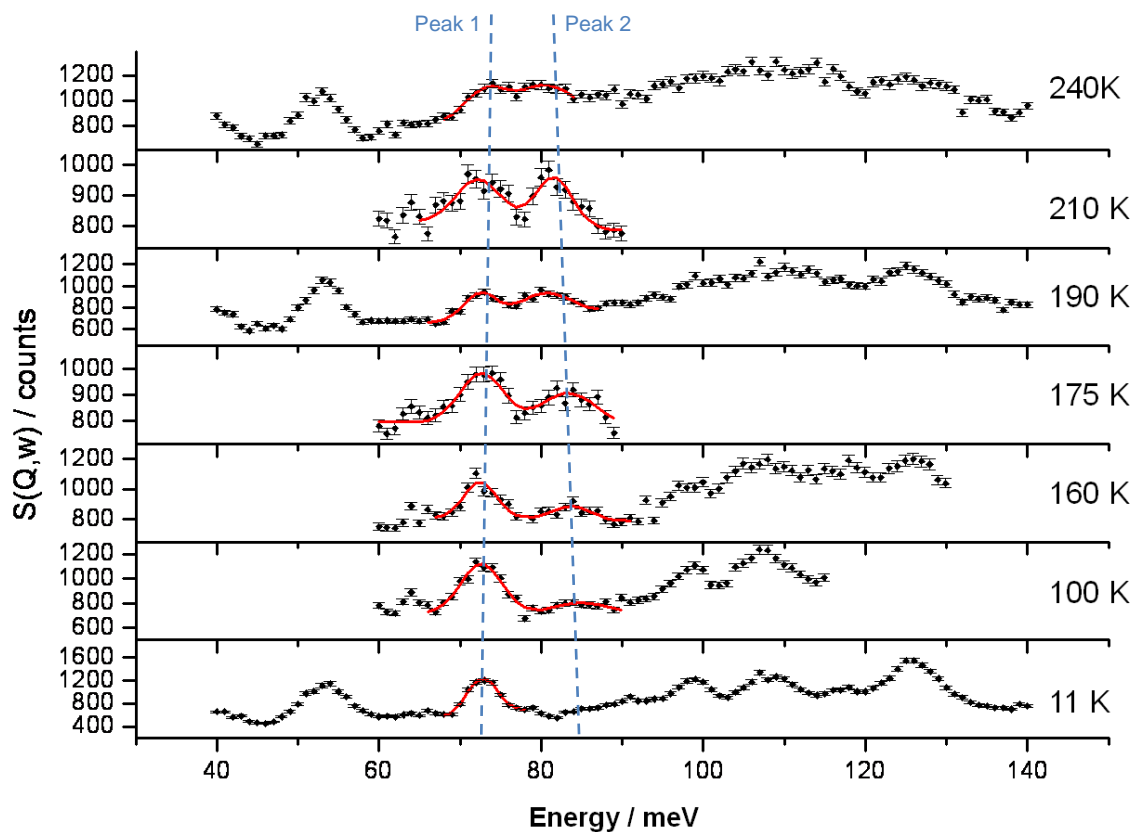
*Figure 4.4: The IN1 data, where the black points correspond to the raw data, and the red curve is a Gaussian curve fitted to the peaks of interest; the dashed blue lines mark the positions of peak 1 and peak 2 at each temperature.*

At 11 K there is a single peak (peak 1, corresponding to the LT species) between 70 and 90 meV (565 and 726 cm$^{-1}$). A second peak (peak 2, corresponding to the HT species) begins to emerge in this energy range at 100 K. The intensity of peak 2 increases as the temperature is further increased, with peak 1 intensity persisting over the temperature range studied; in addition, there is no change in peak positions. This suggests that the N–H···O species is present even at 200 K, contrary to suggestions from diffraction (Chapter 3). Also, if the peaks described here really are representative of the LT and HT species, as thought, it seems that 35PDCA is bistable; the two species (LT and HT) actually co-exist over the temperature range studied, in varying quantities.

The peak areas were determined quantitatively by fitting a Gaussian curve under each peak (as shown by the red curves of Figure 4.4), and the ratios of peak 2: peak 1 were deduced (Figure 4.5a). The resulting trend is shown alongside a plot of the temperature

dependence of the beta angle obtained from powder XRD on the same isotopologue sample (Figure 4.5b).
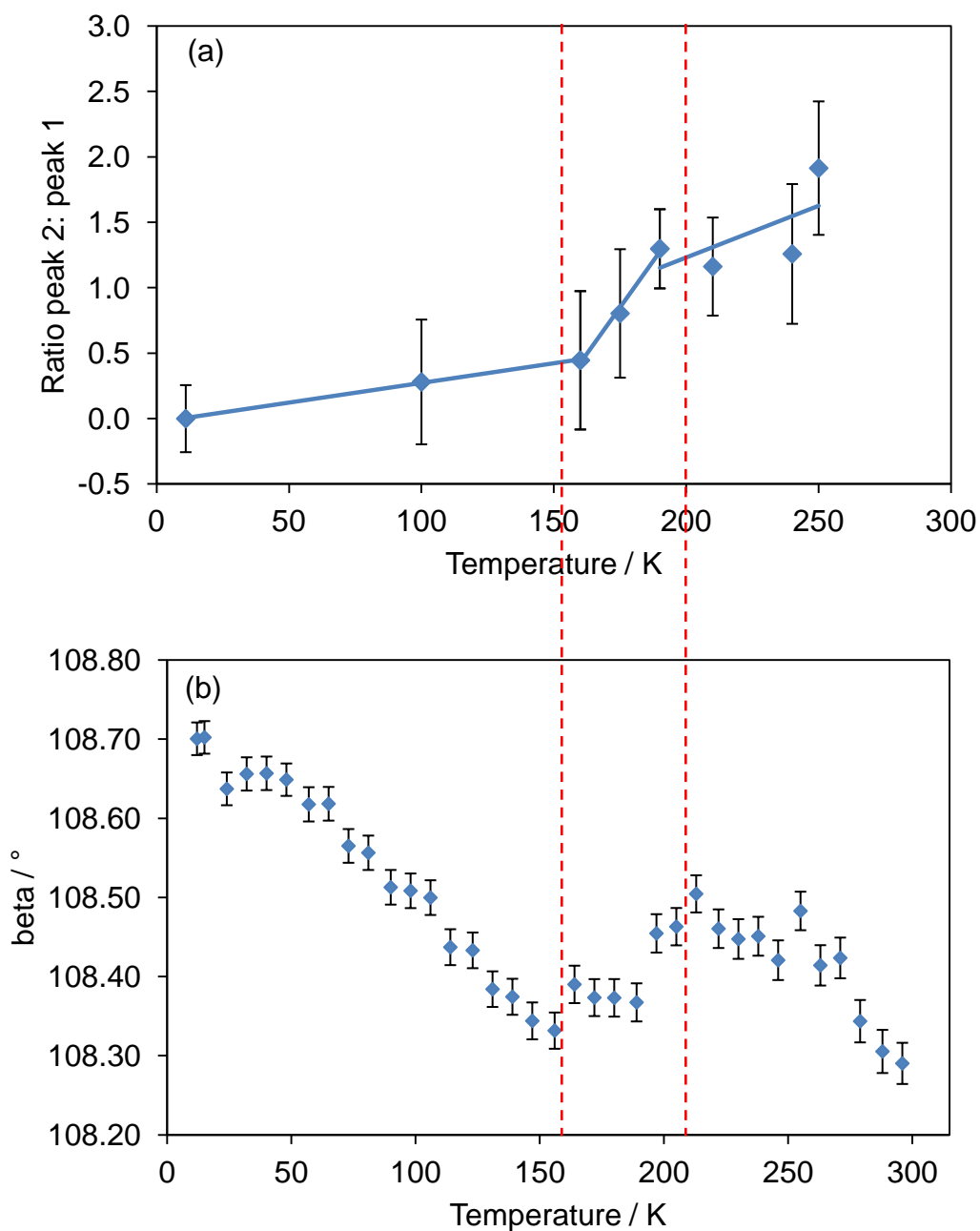


*Figure 4.5: a) The ratio of peak 2: peak 1, fitted with 3 lines of best fit to highlight the evolving trend as a function of temperature. b) A plot of beta angle as a function of temperature obtained from powder XRD on the ring-d-35PDCA sample; the dashed red lines show the points at which gradient changes occur in each plot.*

It can be seen, Figure 4.5a, that at low temperatures peak 1 (the N–H···O species) dominates, but at 190 K the peaks are approximately equal in size, with the ratio between them approximately 1, *i.e.* there is a 50:50 mixture of the two hydrogen bonded species (N–H···O and N···H–O). Beyond 190 K peak 2 (the N···H–O species) begins to dominate, resulting in a peak ratio of approximately 2 at 250 K. The trend in the temperature dependence of these ratios can be compared to that of the $\beta$ angle from powder XRD, Figure 4.5b. In both plots (Figure 4.5a and 4.5b) there are two abrupt gradient changes at similar temperatures (~150 and ~200 K) as the relative ratios of the different hydrogen bonded species change, highlighting the consistency between these sets of data.

Figure 4.6 is an Arrhenius plot ($\ln(k)$ versus inverse temperature), allowing activation energy, $E_a$, to be extracted from Equation 4.2. It should be noted that in order to produce Figure 4.6, the data collected at 100 K were neglected due to the lower reliability of the determined value of $k$ (ratio of peak 2: peak1) at this temperature as a result of the small height of peak 2.
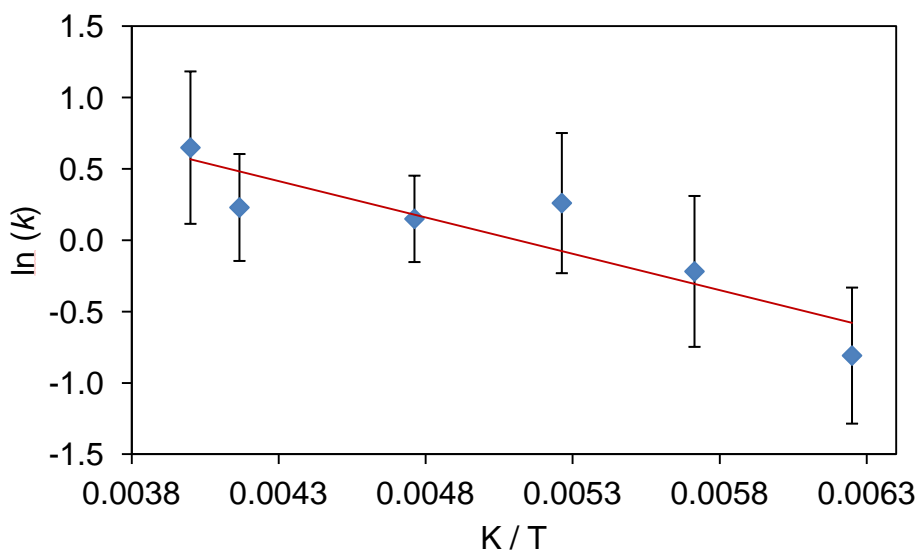


*Figure 4.6: A plot of ln (k) as a function of inverse temperature, omitting the data collected at 100 K for accuracy; a line of best fit (red) has been added to this plot.*

$$k = Ae^{\frac{-Ea}{RT}}$$
(Equation 4.2)

where $k$ is the ratio of peak 2: peak 1.

A line of best fit (seen in red in Figure 4.6) was plotted, and the activation energy, $E_a$, the energy required to produce the HT species from the LT species, of approximately $500 \pm 100$ K ($4.16 \pm 0.83$ kJmol$^{-1}$) was calculated from its gradient; this corresponds well to the activation energy determined by field-cycling NMR (see Chapter 5).

In order to study the effect observed at high temperature, data were collected at 280 K, with a greater number of data points and a longer collection time per data point being employed, over the energy range of interest, Figure 4.7. Despite Debye-Waller effects reducing the scattering intensity at high temperature, these careful measurements show the presence of 4 well-defined peaks in the spectrum, at 64, 71, 75 and 81 meV (516, 573, 605 and 653 cm$^{-1}$).
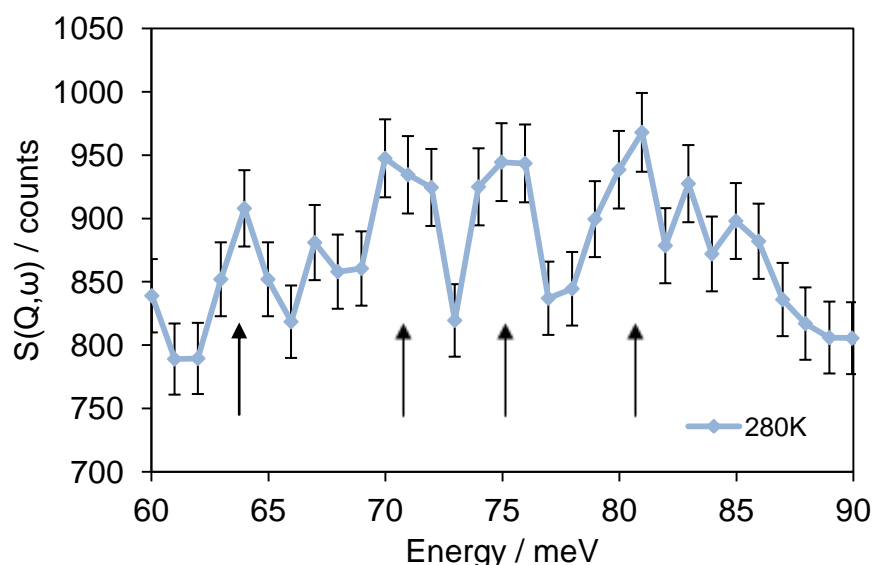


*Figure 4.7: IN1 data obtained for ring-d-35PDCA at 280 K; the arrows mark the positions of the 4 well-defined peaks.*

The peaks seen in Figure 4.7 are likely to correspond to a disordered structure, with the protons in the unit cell no longer being either all at the nitrogen donor or all at the oxygen acceptor but in various combinations instead; each short hydrogen bond can be

in two states, at the nitrogen donor or at the oxygen acceptor. There are two short N···H···O hydrogen bonds per molecule and so, on a molecular scale, there are four possible structures which could be present in the crystal, resulting in four molecular peaks in the spectrum; as suggested by the data at 64, 70, 75 and 80 meV (516, 573, 605 and 653 cm$^{-1}$).

### 4.2.1.2  INS: Supporting Computational Studies

The phase co-existence of the molecular species observed in the INS experiments was modelled using DMol$^3$. The input structures for normal mode calculations were those obtained from single crystal neutron diffraction data collected on the fully deuterated isotopologue, *d*-35PDCA, at 15 K (LT) and 300 K (HT), with the unit cell volumes determined by powder neutron diffraction ($a = 9.7043$ Å, $b = 11.1106$ Å, $c = 6.4402$ Å and $\beta = 108.690°$ for the low temperature structure and $a = 9.7433$ Å, $b = 11.1897$ Å, $c = 6.6307$ Å and $\beta = 108.392°$ for the high temperature structure). These input structures represent the two extremes as studied by diffraction, with the LT structure containing the N–H···O species alone and the HT structure containing the N···H–O species alone.

The eigenvectors resulting from the initial normal mode calculations did not account for deuteration and therefore a routine (described earlier, Section 4.1.3) was written to deuterate the relevant hydrogen atoms, in order to produce the *ring-d*-35PDCA isotopologue, as studied on IN1. A calculation of the partial density of states (for the two hydrogen bond protons) as a function of frequency, for the LT structure alone, gave the pattern depicted in Figure 4.8a. This has been compared with the IN1 spectrum for the LT structure, Figure 4.8b.
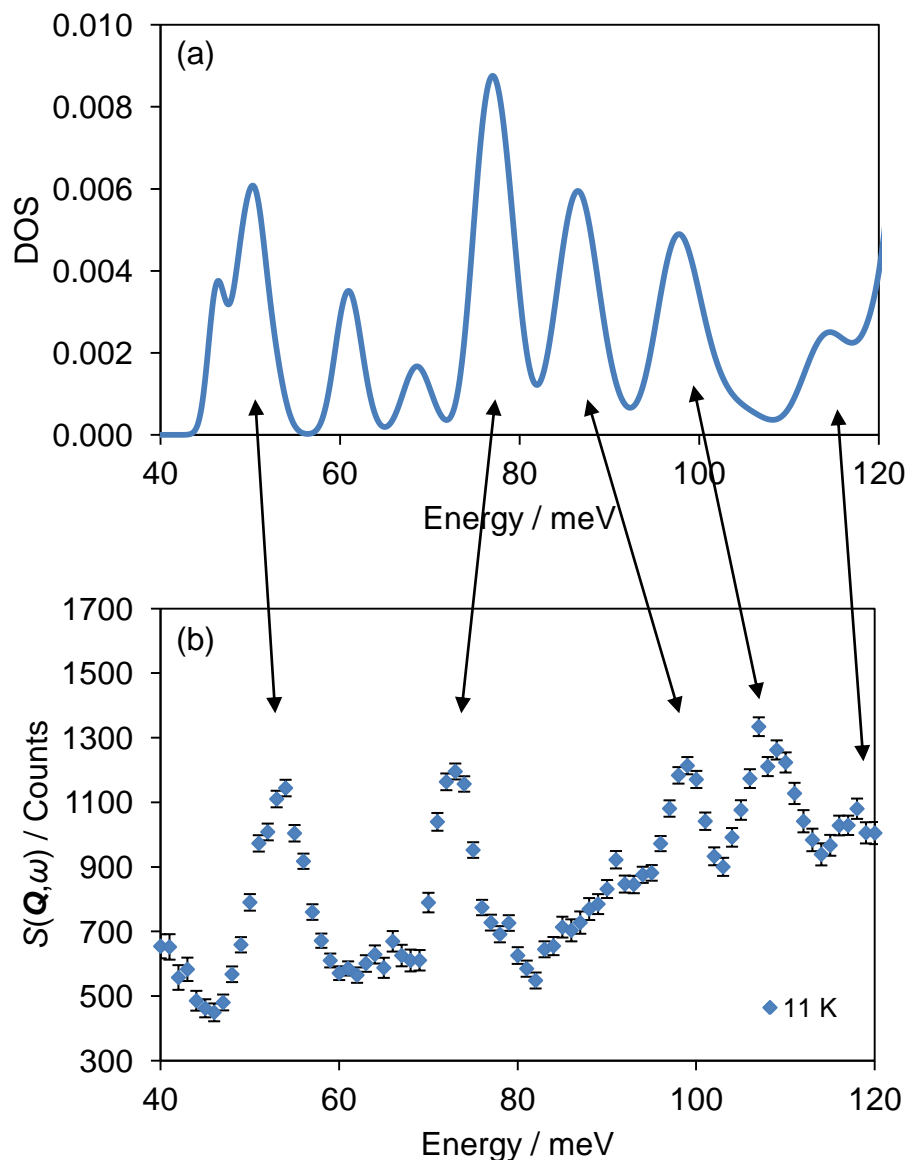
*Figure 4.8: A comparison of a) the calculated partial density of states for the two hydrogen bond protons in the ring-d-35PDCA isotopologue with b) the experimental INS data obtained at 11 K; the arrows have been added to match the equivalent peaks in the two spectra.*

Figure 4.8 shows a reasonable agreement between the experimental and calculated spectra, demonstrating the reliability of the calculation. However, there are a number of discrepancies between the two spectra. For example, the frequencies of the peaks do not match up completely showing that the calculation is not quite right. In addition, the peaks between 60 and 70 meV (484 and 565 cm$^{-1}$) have a very low intensity compared

to those calculated. It is possible that these peaks in the calculated spectrum are actually hidden by the intense peak at 75 meV (605 cm$^{-1}$) in the actual spectrum.

The partial DOS for the two hydrogen bond protons was also calculated for the pure HT species, Figure 4.9, and then those for both the LT and HT species were combined using Equation 4.3. Implementing this equation resulted in a series of calculated DOS for structures containing systematically varying amounts of the two hydrogen bond species, Figure 4.10, equivalent to the effect of changing the temperature experimentally.
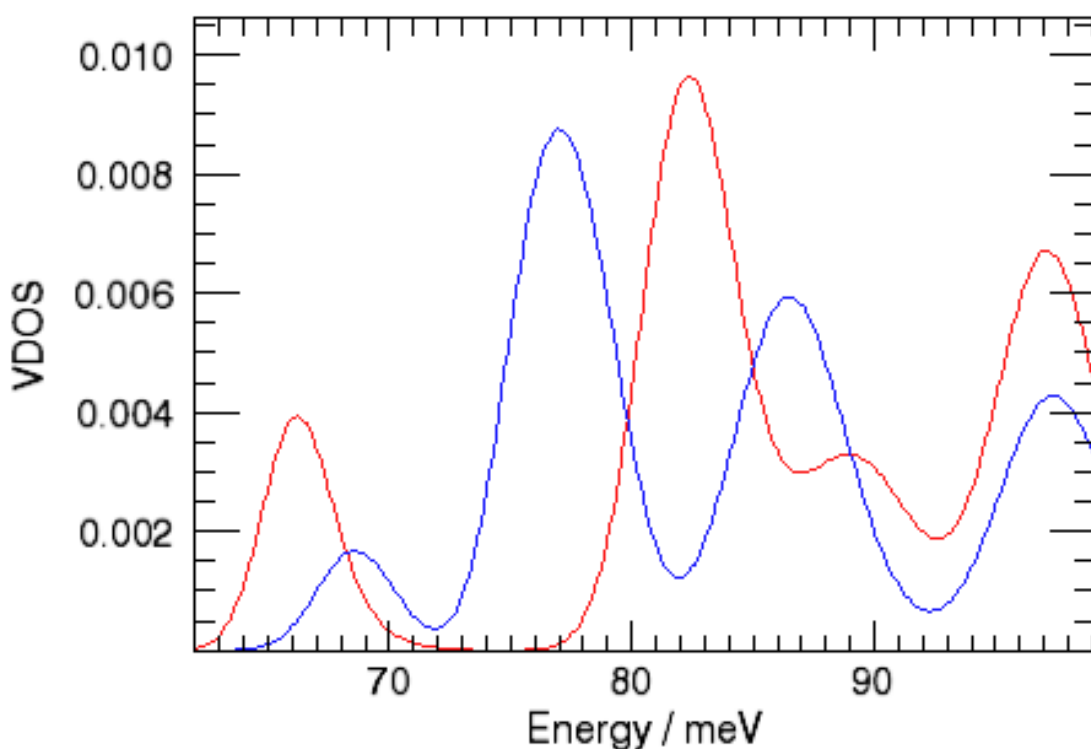


*Figure 4.9: A comparison of the partial DOS for the two hydrogen bond protons for the pure LT species (blue) and pure HT species (red).*

$$DOS = (LT)_{1-x} + (HT)_x : 0 < x < 0.6 \qquad \text{(Equation 4.3)}$$
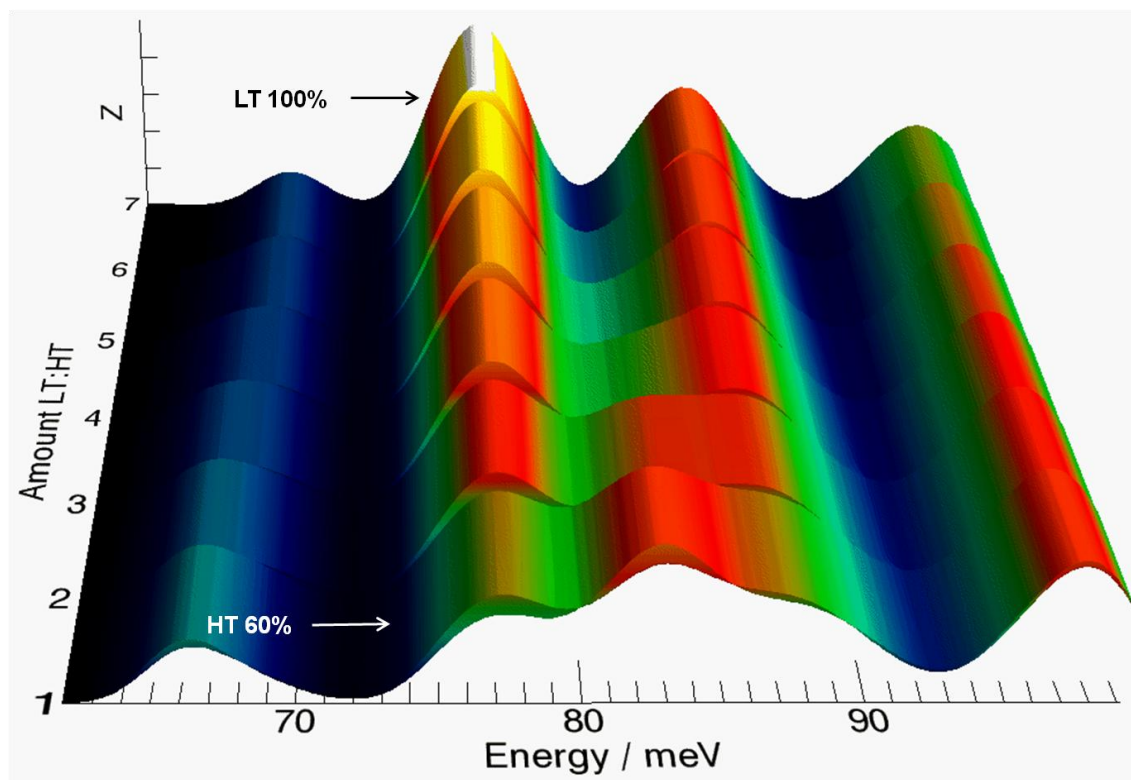
*Figure 4.10: A 3D representation of the density of states (Z) as a function of frequency, for varying quantities of LT and HT structures (calculated using Equation 4.3, where the input structures were those from single crystal neutron diffraction data collected at 15 and 300 K).*

Figure 4.10 shows that when the LT, N–H···O, species is dominant a single peak is present in the frequency range of 74 to 84 meV (approximately 600 to 675 cm$^{-1}$), as observed experimentally. As the amount of the N···H–O species is increased, corresponding to an increase in the temperature of the IN1 experiment, a second peak emerges in the frequency range of interest. Additionally, as in the IN1 experiment, there is no change in the position of the two peaks.

These results confirm that the co-existence observed in the IN1 data is due to the presence of varying amounts of the two different species (N–H···O and N···H–O), where the ratio of the amounts of the two species is dependent on the temperature of the system. It suggests that no continuous migration takes place, but instead the effect seen in the diffraction is simply an average over various quantities of the two species.

Figure 4.11 shows the mode that is being probed in this work. In this illustration, the green arrows represent the displacement vector of each atom and their respective sizes correspond to the size of the atomic displacement. It can be clearly seen that the mode represented in Figure 4.11 modulates the hydrogen bond geometry; whilst there are small displacements of all of the hydrogen/deuterium atoms, it is clear that in this vibrational mode, the main displacement is that of the hydrogen atom in the short N–H···O bond, in the *ab* plane.
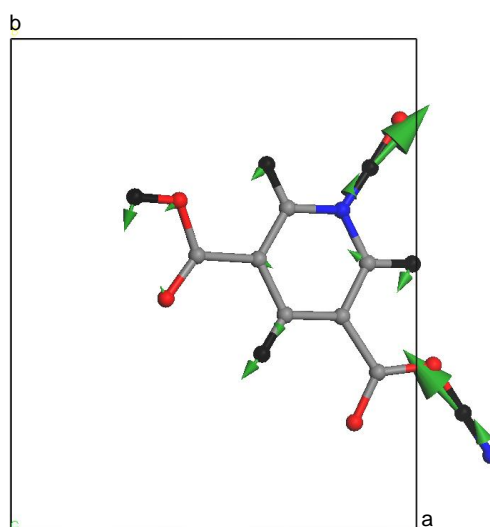


*Figure 4.11: The mode at 77 meV (approximately 620 cm$^{-1}$), used as a probe in this work.*

### 4.2.1.3   Raman Spectroscopy: Experimental Results and Discussion

Other forms of spectroscopy, namely IR and Raman, were also used to study these local effects in the other isotopologue samples. IR and Raman allowed the study of those samples with homogenous protonation/deuteration, namely *h*-35PDCA and *d*-35PDCA, which are less suitable for study by INS as the ring hydrogen/deuterium atoms and those of the hydrogen bonds are not differentiated. Additionally, these forms of spectroscopy afford greater resolution than that in INS. It was found that, while Raman spectroscopy gave the most useful data for *h*-35PDCA, IR gave the most useful data for *d*-35PDCA.

All of the Raman data collected on the *h*-35PDCA isotopologue were normalised by multiplying each of the spectra by a constant. This constant was calculated, for each dataset, by determining the area under the largest full peak (that at $1000 \, cm^{-1}$ (124 meV)), for each individual spectrum, and comparing it with the most intense peak overall at this frequency (that in the spectrum measured at 294 K); the normalised spectra for *h*-35PDCA are given in Figure 4.12a. The spectra collected on the *d*-35PDCA isotopologue have been normalised in the same way and included as Figure 4.12b for comparison.

These spectra are relatively complex, with a number of changes occurring both with temperature and with changing isotope. In general, the peaks themselves appear in similar positions for the two isotopologues, despite the varying isotope composition, demonstrating the small effect that a change in isotope mass has on the resulting spectra (unlike the large differences in the INS spectra caused by a change in the neutron scattering cross-sections). The largest differences occur when a spectral peak corresponds directly to H/D motion, for example the peak corresponding to the ring C–H/C–D stretches, which occurs at approximately $3100 \, cm^{-1}$ (384 meV) for *h*-35PDCA and at approximately $2400 \, cm^{-1}$ (298 meV) for *d*-35PDCA (a frequency reduction of a factor of approximately 1.4 as a result of the higher mass of deuterium compared to hydrogen, Equation 4.4).

$$\omega = \sqrt{\frac{k}{\mu}}$$ 
(Equation 4.4)

where $\omega$ is frequency, $k$ is a force constant and the reduced mass, $\mu$, is isotope dependent.

A striking similarity between the two isotopologues is the presence of a broad feature, emerging in both sets of spectra between 1000 and $2000 \, cm^{-1}$ (124 and 248 meV) at intermediate temperatures (133 and 163 K for *h*-35PDCA, and 133, 163 and 183 K for *d*-35PDCA). This is possibly a result of disorder in the structure in this temperature range.
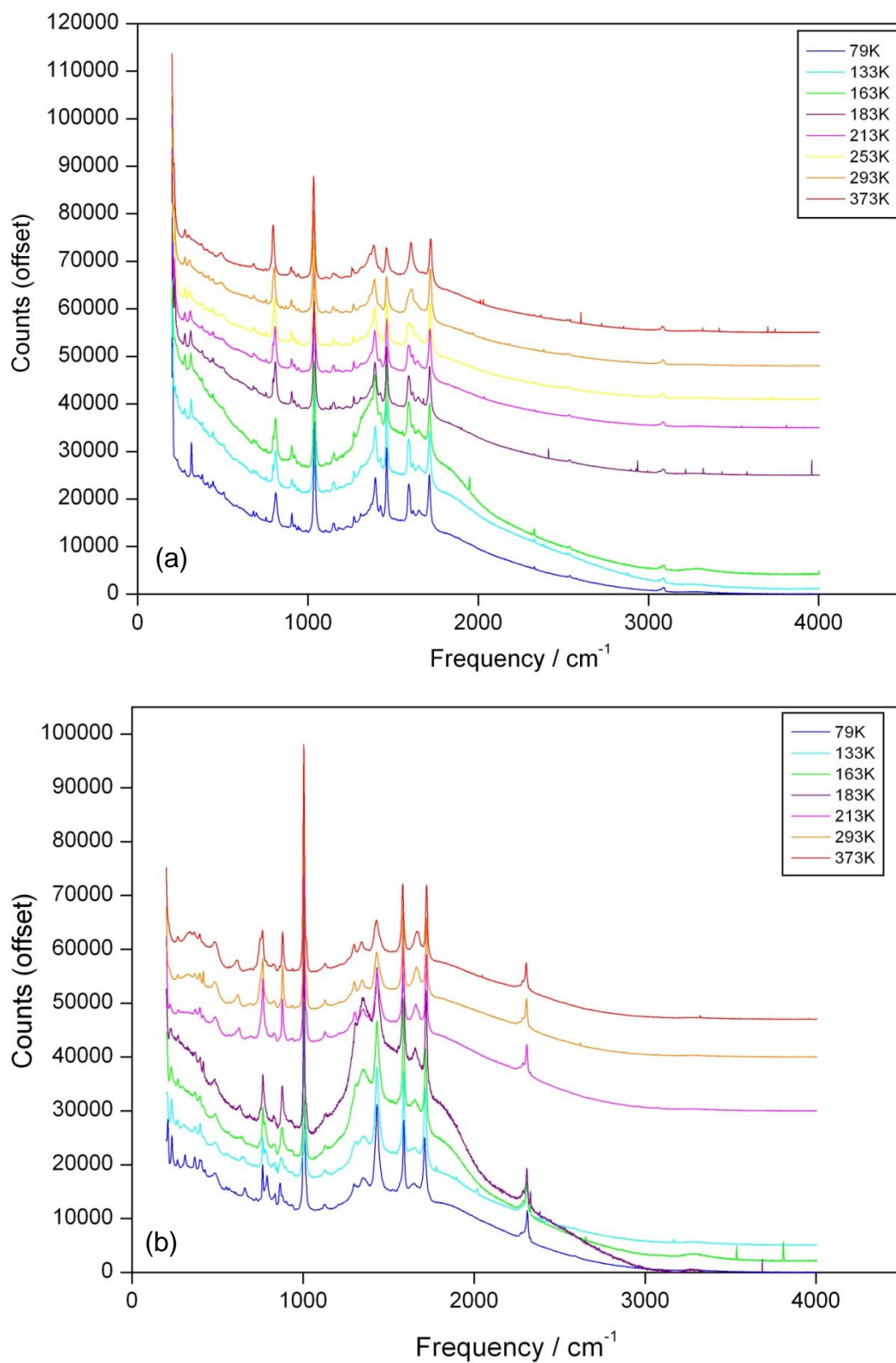
*Figure 4.12: a) All of the Raman spectra measured for h-35PDCA at various temperatures. b) All of the Raman spectra measured for d-35PDCA at various temperatures, included for comparison.*

A detailed study of the changes as a function of temperature highlighted a number of areas of specific interest for the *h*-35PDCA isotopologue, Figure 4.13.
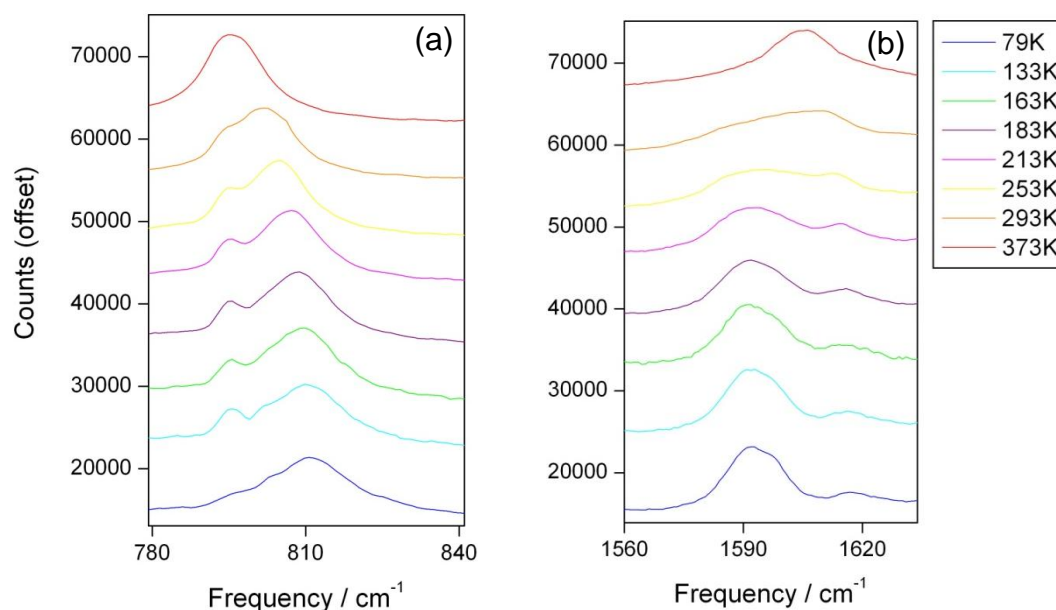


*Figure 4.13 a) and b): Sections of the Raman spectra, showing possible phase co-existence.*

Figure 4.13b shows that, as with the *ring-d*-35PDCA isotopologue (measured on IN1), the two species, N–H···O and N···H–O, co-exist from 79 K (the lowest temperature studied by Raman spectroscopy), up to 300 K (*i.e.* the temperature limit studied by diffraction); indicated by the peaks at 1590 and 1610 cm$^{-1}$ (197 and 200 meV). These peaks persist until 293 K, with the HT peak (right) gaining intensity as temperature is increased. At 293 K the two peaks still seem to be present though they are not resolved very well. However, at 373 K the LT peak (1590 cm$^{-1}$, 197 meV) has entirely disappeared, being replaced by the single peak of the HT species (1610 cm$^{-1}$, 200 meV).

Figure 4.13a shows a similar trend, albeit less well-defined. It seems that at 79 K a single species (LT) is present (810 cm$^{-1}$, 100 meV), with a second species (HT) emerging at a lower frequency (795 cm$^{-1}$, 99 meV) at around 133 K. The peak corresponding to the HT species does not change its position as the temperature is increased. However, unlike previous data, in this case, the peak corresponding to the LT species shifts to a lower frequency on increasing the temperature. Therefore, although it seems that the LT species eventually disappears at very high temperature (373 K), it is

possible that it may be simply overlapping with the peak of the HT species at this temperature.

The 1st moment, Equation 4.5, for the section of spectra displayed in Figure 4.13, was calculated over the frequency range 780 to 840 cm$^{-1}$ (92 to 104 meV), for Figure 4.13a, and over the range 1570 to 1630 cm$^{-1}$ (195 to 202 meV), for Figure 4.13b.

$$1stMoment = \frac{\sum\limits_{F\,min}^{F\,max} IF}{\sum\limits_{F\,min}^{F\,max} I}$$

(Equation 4.5)

where $I$ is the peak intensity and $F$ is the peak position (frequency). The 1st moment calculates an average peak position (frequency) over the frequency range selected, allowing a quantitative analysis at each temperature.

This results in plots (Figures 4.14b and 4.15b) which are directly comparable to diffraction (NH/OH distance versus temperature, Figures 4.14a and 4.15a).
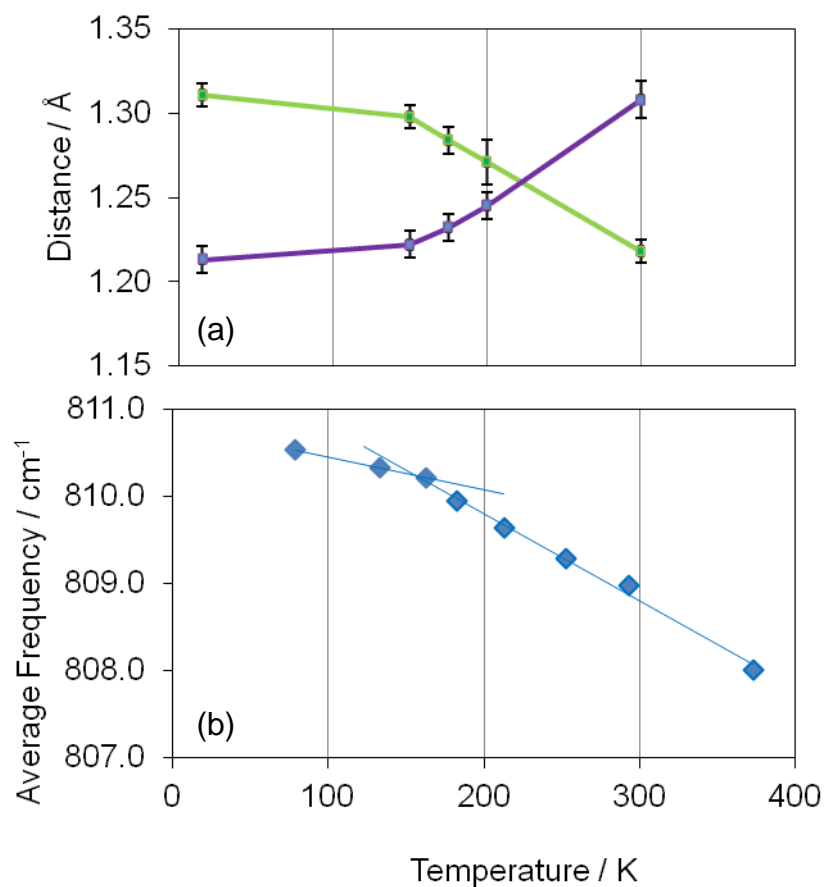
*Figure 4.14: A comparison of results from diffraction with those from spectroscopy for h-35PDCA: a) The temperature dependence of the N···H (purple) and O···H (green) bond lengths of h-35PDCA, obtained by single crystal neutron diffraction and b) The change in the 1$^{st}$ moment as a function of temperature for h-35PDCA in the range 780 to 840 cm$^{-1}$ (97 to 104 meV). In this plot the straight lines have been added as guides to the eye.*
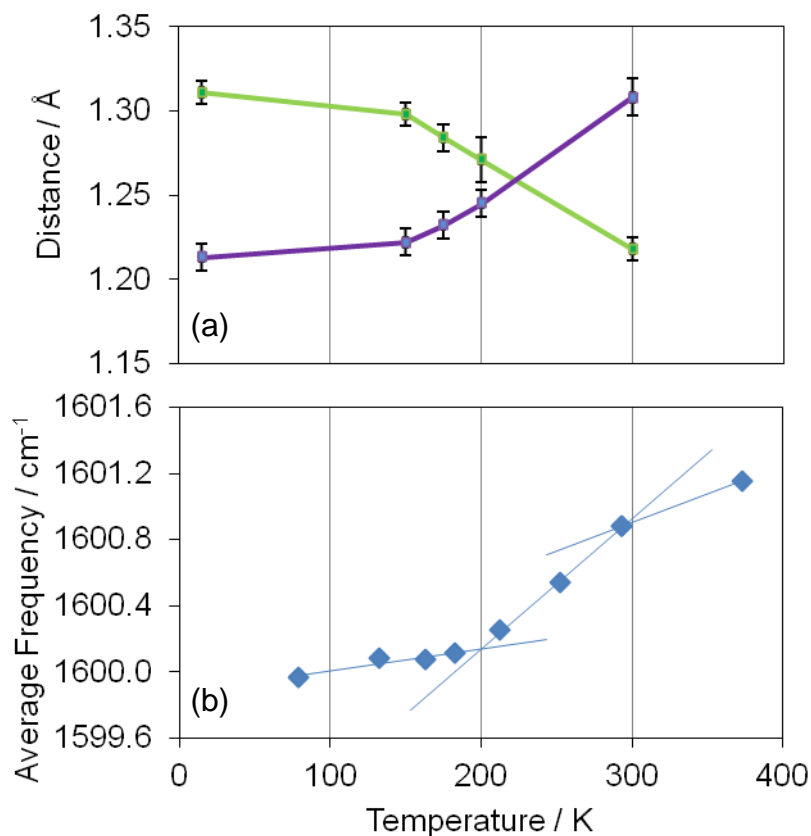
*Figure 4.15: A further comparison of results from diffraction with those from spectroscopy for h-35PDCA: a) as in Figure 4.13 and b) The change in the 1$^{st}$ moment as a function of temperature for h-35PDCA in the range 1570 to 1630 cm$^{-1}$ (195 to 202 meV). In this plot guides to the eye have been included (blue lines).*

It can be seen that, for both frequency ranges shown here, the change in average peak position as a function of temperature from Raman, Figures 4.14b and 4.15b, follows the pattern observed for the change in O···H (green) and N···H (purple) bond lengths, respectively; as seen in the diffraction results up to 300 K, Figures 4.14a and 4.15a. With Raman spectroscopy, however, a higher temperature of 373 K was also accessible. At this point the curve in Figure 4.15b seems to be beginning to tail off, tending towards a pure HT species. Whilst diffraction data for the *h*-35PDCA isotopologue suggest a gradual, continuous migration of the hydrogen atom from one side of the bond to the other, spectroscopy data suggest a bistable arrangement, with the proton situated either at one side of the hydrogen bond or the other, the amounts of these two states varying with temperature.

Contrary to the results plotted in Figure 4.15b, the average peak position shown in Figure 4.14b does not seem to tail off at this higher temperature, even though, visually, it seems that a pure HT species is obtained (Figure 4.13a). This is further evidence that these two peaks (that seen at low temperature and that seen at high temperature) overlap at high temperature, rather than intensity simply switching from one peak to the other. It is possible that the modes driving proton transfer are being hidden due to the behaviour of further contributions to the vibrational modes close to this frequency.

### 4.2.1.4  IR Spectroscopy: Experimental Results and Discussion

For the fully deuterated isotopologue, *d*-35PDCA, co-existence of the N–D···O and N···D–O species is over a much smaller temperature range, shown from diffraction experiments to be 150 to 200 K, and shown from spectroscopy to be somewhere between 90 and 180 K, see below.

All of the IR data collected on the *d*-35PDCA isotopologue are represented in Figure 4.16a, with the data collected on the *h*-35PDCA sample included alongside for comparison, Figure 4.16b. It can be seen that large differences exist between the IR spectra for the two forms, with various changes also occurring for a particular isotopologue on changing temperature. The clearest difference between the two isotopologues is that the peak observed at approximately 3100 cm$^{-1}$ (384 meV) for the protonated form occurs at the lower frequency of approximately 2400 cm$^{-1}$ (298 meV) for the deuterated form; as discussed earlier, Equation 4.4, this is a result of the higher mass of deuterium. In general, the peaks of the *d*-35PDCA isotopologue are more intense and more well-defined than those of *h*-35PDCA, possibly due to the clear phase transition occurring in *d*-35PDCA.
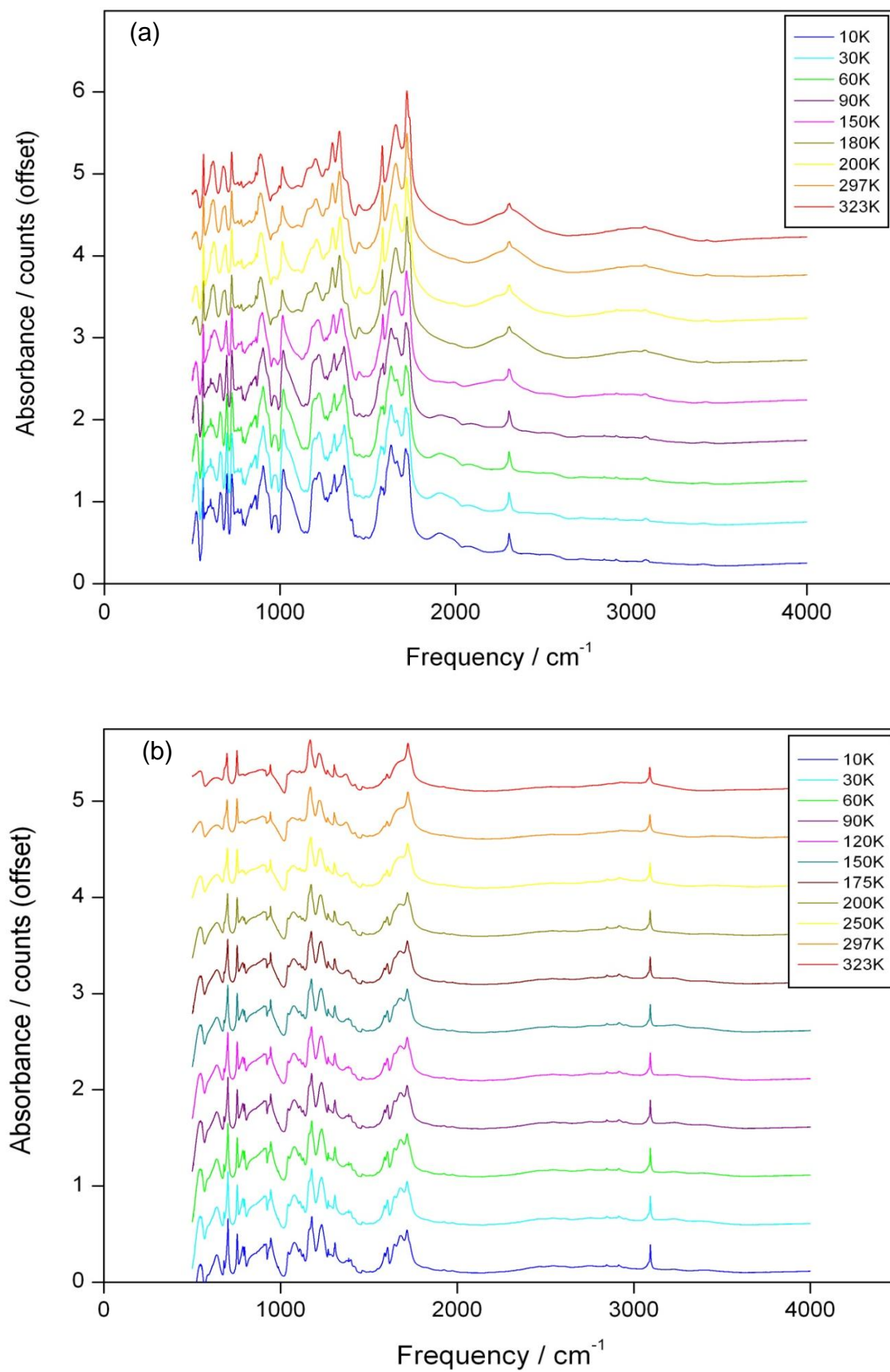
*Figure 4.16: a) All of the IR spectra collected on d-35PDCA at various temperatures. b) All of the IR spectra collected on h-35PDCA at various temperatures, for comparison.*

A detailed study of these spectra highlighted a number of areas of significant interest for the *d*-35PDCA isotopologue, Figures 4.17a and 4.17b.
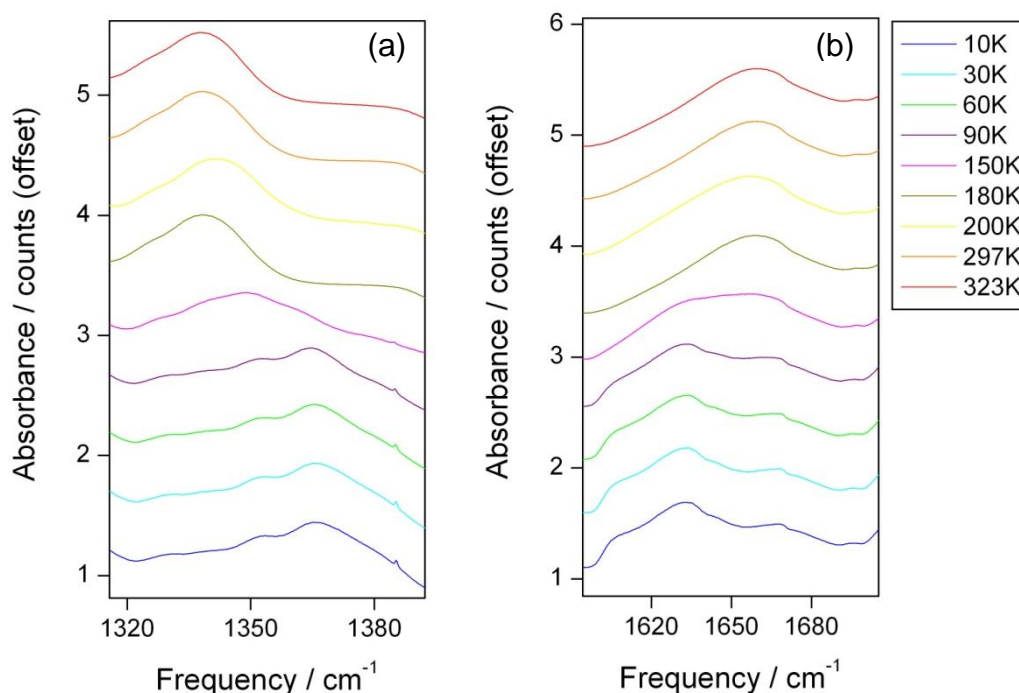


*Figure 4.17: a) and b) Sections of interest of the IR spectra of d-35PDCA.*

Figure 4.17a shows that at low temperature a single peak is observed at approximately 1360 cm$^{-1}$ (169 meV) the position of which varies very little with temperature. However, at a critical temperature between 90 and 180 K, there appears to be a sudden change in the molecule, leading to a switch from this peak to a single peak at approximately 1340 cm$^{-1}$ (166 meV). These peaks are representative of the LT and HT forms of the material, respectively. In addition, the broad peak at 150 K seems to be indicative of a co-existence of these two forms; a lack of data points at intermediate temperatures in this range of interest prevents a more accurate temperature range of phase co-existence being determined.

Figure 4.17b shows a similar, though less well-defined trend. Again, it seems that the LT species (at approximately 1630 cm$^{-1}$, 202 meV) exists up to 150 K and the HT species (at approximately 1655 cm$^{-1}$, 205 meV) exists above 150 K with a short-lived co-existence of the two species around 150 K. However, it seems that at low temperatures a further peak (at approximately 1665 cm$^{-1}$, 205 meV), close to that of the

HT species, is present also. This is likely to be a result of the presence of a further vibrational mode which is not directly related to proton migration.

Calculation of the $1^{st}$ moments for these sections of spectra, over the range 1320 to 1390 cm$^{-1}$ (164 to 172 meV) for Figure 4.17a and over the range 1610 to 1700 cm$^{-1}$ (200 to 211 meV) for Figure 4.17b, gives results which are directly comparable to diffraction (temperature dependence of beta angle, Figures 4.18a and 4.19a, and temperature dependence of NH/OH distances, Figures 4.18b and 4.19b).
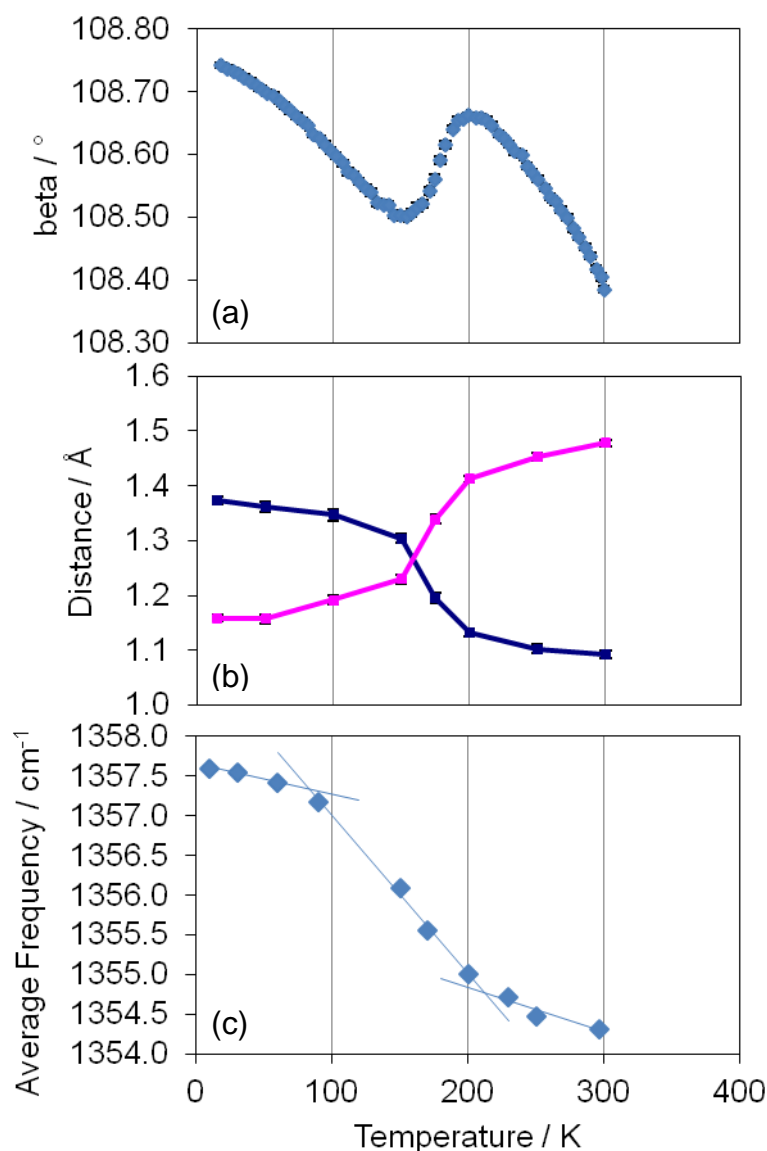


*Figure 4.18: A comparison of results from diffraction with those from spectroscopy for d-35PDCA: a) The temperature dependence of the beta angle of d-35PDCA, obtained by powder XRD, b) The temperature dependence of the N···D (pink) and O···D (blue)*

*bond lengths of d-35PDCA, obtained by single crystal neutron diffraction and c) The change in the 1ˢᵗ moment as a function of temperature for d-35PDCA in the range 1320 to 1390 cm⁻¹(164 to 172 meV), with guides to the eye added (blue lines).*
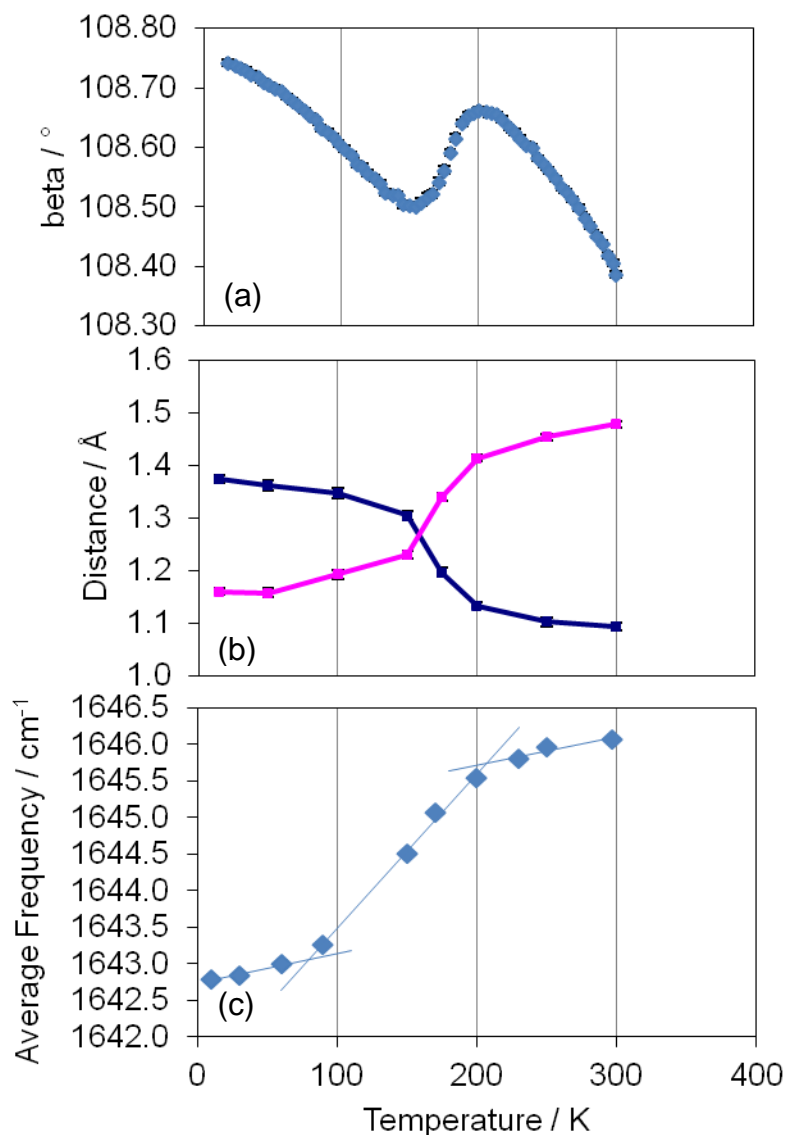


*Figure 4.19: A comparison of results from diffraction and spectroscopy for d-35PDCA: a) and b) as in Figure 4.17 and c) The change in the 1ˢᵗ moment as a function of temperature for d-35PDCA in the range 1610 to 1700 cm⁻¹(200 to 211 meV). The blue lines have been added as guides to the eye.*

The temperature dependence of the average peak positions, Figures 4.18c and 4.19c, obtained by IR spectroscopy, follow the same trends as the O···D (dark blue) and N···D

(pink) bond distances, Figures 4.18b and 4.19b, respectively, as determined by single crystal neutron diffraction studies. Results from IR spectroscopy suggest a bistable arrangement of the deuterium atom, being located on the nitrogen atom at low temperatures, and the oxygen atom at high temperatures. Between these two extremes there is evidence for a short-lived range of phase co-existence, observed close to temperatures in which the transition from one form to the other takes place (approximately 150 K). This vibrational view is consistent with the diffraction results and phase transition previously described for this fully deuterated isotopologue (Chapter 3).

It seems that the major difference between the isotopologues is the extent of conversion between the two forms exhibited over the temperature ranges studied. It is clear that *d*-35PDCA exhibits complete conversion, from a fully N–D species, to a fully O–D species, as shown by the exchange of intensity from one peak to another in the IR spectra. Furthermore, this conversion is completed by 200 K. In those samples with some level of protonation, however, a pure O–H species does not seem to be present until much higher temperatures. The Raman data collected for the *h*-35PDCA sample go some way towards determining this 'finishing' temperature, with the average peak position (1$^{st}$ moment) seemingly beginning to tail off at around 373 K. Additional higher temperature diffraction data, up to 400 K, should be collected in order to complement this work (the melting point of the sample being approximately 450 K).

### 4.2.1.5  IR and Raman Spectroscopy: Supporting Computational Studies

In INS, the change in spectral intensity is directly related to the changes in the hydrogen bonding modes, such as that shown in Figure 4.11. However in IR and Raman spectroscopy, it is not likely that hydrogen bonding modes are observed directly due to their inherent low intensity and very broad nature.[8] The regions of the spectra that have been highlighted in both the IR (at 1350 and 1650 cm$^{-1}$, 167 and 205 meV) and Raman data (at 1600 cm$^{-1}$, 198 meV) likely correspond to various C–O/C=O signals, from the carboxylic acid group associated with the SSHB oxygen acceptor instead. Those from IR and Raman, at approximately 1650 and 1600 cm$^{-1}$ (205 and 198 meV), respectively, correspond to a C=O stretch, and that from IR, at approximately 1350 cm$^{-1}$ (167 meV), to a C–O stretch. These C–O/C=O vibrations can be used to probe changes in the

hydrogen bond structure, as has been done in diffraction (Chapter 3); this is possible due to the proximity of these C–O and C=O bonds to the hydrogen bond, which means that they are affected by the migration of the proton from the nitrogen donor to the oxygen acceptor.

Although various N–H stretching and wagging modes also seem to be present at these frequencies, these would not be observed clearly in the experimental spectra, as discussed above, especially compared to the more defined nature of the peaks corresponding to C–O/C=O stretching modes. Therefore it is thought likely that it is in fact the C–O/C=O vibrations being observed in this case.

In order to provide further evidence for the C–O/C=O vibrations, the results of normal mode calculations, performed in DMol[3], were analysed in detail. A comparison of various partial densities of states with those previously determined by Fontaine-Vive *et al.*[1] using the VASP code,[9, 10] for the *h*-35PDCA isotopologue at 15 K, showed good agreement between the two computational codes.
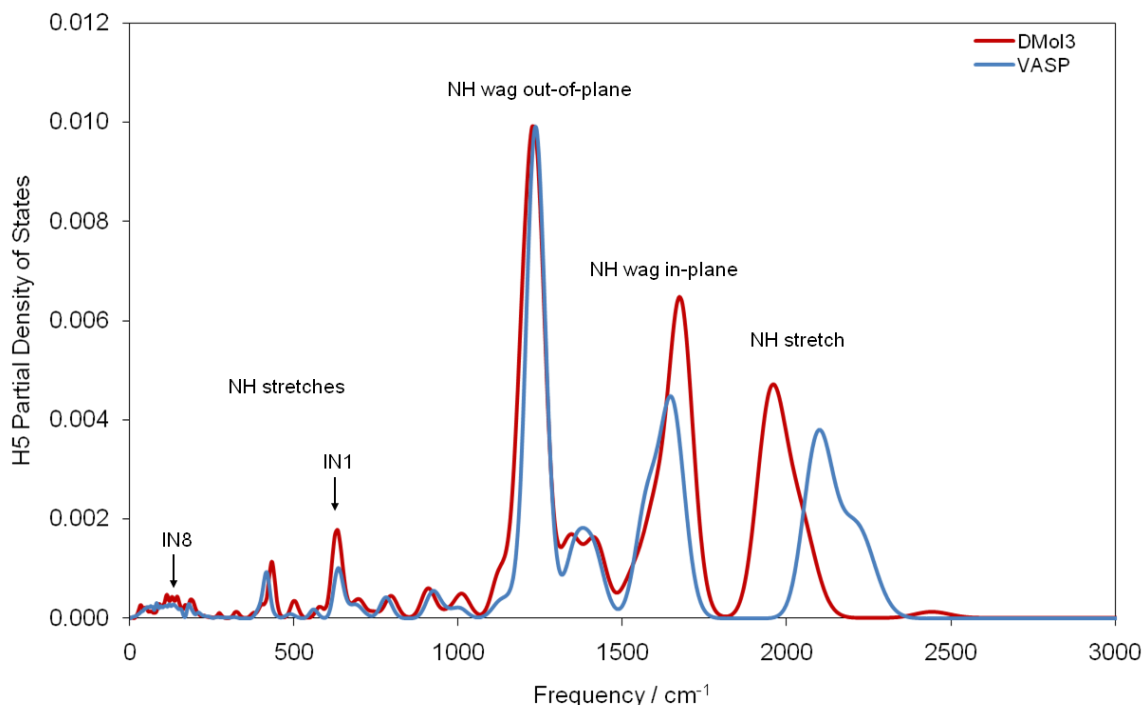


*Figure 4.20: A comparison of the H5 partial densities of states obtained by VASP and DMol[3] for the h-35PDCA isotopologue at 15 K. The modes of interest measured by IN1 (seen earlier) and IN8 (later) have been indicated for comparison.*

An example comparison (of the H5 partial density of states) is given in Figure 4.20, alongside an assignment of the vibrational modes present. The only notable difference between these calculated spectra is in the position of the highest frequency mode (an N–H stretch mode). For this peak, VASP gives a higher estimate of vibrational frequency, approximately 2100 cm$^{-1}$ (260 meV), compared to approximately 1950 cm$^{-1}$ (242 meV) for DMol$^3$. Previous work[1] employed VASP solely; however, due to the comparable results obtained despite the differing codes, DMol$^3$ was used predominantly in this work. This was largely a result of its ability to stabilise the H5 atom at a position closer to the oxygen atom in the larger, high temperature, unit cell, thereby allowing calculations to be effectively performed at 300 K. Such a stabilisation was not possible in VASP and therefore calculations using this program were only performed for the smaller, low temperature, structure.

A routine was written in order to manipulate the files resulting from these normal mode calculations in DMol$^3$, firstly to account for the various deuteration levels studied, and also in order to output various partial densities of states for comparisons at the two different temperatures (methods as described in Section 4.1.3). A comparison of the C–O/C=O partial densities of states at 15 and 300 K is given in Figure 4.21, in order to show the contribution of these species to the vibrational modes.
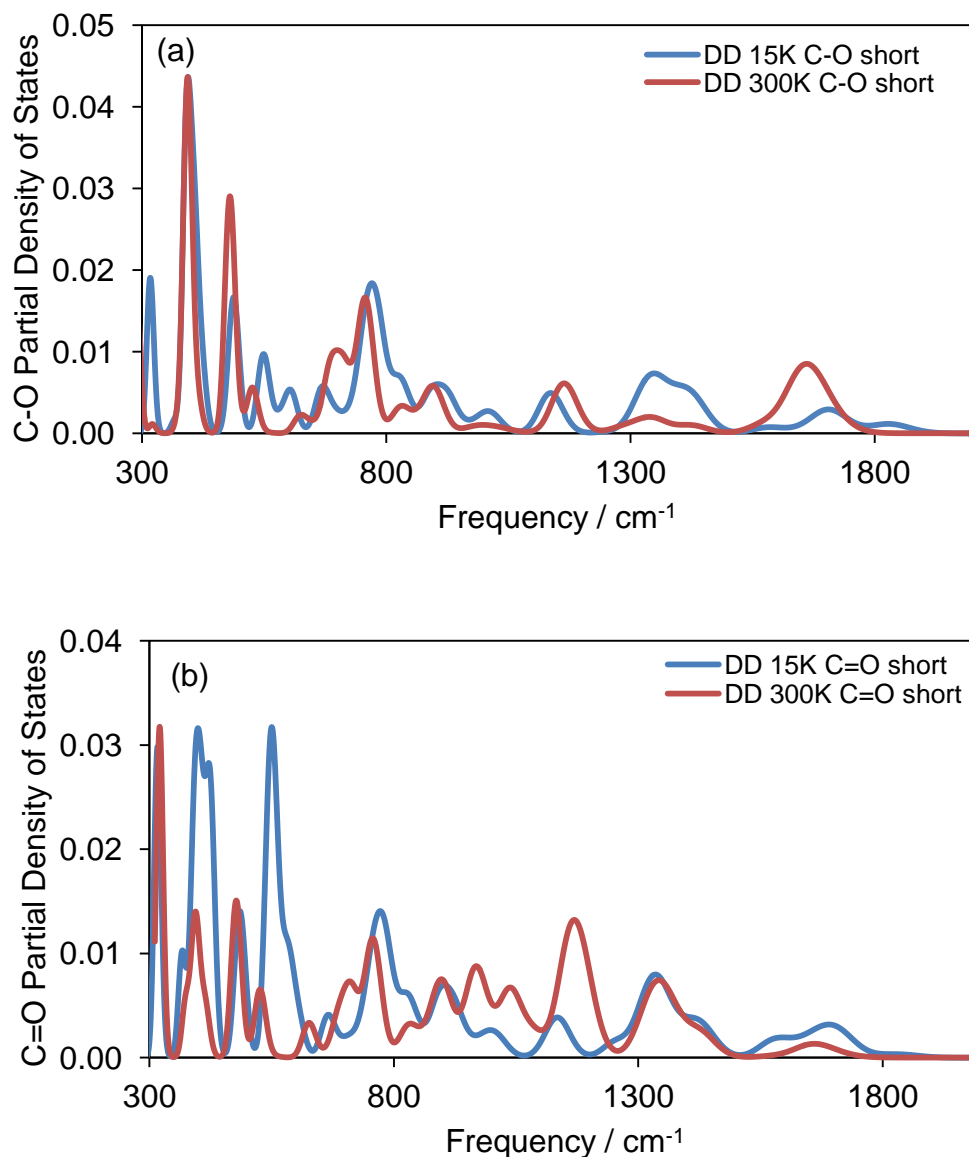
*Figure 4.21: A comparison of the a) C–O and b) C=O partial densities of states in the short strong hydrogen bond (short) of the d-35PDCA isotopologue (DD) at 15 and 300 K.*

The partial densities of states, shown in Figures 4.21a and 4.21b can be compared with the experimental results in Figure 4.16a and 4.17. The contribution of each of the C–O and C=O stretching modes to the experimental data can be clearly seen, in particular to the peaks present at 1300 and 1600 cm$^{-1}$ (161 and 198 meV). While the calculations are not accurate enough to show the subtle increase or decrease of a peak position with temperature, and, in fact, show little change in the peak positions at all, they do allow the identification of particular modes, as shown in Figures 4.21a and 4.21b. The major

discrepancy between the calculated and experimental results seems to be in the low frequency section of the spectra. The calculated C=O partial densities of states (Figure 4.21b) show a large difference between the LT and HT forms between 300 and 650 cm$^{-1}$ (37 and 81 meV); such a change is not seen experimentally, most likely as it masked by other contributions in this frequency range. A depiction of some of the vibrational modes in the spectral regions of interest is given in Figure 4.22.
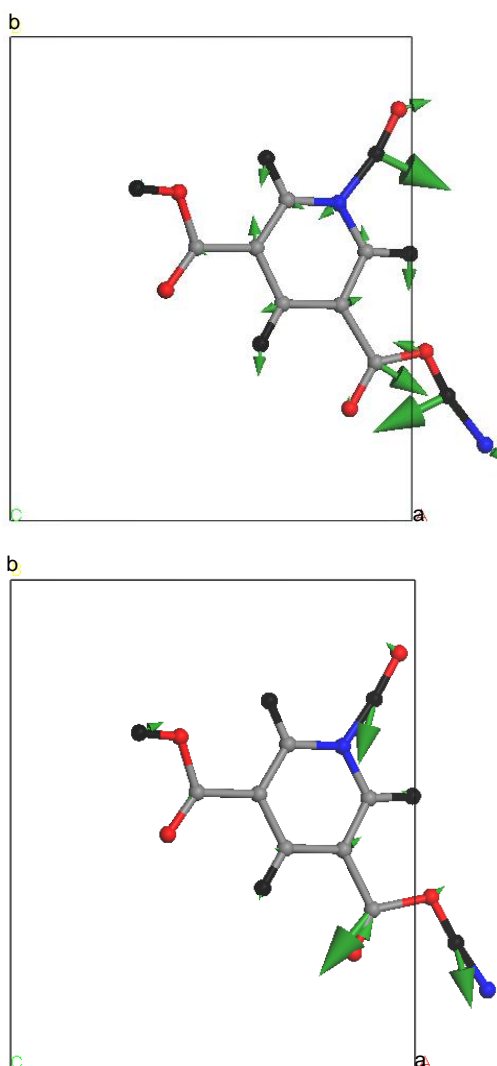


*Figure 4.22: Example vibrational modes in a single molecule of 35PDCA at 300 K: (top) 1363 cm$^{-1}$ (169 meV) and (bottom) 1653 cm$^{-1}$ (205 meV).*

The mode in Figure 4.22 (top) shows a number of displacements; small displacements of the carbon and deuterium atoms of the ring are present as well as much larger stretching displacements from the carbon of the C–O bond of the SSHB and the

deuterium in the O–D bond of the SSHB. Figure 4.22 (bottom) shows that the large stretching displacements of the carbon atom of the C=O bond of the SSHB and the wagging of the deuterium atom of the O–D bond of the SSHB dominate in this vibrational mode. As mentioned previously, although these O–D wagging and stretching contributions to the various modes exist, these would not be observed clearly in the experimental spectra.

The Raman data also highlighted an area of interest at around 800 cm$^{-1}$ (99 meV) for *h*-35PDCA. Figures 4.21a and 4.21b show that both C–O and C=O stretching modes contribute to the vibrations at this frequency, although so do many others, all with similar amplitudes of motion, as shown in Figure 4.23. It is likely, therefore, that these extra modes are preventing the spectroscopic observation of clear proton transfer behaviour at this frequency.
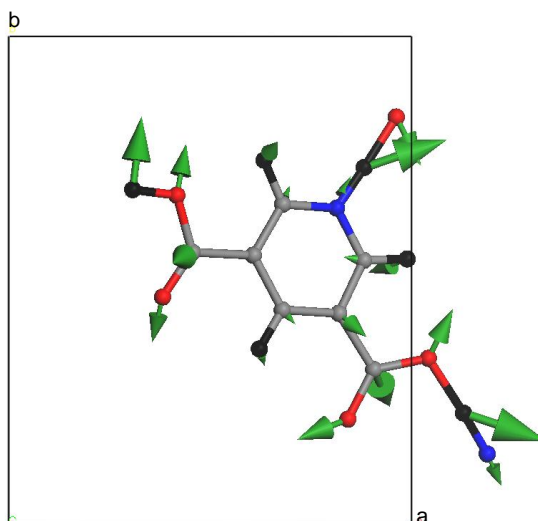


*Figure 4.23: Representation of the mode at 795 cm$^{-1}$ (99 meV).*

## 4.2.2 The Driving Force for Proton Migration

### 4.2.2.1 INS: Experimental Results and Discussion

IN8 was used in order to investigate the temperature dependence of the low frequency phonons that have previously been identified as driving the proton migration in 35PDCA. Figure 4.24 shows a selection of spectra collected in the 070 orientation at various temperatures and Figure 4.26 shows the spectra collected in the 600 orientation. Figures 4.25 and 4.27 show the 1$^{st}$ moments calculated for the 070 orientation, over the

energy range of 17 to 22 meV (137 to 177 cm$^{-1}$), and the 600 orientation, between 17.5 and 20 meV (141 and 161 cm$^{-1}$), respectively. It can be clearly seen that whilst there is no shift of the peaks collected in the 600 orientation on increasing temperature, in the 070 orientation there is some evidence for softening of the peak at 19.5 meV (157 cm$^{-1}$).

This observation is interesting as the 600 orientation is parallel to the normal O–H···O hydrogen bond, which is not expected to change on increasing temperature. The 070 orientation, however, is parallel to the short O4–H5···N1 hydrogen bond of interest, which is known to change on increasing temperature. The peak softening, at approximately 19.5 meV (157 cm$^{-1}$), occurs near to a mode that has previously been identified as driving the proton migration in this short hydrogen bond.[1]

In addition, it can be seen from Figure 4.25 that the temperature dependence of the average energy in the 070 direction changes gradient above 150 K; above this temperature the average peak position shifts more rapidly to lower energy, consistent with the onset of proton transfer in this temperature region.
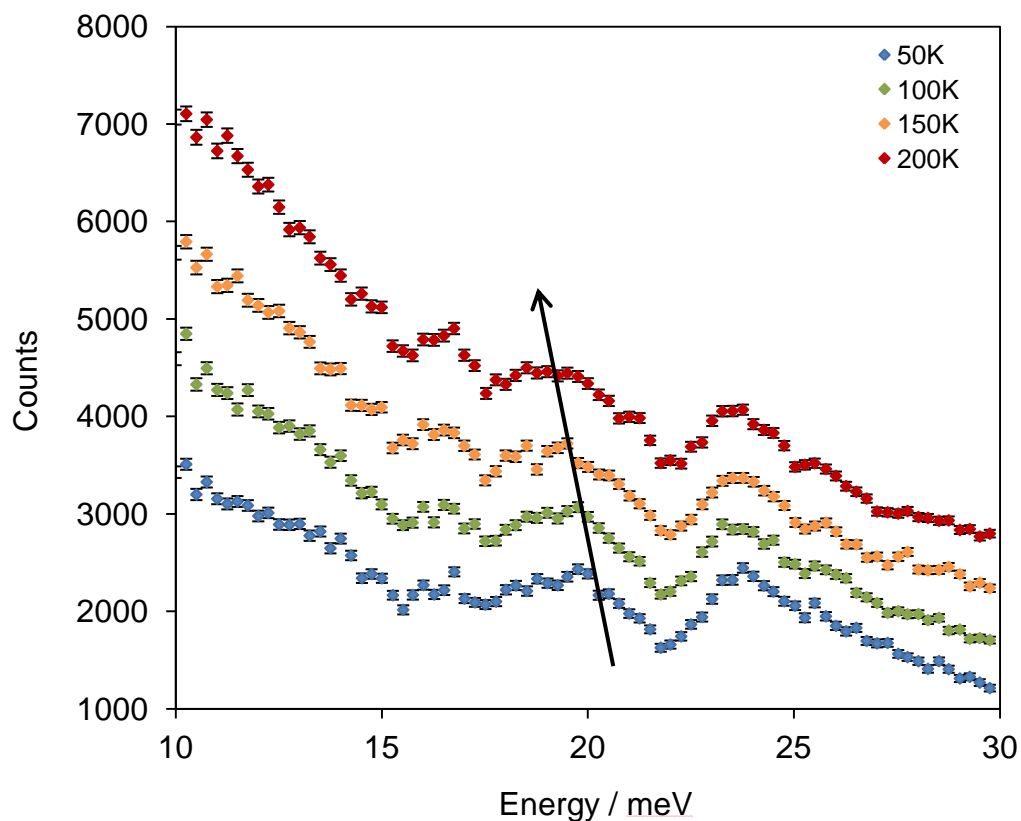
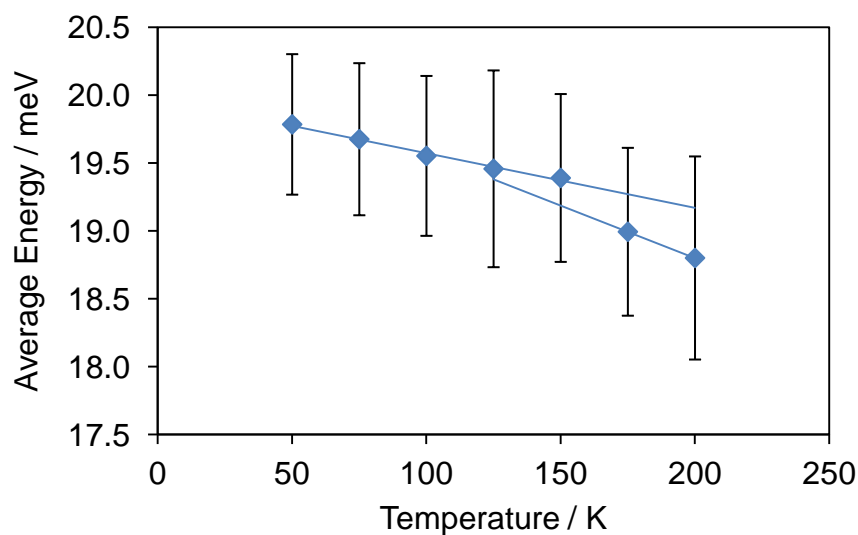*Figure 4.24: A selection of the IN8 results in the 070 direction.*



*Figure 4.25: The average energy as a function of temperature for the IN8 data in the 070 direction. Lines of best fit have been added as guides to the eye.*
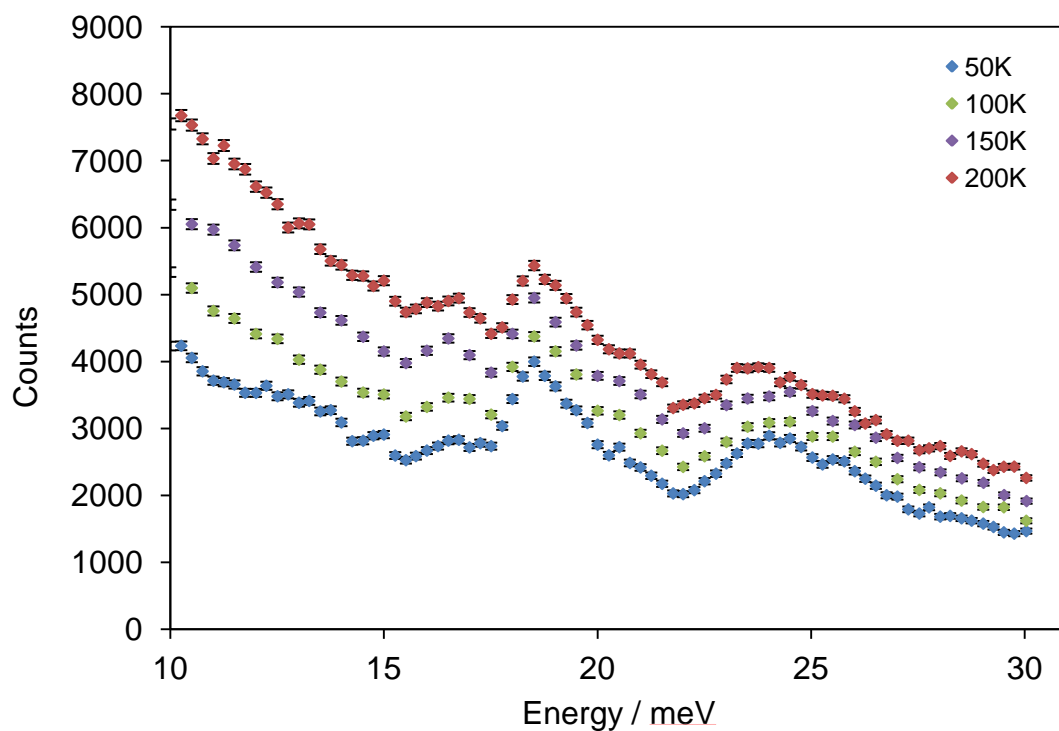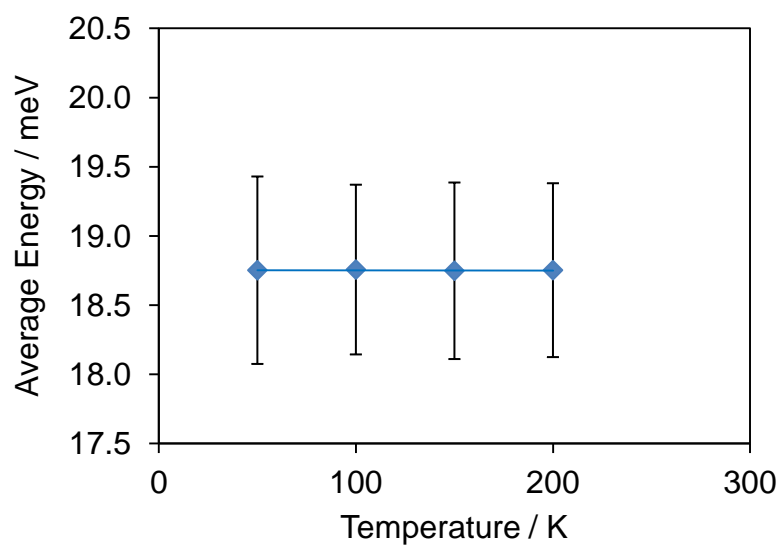
*Figure 4.26: The IN8 results for the 600 direction.*



*Figure 4.27: The average energy as a function of temperature for the IN8 data in the 600 direction. A line of bets fit has been included (blue).*

### 4.2.2.2 INS: Supporting Computational Studies

The density of states, for all hydrogen atoms, along the *a* and *b* directions at 0 K was calculated using VASP, Figure 4.28a. It can be seen that the most significant difference

between these data is in the intensity of the peak at approximately 19.5 meV (157 cm$^{-1}$), which is much more intense in the *b* direction. The density of states, for the H5 atom, along the *a* and *b* directions at 0 K was also calculated, Figure 4.28b. This shows that the intense peak observed at 19.5 meV (157 cm$^{-1}$) is likely to be related to vibrations of the H5 atom (the proton in the SSHB), confirming the experimental conclusion.
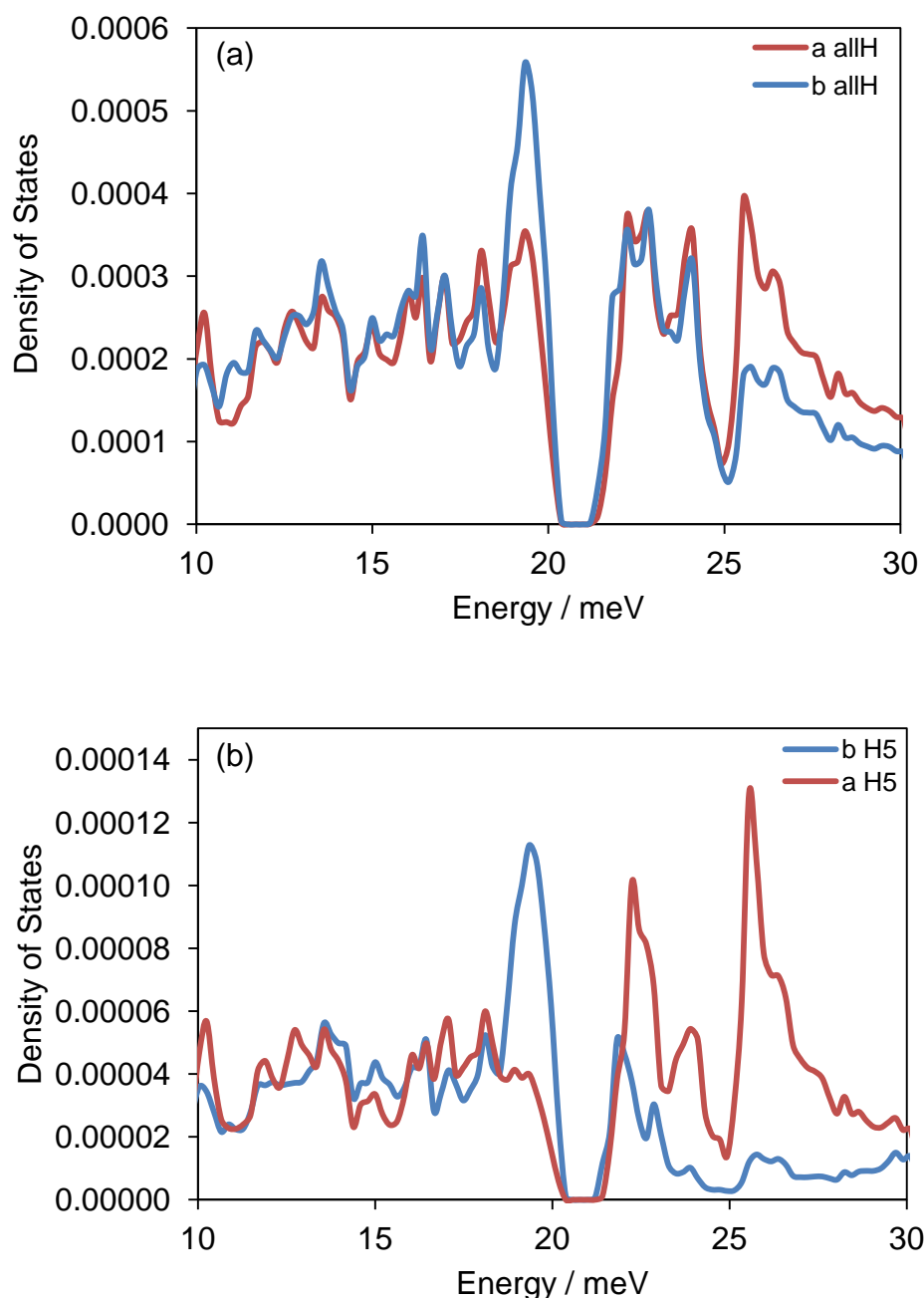


*Figure 4.28: The density of states along the a (red) and b (blue) directions for a) all hydrogen atoms and b) the hydrogen atom in the SSHB (H5).*

A depiction of the actual mode at 19.5 meV (157 cm$^{-1}$), also calculated in VASP, is given in Figure 4.29. This mode shows that, at this frequency, all atoms are displaced along the *b* axis with similar amplitudes. The hydrogen atom in the SSHB is displaced along the hydrogen bond demonstrating that this mode does in fact modulate the geometry of the hydrogen bond.
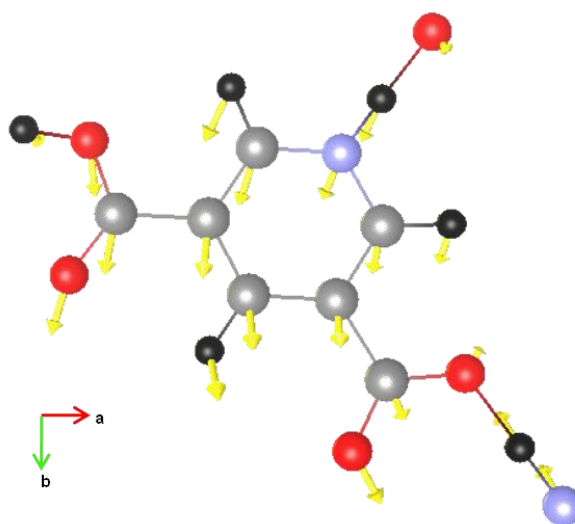


*Figure 4.29: The vibrational mode calculated by VASP, in a single molecule of 35PDCA at 300 K, being used as a probe in this work (155 cm$^{-1}$, 19.2 meV).*

The equivalent mode has also been calculated using DMol$^3$, Figure 4.30, for comparison. In this mode, again, all atoms are displaced with a similar amplitude; however, although the hydrogen atom in the SSHB is displaced along the hydrogen bond, all other atoms are displaced along the *a* axis, rather than the *b* axis as calculated by VASP. This demonstrates the limitations of the calculations at this level and shows that in this case, based on the IN8 data suggesting softening in the *b*-direction, the VASP calculation is better.
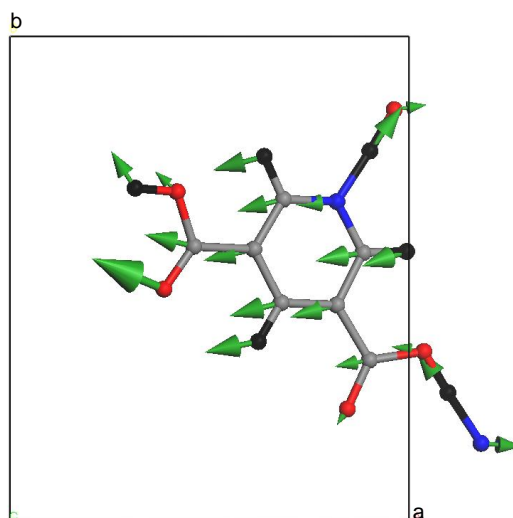
*Figure 4.30: The vibrational mode calculated by DMol$^3$, equivalent to that in Figure 4.29 (145 cm$^{-1}$, 18 meV).*

## 4.3  Conclusions

Various spectroscopic and computational techniques have been used in order to obtain information about the nature of proton hopping in various 35PDCA isotopologues. The alternative methods of spectroscopy give different information about the various samples. Collectively the set of data allows a greater understanding of the mechanism of proton migration.

In Chapter 3, proton migration in the *d*-35PDCA isotopologue was described in terms of a two phase model, with the growth of domains of the pure HT species from the pure LT species on increasing temperature. Spectroscopy can be sensitive to much smaller domains than diffraction (about 1 nm across, much smaller than a typical domain). In addition, AIMD results show that in a model with only 4 molecules, the hydrogen bonds do not all have to be in a pure HT or pure LT form, but in fact may be completely independent, having one, two, three or four hydrogen atoms migrating at any time. That is, domains in the AIMD model can be as small as a single molecule. The domain model previously described for the *d*-35PDCA isotopologue (using diffraction data, Chapter 3) would be described by a (weighted) sum of spectra from a pure LT and a pure HT model.

In the fully deuterated sample, *d*-35PDCA, IR spectroscopy data show that there is a species present at low temperature (N–D···O) and a different species present at high temperature (N···D–O). From the IR results, a relatively sudden switch from the pure N–D···O species to the pure N···D–O species occurs, though some phase co-existence over a narrow temperature range is apparent; this is consistent with the domain model explanation for proton migration previously given for this isotopologue using diffraction data (Chapter 3).

Contrarily, it seems that for those isotopologues with some level of protonation, the two species, N–H···O (LT) and N···H–O (HT), co-exist over a much more significant temperature range, reaching completion close to 400 K, compared to 200 K for the fully deuterated species. The Raman spectra also show additional broad features at intermediate temperatures, possibly as a result of disorder in the structure. Similarly, IN1 data suggest that further species may also be present at higher temperature, due to possible disorder in the structure. The spectroscopic data on the protonated isotopologues, *acid-d*-35PDCA and *h*-35PDCA, are consistent with the AIMD domain model; however they could also be consistent with the domain model from diffraction. The critical parameter in this discussion is the size of the domains. If they were very small, the domain walls would represent a significant fraction of the system and a lot of disorder would be observed. The disorder is hidden in Rietveld analysis of diffraction data for these isotopologues; however some disorder seems to be visible in the spectroscopic data.

Finally, experimental evidence has been provided in order to support the previous conclusion that low frequency phonons drive the proton migration. IN8 shows softening of peaks close to the mode which has been identified as driving proton migration in the SSHB of 35PDCA.

## 4.4 References

1. F. Fontaine-Vive, M. R. Johnson, G. J. Kearley, J. A. Cowan, J. A. K. Howard and S. F. Parker, *J. Chem. Phys.*, 2006, **124**, 234503.
2. B. Delley, *J. Chem. Phys.*, 1990, **92**, 508.
3. B. Delley, *J. Chem. Phys.*, 2000, **113**, 7756.
4. D. C. Patton, D. V. Porezag and M. R. Pederson, *Phys. Rev. B*, 1997, **55**, 7454.
5. J. P. Perdew, K. Burke and M. Ernzerhof, *Phys. Rev. Lett.*, 1996, **77**, 3865.
6. J. P. Perdew, K. Burke and M. Ernzerhof, *Phys. Rev. Lett.*, 1997, **78**, 1396.
7. S. J. Ford, O. J. Delamore, J. S. O. Evans, G. J. McIntyre, M. R. Johnson and I. R. Evans, *Chem. Eur. J.*, 2011, **in press**.
8. P. Schuster, G. Zundel and C. Sardorfy, eds., *The Hydrogen Bond*, North-Holland, 1976.
9. G. Kresse and J. Hafner, *Phys. Rev. B*, 1993, **47**, 558.
10. G. Kresse and J. Furthmuller, *Phys. Rev. B*, 1996, **54**, 11169.

# 5 3,5-Pyridinedicarboxylic Acid: The Dynamics and Thermodynamics of Proton Migration

The role of quantum tunnelling processes in proton dynamics in hydrogen bonds is well established.[1-7] Quantum tunnelling underpins processes that would otherwise be forbidden in a purely classical picture of dynamics, hence allowing functionality at relatively low temperatures. This scenario is particularly valid in the biological domain, where the quantum character of many vital protein-mediated processes is revealed by an approximately exponential dependence of the process rate on the mass of the tunnelling particle.[8-10]

The tunnelling of protons in hydrogen bonds can be described by protons jumping between the minima of a static, asymmetric, two-well potential, where the minima correspond to the stable and meta-stable positions of the proton next to the donor and acceptor atoms, respectively. The length of the hydrogen bond, and therefore its strength, determines the distance between the minima and the height of the potential energy barrier separating them. For normal, medium-length, hydrogen bonds, this barrier is much higher than $k$T at room temperature and proton dynamics are dominated, at all temperatures below room temperature, by tunnelling through the barrier (Figure 5.1, top).

Short strong hydrogen bonds (SSHBs) are of considerable interest because the proton is almost centred in the bond and therefore represents an instability in which it can easily move from donor to acceptor atom. This is an example of a very simple chemical reaction in which the transfer of one proton between molecules can transform a pair of electrostatically neutral molecules into a charged pair, or *vice-versa*. This inherent instability of short, strong hydrogen bonds is known to underpin enzyme catalysis, for example in HIV.[11]

In the one-dimensional potential energy picture of the hydrogen bond, as the hydrogen bond becomes shorter the two wells are pushed together resulting in a lowering of the potential energy barrier (Figure 5.1, middle). In the extreme case of SSHBs, this barrier disappears, leaving a flat-bottomed or (more commonly) asymmetric single well,

depending on the energy bias between the donor and acceptor sites (Figure 5.1, bottom). One immediate difference relative to the medium-length hydrogen bonds is that jumping between the minima of a two-well potential can no longer occur. For the proton to pass from donor to acceptor, as has been observed for a range of systems,[12-16] the asymmetric single-well has to change bias, the minimum moving from the donor to the acceptor site. This type of process has been studied in detail computationally[17-19] and offers an explanation for complete, thermally-driven, proton migration in molecular crystals. *Ab-initio* molecular dynamics (AIMD) show that proton migration is not the result of a static structural reorganisation that lattice expansion may induce; it is rather the time-average of a dynamical process in which collective, structural excitations (lattice phonons in a molecular crystal) modulate the potential causing the proton to jump between donor and acceptor atoms. Recently it has been shown that the high-temperature, proton-transferred state is stabilised by vibrational entropy (Chapter 3).[14]
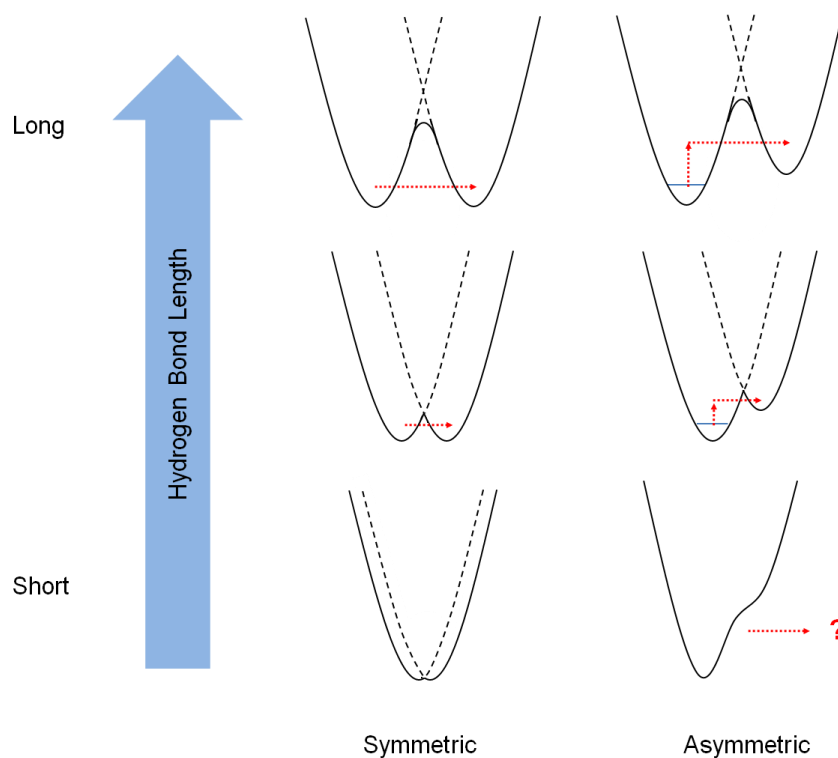


*Figure 5.1: The one-dimensional potential energy picture of hydrogen bonding for the symmetric case (left) and asymmetric case (right). The red arrows represent the quantum tunnelling path.*

Given the importance of quantum tunnelling in, for example, biological processes, and the role of SSHBs in enzyme catalysis, an obvious question is whether or not quantum tunnelling in SSHBs enhances enzyme catalysis. In view of the foregoing, one-dimensional description of the potential wells governing proton tunnelling, it would appear that quantum tunnelling cannot play a role, since the proton does not have a second site to tunnel to. However, there has been much work over the last decade on the coupling of tunnelling and vibrational degrees of freedom, with vibrations promoting or hindering tunnelling.[20-23] In this case the one-dimensional (1D) potential energy well should be extended to a multi-dimensional potential energy surface (PES) in which a 2-well potential, governing proton dynamics, may be found for SSHBs.

In order to make further progress in gaining a full understanding of the proton migration/transfer process and its relevance to various important processes involved with SSHBs, experimental observations of the proton dynamics are highly desirable, including an investigation of the statistical thermodynamics from which some characteristics of the potential energy surface could be inferred. Ideally these aspects of proton dynamics would be investigated directly in enzymes but their complexity currently excludes a sufficiently detailed study and consequently 3,5-pyridinedicarboxylic acid (fully protonated form, *h*-35PDCA), a suitable model structure, has been used throughout this work.

The model system, 35PDCA, contains a short N–H···O hydrogen bond, with a donor-acceptor distance of 2.52 Å at 15 K, in which proton migration from the donor (N) to the acceptor (O) occurs with increasing temperature. A significant proton migration phenomenon is revealed by neutron diffraction and infrared spectroscopy (IR) measurements on the fully deuterated, *d*-35PDCA, isotopologue which displays a structural phase transition associated with a switchover in the populations of the two hydrogen bond species. For the isotopologues containing a level of protonation, *h*-35PDCA, *acid-d*-35PDCA and *ring-d*-35PDCA (Chapter 3), the change seems to be more progressive; inelastic neutron scattering (INS) and Raman spectroscopy studies reveal a co-existence of both the N–H···O (LT) and the N···H–O (HT) species, in varying quantities, over a wide temperature range. X-ray and neutron diffraction measurements extract the average of this behaviour, suggesting a continuous, gradual

migration of the proton from the nitrogen donor to the oxygen acceptor as temperature is increased. Finally, a quasi-elastic neutron scattering (QENS) experiment was attempted in order to measure the dynamic nature of the proton migration, but no evidence of quasi-elastic scattering was found.

Nuclear magnetic resonance is a technique complementary to QENS, and, in the absence of other types of motion which might otherwise obscure the proton migration signature, it has the sensitivity to reveal weak relaxation processes arising from such small atomic displacements. At Nottingham University, NMR relaxometry, involving magnetic field-cycling techniques, was used, giving significant advantages over conventional NMR techniques; the magnetic field dependence of the spin-lattice relaxation rate maps out the spectral density enabling direct measurement of the proton migration rate. Furthermore, the amplitude of the spectral density is determined by the populations of the two hydrogen sites and therefore provides a direct measure of the thermodynamic properties (enthalpy and entropy) of the system. The experimental results from these spin-lattice and relaxometry measurements (performed by the Horsewill group at Nottingham University) will be briefly summarised in this chapter, with particular focus on the low temperature regime where quantum tunnelling would give a limiting, non-zero dynamical rate.

This experimental work is the basis for the work in this chapter where the role of vibrational coordinates in the PES governing proton dynamics was explored. A combination of density functional theory (DFT) based molecular (MD) and lattice (LD) dynamics simulations, and mapping of the PES was used in order to attempt to understand the proton migration/transfer and tunnelling behaviour.

## 5.1 Experimental

A single crystal sample of *h*-35PDCA was prepared for this work, as described in Section 3.1 of Chapter 3.

NMR experiments were then performed by the Horsewill group at Nottingham University (Department of Physics). A single crystal of *h*-35PDCA was selected and oriented so that the *c*\* crystal axis was aligned parallel with the applied static magnetic

field. The $^1$H spin-lattice relaxation, $T_1^{(H)}$, was measured as a function of both temperature, $T$, and magnetic field, $B_0$, using a saturation-recovery pulse NMR sequence.[24, 25]

## 5.2  Computational

In the context of this work, previous AIMD simulations using the VASP DFT code[26, 27] have been extended to include further temperatures and larger simulation cells in order to investigate finite size effects on the proton dynamics (details below). Details of previous calculations, performed by Fontaine-Vive *et al.* at temperatures of 15, 250, 300 and 400 K, are given in Reference 18.

All of the VASP DFT simulations performed in this work used projector augmented wave (PAW) pseudopotentials in combination with the PBE functional.[28, 29]  An energy cutoff of 700 eV was used; however, as the precision was set to 'low' in the input (INCAR) file, the actual energy cutoff was 500 eV. A single *k*-point was used and this was placed at the Γ-point, origin (0,0,0), for calculations in reciprocal space.

MD simulations performed in VASP were run in the NVT ensemble using a Nosé-Hoover thermostat.[30, 31] A number of supercells were constructed, by sequentially doubling one of the axes of the optimised unit cell. This allowed the possibility to study changes in the proton jump rate with increasing cell size and also allowed the probing of any axis-related effects. All supercell structures were studied at 400 K, with simulation times up to 10 ps, whilst the single cell structure (subcell) was studied at both 150 and 200 K, with simulation times of 17 ps. A time step of 1 fs was used in all cases.

In addition, a range of DFT calculations (molecular and lattice dynamics, and transition state (TS) searches) were performed using the DMol$^3$ code[32, 33] available in the Materials Studio software suite (version 5.53). In contrast to the VASP code, which uses a plane-wave basis set, DMol$^3$ uses a basis set of localised, numerical functions. The main reason for using DMol$^3$ was that it allowed the high temperature (N···H–O) structure of 35PDCA to be stabilised and, thereafter, a TS search to be performed, which was not possible to achieve with plane-wave codes.

All DMol$^3$ calculations were performed using the GGA-PBE functional[29, 34, 35] for consistency with the VASP DFT calculations. The basis functions were double numerical with polarisation, with a global orbital cut-off of 3.7 Å, and a *k*-point grid of (3,2,4). All results were converged with respect to the choice of basis functions and *k*-point spacing. The energy tolerance for SCF cycles was $1 \times 10^{-6}$ Ha. For geometry optimisation the tolerance for energy change with respect to atomic coordinates was $1 \times 10^{-5}$ Ha and maximum residual force was $2 \times 10^{-3}$ HaÅ$^{-1}$. Molecular dynamics simulations were performed in NVE and NVT ensembles, using a Nosé-Hoover thermostat in the latter case. The time step for integrating the equations of motion was 1 fs.

By convention, values of energy from the NMR experiments are quoted in units of K, and those from calculations are quoted in units of eV. Results in this chapter follow this convention. However, for ease of analysis, units of K have been used throughout the discussions. For reference, 1 K = 8.62 x $10^{-5}$ eV (= 8.314 x $10^{-3}$ kJmol$^{-1}$).

## 5.3 Experimental Results Summary and Discussion

### 5.3.1 Dynamical Rate

The inverse temperature dependence of the $^1$H spin-lattice relaxation time recorded at $B_0 = 0.864$ T is plotted in Figure 5.2. A shallow minimum occurs when the frequency of the dynamics causing relaxation (the proton transfer) matches the $^1$H Larmor frequency specific to this magnetic field; in this case this is observed at a temperature of around 100 K. Below 55 K and, similarly, above 170 K, the $^1$H spin-lattice relaxation rate seems to be almost temperature independent.
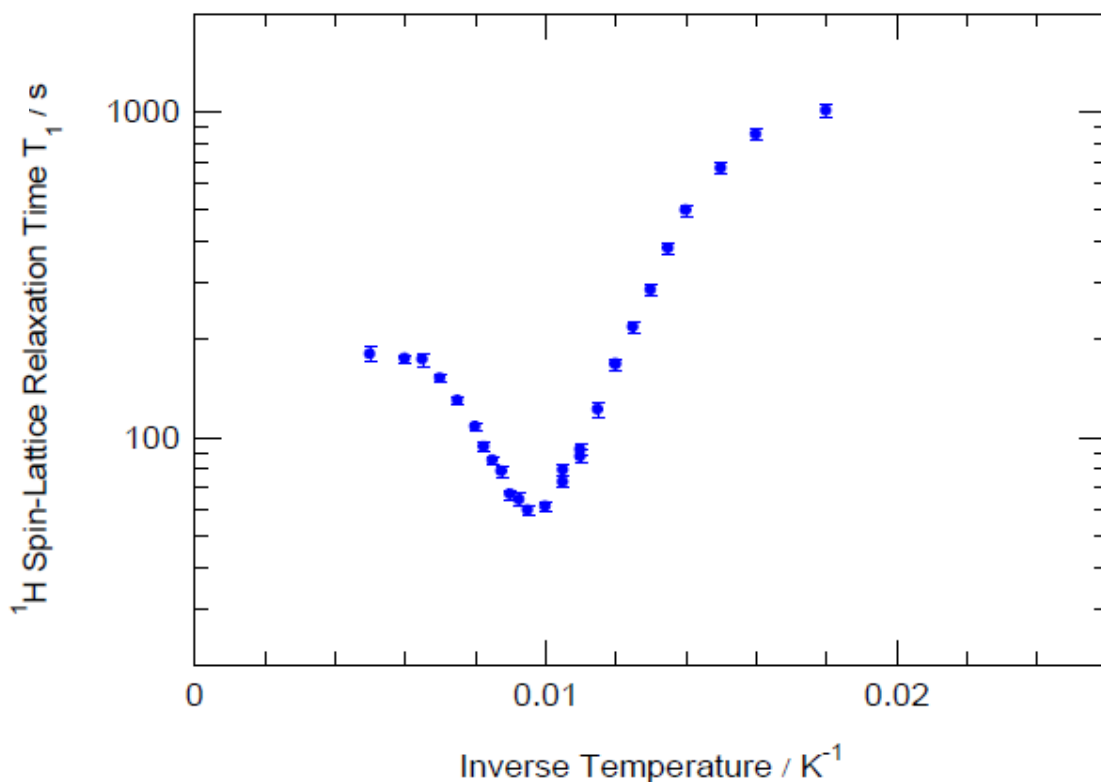
*Figure 5.2: The dependence of the $^1$H spin-lattice relaxation time in h-35PDCA on inverse temperature, recorded at a fixed field, $B_0 = 0.864$ T.*

In Figure 5.3 the magnetic field dependence of the $^1$H spin-lattice relaxation rate is presented at seven temperatures in the region of interest. At the three lowest temperatures, 71.4, 79.6 and 83.3 K, the curves are almost parallel, differing only in amplitude, indicating that the correlation rate, $\tau_c^{-1}$ (spectral density width), is independent of temperature in this region. At 90.9 K the spectral density begins to broaden indicating that $\tau_c^{-1}$ is increasing. This trend progresses with increasing temperature although at the two highest temperatures studied, 125.0 and 142.9 K, the curves again appear almost parallel, indicating that $\tau_c^{-1}$ is once again independent of temperature. It can be seen that at a magnetic field of 0.864 T (that used in the recording of Figure 5.2, see dotted line in Figure 5.3), the $^1$H spin-lattice relaxation rate increases with temperature from 71.43 K to a maximum at 100.0 K. Above 100.0 K further temperature increases result in a decrease in the spin-lattice relaxation rate; this is exactly the trend observed in Figure 5.2.
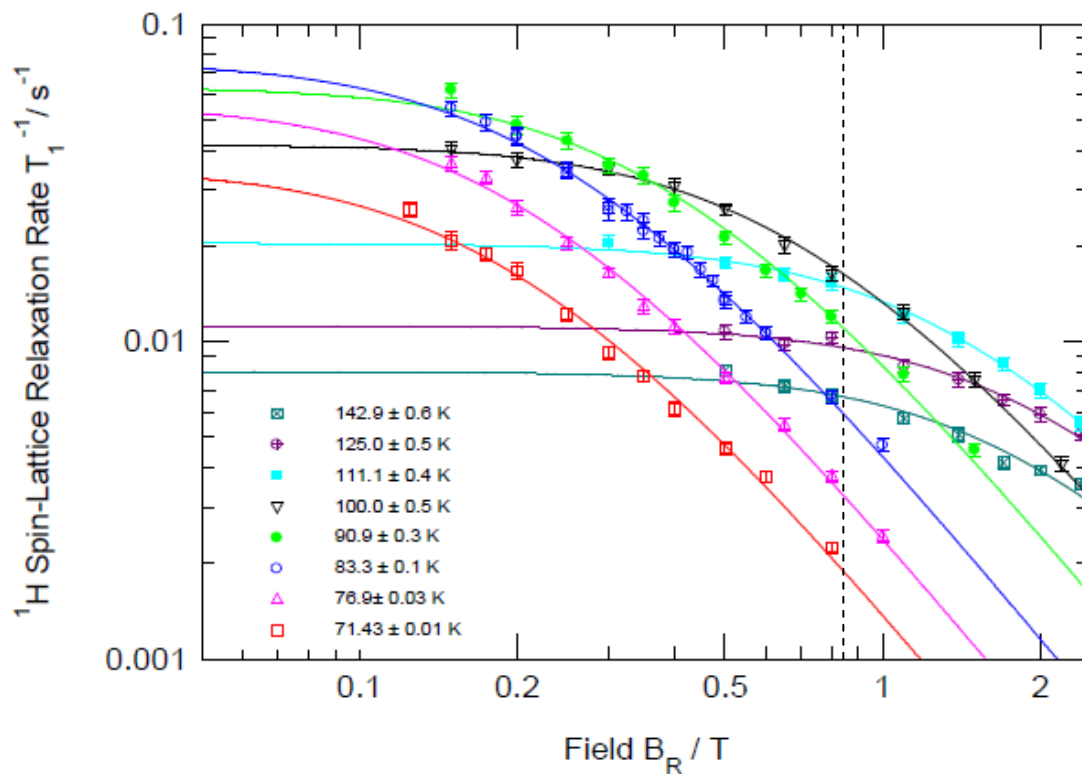
*Figure 5.3: The spectral density profiles determined from the magnetic field dependence of the $^1H$ spin-lattice relaxation time recorded in h-35PDCA. A dashed black line is drawn at approximately 0.864 T in order to show the relation between this and Figure 5.2.*

Figure 5.4 shows a plot of correlation rate, $\tau_c^{-1}$, as a function of inverse temperature (with the solid symbols calculated as the spectral density widths from Figure 5.3, and the open symbols are determined from a numerical inversion of the data in Figure 5.2) which is related to the rate at which the proton is jumping from one site (N) to the other (O). It can be seen that this jumping rate is on a ns timescale. The trend inferred from a qualitative interpretation of Figure 5.3 is also confirmed; at the highest temperatures, $\tau_c^{-1}$ appears to be independent of temperature, levelling off at a value of $9 \times 10^8$ s$^{-1}$, and again, at the lowest temperatures, levelling off at a value of $8 \times 10^7$ s$^{-1}$. This observation at low temperature is interesting; it would be expected that this value would tend to zero towards 0 K; however, the fact that it does not indicates that dynamics are still present at this temperature, *i.e.* a quantum tunnelling contribution to proton jumping must be present.
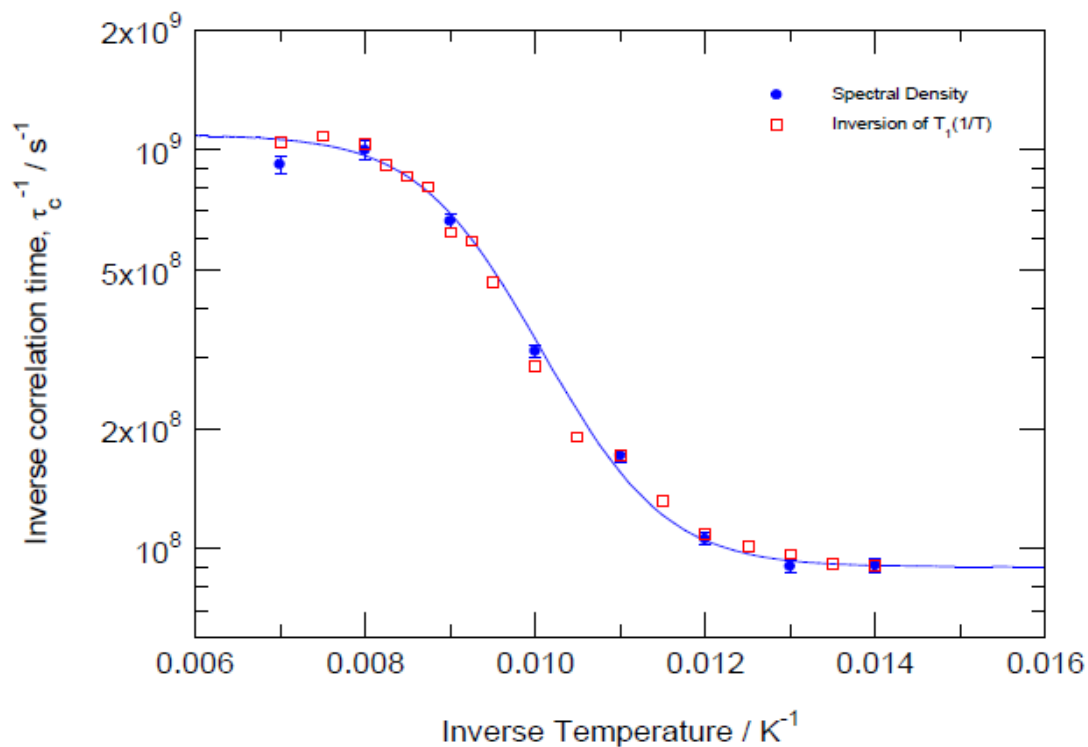
*Figure 5.4: The dependence of the correlation rate, $\tau_c^{-1}$ on inverse temperature, relating to proton transfer in h-35PDCA. The solid symbols have been determined directly from the spectral density profiles in Figure 5.3 and the open symbols have been determined from a numerical inversion of the fixed field data in Figure 5.2.*

### 5.3.2  The Role of Entropy

In Figure 5.5 the spectral density amplitudes (determined from the areas under the curves in Figure 5.3, and given by Equation 5.1) are plotted as a function of inverse temperature.

$$K(T) = C_D \frac{\exp(\Delta G / k_B T)}{(1 + \exp(\Delta G / k_B T)^2}$$  (Equation 5.1)

where $K(T)$ is the spectral density amplitude, $\Delta G$ is the free energy and $C_D$ is a dipolar constant. Significant to this work is the dependence of the amplitude, $K(T)$, on the populations of the N–H···O and N···H–O species.
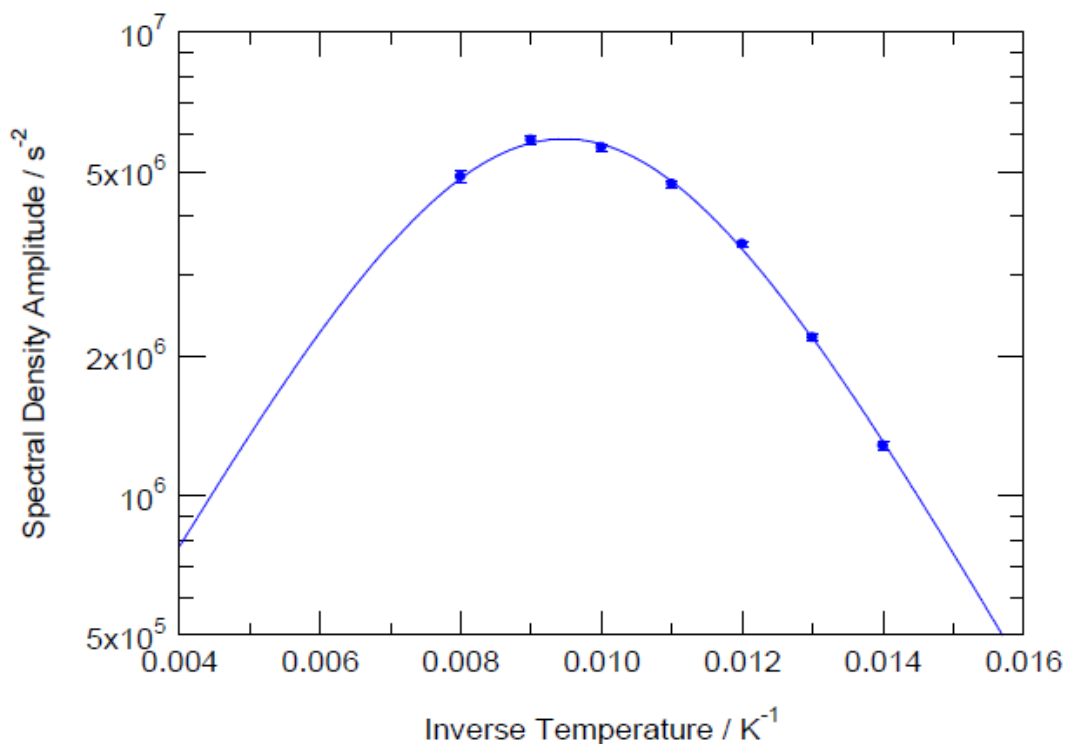
157

*Figure 5.5: The dependence of the spectral density amplitude on inverse temperature, determined from fitting to the data in Figure 5.3.*

This plot exhibits a peak at approximately 105 K, indicating a switchover from one hydrogen bond species to the other. The gradient of this curve at low temperature has been calculated to be 500 K, providing an estimate of the activation energy, *i.e.* the energy difference between the N–H···O and N···H–O species. However, the start of the switchover at high temperature, and, consequently, the presence of a peak in this curve, suggests that the populations of the two sites cannot be determined solely by enthalpy. It was found that the introduction of entropy into the thermodynamic description, governed by the free energy, $\Delta G$ (Equation 5.2), accounts for the observed shape of this curve.

$$\Delta G = \Delta H - T\Delta S \qquad \text{(Equation 5.2)}$$

A constant value of entropy, *S*, is used in the analysis of the NMR data. If *S* is vibrational entropy, which has been analysed in the context of Chapter 3, then it will show a dependence on the temperature, *T*. This will not, however, affect the temperature

of the spectral density amplitude maximum and therefore the switchover of the relative populations of the two proton sites will remain unchanged.

This switchover temperature of 100 K is much lower than that observed with other experimental techniques (diffraction and vibrational spectroscopy, Chapters 3 and 4). Diffraction shows a switchover from LT to HT species, for the fully protonated material, *h*-35PDCA, at approximately 225 K, whereas Raman spectroscopy suggests that a fully N···H–O species is not fully present until approximately 400 K, though a small amount of the HT species starts to emerge at around 100 K. For the fully deuterated isotopologue, *d*-35PDCA, the switchover occurs between 150 and 200 K. Due to the fact that the lattice phonons responsible for the proton transfer are of a lower frequency for the deuterated material than those of the protonated molecule, deuterium dynamics are activated at a lower temperature than those of hydrogen. Generally, however, the larger mass of deuterium compared to hydrogen and the correspondingly lower level of the ground eigen-state in the potential well, would result in hydrogen dynamics occurring at a lower temperature than deuterium dynamics. The NMR measurements are interesting in this respect. These NMR studies should be extended to the *d*-35PDCA compound in order to observe how the switchover temperature compares with that of the *h*-35PDCA compound.

The observation from NMR could be explained by the onset of the proton hopping in a small domain of the crystal structure (rather than the bulk). Alternatively, dynamics in the normal, medium-length, O–H···O hydrogen bond may be perturbing the experiment at higher temperature (above 100 K) and so a clear switchover from LT to HT species might not be observed using this NMR technique.

## 5.4 Computational Results and Discussion

### 5.4.1 Jump Rates

DFT calculations give insight into the principal findings of the NMR experiments. The first experimental observation is that proton dynamics occur on the nanosecond timescale, accessible by NMR. In contrast, the original plane-wave AIMD simulations[18] predicted proton dynamics on the 1-10 ps timescale that is accessible by that method.

The AIMD simulations were reported at 15 K, 250 K and above. These simulations have been repeated at lower temperatures and in larger simulation cells to look for finite size effects.

From a typical plot of N–H bond length as a function of time (shown in Figure 5.6 and taken from Reference 18) it is not straightforward to determine a realistic jump rate from the relatively short simulation times used. The jump rate here has been calculated by normalising the N–H bond length to the instantaneous N–O distance for each hydrogen bond and counting the number of times this ratio changes from below 0.5 (N–H⋯O species) to above 0.5 (N⋯H–O species) or *vice-versa*. In this way, a large number of rapid back and forth jumps (a selection of which are shown by the arrows in Figure 5.6) contribute significantly to the jump rate, over-estimating what could be regarded as the real jump rate. A reduction in the calculated jump rate, by a factor of approximately 10, between 300 and 150 K is obtained in this way. An activation energy of 505 K can be extracted from the temperature-dependent jump rate, which can be compared with the activation energy of 500 K obtained from both the NMR data (described above) and the vibrational spectroscopy data (IN1, described in Chapter 4).
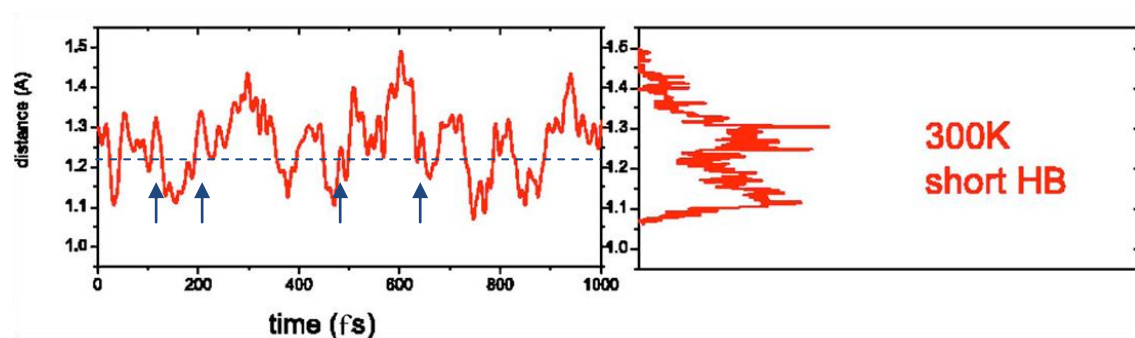


*Figure 5.6: N-H distance as a function of time over 1 ps, where the dotted line represents the mid-point of the hydrogen bond and the arrows show a selection of the rapid back and forth jumps (left), and a histogram integrated over the whole trajectory (right). Taken from Reference 18.*

AIMD simulations performed in bigger cells show a reduction in the jump rate, by a factor of approximately two, when the simulation cell is doubled along the *c*-axis. In a single unit cell, concerted proton jumps were only observed in hydrogen bonds separated by approximately 3.5 Å between neighbouring sheets of 35PDCA but not

within molecular sheets. Extending the simulation cell in the *c*-direction reduced this correlated motion significantly, while extending the cell in the *a*- and *b*-directions did not give a further reduction in jump rate. Thus the calculated jump rate using plane-wave DFT methods (VASP) remains about two orders of magnitude higher than that observed by NMR.

Since DMol[3] has been used to stabilise the high temperature structure and thereafter perform LD calculations and TS searches, MD simulations were also performed with DMol[3] in exactly the same way as the published, and discussed, plane-wave (VASP) MD simulations.[18] DMol[3] gives similar results to those obtained from VASP owing to the similarity of the vibrational density-of-states of the N–H⋯O proton, and the proton jump mechanism (see later), between the two codes. However, DMol[3] does indeed give a much lower jump rate, in better agreement with the NMR data. The difference in proton jump rates obtained from two DFT codes, used in similar ways, indicate that these simulations should be used to investigate the mechanism of proton migration rather than the absolute jump rate. They serve to highlight the difficulty of accurately calculating dynamical rates with relatively small and short first principles simulations and therefore demonstrate the value and necessity of the experimental data.

On the other hand, the time spent by the proton close to the oxygen atom is much lower in the DMol[3] simulations (Figure 5.7b), the bimodal proton distribution reported in Figure 5.6 (from Reference 18) is not observed (in ps simulations), and so the agreement with the diffraction results (Chapter 3) is less good. Figure 5.7 shows plots of NH (blue) and OH (red) bond distance as a function of time, for a small portion of the trajectories for clarity, calculated using both DMol[3] (Figure 5.7a) and VASP (Figure 5.7b). A jump of the proton occurs when the blue and red lines cross, *i.e.* when the N–H distance becomes longer than the O–H distance or *vice-versa*.
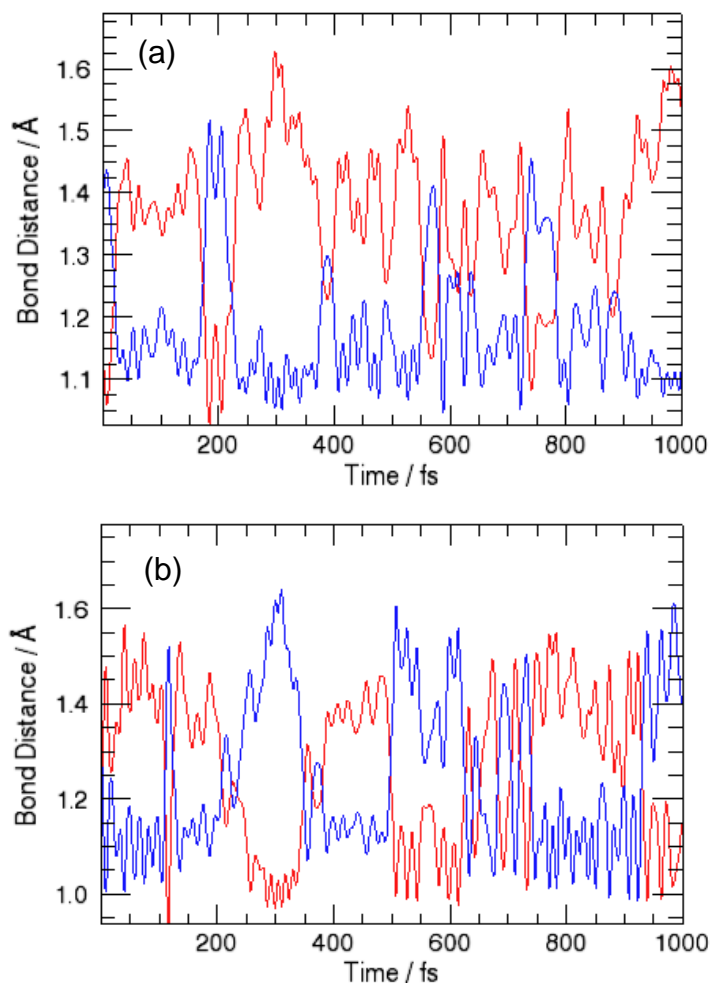
*Figure 5.7: Small sections of the plots of NH (blue) and OH (red) distance as a function of time, extracted from MD simulations calculated in: a) DMol$^3$ and b) VASP.*

It appears that the jumps calculated by DMol$^3$ are in fact instantaneous; when a proton jumps from donor (N) to acceptor (O), it does not remain close to the acceptor for any prolonged period of time but in fact returns swiftly to the nitrogen atom, with the entire proton jump (from donor to acceptor and back to donor) over a maximum of 50 fs, as demonstrated by the small periods of time that the blue lines are present at large bond distances in Figure 5.7a. It is possible that such short residence times of the proton at the oxygen atom would not allow for the relaxation of nuclear magnetisation in NMR experiments. Even the longer residence times calculated in the VASP simulations (approximately 100-200 fs, as shown by the longer periods of time in which the blue lines in Figure 5.7b spend at large bond distances), may still be too short to give rise to relaxation. In this way many of the calculated jumps could be missed by NMR and

therefore the time-averaged numbers from simulations cannot be quantitatively compared with NMR values.

## 5.4.2  Calculation of 2-well Potentials

The most striking feature of the temperature dependence of the proton correlation time, Figure 5.4, is that, at low temperature, there is a non-zero, limiting value, indicative of proton jumping *via* a quantum tunnelling mechanism. This observation can only be understood in terms of a 2-well potential which, given the known 1D single-well potential, has to be sought in a multi-dimensional PES which is based on a tunnelling, or proton transfer, coordinate and a second coordinate describing the structural change that accompanies proton transfer. The second, structural, coordinate is often referred to as a vibrational coordinate since one or more vibrational modes may drive the structural change and therefore proton transfer. In this case a 2D (proton transfer-vibration) PES is considered for each mode, with the vibrations being orthogonal in a harmonic analysis.

For reference, as previously described in Chapter 3, 35PDCA crystallises with four molecules in the unit cell, arranged in two parallel sheets, Figure 5.8a. The two dimensional structure is stabilised by a number of intermolecular hydrogen bonds in the sheets, including short N–H···O bonds (the SSHBs) and normal, medium-length, O–H···O bonds, Figure 5.8b. In total, there are four SSHBs per unit cell (two per sheet).
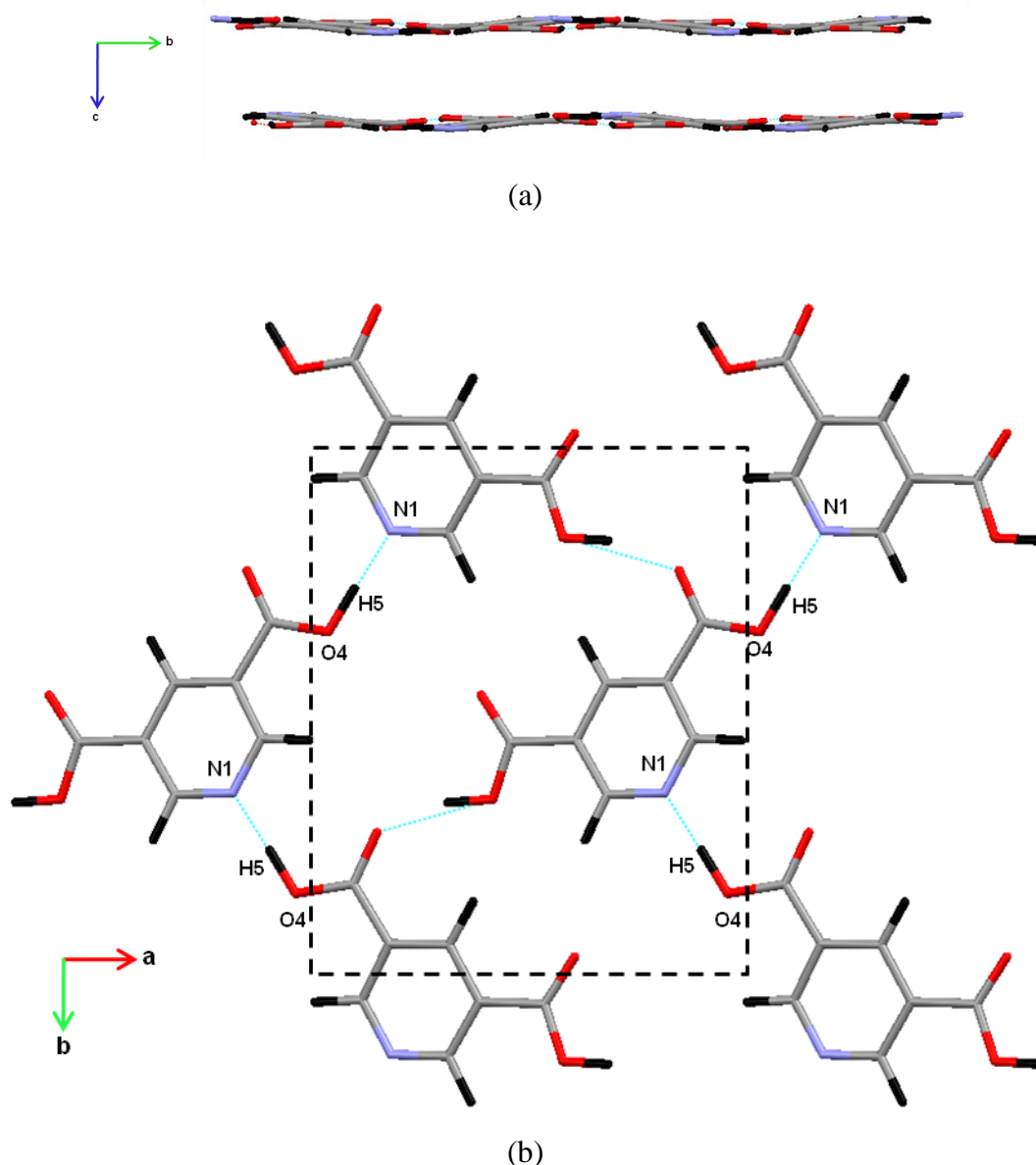
(a)



(b)

*Figure 5.8: a) The packing in 35PDCA, as viewed down the a axis. b) A section of a single layer of 35PDCA, as viewed down the c axis, showing the SSHBs (N1–H5···O4). The dashed rectangle highlights part of a single unit cell; note that there are two SSHBs in each layer of the unit cell (i.e. four in total in the unit cell).*

### 5.4.2.1 Molecular Dynamics

From AIMD simulations the vibrational or structural change when a proton moves along the short hydrogen bond can be visualised from a series of structures when the proton undergoes a rapid jump (10-20 fs). Figure 5.9 shows a typical jump in which there appears to be a concomitant translation/rotation of the molecule as it attempts to

follow the proton, pivoting about the carbon atom of the ring adjacent to the normal, medium-length, hydrogen bond (C3, labelled). This picture is, however, complicated by the fact that the structural changes observed are due to both the proton jump and all other, unrelated, molecular vibrations. By studying a large number of jumps, it has not been possible to determine the average structural change accompanying a jump, suggesting that the local structural changes due to proton jumping are not dominant in the overall structural fluctuations of the MD simulations.
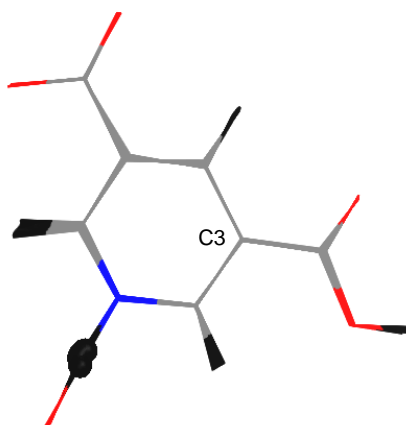


*Figure 5.9: The structural changes occurring in 35PDCA during a single jump in an MD simulation. Only a single molecule of 35PDCA is shown for clarity, and the hydrogen atom of interest is represented as a ball.*

Similarly, a 2-well potential, which is the result of the combined tunnelling (or proton transfer) and vibrational coordinates, could be extracted from the potential energy variation of the crystal in the MD simulation when a proton undergoes a rapid jump, Figure 5.9. There is a tendency to observe a local, potential energy maximum in the middle of a proton jump but the contribution from other vibrational degrees of freedom gives rise to a strong variation in the 2-well potentials when these are observed, making this approach unsuitable for a quantitative estimation of the 2-well potential.
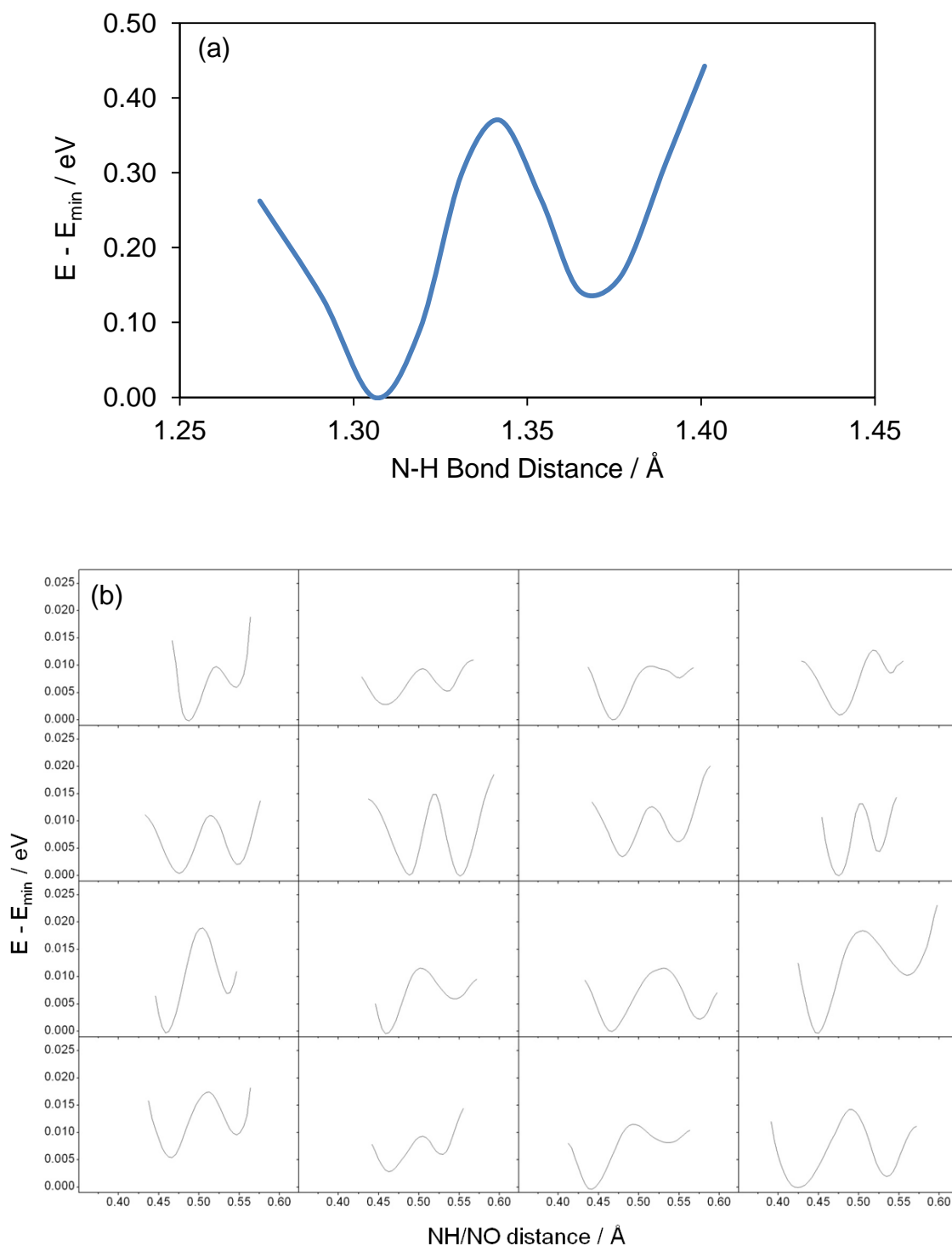
*Figure 5.10: A range of 2-well potentials extracted from the potential energy changes of the crystal during proton jumps in various MD simulations performed using a) DMol[3] and b) VASP.*

Figures 5.10a and 5.10b differ as they were obtained using different codes; Figure 5.10a was obtained using DMol[3] whilst Figure 5.10b was obtained using VASP. It can be seen

that the potential energy variation obtained in VASP is much lower than that obtained by DMol$^3$, with a typical energy difference between the two minima of approximately 0.005-0.01 eV from VASP, compared to 0.1 eV from DMol$^3$, and a typical potential energy barrier height of 0.005-0.02 eV for VASP, compared to 0.4 eV from DMol$^3$. These differences may explain the large discrepancy in the dynamical rate obtained using the two codes. (In addition, due to the greater jump rate found by VASP, and the larger simulation times employed, a larger selection of 2-well potentials was obtained).

### 5.4.2.2  TS Search, 4 Protons Moved

An alternative approach to calculating the 2-well potential is to perform a transition state search, where the 'reactants' and 'products' are well-defined structures: the low temperature (LT, N–H···O form) and high temperature (HT, N···H–O form) crystal structures. Since there is a lattice change between these structures, the LT atomic coordinates have been optimised in the HT crystallographic cell, giving an N–H bond length of 1.125 Å. The atomic coordinates of the HT structure have also been optimised giving an N–H bond length of 1.409 Å. The initial transition state trajectory can be sought starting from a linear interpolation of these two structures and Figure 5.11 shows an overlay of ten such structures. Note that the ring carbon adjacent to the normal, medium-length, hydrogen bond (C3, labelled) does not move, as in Figure 5.9.
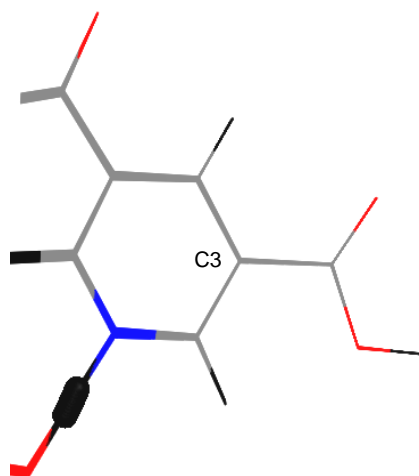


*Figure 5.11: The structural changes occurring in 35PDCA in a calculated TS trajectory. Only a single molecule of 35PDCA is shown, with the migrating hydrogen atom represented as a ball.*

The corresponding potential energy variation, resulting from total energy calculations for each of the structures, is shown in Figure 5.12 (though only the minima of the two wells are shown, see blue curve, 2D TS). The energy difference between the LT (red) and HT (yellow) structures is 1140 K and the barrier height is 295 K greater than the energy of the HT structure. Due to the small differences between the LT and HT structures, a full TS search did not converge. At the saddle point, the proton was displaced perpendicular to the trajectory. The potential energy, $E$(eV), increases quadratically as a function of the perpendicular displacement $x$(Å), $E = 108.4x^2$, demonstrating that the saddle point has the lowest potential energy. For the level of calculation employed, Figure 5.12 gives the best representation of the 2-well potential, in the multi-dimensional tunnelling and vibrational space, governing the simultaneous jumping of all four protons of a unit cell. For four uncoupled hydrogen bonds, the energy to transfer a single proton would be (1140/4=) 285 K. This is the activation energy, $E_a$; analogous to that previously obtained from various sources (NMR, vibrational spectroscopy and dynamical rate calculations which all give a value for $E_a$ of approximately 500 K).
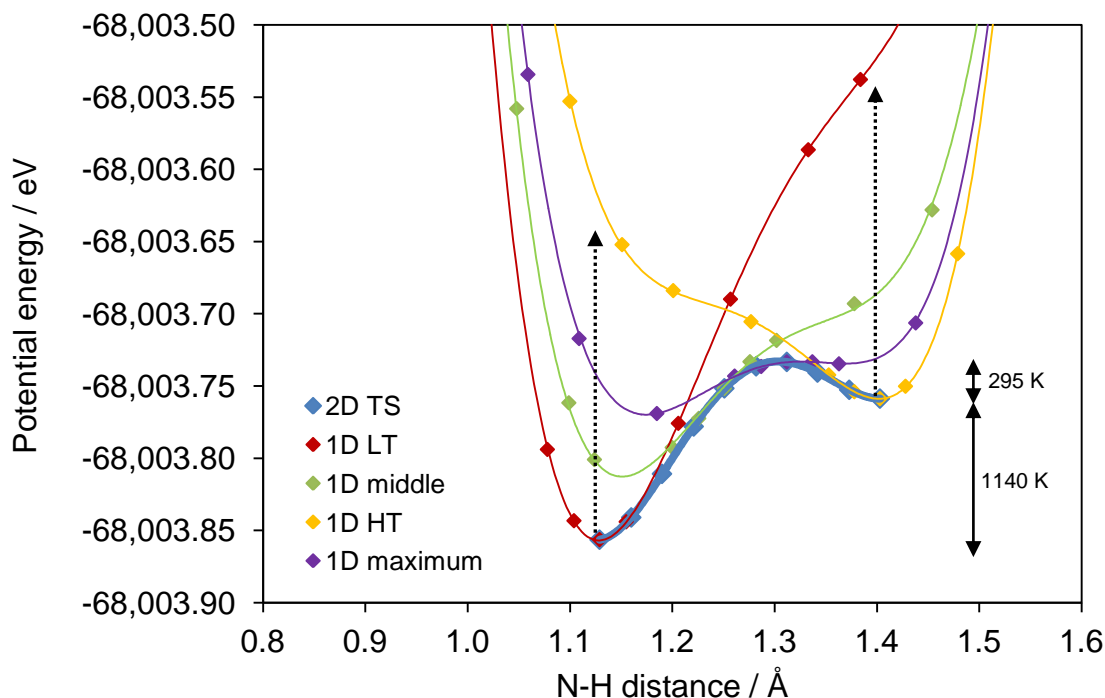


*Figure 5.12: Blue: 2D TS potential energy variation (2D TS). Red, green, orange and purple: 1D potential wells determined by moving the hydrogen atom of interest across the hydrogen bond, starting from the low temperature structure (1D LT), an*

*intermediate structure (1D middle), the highest energy structure (1D maximum) and the high temperature structure (1D HT).*

### 5.4.2.3  TS Search, 2 Protons Moved

Working towards determining the potential energy variation for one proton transfer, a similar set of TS calculations were performed for transferring two protons in one of the two molecular sheets in the unit cell (*i.e.* half of the unit cell). A similar two-well potential is observed (and again only the minima of the two wells are shown, Figure 5.13, red) in which the barrier height is 93 K greater than the energy of the HT structure, to be compared with (295/2=) 148 K from the 4-proton calculation. The energy difference between the LT and 2-proton-transferred structures is (650/2=) 325 K per proton, to be compared with (1140/4=) 285 K above (*i.e.* tending towards the experimental value). These numbers indicate a weak inter-sheet coupling which increases the potential barrier but decreases the energy difference between the ground and proton-transferred states.
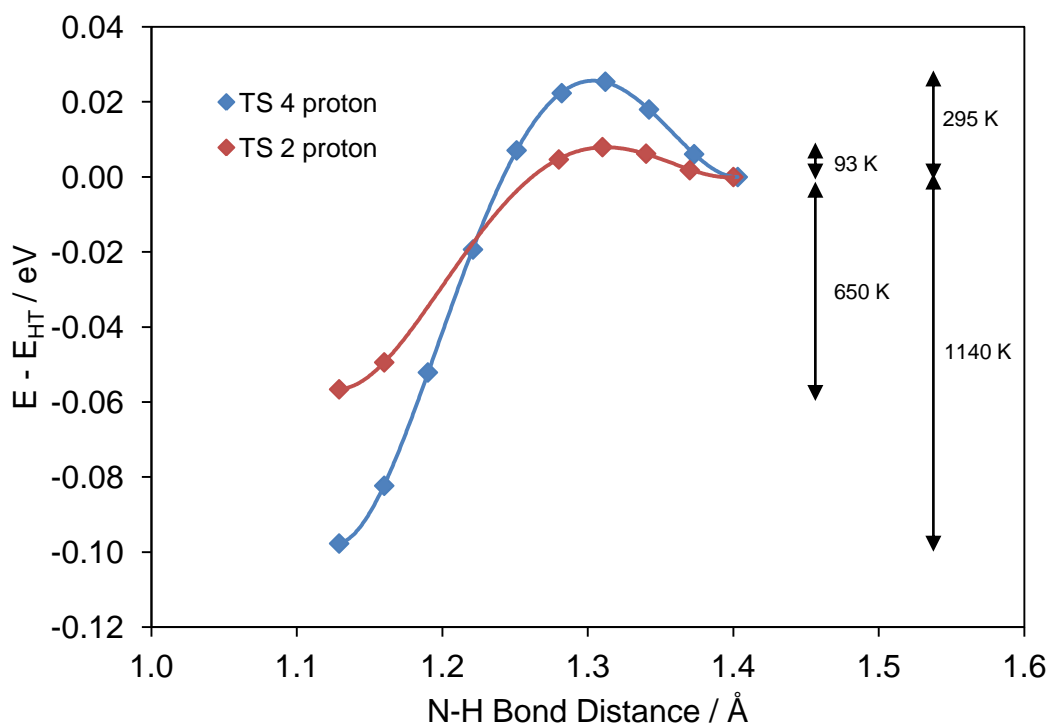


*Figure 5.13: A comparison of the 2D TS potential energy variation for the movement of 4 protons simultaneously (blue, as drawn in Figure 5.12 also) and the movement of 2 protons simultaneously (red).*

#### 5.4.2.4  TS Search, 1 Proton Moved

For the transfer of a single proton, a constrained geometry optimisation was required to fix the N–H bond length at 1.4 Å. A 2-well potential was not obtained and unconstrained optimisation of the atomic coordinates restored the short N–H distance of 1.1 Å. The energy difference between the LT structure and the HT structure was 731 K, to be compared with values from above, of 285 and 325 K for one proton. The high value for the energy difference suggests that structural reorganisation cannot reduce the potential energy as much when the next hydrogen bond in the molecular sheet hinders relaxation. This constraint is relieved by MD simulations by thermally activated vibrations, allowing jumping of single protons. It should be noted that the set of values quoted here (285, 325 and 731 K) lie above and below the experimentally determined value of 500 K.

#### 5.4.2.5  1D, 4 Proton Potential Wells

The one-dimensional, potential energy variation along the tunnelling (proton transfer) coordinate is also shown in Figure 5.12 for the HT and LT extremes and two intermediate positions (middle and maximum). These curves closely resemble those determined from instantaneous structures in MD simulations (see Figure 6 in Reference 18), with an almost flat-bottomed potential obtained at the saddle point (purple, Figure 5.12). By comparing the 2-well, TS potential with the extreme, 1D, single-well potentials, the contribution of the structural change to the total energy accompanying proton transfer (see vertical arrows in Figure 5.12) can be estimated to be 2670 K, compared to a total energy change of 3810 K if only the protons are transferred. In other words, structural reorganisation reduces the energetic cost of proton transfer by about two-thirds, which is a measure of the strength of the coupling between proton transfer (tunnelling) and vibrational degrees of freedom.

#### 5.4.2.6  1D Coupling Calculations

The calculations reported thus far demonstrate strong coupling between proton transfer and structural reorganisation. Insight into the coupling between proton transfer in neighbouring hydrogen bonds can be obtained from calculations in which protons are moved along the hydrogen bonds. This approach is analogous to work on molecular

rotors for which rotational coordinates are the principle degrees of freedom.[36, 37] Figure 5.14 shows the 1D single proton potentials as a function of the position of the closest hydrogen bond proton either in the same molecular sheet (Figure 5.14a) or an adjacent molecular sheet (Figure 5.14b). The blue curves in each case represent the changes in crystal energy as a single proton is moved along the hydrogen bond from the donor (N) to the acceptor (O). With this first proton in the transferred position, the red curves represent further changes in the crystal energy as a second proton (either in the same molecular sheet, Figure 5.14a, or an adjacent molecular sheet, Figure 5.14b) is then moved. If there was no coupling between these protons, the blue and red curves of Figure 5.14 would be identical. It can be seen that this is not the case and in fact the red curves have consistently lower gradients as a result of the smaller energy change of moving a second proton (this is particularly clear in Figure 5.14a). These plots therefore represent intra- and inter-sheet coupling of hydrogen bonds, respectively (coupling between hydrogen bonds in the same sheet and in an adjacent sheet of the 35PDCA structure, respectively).
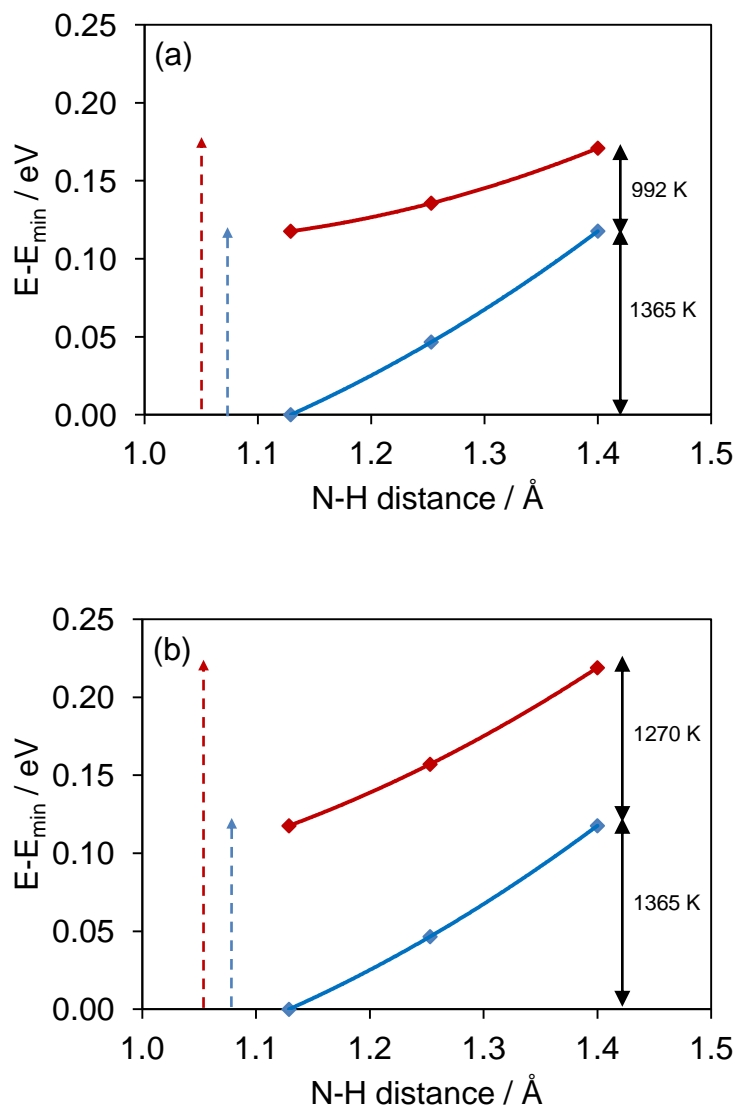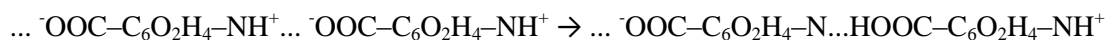
*Figure 5.14: Potential energy as a function of NH distance representing (a) intra and (b) inter-molecular coupling. The blue curves represent the 1D proton transfer potential for a single hydrogen bond. The red curves represent the same potential with the neighbouring hydrogen bond proton in the transferred position. The blue dashed arrows represent the energy cost of transferring a single proton and the red dashed arrows represent the cost of transferring two protons.*

The energy cost of transferring one proton is 1365 K. The energy cost is reduced slightly (by 7 %) to 1270 K by inter-sheet coupling (Figure 5.14b) and more significantly, by intra-sheet coupling (by 27 %), to 992 K (Figure 5.14a). Intra-sheet coupling is therefore much stronger than inter-sheet coupling and, in this case, the 27 % reduction in the hydrogen bond potential is a measure of the electronic change caused

by the chemical reaction (below) without the structural contribution that has been discussed above.

$$... \text{ }^-OOC–C_6O_2H_4–NH^+ ... \text{ }^-OOC–C_6O_2H_4–NH^+ \rightarrow ... \text{ }^-OOC–C_6O_2H_4–N...HOOC–C_6O_2H_4–NH^+$$

The potential energy change as a function of NH distance does not result in a 2-well potential in the cases shown in Figure 5.14. One possible reason for this is that, although the starting structure for the movement of the second proton was perturbed from an equilibrium position (by the movement of the first proton), the method of calculating these 1D potentials does not take into account any further structural changes of the molecule associated with proton migration.

### 5.4.2.7  Identification of the Promoting Vibrations

Proton transfer-vibration coupling has been explored in detail, identifying promoting modes, in systems that can be reasonably treated in terms of isolated molecules or, for example, dimers.[38-41] In these cases the tautomers are equivalent and have the same vibrational modes in the two equally stable states. In contrast, 35PDCA must be treated, at least, as a 2D molecular sheet, and the tautomeric forms are clearly inequivalent. The 1D hydrogen bond potential has been calculated for all of the proton displacements of the LT structure, for modes up to $250 \text{ cm}^{-1}$, an example of which is shown in Figure 5.15. For these calculations the starting structures were based on the equilibrium structure, which had been perturbed by vibrations of varying amplitudes. As in the TS calculation and corresponding 1D potential calculations (Figure 5.12) all 4 protons in the SSHBs were moved along the donor-acceptor direction systematically and simultaneously, since the phonons make symmetric perturbations of the crystal structure, with the total energy calculated at each position.
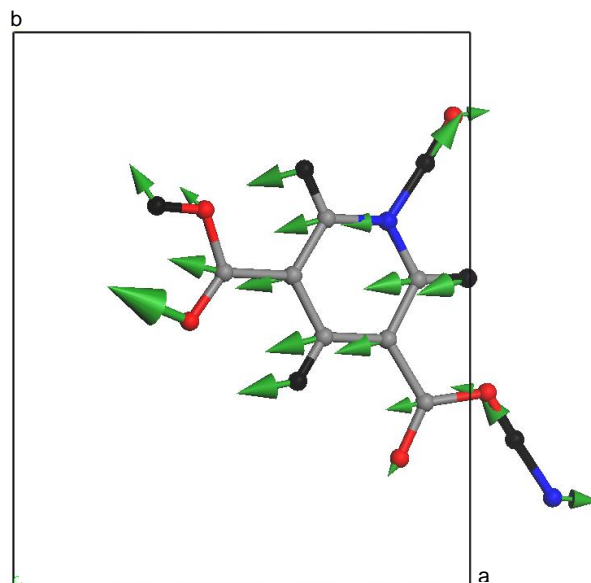
*Figure 5.15: The vibrational mode at 145 cm$^{-1}$ polarised along the a axis, calculated by DMol$^3$. In this vibrational mode all atoms are displaced with similar amplitudes of motion.*

This method failed to produce a 2-well potential. For reasonable displacement amplitudes, the 1D potential remains single-well and biased towards the nitrogen atom, whereas a promoting mode would be expected to bias the potential towards the oxygen atom. In conclusion, using DMol$^3$, it has not been possible to identify a single phonon which perturbs the structure in a way that favours the proton position on the oxygen site. Given the results of the IN8 work in Chapter 4, in which it was found that the vibrational modes which drive the proton migration (for an example, see Figure 5.16) are polarised along the *b*-direction, the results of this study, using the mode in Figure 5.15 (predominantly polarised along the *a* axis), calculated by DMol$^3$, are as expected. Again, as discussed in Chapter 4, these differences between the VASP and DMol$^3$ results pose potential problems.
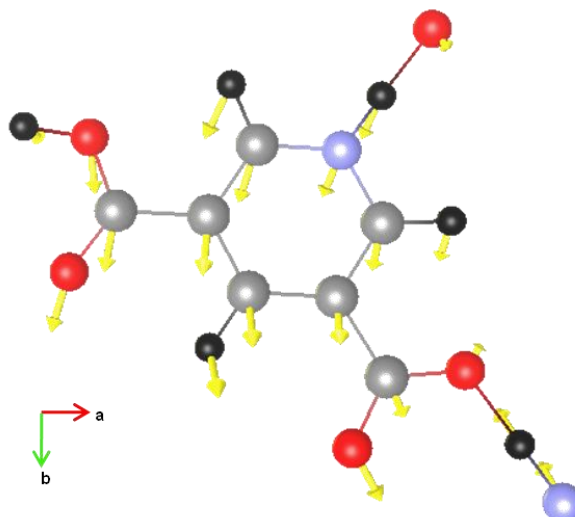
*Figure 5.16: The vibrational mode at 155 cm$^{-1}$ polarised along the b axis, calculated by VASP; in this mode all atoms are displaced and their amplitudes of motion are similar.*

### 5.4.2.8   Single Sheet Calculations

In one further attempt to investigate coupling, the proton transfer calculations were repeated removing one of the two molecular sheets in the unit cell. In the remaining sheet, both N–H···O protons were transferred simultaneously, giving an energy change of 476 K, that is 238 K per proton. However in this case the LT species was the higher energy structure and optimisation of the atomic coordinates displaced the protons to the oxygen sites, almost completely inverting the relative stability of the proton sites, comparing +285 K with -238 K. The coupling between protons in neighbouring sheets has been shown to be weak but it is the close proximity of the neighbouring sheet that stabilises the LT zwitterionic form of the hydrogen bond. Isolated molecular sheets favour the HT, N···H–O, hydrogen bond structure, whereas inter-sheet, van der Waals and electrostatic interactions result in the LT, N$^+$–H···O$^-$, structure being energetically more favourable.

## 5.5   Conclusions

Results have shown that the NMR data collected reveal a dynamical rate on a nanosecond timescale. The observation of a non-zero dynamical rate at temperatures close to 0 K provides evidence for the presence of a quantum tunnelling contribution to

proton transfer. Furthermore, investigations of spectral density amplitudes (determined from a plot of the $^1$H spin-relaxation rate as a function of magnetic field) shows a definite contribution of entropy to the free energy of the system. The activation energy (the energy difference between the N–H···O (LT) species and the N···H–O (HT) species for a single hydrogen bond) of 500 K was found, consistent with that found in dynamical rate calculations and vibrational spectroscopy.

A comparison of the NMR results with those obtained using diffraction and vibrational spectroscopy techniques shows a discrepancy in the temperature scales, with the switchover from LT to HT structure seemingly occurring at a much lower temperature with NMR. As discussed in the text, it is possible that the proton transfer in the SSHB is masked by a stronger signal from the normal, medium-length, O–H···O hydrogen bond at higher temperatures, preventing the observation of a reliable switchover from LT to HT species. Alternatively, only proton hopping in a small domain of the crystal structure may be being observed.

DFT calculations over-estimate the dynamical rate, especially with VASP, and so the results obtained from simulations cannot be quantitatively compared with NMR values. In addition, due to large discrepancies in the rates obtained from the two DFT codes used, it seems that the calculation of dynamical rates in this way is not reliable.

Transition state calculations for both the entire crystal and a single molecular sheet have shown that the reorganisation within the structure as a whole reduces the energy cost of proton transfer. This confirms the presence of a 2-well potential in the system which underpins the observation of tunnelling in the hydrogen bond; although the barrier height seems low. PES mapping shows that coupling occurs not only between proton transfer and structural reorganisation, but also between proton transfer and electronic structure, and between hydrogen bonds.

In addition, the transition state calculations for a single molecular sheet show that it is all of the interactions with the neighbouring sheets, caused by the close proximity of the sheets at low temperature, which stabilise the LT zwitterionic form of the hydrogen bond. At room temperature the larger separation of the sheets reduces these interactions and results in the N···H–O hydrogen bond structure being most stable. It would

therefore be expected that, when the molecular sheets are forced together experimentally (for example, by lowering the system temperature, or increasing the pressure, as seen in Chapter 3), the proton-transferred zwitterionic form would be the most favourable configuration, providing a critical *c*-axis length is reached; this is the case upon decreasing temperature, and also provides additional evidence to merit further investigation of the changes in the atomic position of the significant hydrogen atom in 35PDCA as a function of pressure (see Chapter 3).

Compared to single molecule calculations, for which more accurate hybrid functionals and sophisticated basis sets are available, solid state calculations as presented here offer a lower level of precision. Thus the precise values of energy differences and barrier heights, although clearly reasonable, should be treated with caution. Higher precision, solid state calculations involving only hybrid functionals are only now becoming available.

## 5.6  References

1.  T. Jonsson, M. H. Glukman, S. Sun and J. P. Klinman, *J. Am. Chem. Soc.*, 1996, **118**, 10319.
2.  P. Ball, *Nature*, 2004, **431**, 396.
3.  Y. Cha, C. J. Murray and J. P. Klinman, *Science*, 1989, **243**, 1325.
4.  B. J. Bahnson, T. D. Colby, J. K. Chu, B. M. Goldstein and J. P. Klinman, *Proc. Natl. Acad. Sci. U.S.A.*, 1997, **94**, 12797.
5.  A. Kohen, T. Jonsson and J. P. Klinman, *Biochemistry*, 1997, **36**, 2603.
6.  M. J. Knapp, K. Rickert and J. P. Klinman, *J. Am. Chem. Soc.*, 2002, **124**, 3865.
7.  P. O. Lowdin, *Rev. Mod. Phys.*, 1963, **35**, 724.
8.  A. J. Horsewill, *J. Phys. Org. Chem.*, 2010, **23**, 580.
9.  Q. Xue, A. J. Horsewill, M. R. Johnson and H. P. Trommsdorff, *J. Chem. Phys.*, 2004, **120**, 11107.
10. A. J. Horsewill, *Prog. Nucl. Magn. Reson. Spectrosc.*, 2008, **52**, 170.
11. J. Trylska, P. Grochowski and J. A. McCammon, *Protein Sci.*, 2004, **13**, 513.
12. C. C. Wilson, *Acta Crystallogr., Sect. B*, 2001, **57**, 435.
13. T. Steiner, I. Majerz and C. C. Wilson, *Angew. Chem. Int. Ed.*, 2001, **40**, 2651.
14. S. J. Ford, O. J. Delamore, J. S. O. Evans, G. J. McIntyre, M. R. Johnson and I. R. Evans, *Chem. Eur. J.*, 2011, **in press**.
15. J. A. Cowan, J. A. K. Howard, G. J. McIntyre, S. M. F. Lo and I. D. Williams, *Acta Crystallogr., Sect. B*, 2003, **59**, 794.
16. C. C. Wilson, L. H. Thomas and C. A. Morrison, *Chem. Phys. Lett.*, 2003, **381**, 102.
17. C. A. Morrison, M. M. Siddick, P. J. Camp and C. C. Wilson, *J. Am. Chem. Soc.*, 2005, **127**, 4042.

18. F. Fontaine-Vive, M. R. Johnson, G. J. Kearley, J. A. Cowan, J. A. K. Howard and S. F. Parker, *J. Chem. Phys.*, 2006, **124**, 234503.
19. F. Fontaine-Vive, M. R. Johnson, G. J. Kearley, J. A. K. Howard and S. F. Parker, *J. Am. Chem. Soc.*, 2006, **128**, 2963.
20. M. J. Wojcik, *J. Mol. Liq.*, 2008, **141**, 39.
21. M. J. Wojcik, W. Tatara and S. Ikeda, *J. Mol. Struct.*, 2002, **614**, 109.
22. M. J. Wojcik, K. Szczeponek and M. Boczar, *Int. J. Mol. Sci.*, 2003, **4**, 422.
23. M. J. Wojcik, H. Nakamura, S. Iwata and W. Tatara, *J. Chem. Phys.*, 2000, **112**, 6322.
24. F. Noack, *Prog. Nucl. Magn. Reson. Spectrosc.*, 1986, **18**, 171.
25. A. J. Horsewill and Q. Xue, *Phys. Chem. Chem. Phys.*, 2002, **4**, 5475.
26. G. Kresse and J. Hafner, *Phys. Rev. B*, 1993, **47**, 558.
27. G. Kresse and J. Furthmuller, *Phys. Rev. B*, 1996, **54**, 11169.
28. P. E. Blochl, *Phys. Rev. B*, 1994, **50**, 17953.
29. J. P. Perdew, K. Burke and M. Ernzerhof, *Phys. Rev. Lett.*, 1997, **78**, 1396.
30. S. Nose, *J. Chem. Phys.*, 1984, **81**, 511.
31. W. G. Hoover, *Phys. Rev. A*, 1985, **31**, 1695.
32. B. Delley, *J. Chem. Phys.*, 1990, **92**, 508.
33. B. Delley, *J. Chem. Phys.*, 2000, **113**, 7756.
34. D. C. Patton, D. V. Porezag and M. R. Pederson, *Phys. Rev. B*, 1997, **55**, 7454.
35. J. P. Perdew, K. Burke and M. Ernzerhof, *Phys. Rev. Lett.*, 1996, **77**, 3865.
36. P. Schiebel, G. J. Kearley and M. R. Johnson, *J. Chem. Phys.*, 1998, **108**, 2375.
37. M. R. Johnson and G. J. Kearley, *Ann. Rev. Phys. Chem.*, 2000, **51**, 297.
38. V. A. Benderskii, E. V. Vetoshkin, S. K. Grebenshchikov, L. vonLaue and H. P. Trommsdorff, *Chem. Phys.*, 1997, **219**, 119.
39. M. Plazanet, M. R. Johnson and H. P. Trommsdorff, *Opt. Spectrosc.*, 2005, **98**, 692.
40. V. A. Benderskii, E. V. Vetoshkin, I. S. Irgibaeva and H. P. Trommsdorff, *Chem. Phys.*, 2000, **262**, 393.
41. V. A. Benderskii, E. V. Vetoshkin, I. S. Irgibaeva and H. P. Trommsdorff, *Russ. Chem. Bull., Int. Ed.*, 2001, **50**, 1148.

# 6  Additional Short Strong Hydrogen Bond Systems

In addition to the work on 35PDCA, the CSD was searched in order to identify further candidates for temperature-dependent proton migration.[1, 2] A search for compounds containing short, intermolecular O–H···O and O–H···N hydrogen bonds, comparable to those in UPA and 35PDCA, was undertaken. The search used the parameters: organics only, 3D coordinates determined, no ions, no powders and no disordered structures. Three promising structures, with very short hydrogen bonds, were found (3,5-dinitrobenzoic acid-nicotinic acid, 4-aminobenzoic acid-nicotinic acid and benzimidazolium hydrogen phenylmalonate); each of these has previously been studied at room temperature and by X-ray diffraction (XRD) only.[3-5]

The crystal structures of 3,5-dinitrobenzoic acid-nicotinic acid[3] (35DBNA) and 4-aminobenzoic acid-nicotinic acid[4] (4ABNA) exhibit certain similarities with 35PDCA, as they also contain two competing intermolecular interactions, a short N···O and a normal, medium-length, O···O bond, both in a planar arrangement. In addition, at room temperature the protons in the short N···O bonds of these compounds are found bonded to the oxygen atom. These structural similarities make the N···H–O bonds of 35DBNA and 4ABNA candidates for temperature-dependent proton migration.

Another interesting and potentially exploitable temperature-dependent phenomenon is proton ordering in short hydrogen bonds, leading to ferroelectric phase transitions. In the reported structure, benzimidazolium hydrogen phenylmalonate[5] (BHPM) contains protons disordered in a short O···O hydrogen bond at room temperature and, as such, is of interest due to its similarities with 2-aminopyridine dihydrogenphosphate ($\alpha$-2APP), a compound which is known to undergo a ferroelectric phase transition accompanied by an order-disorder phase transition involving protons in a short O···O hydrogen bond.[6] The similarities between the O···O bonds of these two compounds suggest that BHPM is also a candidate for temperature-dependent proton ordering.

In order to investigate the proton behaviour in these short hydrogen bonds, a combined experimental and computational approach was taken, the results of which are reported here.

## 6.1  3,5-Dinitrobenzoic Acid – Nicotinic Acid (1:1)

3,5-Dinitrobenzoic acid and nicotinic acid, Figure 6.1, co-crystallise to form an adduct (35DBNA, CSD Refcode: AWUDEB) which is comparable to 35PDCA in the nature of its hydrogen bonding patterns and geometries. The room temperature structure of 35DBNA was first reported by Zhu *et al*. using XRD analysis only.[3] This compound crystallises in the monoclinic space group, $P2_1/n$, and is stabilised by a network of hydrogen bonds. It is similar to 35PDCA as it contains two types of intermolecular hydrogen bond, a short O–H···N bond of 2.54 Å, and a normal, medium-length, O–H···O bond of 2.56 Å, at 296 K.[3] In addition, in the room temperature single crystal XRD work of Zhu *et al.*, the proton of the SSHB was found in an asymmetric position closer to the oxygen atom, analogous to that in 35PDCA. In 35DBNA four molecules are joined by O–H···N and O–H···O hydrogen bonds to form approximately 20-membered rings; these rings then pack in a zigzag fashion, stabilised by very weak O···O interactions between the nitro groups, Figures 6.2 and 6.3. Contrarily, in 35PDCA the hydrogen bonding extends infinitely throughout the structure.
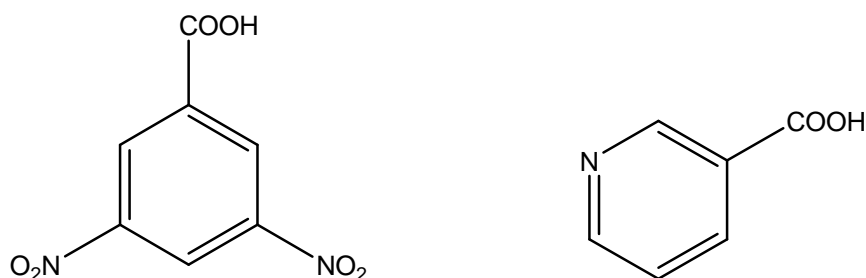


*Figure 6.1: The components of 35DBNA; 3,5-dinitrobenzoic acid (left) and nicotinic acid (right).*

In this work the structure of 35DBNA has been studied at various temperatures in order to observe any changes in proton position with temperature. The structures of 35DBNA, determined from single crystal neutron diffraction data collected at 30 and 300 K, and supporting characterisation of this material by variable temperature single crystal and powder XRD, are discussed in this section. The results of complementary DFT simulations are also reported.
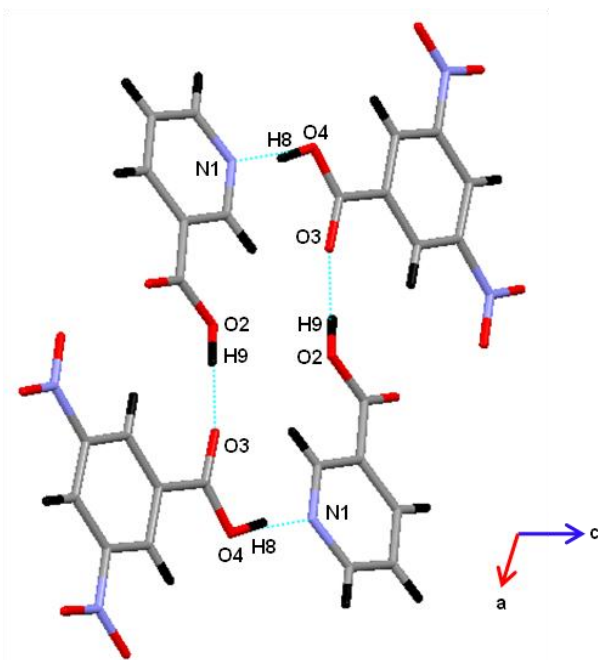
*Figure 6.2: The hydrogen bonding in 35DBNA, viewed down the b axis, with the important atoms labelled. Hydrogen atoms are black, nitrogen atoms are blue, carbon atoms are grey and oxygen atoms are red.*
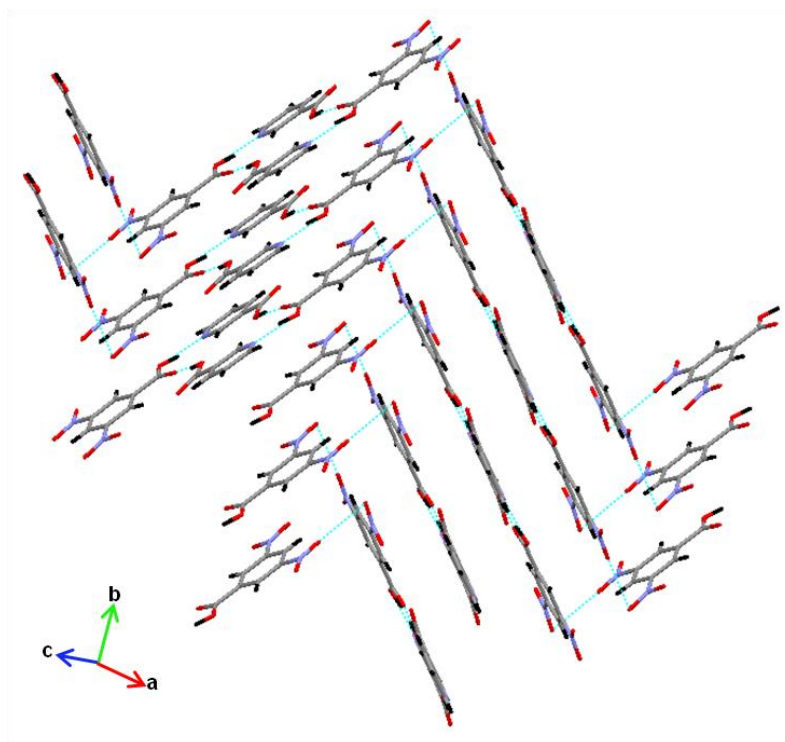


*Figure 6.3: The packing in 35DBNA, with hydrogen atoms in black, nitrogen atoms in blue, carbon atoms in grey and oxygen atoms in red.*

### 6.1.1 Experimental Details

Crystals of 35DBNA, suitable for X-ray analysis, were grown hydrothermally in a 23 cm$^3$ lab scale Parr$^®$ General Purpose Acid Digestion Bomb. The reagents, 3,5-dinitrobenzoic acid (0.350 g, 1.65 mmol, Aldrich, 99 %) and nicotinic acid (0.203 g, 1.65 mmol, Aldrich, 98 %) were used as obtained with no further purification. Colourless, rod shaped crystals resulted after 2 hours at 448 K and a slow cooling regime. Larger crystals for neutron analysis were grown following an initial solubility screen with a range of solvents. A minimal amount of ethanol was used to dissolve 3,5-dinitrobenzoic acid (0.010 g, 0.081 mmol, Aldrich, 99 %) while nicotinic acid (0.017 g, 0.081 mmol, Aldrich, 98 %) was dissolved in a minimal amount of water; these solutions were then mixed in a vial, effectively leading to a 1:2 ethanol:water mixture. The vial was sealed with a cap containing four small apertures, and colourless, rod-shaped crystals resulted after 3 weeks *via* slow evaporation of the solvent.

A crystal measuring $0.08 \times 0.20 \times 0.24$ mm$^3$ was selected for single crystal XRD analysis. Data were collected at a range of temperatures between 100 and 300 K on the Bruker SMART 1000 diffractometer. A full sphere of data was collected at each temperature by a series of $\omega$ scans, using a frame width of 0.3° in $\omega$ and an exposure time of 20 seconds per step. The raw data were collected using the SMART software and integrated using the SAINT suite of programs;[7-9] Structure refinement on $F^2$ was carried out using CRYSTALS.[10] All non-hydrogen atoms were refined anisotropically. Hydrogen atoms were located using Fourier difference maps and refined isotropically; a three parameter Chebyschev weighting scheme was also used.

A crystal measuring $0.5 \times 0.8 \times 1.1$ mm$^3$ was selected for single crystal neutron diffraction analysis. Single crystal neutron diffraction data were collected on VIVALDI at the ILL.[11] Data were collected at 30 and 300 K; ten diffraction patterns, each accumulated over six hours, were collected at each temperature with successive patterns distinguished by a rotation of 20° of the crystal perpendicular to the incident beam. The data were processed using the CCP4 Laue suite of programs.[12-15] Structure refinement on $F^2$ was carried out using SHELXTL.[16, 17] Atomic coordinates and anisotropic displacement parameters were refined for all atoms.

Powder XRD data were collected on the Bruker D8 ADVANCE diffractometer. A series of 20 minute scans were recorded from 5 to 60° $2\theta$ with a step size of 0.014° $2\theta$ while cooling the diffractometer from 295 to 12 K at a rate of 15 K per hour. Data processing and analysis were carried out using the TOPAS Academic software.[18]

The dynamics of 35DBNA were investigated using the VASP DFT code.[19, 20] PAW pseudopotentials in combination with the PBE functional were used, giving an energy cutoff of 700 eV.[21] Geometry optimisation was used to determine the initial structure for AIMD simulations. The simulations presented here were obtained in the NVT ensemble, with a range of temperatures between 30 and 400 K being employed. A time step of 1 fs and a total simulation time of 10 ps were used in each case. The *k*-point spacing was typically 0.1 Å$^{-1}$.

### 6.1.2  Results and Discussion

Single crystal XRD data were collected at four temperatures between 100 and 300 K in order to observe any structural features suggesting a change in the proton position. The changes in the lengths of the important short hydrogen bonds as a function of temperature are shown in Figure 6.4, while the donor-acceptor distances in the short N1···O4 and the normal O2···O3 bond lengths are shown in Figure 6.5.
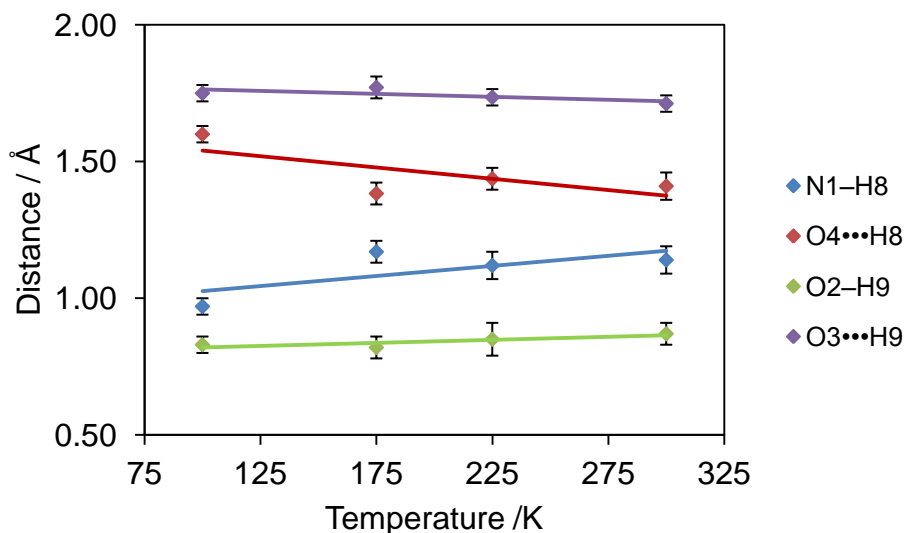
*Figure 6.4: Temperature dependence of N1H8, O4H8, O2H9 and O3H9 obtained from single crystal XRD.*
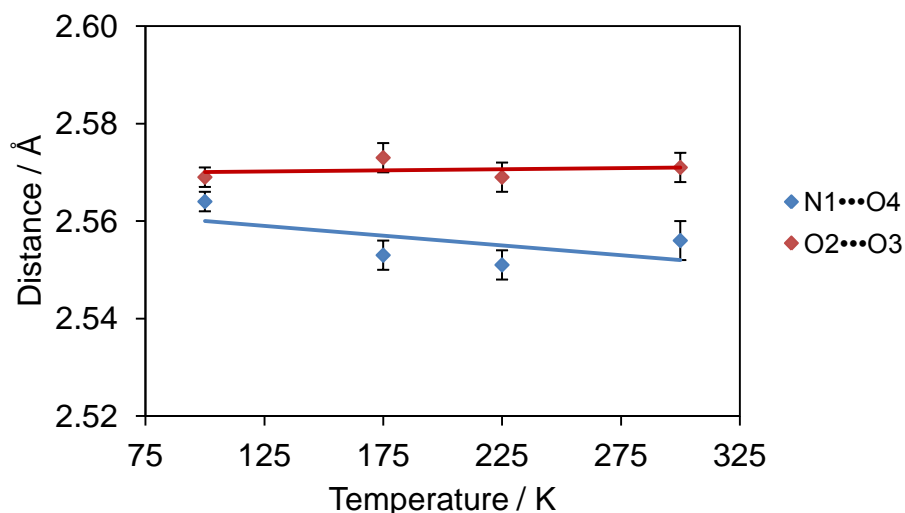


*Figure 6.5: Temperature dependence of N1O4 and O2O3 distances obtained from single crystal XRD.*

The parameters shown in Figure 6.4 suggest that the two hydrogen bonds in 35DBNA behave differently as a function of temperature. The O2···H9 and O3···H9 bond lengths in the normal O···O hydrogen bond remain unchanged. In contrast, the N1···H8 and O4···H8 bond lengths in the short N···O interaction seem to increase and decrease, respectively, between 100 and 300 K. In both cases, the donor-acceptor distances (N1···O4 and O2···O3) do not change significantly with increasing temperature, with

corresponding gradients of 0.00000(2) and -0.00004(4), respectively, suggesting that any changes in the O4···H8 and N1···H8 bond lengths are not simply a result of thermal expansion of the N1···O4 distance.

Although single crystal XRD data appear to suggest some temperature-induced proton migration within the short N1–H8···O4 hydrogen bond, the retrieval of accurate hydrogen atom positions and hence hydrogen bond information from XRD data should be interpreted with caution. Subtle structural changes involving hydrogen atoms (such as proton ordering in short hydrogen bonds) can, however, manifest themselves as subtle changes in the unit cell parameter trends obtained from VT powder XRD. A pure polycrystalline sample of 35DBNA was analysed by powder XRD between room temperature and 12 K to determine the unit cell parameter trends as a function of temperature and also to obtain accurate unit cell parameters to use with single crystal neutron Laue diffraction data.
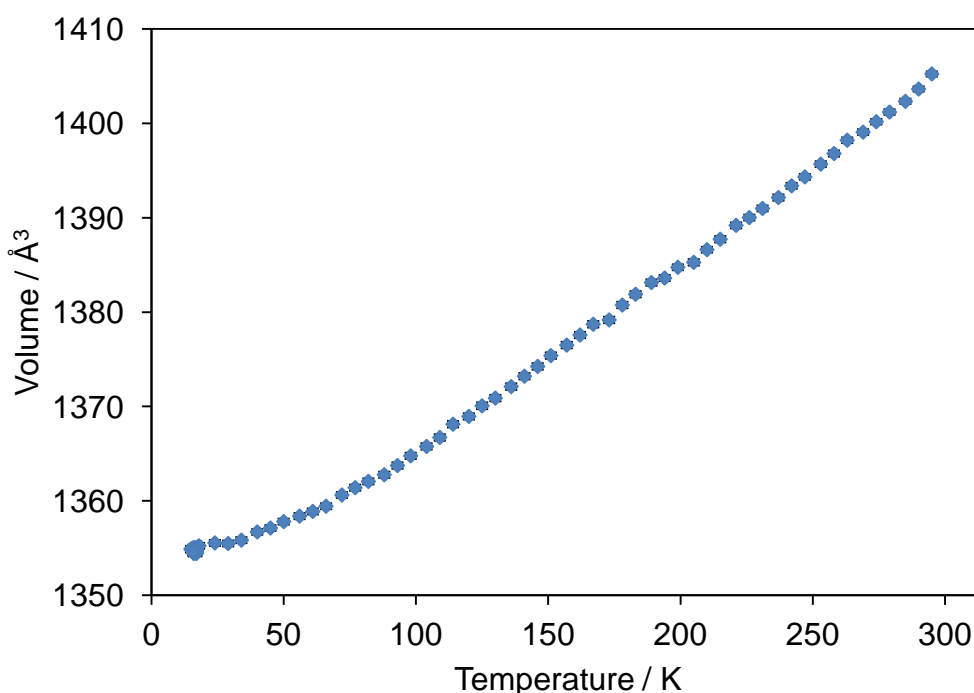


*Figure 6.6: Temperature dependence of the unit cell volume for 35DBNA obtained from powder XRD.*

Data were analysed by Rietveld refinement, in which the fractional atomic coordinates obtained from single crystal work at room temperature were kept fixed and the

parameters refined included the unit cell parameters, an overall isotropic temperature factor, sample height displacement, 6 terms to model the background contribution and 4 peak shape function parameters. The unit cell parameters vary smoothly with temperature, showing only the expected thermal expansion (Figure 6.6), suggesting the absence of a crystallographic phase transition. It should be noted, however, that the absence of any clear changes in the unit cell parameter trends does not necessarily rule out the possibility of proton migration occurring, as evidenced by the example of *h*-35PDCA (Chapter 3).

In order to obtain accurate hydrogen atom positions and determine reliably the extent of any temperature-induced proton migration, the crystal structure of 35DBNA was refined from single crystal neutron diffraction at 30 and 300 K. The crystallographic details are summarised in Table 6.1 and the structures are shown in Figure 6.7.

Since only ratios between unit cell dimensions can be determined in the white-beam Laue technique, it is necessary to use cell dimensions found by some other means; in this case, cell parameters determined from VT powder XRD were used.

*Table 6.1: Crystallographic details for 35DBNA at 30 and 300 K.*

|  | 30 K | 300 K |
|---|---|---|
| Chemical Formula | $C_{13}H_9N_3O_8$ | $C_{13}H_9N_3O_8$ |
| $M_r$ | 335.23 | 335.23 |
| Cell setting, space group | Monoclinic, $P12_1/n1$ | Monoclinic, $P12_1/n1$ |
| $a$ /Å | 14.061(6) | 14.126(6) |
| $b$ /Å | 5.039(2) | 5.071(2) |
| $c$ /Å | 19.598(8) | 20.163(8) |
| $\beta$ /° | 102.641(8) | 103.469(8) |
| $V$ /Å$^3$ | 1354(1) | 1405(1) |
| $Z$ | 4 | 4 |
| Data collection method | Laue method | Laue method |
| No. of measured and independent reflections | 9732, 2520 | 7737, 2085 |
| $R_{int}$ | 0.291 | 0.312 |
| $R[F^2 > 4\sigma(F^2)]$, $wR(F^2)$ | 0.125, 0.306 | 0.162, 0.364 |
| No. of reflections | 2520 | 2085 |
| No. of parameters | 298 | 298 |

30 K

(a)
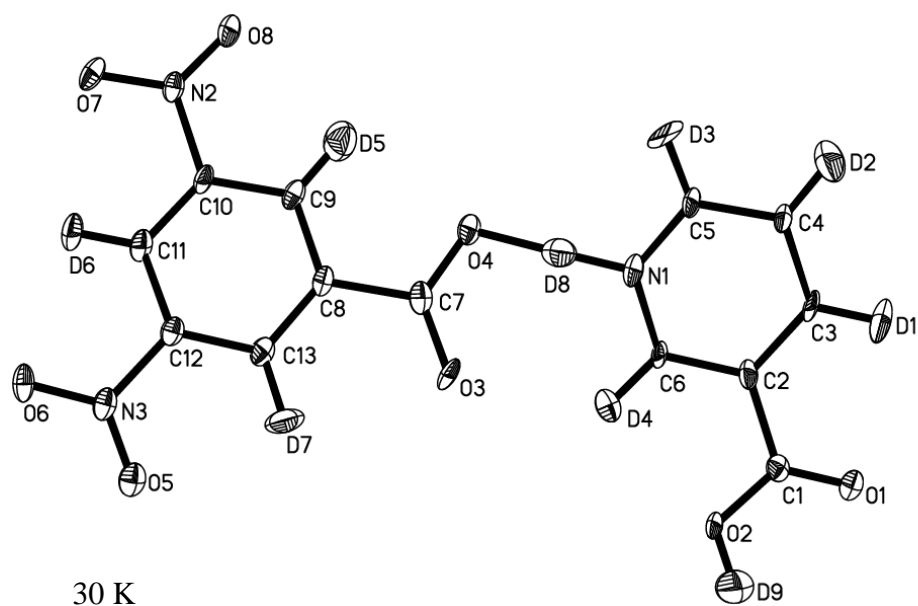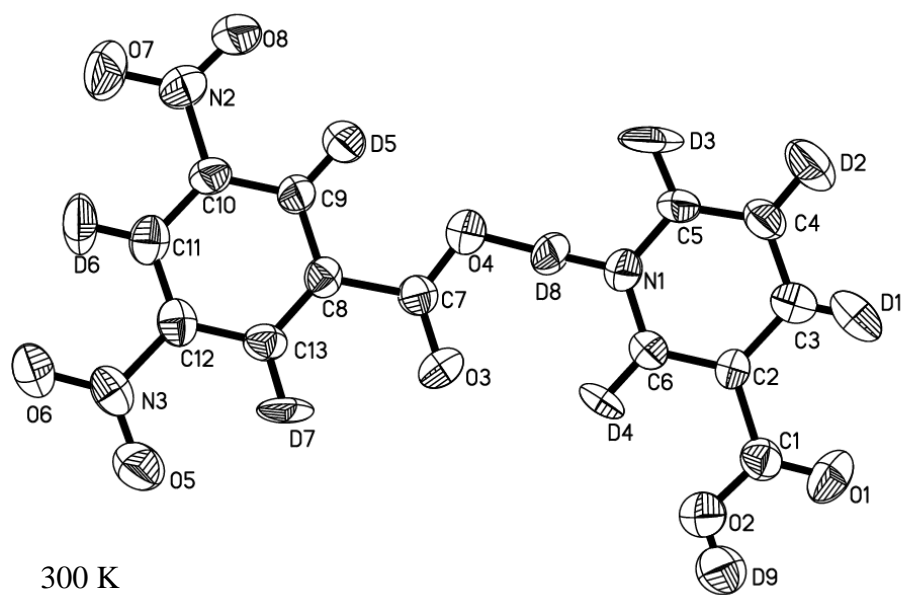


300 K

(b)

*Figure 6.7: The structure of 35DBNA, as determined by single crystal neutron diffraction at a) 30 K and b) 300 K. Hydrogen atoms have been labelled as D for refinement purposes and ADPs are drawn at the 50 % probability level.*

*Table 6.2: Hydrogen bond parameters obtained by single crystal neutron diffraction.*

|  | 30 K | 300 K |
|---|---|---|
| **O4N1 distance/Å** | 2.57(2) | 2.55(2) |
| **O4H8 distance/Å** | 1.42(1) | 1.38(2) |
| **H8N1 distance/Å** | 1.16(1) | 1.18(2) |
| **O2O3 distance/Å** | 2.58(1) | 2.58(1) |
| **O2H9 distance/Å** | 1.02(2) | 0.95(4) |
| **H9O3 distance/Å** | 1.59(2) | 1.64(2) |

The relevant hydrogen bond parameters determined by single crystal neutron diffraction at 30 and 300 K are summarised in Table 6.2. The N1–H8 distances at 30 and 300 K show that the proton is closer to the nitrogen atom throughout this temperature range, in agreement with the X-ray work. Although there may be a small amount of proton migration, H8 does not transfer from one side of the hydrogen bond to the other. The hydrogen bond asymmetry, Δ, calculated as the difference between the non-bonded O4···H8 and bonded N1–H8 distances,[22] is 0.23 at 30 K and 0.20 at 300 K, suggesting a slight migration of the proton to a more central position in the hydrogen bond at higher temperature. The change in the asymmetry value is, therefore, 0.03, and is small compared to those systems in which prominent proton migration has been found over the same temperature range (0.188 for *h*-35PDCA,[23] 0.601 for *d*-35PDCA and 0.180 for BTA-BPY[24]), further suggesting a lack of significant proton migration in the present compound.

Overall, the two-temperature diffraction study of 35DBNA at 30 and 300 K suggests that the hydrogen atom (H8) may migrate to a slightly more central position in the short hydrogen bond with increasing temperature.
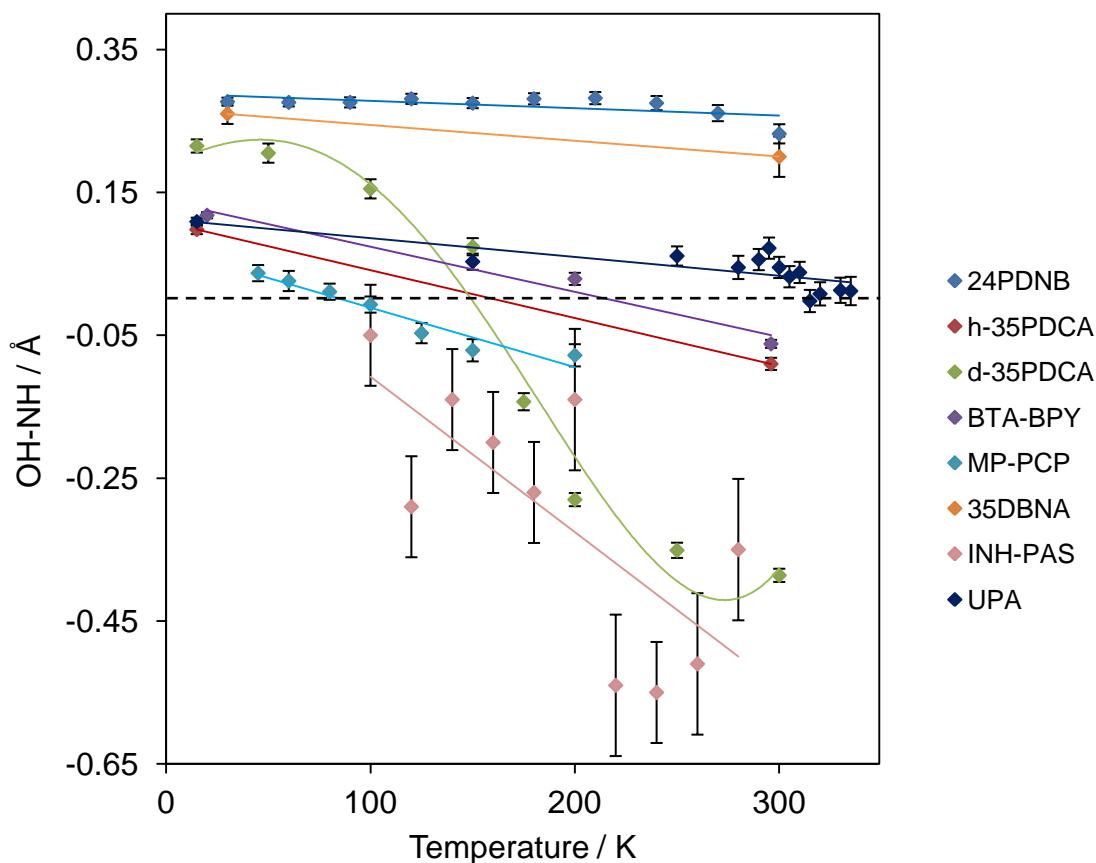
*Figure 6.8: Comparison of the temperature dependence of various SSHB OH and NH distances, where 24PDNB is pyridinium 2,4-dinitrobenzoate,[25] h-35PDCA is fully protonated 3,5-pyridinedicarboxylic acid,[23] d-35PDCA is fully deuterated 3,5-pyridinedicarboxylic acid,[26] BTA-BPY is 1,2,3,4-tetracarboxylic acid-4,4'-bipyridyl,[24] MP-PCP is 4-methylpyridine-pentachlorophenol,[27] 35DBNA is 3,5-dinitrobenzoic acid-nicotinic acid (this work), INH-PAS is isoniazid-4-aminosalicylic acid[28] and UPA is urea-phosphoric acid.[29, 30] A dashed line is drawn at y=0 for reference. Lines of best fit have been added as guides to the eye for all compounds except d-35PDCA; for d-35PDCA a polynomial has been added as a guide to the eye.*

The asymmetry values for 35DBNA, discussed previously, have been plotted for visual comparison with similar SSHB systems for which temperature-dependent proton migration is known (Figure 6.8). These are predominantly compounds with N···O hydrogen bonds; however, the O···O hydrogen bond of UPA has been included for completeness. The steeper the line of best fit for each compound, shown in Figure 6.8, the greater the extent of proton migration; migration through the centre of the hydrogen

bond is shown by the line of best fit crossing $y=0$ (see dashed line in Figure 6.8). It can be seen that, among the listed compounds, the greatest migration is observed for *d*-35PDCA and the lowest for 2,4-dinitrobenzoate (24PDNB).[25] Given the similar gradients, the extent of migration in 35DBNA seems to be similar to that of UPA, but in 35DBNA the proton is found in a much more asymmetric position in the hydrogen bond throughout the temperature range studied. However, this conclusion is made based on only two experimental data points for 35DBNA and therefore this compound has been further studied by computational methods.

Computational studies, using molecular dynamics simulations (MD), were used to complement the work on 35DBNA. The starting structure used for these MD simulations was the geometry optimised structure, in which the residual forces on the atoms were close to zero. In this structure the H8 atom was located at the donor nitrogen atom (N1), with N1–H8 and O4···H8 distances of 1.134 and 1.409 Å, respectively; the donor-acceptor distance, N1···O4, was 2.542 Å. All of these distances are slightly shorter than those observed experimentally.

MD simulations were undertaken, using the geometry optimised structure, at 15, 100, 200, 250, 300 and 400 K. The variation in the N1–H8, O4···H8, O2–H9 and O3···H9 bond lengths over the course of the trajectory were then output using a local routine. The bond lengths are plotted as a function of frame number (time/fs) in Figure 6.9.

The plots in Figure 6.9 show, qualitatively, the presence or absence of proton migration in 35DBNA, 35PDCA and 3,4-pyridinedicarboxylic acid (34PDCA). For example, in Figure 6.9b, a proton hops from one side of the hydrogen bond to the other where the NH and OH bonds (blue and red lines, respectively) cross. In this case, the length of the OH bond becomes shorter than that of the NH bond, *i.e.* we have an O4–H8 bond and an N1···H8 bond. It can be seen that at 15 K no proton hopping occurs between the O4 and N1 atoms, (Figure 6.9a); however, at 400 K, proton hopping is present (Figure 6.9b). The possibility that this is simply a thermal effect of the increased temperature is ruled out by the lack of proton hopping in the normal O2–H9···O3 hydrogen bond, despite the increased temperature (Figure 6.9c and 6.9d). Additionally, a comparison has been made with two extreme situations; the N1–H5···O4 bond in 35PDCA at 400 K (Figure 6.9e) in which a significant proton migration is observed experimentally,[26] and

the O1–H4···O3 bond in 34PDCA at 400K (Figure 6.9f) in which no migration is observed experimentally.[31] It is clear that the effect in the N1···H8 of 35DBNA (Figure 6.9c) is intermediate between these two extremes.

In addition, Figure 6.9 demonstrates how this method of calculation can be used to predict proton migration in compounds before attempting the collection of experimental data. As discussed by Fontaine-Vive *et al.*,[32] MD simulations such as this show the same effect as seen in neutron diffraction, although usually to a lesser extent, providing the DFT geometry optimisation method allows the hydrogen bond geometry to be accurately determined.

The average amount of time that the H8 proton spends at the O4 atom in 35DBNA was calculated as a function of temperature and the results of this quantitative analysis are shown in Figure 6.10. It can be seen that this value increases smoothly as a function of temperature; however, it seems that the proton cannot be stabilised on the O4 atom for any significant period, spending an average of only 8 % of the time in this position at 400 K (compared to approximately 50 % for 35PDCA and 0 % for 34PDCA).
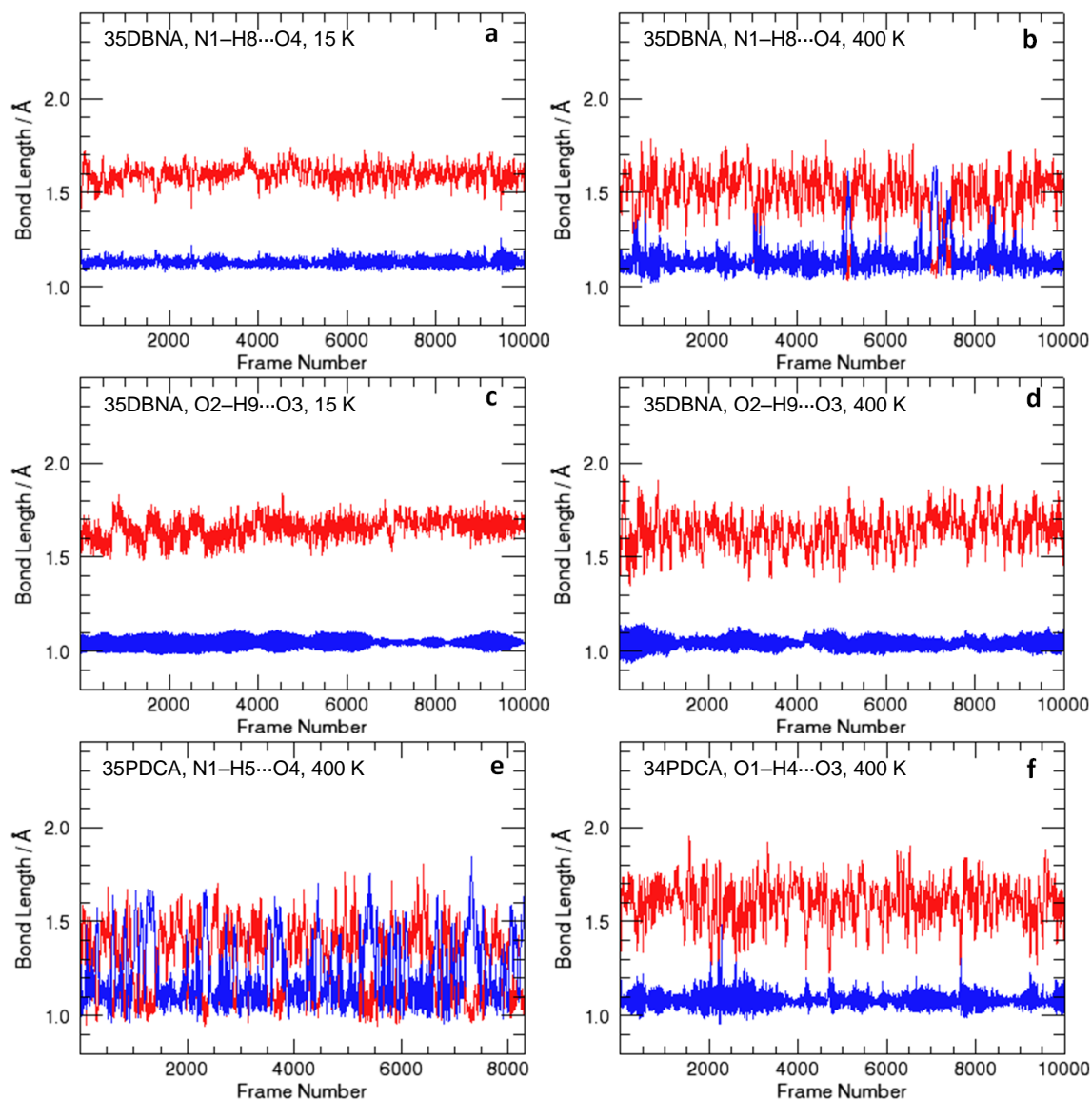
*Figure 6.9: (Top) N1–H8 (blue) and O4···H8 (red) at a) 15K and at b) 400K in 35DBNA. (Centre): O2–H9 (blue) and O3···H9 (red) at c) 15K and d) 400 K in 35DBNA. (Bottom): e) N1–H5 (blue) and O4···H5 (red) at 400K in 35PDCA and f) O1–H4 (blue) and O3···H4 (red) at 400K in 34PDCA.*
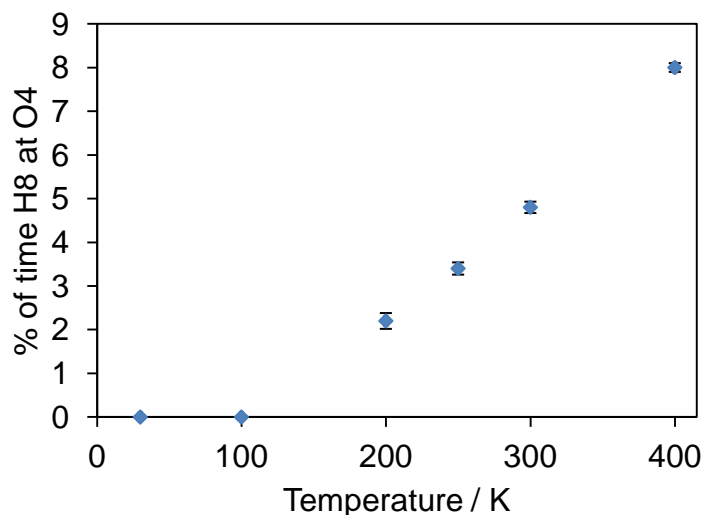
*Figure 6.10: The temperature dependence of the % of time that the H8 proton spends at the O4 atom.*

In conclusion, neutron diffraction studies suggest that the proton in the SSHB of 35DBNA migrates slightly with temperature, from a position closer to the donor nitrogen atom at 30 K, to a position closer to the acceptor oxygen atom at 300 K; however, no migration through the centre of the hydrogen bond, analogous to that in 35PDCA, is observed. MD simulations show a number of instantaneous proton hops from the donor to the acceptor atom over the course of a trajectory, resulting in the H8 proton spending an average of 8 % of its time at the oxygen atom at 400 K. Finally, the predictive power of such simulations, for determining whether or not proton migration might be exhibited by a compound, before the collection of experimental data, has been shown.

## 6.2  4-Aminobenzoic Acid – Nicotinic Acid (2:1)

4-aminobenzoic acid (4AB) and nicotinic acid (NA), Figure 6.11, co-crystallise to form an adduct (4ABNA, CSD Refcode: SESLIM), the structure of which was first reported by Jebas *et al*. using XRD analysis at room temperature only.[4]
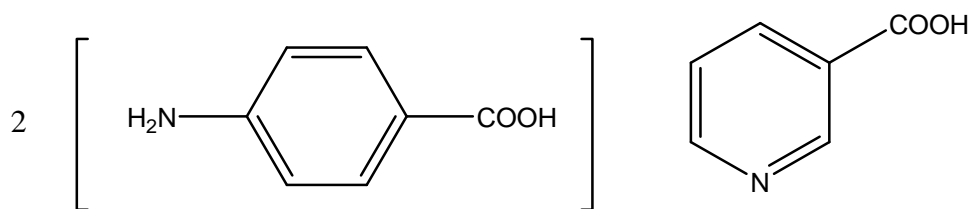
*Figure 6.11: The components of 4ABNA: 4-aminobenzoic acid (4AB, left) and nicotinic acid (NA, right).*

4ABNA crystallises in the monoclinic space group *Cc* and is stabilised by an extensive network of N–H···O, O–H···O and O–H···N hydrogen bonds. The NA molecules form infinite chains perpendicular to the *a* axis, linked by short N···H–O bonds with donor-acceptor distances of 2.548 Å at 303 K. This is analogous to the situation in 35PDCA in which infinite hydrogen-bonded chains are also present, stabilised by a SSHB, with the proton in the SSHB found in an asymmetric position closer to the oxygen atom at room temperature. In contrast to 35PDCA, however, a second species, 4AB, is also present in 4ABNA. Amongst NA chains, 4AB molecules form a network of chains, stabilised by long N–H···O and normal O–H···O hydrogen bonds (with donor-acceptor distances of 2.930 and 2.619 Å, respectively), which criss-cross each other; long N–H···O bonds also exist between the independent NA and 4AB chains, stabilising the overall structure. The SSHB in 4ABNA is given in Figure 6.12 and the complex packing within 4ABNA is shown in Figure 6.13.
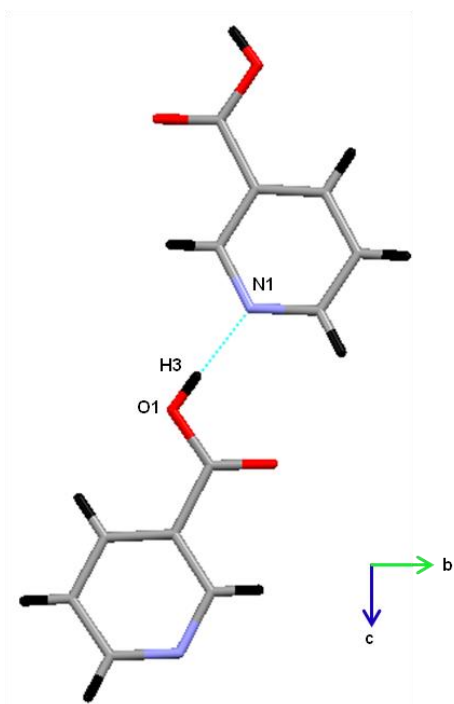
*Figure 6.12: The SSHB in 4ABNA, viewed down the a axis. The 4-aminobenzoic acid molecules have been omitted for clarity. (Blue: nitrogen, red: oxygen, grey: carbon and black: hydrogen).*
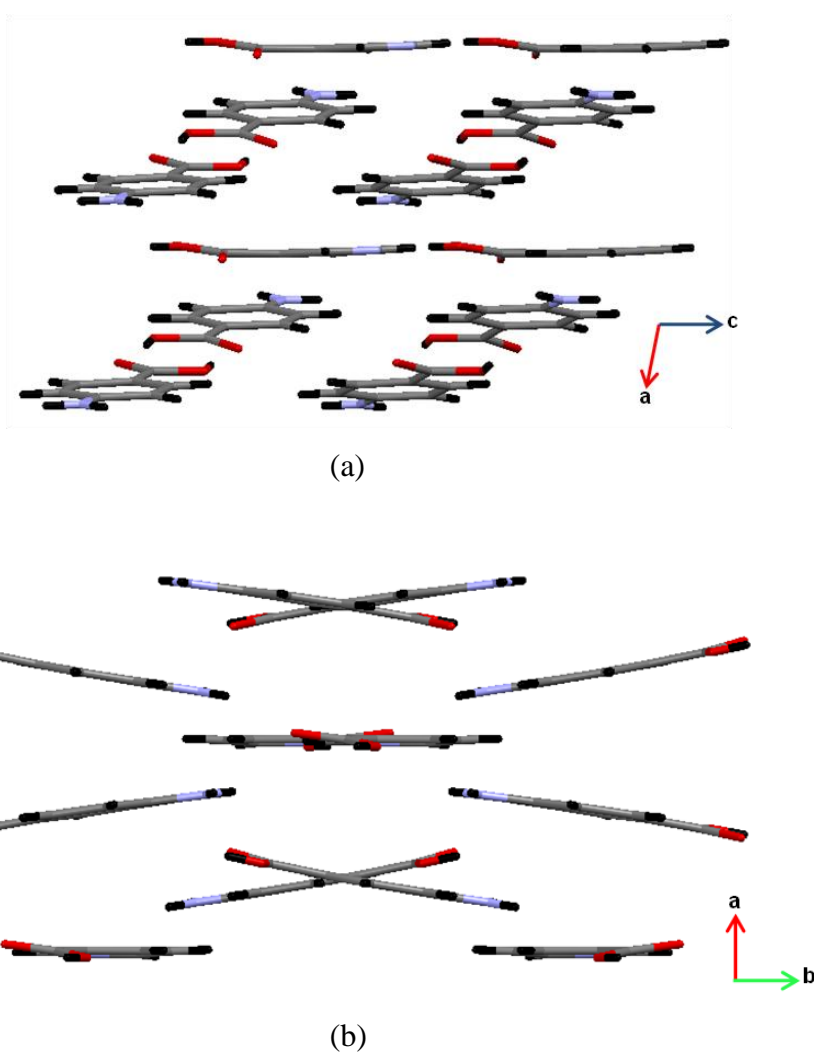
(a)



(b)

*Figure 6.13: The packing in 4ABNA, viewed down a) the b axis and b) the c axis. In each case, hydrogen atoms are drawn in black, nitrogen atoms in blue, carbon atoms in grey and oxygen atoms in red.*

In this section the structures of 4ABNA, determined from single crystal XRD data at 120 and 300 K, are reported. Complementary DFT simulations, which were used to guide and enhance the conclusions from experiments, are also presented.

## 6.2.1  Experimental Details

Following an initial solubility screen with a range of solvents, the method of Jebas *et al.* was adopted for the preparation of the 4-aminobenzoic acid-nicotinic acid co-crystal in solution.[4] The starting reagents, 4-aminobenzoic acid (0.0223 g, 0.16 mmol, Aldrich, 99 %) and nicotinic acid (0.010 g, 0.08 mmol, Aldrich, 98 %), used as received without

196

further purification, were dissolved in a minimum amount of ethanol and warmed in a water bath for 2 hours. This was then transferred to a small vial and sealed with a cap containing four small apertures. Pale yellow crystals were obtained after three weeks *via* slow evaporation of the solvent.

A number of suitable single crystals were found and tested on the Bruker SMART 1000 diffractometer in perfluoropolyether oil at 120 K. After successful identification of the unit cell in each case, an approximately cuboid-shaped crystal, measuring $0.20 \times 0.22 \times 0.46 \text{ mm}^3$, was then mounted in superglue. A full sphere of data was collected by a series of $\omega$ scans, using a frame width of $0.3°$ in $\omega$ and a time of 20 seconds per step. This was then repeated at 300 K.

The data were processed as described in Section 2.3.1.1 and structure refinement on $F^2$ was carried out at all temperatures using CRYSTALS.[10] Atomic coordinates and anisotropic displacement parameters were refined for all non-hydrogen atoms. All hydrogen atoms except H3 (that in the SSHB) were located geometrically and treated using a riding model. The hydrogen atom in the SSHB, H3, was located using Fourier difference maps and its atomic position refined; a three parameter weighting scheme was also used.

A small quantity of the sample was ground up and prepared for powder XRD as described in Section 2.2.1.4. Patterns were recorded on the Bruker D8 ADVANCE diffractometer from 5 to $60°$ $2\theta$ with a step size of $0.014°$ $2\theta$. Rietveld refinement was then carried out in TOPAS Academic. A total of 55 parameters were refined, including 8 coefficients of a Chebyschev polynomial to model the background, a zero point error, 4 lattice parameters for each phase, 3 parameters to describe the isotropic thermal displacement of the atoms (1 for each phase) and 4 parameters to define the TCHZ peak shape for each phase; a $4^{\text{th}}$ order spherical harmonic function was also used to correct for preferred orientation.

The dynamics of 4ABNA were investigated using the VASP DFT code.[19, 20] PAW pseudopotentials in combination with the PBE functional were used, giving an energy cutoff of 700 eV.[21] Geometry optimisation of the structure obtained from single crystal XRD at 300 K was used to determine the initial structure for AIMD simulations. The

simulations presented here were obtained in the NVT ensemble, with temperatures of 120 and 400 K being employed. A time step of 1 fs and a total simulation time of 1 ps were used in each case. The *k*-point spacing was typically 0.1 $Å^{-1}$.

## 6.2.2  Results and Discussion

Single crystal XRD data were collected on 4ABNA at 120 and 300 K in order to observe any structural features suggesting a change in the proton position. A summary of the crystallographic data is given in Table 6.3, and the various bond lengths of interest are summarised in Table 6.4. The structures obtained from data collected at 120 and 300 K are shown in Figure 6.14.

*Table 6.3: Crystallographic data for the single crystal XRD structure of 4ABNA at 120 and 300 K.*

|  | 120 K | 300 K |
|---|---|---|
| Chemical formula | $C_{20}H_{19}N_3O_6$ | $C_{20}H_{19}N_3O_6$ |
| $M_r$ | 397.39 | 397.39 |
| Cell setting, space group | Monoclinic, *C*1*c*1 | Monoclinic, *C*1*c*1 |
| *a*/Å | 9.9320 (5) | 10.1820 (8) |
| *b*/Å | 13.7476 (7) | 13.7773 (11) |
| *c*/Å | 13.6449 (7) | 13.6462 (11) |
| β/° | 99.9590 (10) | 99.738 (2) |
| *V*/$Å^3$ | 1835.02 (16) | 1886.7 (3) |
| *Z* | 4 | 4 |
| No. of measured and independent reflections | 13868, 2668 | 14255, 2743 |
| $R_{int}$ | 0.031 | 0.031 |
| $R[F^2 > 2\sigma(F^2)]$, $wR(F^2)$, $S$ | 0.062, 0.092, 1.03 | 0.057, 0.079, 1.02 |
| No. of parameters | 266 | 266 |

*Table 6.4: The selected bond lengths of interest at 120 and 300 K.*

|  | 120 K | 300 K |
|---|---|---|
| **N1O1 distance/Å** | 2.519(5) | 2.484(5) |
| **H3N1 distance/Å** | 0.91(3) | 1.08(4) |
| **O1H3 distance/Å** | 1.68(3) | 1.44(4) |
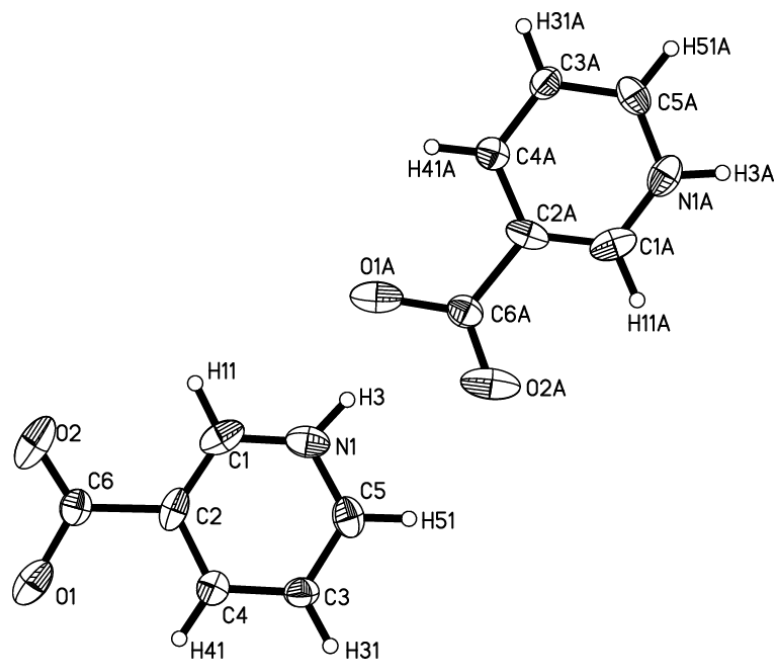
120 K



(a)

300 K
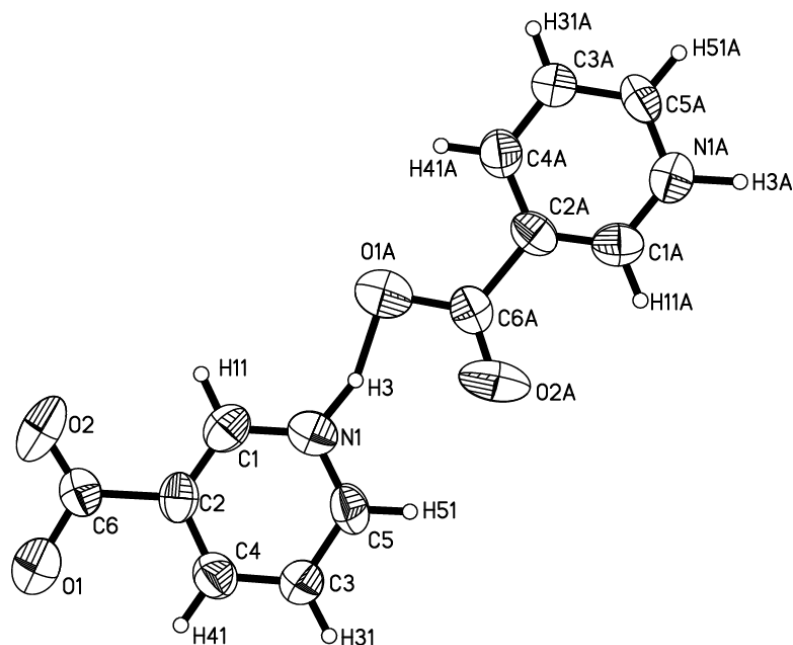


(b)

*Figure 6.14: The structure of 4ABNA, determined by single crystal XRD at a) 120 K and b) 300 K; in these structures the 4-aminobenzoic acid molecules have been omitted for clarity and ADPs are plotted at the 50 % probability level.*

As expected, the lattice parameters and cell volume increase as a function of temperature, with the largest change occurring in the *a* axis. This is the axis perpendicular to the layers, as shown in Figure 6.13b, which is not stabilised by hydrogen bonding. Therefore, as temperature is increased, this axis has more freedom to lengthen.

It appears that, although the proton seems to migrate along the hydrogen bond slightly, from a position very close to the nitrogen atom (N1) at 120 K ($\Delta = 0.77$) to a more central position in the bond at 300 K ($\Delta = 0.36$), it remains in an asymmetric position closer to N1 at both temperatures; this is contrary to the original literature which states that the proton is located at the oxygen atom (O1) at 303 K. However, as can be seen in Table 6.4, the errors on the current N–H and O···H distances are large and therefore these results may be unreliable. Additionally, it may simply be the large change in the actual N···O distance (from 2.519(5) at 120 K to 2.482(5) Å at 300 K) that is aiding or causing this large change in asymmetry values.

The donor-acceptor (N1···O1) distance resulting from the work at 300 K is much shorter than that reported in the original literature (this work, 2.482(5) Å at 300 K, compared to previous work, 2.548 Å at 303 K, with no error given[4]). It is also much shorter than that obtained in the current work at 120 K (2.519(5) Å). In addition, optimisation of the current high temperature structure in CASTEP resulted in a donor-acceptor distance of 2.580 Å, which is much closer to the original literature value of 2.548 Å. However, the small errors obtained for the N1···O1 distances in the current work indicate that these results are reliable, despite the possible unreliability of the bond distances to H3, making this one of the shortest N–H···O hydrogen bonds that exists, see Figure 1.1b of Chapter 1.

The refinements themselves were tentative, with small changes in the weighting used having a large effect on the proton position, particularly for the data collected at 300 K. In this case, it was more sensible to study the Fourier difference maps, Figure 6.15.[33]
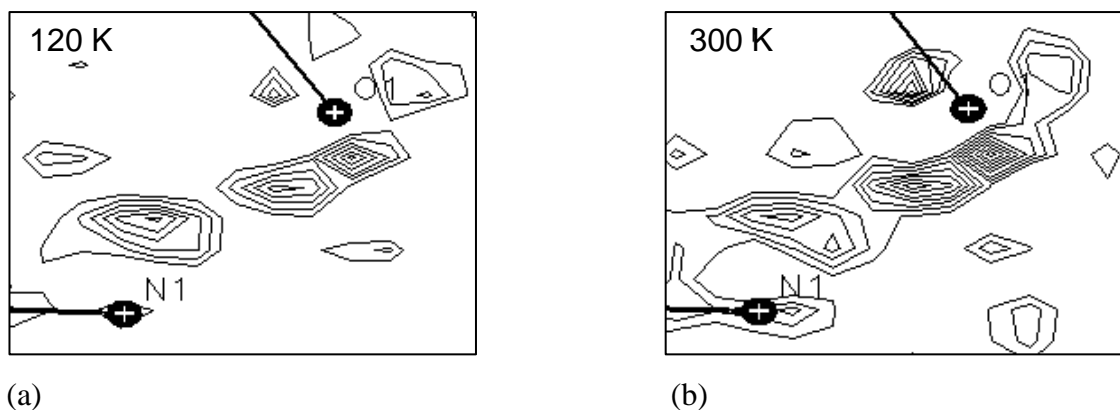
(a)                                        (b)

*Figure 6.15: Fourier difference maps ($F_o$-$F_c$) for the bond of interest, obtained from single crystal XRD at a) 120 K and b) 300 K. For the calculation of each map the hydrogen atom of interest (H3) was removed.*

The Fourier difference maps, Figure 6.15, do not show a well-defined single area of electron density between the O1 and N1 atoms but, in fact, show two maxima for the hydrogen atom, one closer to O1 and one closer to N1 at both temperatures. This suggests that proton disorder is present in this compound and may also explain the difficulties in the refinement. Although the positions of these maxima appear to be invariant as a function of temperature, the contours suggest that at 300 K the proton occupancy is greater closer to O1. However, it was not possible to obtain a converged refinement with the proton in this position. In order to accurately locate the hydrogen atom positions and occupancies and, hence, make a definitive conclusion about its temperature-dependent behaviour in this compound, neutron diffraction would be required; it has not been possible to isolate crystals large enough for analysis by this technique.

An attempt was made to further analyse 4ABNA by VT powder XRD, in order to determine the effects of continuous temperature changes on the structure. An example Rietveld profile, Figure 6.16, shows the poor quality of the polycrystalline material, demonstrated by the very poor fit of the calculated pattern (red) to the experimental data (blue). Much of the starting materials remain present and, in addition, there appear to be further unidentified impurities, possibly as a result of solvent crystallisation. A number of repeats of this synthesis have resulted in similar mixtures and therefore it has not been possible to carry out a VT powder XRD experiment on a pure sample.
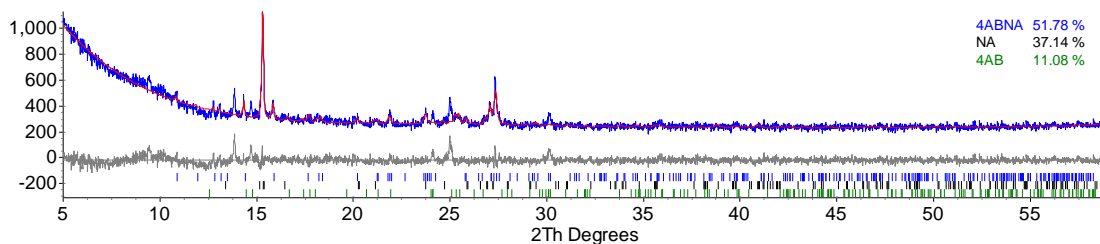
*Figure 6.16: The Rietveld fit of SESLIM in scan d9_03225. The calculated structure is shown in red, the experimental data in blue and the difference between these shown as a difference plot in grey.*

Computational studies were used to determine whether or not proton hopping occurs in 4ABNA. The room temperature structure obtained from single crystal XRD was optimised, resulting in the residual forces on the atoms being close to zero. In this optimised structure the H3 atom resides at the nitrogen atom (N1), as would be expected based on the, albeit poor, conclusions from the diffraction data collected at 300 K. The optimised N···O distance of 2.580 Å is much longer than that observed experimentally. MD simulations were undertaken at 120 and 400 K. The variations in the N1–H3 and O1···H3 bond lengths over the course of the trajectory were then output and plotted as a function of frame number (time/fs), Figure 6.17.

In Figure 6.17, the blue lines represent the variation of the N1–H3 bond length with time, and the red the variation of the O1···H3 bond length with time. Proton hopping, where the proton moves from one side of the hydrogen bond to the other, would be represented by the overlapping of these lines. It can be seen that in 1 ps, at both 120 and 400 K, no proton hopping occurs (Figure 6.17a and 6.17b, respectively), suggesting that no proton migration is present in this compound. This may be realistic; however this lack of migration may be a result of the much larger N1···O1 separation of 2.580 Å obtained computationally compared to that obtained experimentally.
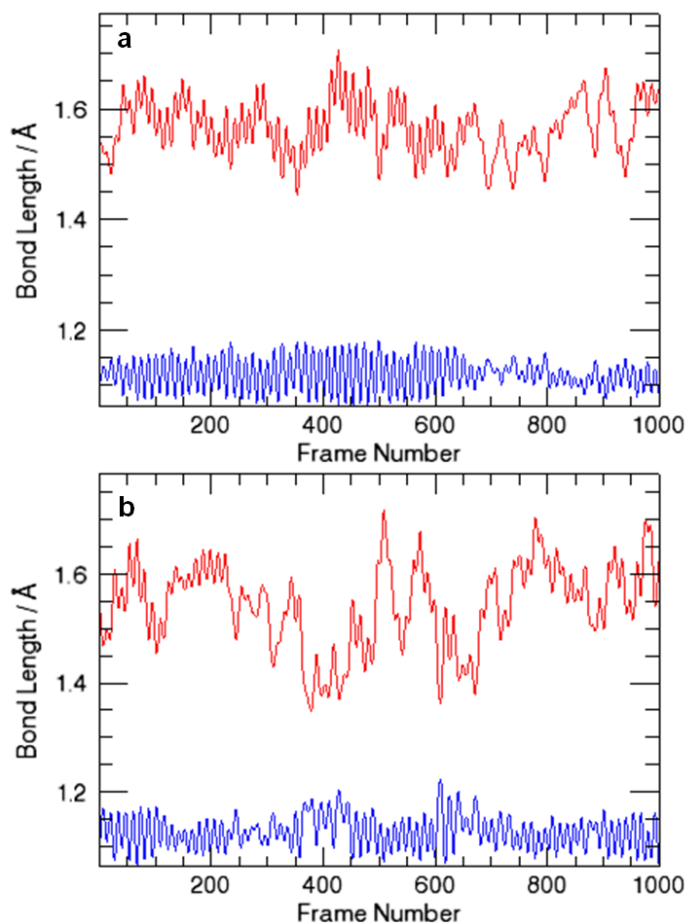
*Figure 6.17: N1–H3 (blue) and O1···H3 (red) over 1 ps at a) 120 K and b) 400 K.*

In summary, the structure of 4ABNA has been studied using single crystal XRD at 120 and 300 K. Extraction of the N1–H3 and O1···H3 bond distances shows a small migration of the H3 atom to a more central position in the hydrogen bond, but with no migration through the hydrogen bond centre. However, the errors on these distances are large and, as such, this conclusion is tentative. If this migration is in fact real it is likely that it is simply a result of the large changes in the donor-acceptor distance of the hydrogen bond itself. In contrast, Fourier difference maps show possible proton disorder to be present, explaining the refinement difficulties. MD simulations show that no migration occurs in this compound; however, as with UPA and 35PDCA[32, 34], the donor-acceptor distance was overestimated by this solid state DFT method and hence potential proton migration behaviour may be being suppressed.

It is apparent that current XRD results are inconclusive. However they do suggest the presence of potential proton disorder or migration. In addition, the donor-acceptor

distance of 2.48 Å obtained at 300 K makes this one of the shortest N–H···O hydrogen bonds that exists (see Figure 1.1 of Chapter 1). It is clear that these factors merit further study of this compound. The relevant hydrogen bond distances could be reliably achieved if large single crystals could be grown for use in single crystal neutron diffraction.

## 6.3  Benzimidazolium Hydrogen Phenylmalonate

A part of the work in this thesis has been focused on finding materials which show temperature-dependent proton migration behaviour analogous to that in 35PDCA. Another interesting temperature-dependent phenomenon is proton ordering in short hydrogen bonds and, in some cases, such ordering has been found to lead to ferroelectric phase transitions. This has been observed in many KDP-based hybrid organic-inorganic materials[35] and in other co-crystals containing disordered protons in phosphate groups. Recent structural studies on 2-aminopyridine dihydrogenphosphate ($\alpha$-2APP) at room temperature and 30 K show that the ferroelectric phase transition in this material is accompanied by an order-disorder phase transition involving protons in a short O···O (2.47 Å) hydrogen bond.[6] Benzimidazolium hydrogen phenylmalonate exhibits certain structural similarities with $\alpha$-2APP and therefore may also demonstrate a ferroelectric phase transition.

The room temperature crystal structure of benzimidazolium hydrogen phenylmalonate (BHPM, CSD Refcode: FONDES) was reported by Ueda *et al.*[5] This compound crystallises in the triclinic space group $P\bar{1}$ and is stabilised by a network of hydrogen bonding interactions. It consists of a 1:1 molar ratio of benzimidazolium cations and hydrogen phenylmalonate anions, Figure 6.18.
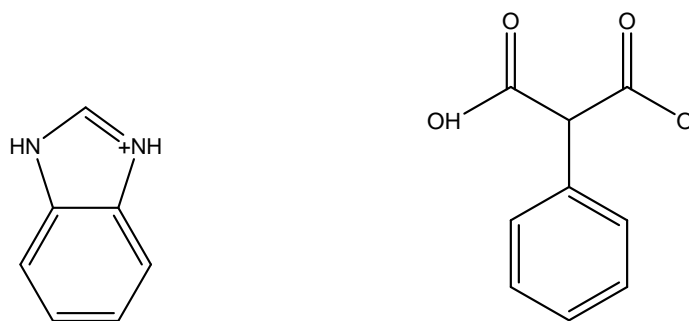
*Figure 6.18: The components of BHPM: the benzimidazolium ion (left) and the hydrogen phenylmalonate ion (left)*

In the structure of BHPM, Figures 6.19 and 6.20, hydrogen phenylmalonate anions, related by an inversion centre, are connected through short O···O hydrogen bonds (O1···O1' and O3···O3', of 2.504 and 2.494 Å, respectively) forming zigzag chains along [110].[5] It can be seen from the histogram in Chapter 1 (Figure 1.1a) that these are short. In these short hydrogen bonds, the hydrogen atoms (H1 and H3, respectively) are disordered over two sites. Benzimidazolium cations then connect to these anion chains, through normal N–H···O hydrogen bonds, forming layers extending perpendicular to them; additional hydrogen bonding interactions, namely C–H···O and C–H···$\pi$ bonds, exist within these layers, further stabilising the structure.

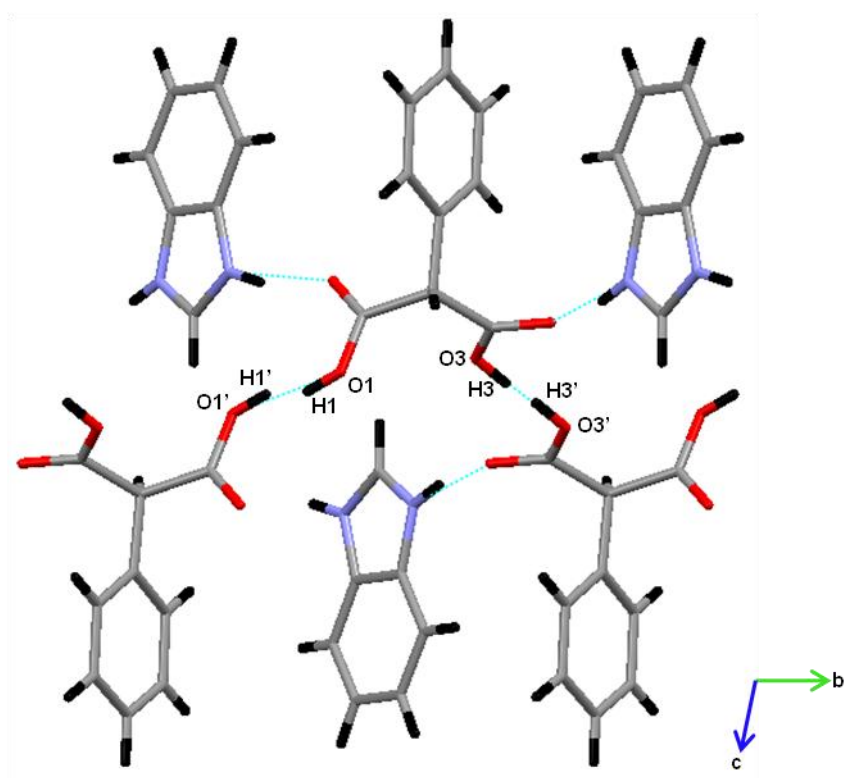*Figure 6.19: The packing in BHPM at room temperature, viewed down the a axis showing the bonding in the SSHBs;[5] the hydrogen atoms (H1 and H3) are disordered over two positions and, concurrently, each have an occupancy of 0.5. H1', O1', H3' and O3' are related to H1, O1, H3 and O3, respectively, by an inversion centre. Hydrogen is drawn in black, nitrogen in blue, carbon in grey and oxygen in red.*
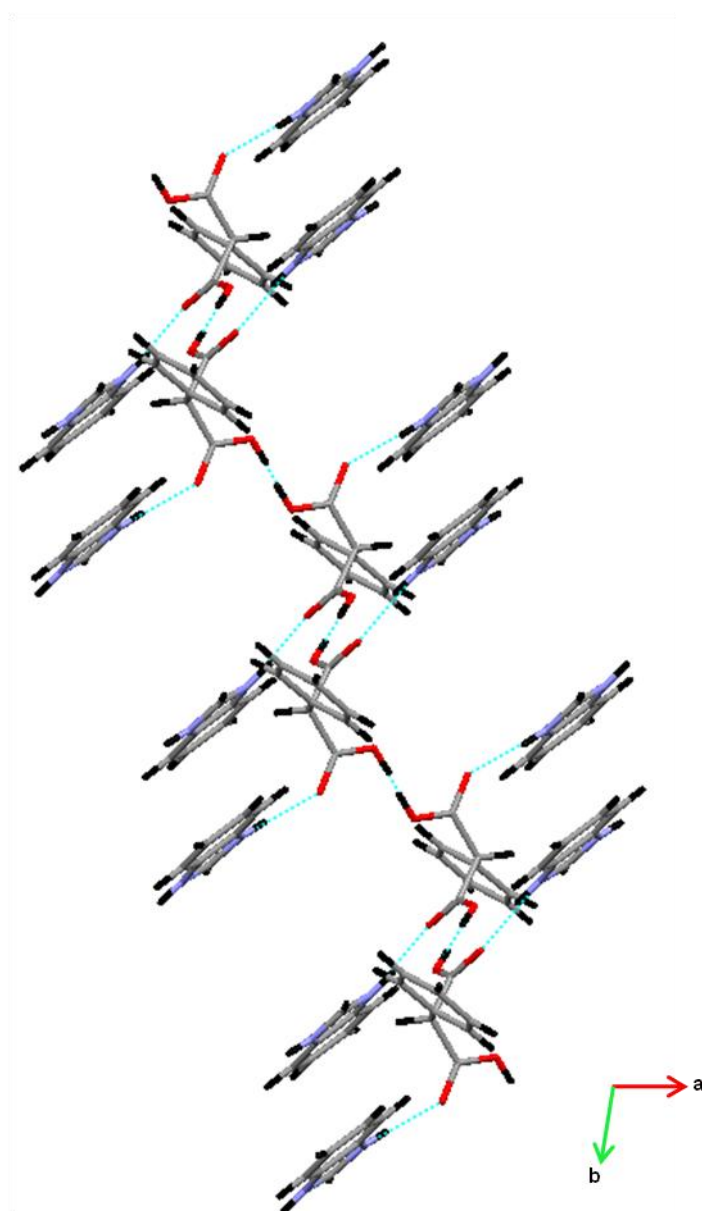
*Figure 6.20: The packing in BHPM at room temperature, as viewed down the c axis. A zigzag anion chain can be seen running through the centre, with the cations forming layers surrounding them. Hydrogen atoms are drawn in black, nitrogen atoms in blue, carbon atoms in grey and oxygen atoms in red.*

This disordered structure, as reported in the literature, is analogous to the high temperature form of $\alpha$-2APP,[6] which also exhibits protons located on sites around an inversion centre, in O⋯O hydrogen bonds of similar length. However, on cooling to 30 K, protons in $\alpha$-2APP order, adopting positions such that they become bonded to one of the oxygen atoms in the hydrogen bond, in a non-centrosymmetric polar

arrangement. Crystallographically, this is manifested as a structural phase transition from the centrosymmetric space group $C2/m$ at room temperature to its non-centrosymmetric polar subgroup $Cc$. BHPM is of interest due to its potential to exhibit proton ordering and a similar phase transition. The aim of this work was to study the structure of BHPM at various temperatures in order to determine whether such a phase transition is exhibited by this compound; various diffraction methods were used in order to determine whether proton ordering, and hence a possible transition to a non-centrosymmetric space group ($P1$), occurs in this compound at low temperature. The structures of BHPM, determined from single crystal neutron diffraction at 15 and 300 K, and supporting characterisation of this material by variable temperature single crystal and powder XRD, are reported in this section.

### 6.3.1 Experimental Details

Following an initial solubility screen with a range of solvents, a method was developed, based on that of Ueda *et al.*,[5] to successfully produce crystals of BHPM. The reagents, benzimidazole (0.0100 g, 0.085 mmol, Fluka, 98 %) and phenylmalonic acid (0.0143 g, 0.085 mmol, Aldrich, 98 %) were used as received without further purification. These were separately dissolved in a minimum amount of ethanol, before being transferred to the same vial and mixed. The vial was then sealed with a cap containing four small apertures. Colourless, rod-shaped crystals were obtained after a day *via* slow evaporation of the solvent.

A crystal measuring $0.06 \times 0.14 \times 0.28$ mm$^3$ was selected for single crystal XRD analysis. Data were collected at 120 K on the Bruker SMART 1000 diffractometer. A full sphere of data was collected by a series of $\omega$ scans, using a frame width of 0.3° in $\omega$ and an exposure time of 20 seconds per step. The raw data were collected using the SMART software and integrated using the SAINT suite of programs;[7-9] Structure refinement on $F^2$ was carried out using SHELXL.[16, 17] Atomic coordinates were refined for all atoms. All non-hydrogen atoms were refined anisotropically. Hydrogen atoms were located using Fourier difference maps and refined isotropically; a three parameter Chebyschev weighting scheme was also used.

A crystal measuring $0.3 \times 0.8 \times 2.7$ mm$^3$ was selected for single crystal neutron diffraction analysis. Single crystal neutron diffraction data were collected on VIVALDI at the ILL.[11] Data were collected at 15 and 300 K; ten diffraction patterns, each accumulated over six hours, were collected at each temperature with successive patterns distinguished by a rotation of 20° of the crystal perpendicular to the incident beam. The data were processed using the CCP4 Laue suite of programs.[12-15] Structure refinement on $F^2$ was carried out using SHELXL.[16, 17] Atomic coordinates and anisotropic displacement parameters were refined for all atoms.

Powder diffraction data were collected on the Bruker D8 ADVANCE diffractometer; an initial 20 minute scan at room temperature, to test the sample purity, was followed by a VT experiment from 300 to 12 K. For this, the sample was cooled at a rate of 15 K per hour using the PheniX and, simultaneously, a series of 20 minute scans were recorded from 5 to 60° $2\theta$ with a step size of 0.014° $2\theta$. Data processing and analysis were carried out using the TOPAS Academic software.[18]

### 6.3.2  Results and Discussion

Initially, single crystal XRD data were collected on BHPM at 120 K, and compared with literature data obtained at 300 K, in order to observe any structural features suggesting a change in the proton position. A summary of the crystallographic data is given in Table 6.5, and the various bond lengths of interest are summarised in Table 6.6, with the room temperature literature values listed for comparison. The low temperature structure is given in Figure 6.21.

*Table 6.5: Crystallographic data for the single crystal XRD structure of BHPM at 120 K.*

|  | 120 K |
|---|---|
| Chemical formula | $C_{16}H_{14}N_2O_4$ |
| $M_r$ | 298.3 |
| Crystal setting, space group | Triclinic, $P\bar{1}$ |
| Temperature/K | 120 |
| $a$/Å | 5.0736 (2) |
| $b$/Å | 9.1994 (4) |
| $c$/Å | 15.2015 (6) |
| $\alpha$/° | 102.164 (2) |
| $\beta$/° | 90.231 (2) |
| $\gamma$/° | 100.594 (2) |
| $V$/Å$^3$ | 681.09 (5) |
| $Z$ | 2 |
| No. measured and independent reflections | 8540, 3702 |
| $R_{int}$ | 0.038 |
| $R[F^2 > 2\sigma(F^2)]$, $wR(F^2)$, $S$ | 0.048, 0.145, 0.90 |
| No. of parameters | 254 |

*Table 6.6: A comparison of selected bond lengths of interest in BHPM from single crystal XRD at 120 K and literature values obtained at 298 K.[5] *Literature values.*

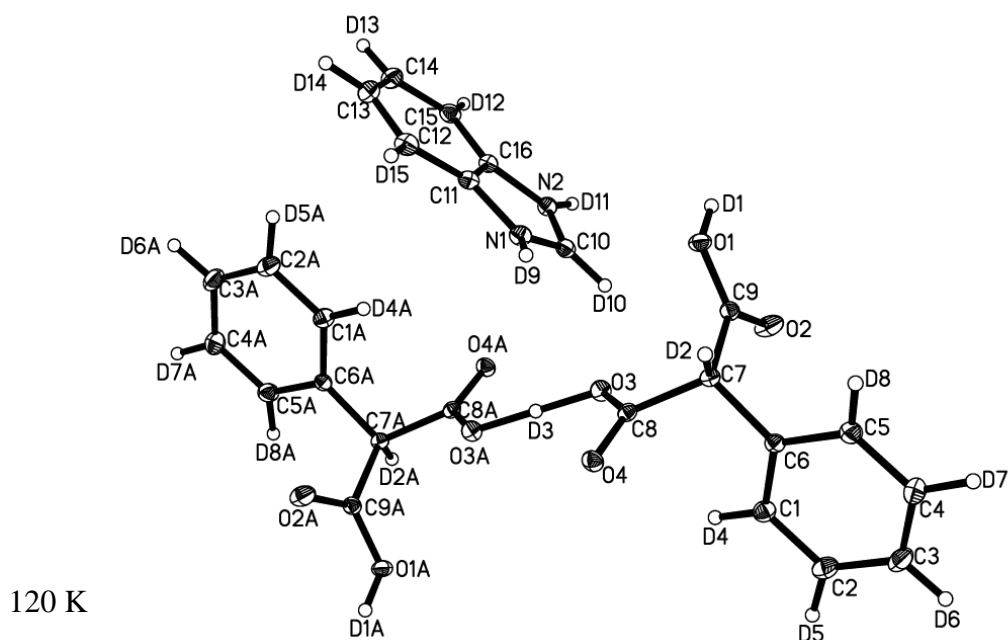|  | 120 K | 298 K* |
|---|---|---|
| **O1O1' distance/Å** | 2.488(1) | 2.504(3) |
| **O1H1 distance/Å** | 0.942(1) | 0.82(6) |
| **H1O1' distance/Å** | 1.554(1) | 1.70(7) |
| **O3O3' distance/Å** | 2.490(1) | 2.494(3) |
| **O3H3 distance/Å** | 1.245(1) | 0.87(6) |
| **H3O3' distance/Å** | 1.245(1) | 1.63 (6) |

*Figure 6.21: The single crystal XRD structure of BHPM, obtained from data collected at 120 K. All hydrogen atoms have been labelled as D for consistency with the neutron data shown later. D1A, O1A and O3A are related to D1, O1 and O3, respectively, by an inversion centre. ADPs have been drawn at the 35 % probability level.*

The parameters, given in Table 6.6, suggest that the two hydrogen bonds in BHPM behave differently as a function of temperature. While the O1–H1 and H1···O1' bond lengths increase and decrease, respectively, on decreasing the temperature to 120 K, the hydrogen atom (H1) remains disordered over two sites. In contrast, there is a significant change in the O3···H3 and H3···O3' bond lengths, and at 120 K the H3 atom appears to be ordered, occupying an inversion centre halfway between the two oxygen sites.

The X-ray work described therefore suggests that the hydrogen atom in one of the SSHBs is ordered on the inversion centre on decreasing the temperature to 120 K, with the other remaining disordered over two sites. However, due to the inherent difficulty of obtaining reliable hydrogen atom positions from XRD, this conclusion may not be accurate. VT powder XRD work was therefore undertaken, in order to study the unit cell parameter trends as a function of temperature for any subtle changes in gradient which may be related to hydrogen atom behaviour. In addition, VT powder XRD allows

the retrieval of accurate unit cell parameters to use with single crystal neutron Laue diffraction data.

An initial scan of the polycrystalline sample at room temperature, d9_03177, was analysed by Rietveld refinement. A total of 34 parameters were refined, including 6 coefficients of a Chebyschev polynomial to model the background, a zero point error, 6 lattice parameters, 1 parameter to describe the isotropic thermal displacement of all of the atoms, 4 parameters to define the TCHZ peak shape and a scale factor; a 4$^{th}$ order spherical harmonic function was also used to correct for the significant preferred orientation. A relatively good fit between the structural model and the recorded data was obtained, Figure 6.22, with a final $R_{wp}$ value for the refinement of 8.003 %. However, the preferred orientation of the crystallites is significant.
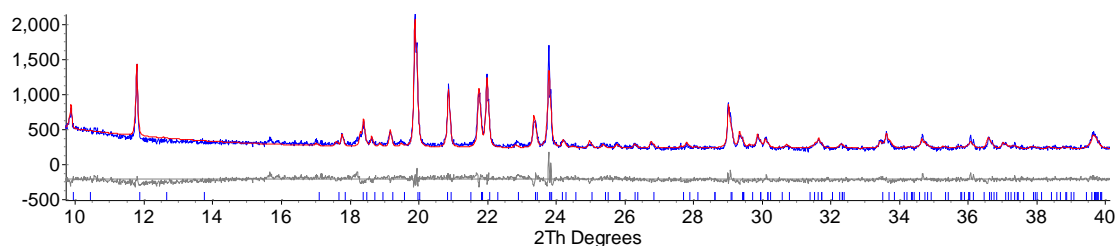


*Figure 6.22: The Rietveld fit of BHPM in scan d9_03177; the calculated pattern is shown in red, the observed pattern is shown in blue and the difference plot is shown in grey. Due to the large preferred orientation in this sample, only the range 10-40° 2θ has been shown for clarity.*

Variable temperature data were then obtained between 300 and 12 K (scan label d9_03178). These data were analysed as discussed previously, with a sample height displacement parameter being refined in place of the zero point error. The unit cell volume as a function of temperature is shown in Figure 6.23 and is seen to increase smoothly as a result of the expected thermal expansion. However, there appear to be no significant changes in the shape or gradient of the curve, suggesting the absence of any major structural changes in the system. This behaviour is similar to that observed for the fully protonated 35PDCA sample, which exhibits proton migration despite no abrupt changes in the lattice parameters.
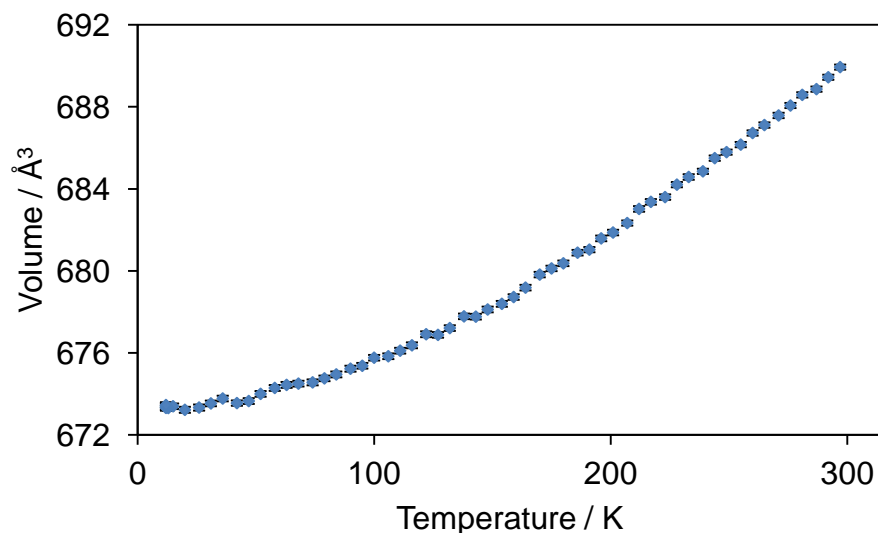
*Figure 6.23: The change in cell volume of BHPM as a function of temperature in scan d9_03178.*

In order to obtain accurate hydrogen atom positions and determine the extent of any temperature induced changes in position, single crystal neutron diffraction data were collected at 15 and 300 K. A summary of the crystallographic data is given in Table 6.7, and the various bond lengths of interest are summarised in Table 6.8. The structures are shown in Figure 6.24.

As previously described, only ratios between unit cell dimensions can be determined in the white-beam Laue technique and cell parameters determined from VT powder XRD have been used.

*Table 6.7: Crystallographic data for the single-crystal neutron diffraction of BHPM at 15 and 300 K.  \*Determined from powder XRD.*

|  | 15 K | 300 K |
|---|---|---|
| Chemical formula | $C_{16}H_{14}N_2O_4$ | $C_{16}H_{14}N_2O_4$ |
| $M_r$ | 299 | 299 |
| Crystal setting, space group | Triclinic, $P\bar{1}$ | Triclinic, $P\bar{1}$ |
| Temperature/K | 15 | 300 |
| $a$/Å * | 5.0544 (13) | 5.0905 (13) |
| $b$/Å * | 9.162 (3) | 9.233 (3) |
| $c$/Å * | 15.153 (4) | 15.259 (4) |
| $\alpha$/° * | 102.1 (5) | 102.2 (5) |
| $\beta$/° * | 90.08 (2) | 90.64 (2) |
| $\gamma$/° * | 100.76 (2) | 99.84 (2) |
| $V$/Å$^3$ * | 673.4 (3) | 689.9 (3) |
| $Z$ | 2 | 2 |
| No. measured and independent reflections | 7024, 3214 | 4185, 1724 |
| $R_{int}$ | 0.199 | 0.242 |
| $R[F^2 > 2\sigma(F^2)]$, $wR(F^2)$, $S$ | 0.116, 0.172, 1.65 | 0.121, 0.174, 1.64 |
| No. of parameters | 320 | 328 |

*Table 6.8: A comparison of selected bond lengths of interest in BHPM from single crystal neutron diffraction at 15 and 300 K.*

|  | 15 K | 300 K |
|---|---|---|
| **O1O1' distance/Å** | 2.478(5) | 2.508(8) |
| **O1H1 distance/Å** | 1.239(4) | 1.254(9) |
| **H1O1' distance/Å** | 1.239(4) | 1.254(9) |
| **O3O3' distance/Å** | 2.468(4) | 2.502(9) |
| **O3H3 distance/Å** | 1.234(6) | 1.251(9) |
| **H3O3' distance/Å** | 1.234(6) | 1.251 (9) |

15 K
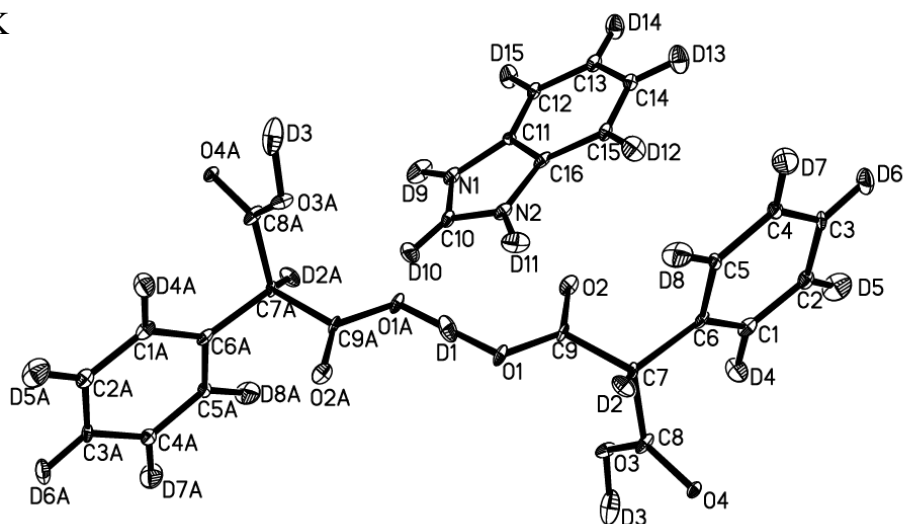


(a)

300 K
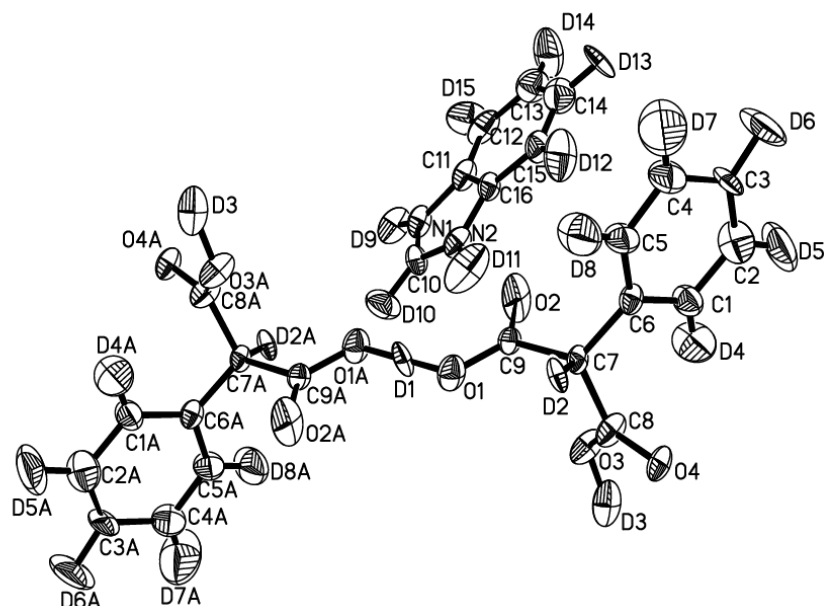


(b)

*Figure 6.24: The single crystal neutron diffraction structure of BHPM calculated from data collected at a) 15 K and b) 300 K; in both cases O1A and O3A are related to O1 and O3, respectively, by an inversion centre. ADPs are drawn at the 35 % probability level and all hydrogen atoms have been labelled as D for refinement purposes.*

The main changes on increasing temperature are the expected increases in bond lengths due to thermal expansion, and the expected increase in the anisotropic displacement parameters. The parameters in Table 6.8 show that, in contrast to previously reported

X-ray work, both hydrogen atoms are ordered at all temperatures studied, *i.e.* both protons occupy inversion centres (sites 1a and 1e for H1 and H3, respectively) halfway between the two oxygen sites, with large anisotropic thermal parameters along the direction of the bond. In addition, it must be noted that the position of the hydrogen atom in the normal N–H⋯O bond remains invariant as a function of temperature.

Although the analysis of neutron diffraction data found the protons to be placed in a symmetric position in the hydrogen bond at all temperatures studied, it is possible that two sites for the proton exist, as made evident by the large anisotropic displacement parameters elongated along the hydrogen bond. Due to the nature of the short hydrogen bond (O⋯O of less than 2.5 Å at 15 K), any split proton sites would be spatially very close (around 0.2 Å apart, in contrast to the situation in benzoic acid where disordered hydrogen atoms are separated by 0.6-0.7 Å).[36-38] Such spatial separation would not be resolved by the space- and time-averaged technique of neutron diffraction, and so a faster local probe technique, such as NMR, would have to be employed to observe this. Regardless of this, neutron diffraction provides unambiguous evidence that BHPM does not undergo a symmetry-lowering order-disorder phase transition at low temperature.

## 6.4 Conclusions

The CSD was searched for further systems, containing SSHBs, with the potential to exhibit interesting temperature-dependent proton behaviour. Two of the resulting compounds, 35DBNA and 4ABNA, contain features analogous to those in 35PDCA, and therefore were thought to be potential candidates for temperature-dependent proton migration. A further compound, BHPM, is structurally similar to $\alpha$-2APP[6], and therefore was thought to have the potential to exhibit a temperature-dependent ferroelectric transition associated with a proton order-disorder transition.

The structure of 35DBNA was determined by single crystal neutron diffraction at 30 and 300 K. At both temperatures, the hydrogen atom of interest (H8) is located in an asymmetric position closer to the nitrogen atom (N1) rather than the carboxylic acid oxygen (O4), as suggested for the 300 K structure in previous literature.[3] No proton migration through the hydrogen bond centre has been found; however, the proton does seem to shift in the hydrogen bridge towards the acceptor oxygen atom. MD simulations

can be used to predict whether or not proton migration might be observed experimentally, providing geometry optimisation allows the accurate determination of the SSHB geometry. These simulations show proton 'hopping' over the N–H⋯O hydrogen bond which increases with temperature. This proton hopping results in short periods along the trajectory in which the proton is located at the O4 atom. The structure observed by diffraction at higher temperature is an average structure, taking into account this proton hopping.

The structure of 4ABNA was studied by single crystal XRD at 120 and 300 K and some temperature-dependent proton migration was found, though the refinements were problematic. At both temperatures the hydrogen atom (H1) refined most reliably to a position closer to the nitrogen atom (N1). This is in contrast to previous literature which found it to be located on the oxygen atom (O1) at 300 K.[4] In addition, the donor-acceptor distance of 2.48 Å, found at 300 K is one of the shortest hydrogen bonds in existence. Fourier difference maps suggest that some proton disorder may be present in the structure, explaining the refinement difficulties. MD simulations confirmed the proton location at nitrogen at all temperatures but did not show any proton migration/hopping behaviour, possibly as a result of the overestimation of its N⋯O distance. It is clear that XRD results for this compound are inconclusive; however the very short hydrogen bond at 300 K, and the potential proton disorder found merit further study. In order to draw reliable conclusions regarding proton migration or disorder, large crystals, suitable for a single crystal neutron diffraction experiment, should be grown.

Neutron diffraction studies on BHPM at 15 and 300 K showed that the published literature structure,[5] obtained at room temperature using XRD, was incorrect. It was found that the hydrogen atoms in the SSHBs are ordered on inversion centres at all temperatures, lying in symmetric positions in the bonds. Furthermore, no changes in their positions were observed on varying temperature.

The work in this chapter has provided subtle evidence for proton migration in two SSHB compounds, 35DBNA and 4ABNA. Given these results it would appear that the presence of a SSHB is not a sufficient condition for proton migration to occur. Whilst

there is subtle evidence for proton migration in 4ABNA, the lack of any large scale proton migration through the hydrogen bond centre, as observed in 35PDCA, is especially interesting given the smaller donor-acceptor bond distance in 4ABNA at all temperatures. In order to investigate this further, crystals of a suitable size for neutron diffraction would need to be grown to further study the presence of proton migration in 4ABNA. In addition, other systems with hydrogen bonds with a similar length should also be investigated. Furthermore, the lack of evidence for an order-disorder transition in BHPM should not dissuade the investigation of this effect in other systems structurally similar to *α*-2APP.

## 6.5 References

1.      F. H. Allen, *Acta Crystallogr. Sect. B.*, 2002, **58**, 380.
2.      F. H. Allen and W. D. S. Motherwell, *Acta Crystallogr. Sect. B.*, 2002, **58**, 407.
3.      J. Zhu and J. M. Zheng, *Chin. J. Struct. Chem.*, 2004, **23**, 417.
4.      S. R. Jebas and T. Balasubramanian, *Acta Crystallogr., Sect. E*, 2006, **62**, O5621.
5.      S. Ueda, F. A. Takeo and H. Ishida, *Acta Crystallogr., Sect. E*, 2005, **61**, O1845.
6.      I. R. Evans, J. A. K. Howard and J. S. O. Evans, *Cryst. Growth & Des.*, 2008, **8**, 1635.
7.      *Bruker SMART v5.629*, Bruker AXS Inc., Madison, WI, USA, 2000.
8.      *Bruker SAINT+ v6.45*, Bruker AXS Inc., Madison, WI, USA, 2003.
9.      G. M. Sheldrick, *SADABS*, University of Gottingen, Germany, 1996.
10.     P. W. Betteridge, J. R. Carruthers, R. I. Cooper, K. Prout and D. J. Watkin, *J. Appl. Crystallogr.*, 2003, **36**, 1487.
11.     C. J. Wilkinson, J. A. Cowan, D. A. A. Myles, F. Cipriani and G. J. McIntyre, *Neutron News*, 2002, **13**, 37.
12.     J. W. Campbell, *J. Appl. Crystallogr.*, 1995, **28**, 228.
13.     J. W. Campbell, Q. Hao, M. M. Harding, N. D. Nguti and C. J. Wilkinson, *J. Appl. Crystallogr.*, 1998, **31**, 23.
14.     J. W. Campbell, J. Habash, J. R. Helliwell and K. Moffat, *Information Quarterly for Protein Crystallography, No. 18*, SERC, Daresbury Laboratory, Warrington, England, 1986.
15.     C. J. Wilkinson, H. W. Khamis, R. F. D. Stansfield and G. J. McIntyre, *J. Appl. Crystallogr.*, 1988, **21**, 471.
16.     G. M. Sheldrick, *SHELXL* Bruker AXS Inc., University of Gottingen, Germany, 2000.
17.     G. M. Sheldrick, *Acta Crystallogr., Sect. A*, 2008, **64**, 112.
18.     A. A. Coehlo, *TOPAS Academic: General profile and structure analysis software for powder diffraction data*, Bruker AXS, Karlsruhe, 2005.
19.     G. Kresse and J. Hafner, *Phys. Rev. B*, 1993, **47**, 558.
20.     G. Kresse and J. Furthmuller, *Phys. Rev. B*, 1996, **54**, 11169.
21.     P. E. Blochl, *Phys. Rev. B*, 1994, **50**, 17953.
22.     C. C. Wilson, *Acta Crystallogr., Sect. B*, 2001, **57**, 435.

23.     J. A. Cowan, J. A. K. Howard, G. J. McIntyre, S. M. F. Lo and I. D. Williams, *Acta Crystallogr., Sect. B*, 2005, **61**, 724.
24.     J. A. Cowan, J. A. K. Howard, G. J. McIntyre, S. M. F. Lo and I. D. Williams, *Acta Crystallogr., Sect. B*, 2003, **59**, 794.
25.     I. Majerz and M. J. Gutmann, *J. Phys. Chem. A*, 2008, **112**, 9801.
26.     S. J. Ford, O. J. Delamore, J. S. O. Evans, G. J. McIntyre, M. R. Johnson and I. R. Evans, *Chem. Eur. J.*, 2011, **in press**.
27.     T. Steiner, I. Majerz and C. C. Wilson, *Angew. Chem. Int. Ed.*, 2001, **40**, 2651.
28.     P. Grobelny, A. Mukherjee and G. R. Desiraju, *Crystengcomm*, 2011, **13**, 4358.
29.     C. C. Wilson, K. Shankland and N. Shankland, *Z. Kristall.*, 2001, **216**, 303.
30.     C. C. Wilson and C. A. Morrison, *Chem. Phys. Lett.*, 2002, **362**, 85.
31.     I. R. Evans, J. A. K. Howard, J. S. O. Evans, S. R. Postlethwaite and M. R. Johnson, *Crystengcomm*, 2008, **10**, 1404.
32.     F. Fontaine-Vive, M. R. Johnson, G. J. Kearley, J. A. Cowan, J. A. K. Howard and S. F. Parker, *J. Chem. Phys.*, 2006, **124**, 234503.
33.     L. H. Thomas, A. J. Florence and C. C. Wilson, *New J. Chem.*, 2009, **33**, 2486.
34.     F. Fontaine-Vive, M. R. Johnson, G. J. Kearley, J. A. K. Howard and S. F. Parker, *J. Am. Chem. Soc.*, 2006, **128**, 2963.
35.     R. Blinc and B. Zeks, *Adv. Phys.*, 1972, **21**, 693.
36.     C. C. Wilson and L. H. Thomas, *C. R. Chimie*, 2005, **8**, 1434.
37.     C. C. Wilson, N. Shankland and A. J. Florence, *Chem. Phys. Lett.*, 1996, **253**, 103.
38.     C. C. Wilson, N. Shankland and A. J. Florence, *J. Chem. Soc. Faraday Trans.*, 1996, **92**, 5051.

# 7 New Medium Length Hydrogen Bond Compounds

Significant temperature-dependent proton migration reported in the short strong hydrogen bonded (SSHB) compound, 4-methylpyridine-pentachlorophenol (MP-PCP),[1] prompted the attempted synthesis of similar systems. In the crystal structure of MP-PCP, 4-methylpyridine and pentachlorophenol are linked by a very short N–H···O bond with a donor-acceptor distance of 2.506 Å at 20 K. The hydrogen atom in this bond has been found to migrate as a function of temperature, from a position closer to the oxygen atom at 296 K, to a position closer to the nitrogen atom at 20 K.

The syntheses reported in this chapter used reagents with molecular structures based on the components of MP-PCP and include 4-methylpyridine and pentachlorophenol amongst others. The additional reagents used in these syntheses, pyrazine and tetrachlorohydroquinone, are slight modifications of 4-methylpyridine and pentachlorophenol, respectively, in terms of substituents, Figure 7.1. Given the potential similarities between the new compounds and MP-PCP, it was proposed that the products of these new syntheses may also contain SSHBs which exhibit temperature dependent proton migration.
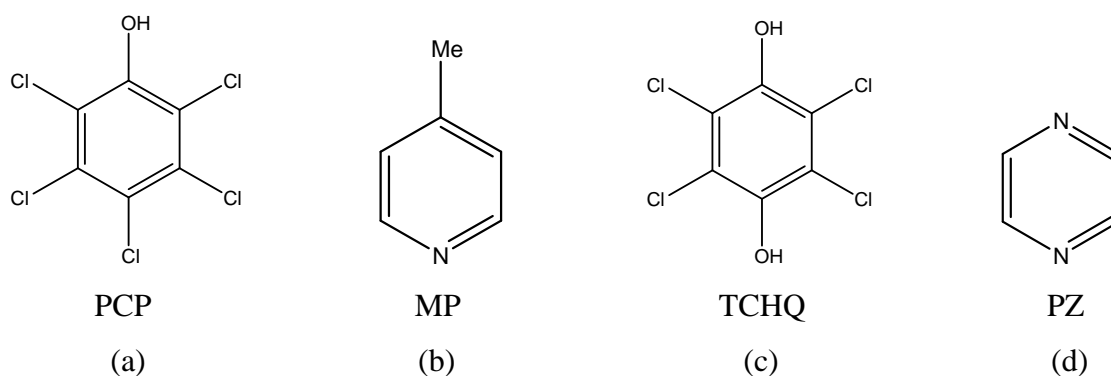


*Figure 7.1: The reagents used in the new syntheses: a) pentachlorophenol, b) 4-methylpyridine c) tetrachlorohydroquinone and d) pyrazine*

Tetrachlorohydroquinone (Figure 7.1c) differs from pentachlorophenol (Figure 7.1a) by the inclusion of an extra hydroxyl group in place of the chlorine atom in the position 'para' to the existing hydroxyl group. With this extra proton donor group it was thought that a compound could be synthesised in which hydrogen bonding propagated infinitely

along chains, analogous to the bonding in 35PDCA. Pyrazine (Figure 7.1d) differs from 4-methylpyridine (Figure 7.1b) as it contains an additional nitrogen atom in a position 'para' to the existing nitrogen atom, in place of a methyl group at this position. Again, the inclusion of this extra proton acceptor group was to encourage the formation of larger motifs than dimers.

In this chapter the attempted syntheses of TCHQ-PZ, PCP-PZ and MP-TCHQ are reported, alongside descriptions of the analysis of successful products by X-ray and neutron diffraction.

## 7.1  Tetrachlorohydroquinone-Pyrazine

The first composition attempted was the tetrachlorohydroquinone-pyrazine co-crystal (TCHQ-PZ), containing the components shown in Figure 7.2.
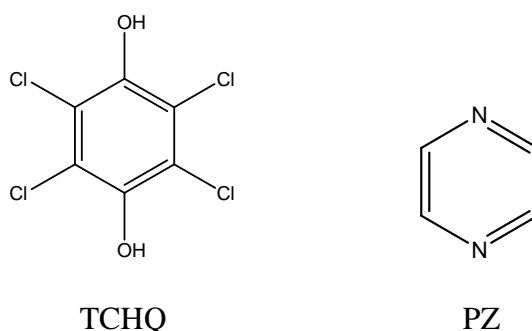


*Figure 7.2: The components of the tetrachlorohydroquinone-pyrazine co-crystal.*

### 7.1.1  Experimental

Following an initial solubility screen with a range of solvents, a successful method was found for the preparation of the tetrachlorohydroquinone-pyrazine (TCHQ-PZ) co-crystals in solution. In order to produce crystals of a suitable size for single crystal X-ray diffraction (XRD), the starting reagents, tetrachlorohydroquinone (0.0400 g, 0.16 mmol, Acros Organics, 99 %) and pyrazine (0.0129 g, 0.16 mmol, Aldrich, 99+ %) were separately dissolved in a minimum amount of ether. These were then mixed in a sample vial and sealed using a plastic cap containing four small apertures. Small, colourless, plate-like crystals were obtained after one day *via* slow evaporation of the

solvent. Larger crystals, suitable for single crystal neutron diffraction, were obtained using the same method, using methanol as the solvent. For this synthesis, the sealed vial was placed in the fridge to allow a slower evaporation. Colourless, cuboid-shaped crystals were obtained after one week.

Single crystal XRD data were collected on the Bruker SMART 1000 diffractometer at 40, 120 and 300 K. Initially, a number of crystals were found and tested, and a full data collection was carried out at 120 K on a colourless, plate-like crystal, measuring $0.08 \times 0.15 \times 0.26$ mm$^3$. On a further occasion, data were collected at 40 and 300 K on a colourless cube-shaped crystal, measuring $0.12 \times 0.16 \times 0.20$ mm$^3$. In each case, full spheres of data were collected by a series of $\omega$ scans, using a frame width of 0.3° in $\omega$ and a time of 30 seconds per frame. The data were processed as described in Section 2.3.1.1. Structure solution using direct methods, followed by refinement on $F^2$, was carried out using CRYSTALS.[2] Atomic coordinates and anisotropic displacement parameters were refined for all non-hydrogen atoms. Hydrogen atoms were located using Fourier difference maps and their atomic coordinates were refined; a three parameter weighting scheme was also used.

Single crystal neutron diffraction data were collected on VIVALDI at the ILL[3] on a crystal measuring $1.0 \times 2.5 \times 3.0$ mm$^3$. Data were collected at 30, 120 and 300 K; ten diffraction patterns, each accumulated over 30 minutes, were collected at each temperature with successive patterns distinguished by a rotation of 20° of the crystal perpendicular to the incident beam. The data were processed using the CCP4 Laue suite of programmes[4-6] and refinement on $F^2$ was carried out using SHELXTL.[7] Atomic coordinates and anisotropic displacement parameters were refined for all atoms.

A small quantity of the sample was ground up and prepared for powder XRD as described in Section 2.3.2.1. Data were collected on the Bruker D8 ADVANCE, in the range 5 to 60° $2\theta$ with a step size of 0.014° $2\theta$ at 0.3 seconds per step (for short 20 minute scans) or with a step size of 0.021° $2\theta$ at 1.4 seconds per step (for long 60 minute scans). Rietveld refinement was then performed in TOPAS Academic. For VT analysis the sample was cooled using the PheniX, from 300 to 12 K at a rate of 15 K per hour. Simultaneously, continuous 20 minute diffraction patterns were recorded from 5 to 60° $2\theta$ with a step size of 0.014° $2\theta$ at 0.3 seconds per step; in total 100 patterns

were recorded and these were analysed using the local routine, *multitopas*, as described in Section 2.3.2.1. In each refinement a total of 35 parameters, including a zero error, 4 lattice parameters, 1 parameter to describe the isotropic thermal displacement of all of the atoms, 4 parameters to define the TCHZ peak shape and a scale factor; this number increased in some refinements where the preferred orientation of individual phases required modelling.

## 7.1.2  Results and Discussion

### 7.1.2.1  Single Crystal X-ray Diffraction

A single crystal of TCHQ-PZ was tested at 120 K using XRD. This indexed to a cell with the parameters: $a \sim 8.6$ Å, $b \sim 7.1$ Å, $c \sim 10.0$ Å, $\alpha \sim 90°$, $\beta \sim 92.5°$, $\gamma \sim 90°$, unreported in the CSD, suggesting that a new compound had been prepared. A full data collection was subsequently performed on this sample and a summary of the crystallographic data is given in Table 7.1.

*Table 7.1: Crystallographic data for TCHQ-PZ, obtained using single crystal XRD at 120 K.*

|  | 120 K |
|---|---|
| Chemical formula | $C_{10}H_6Cl_4N_2O_2$ |
| $M_r$ | 327.98 |
| Crystal system, space group | Monoclinic, $C12/m1$ |
| $a$/Å | 8.6087 (12) |
| $b$/Å | 7.0247 (10) |
| $c$/Å | 9.8586 (13) |
| $\beta$/° | 92.488 (2) |
| $V$/Å$^3$ | 595.62 (14) |
| $Z$ | 2 |
| $\rho$/g cm$^{-3}$ | 1.829 |
| $\mu$/mm$^{-1}$ | 0.99 |
| Data collection method | $\omega/2\theta$ |
| No. of measured, independent and observed reflections | 7014, 1619, 1023 |
| Criterion for observed reflections | $I > 2.0\sigma(I)$ |
| $R_{int}$ | 0.050 |
| Refinement on | $F^2$ |
| $R[F^2 > 2\sigma(F^2)]$, $wR(F^2)$, $S$ | 0.046, 0.099, 0.87 |
| No. of parameters | 57 |

The crystal structure of TCHQ-PZ was solved from data collected at 120 K. This compound crystallises in the monoclinic space group $C2/m$, forming infinite chains

perpendicular to the *b* axis, Figure 7.3. The structure is stabilised by N···H–O hydrogen bonds within the chains, although no significant interactions occur between the chains. In each hydrogen bond the nitrogen atoms of pyrazine act as the hydrogen acceptors and the oxygen atoms of tetrachlorohydroquinone act as the hydrogen donors; no proton disorder over these sites has been observed. The C–O bond lengths of 1.348(5) Å are close to an average value of 1.32 Å, given in Figure 3.12, and the pyrazine C–N–C angles of 115.8(3)° conform to the average value for the unprotonated state (116°).[8] This provides further evidence for an N···H–O hydrogen bond with no proton disorder.

The N···H–O hydrogen bonds have a donor-acceptor distance of 2.818(6) Å at 120 K. Although this cannot be considered a short hydrogen bond (see Figure 1.1a of Chapter 1) it is similar in length to the medium-length hydrogen bond in the co-crystal of phenazine and chloranilic acid ($H_2$ca-Phz), in which temperature-dependent proton migration associated with a ferroelectric phase transition has been observed, as described in Chapter 1.[9]
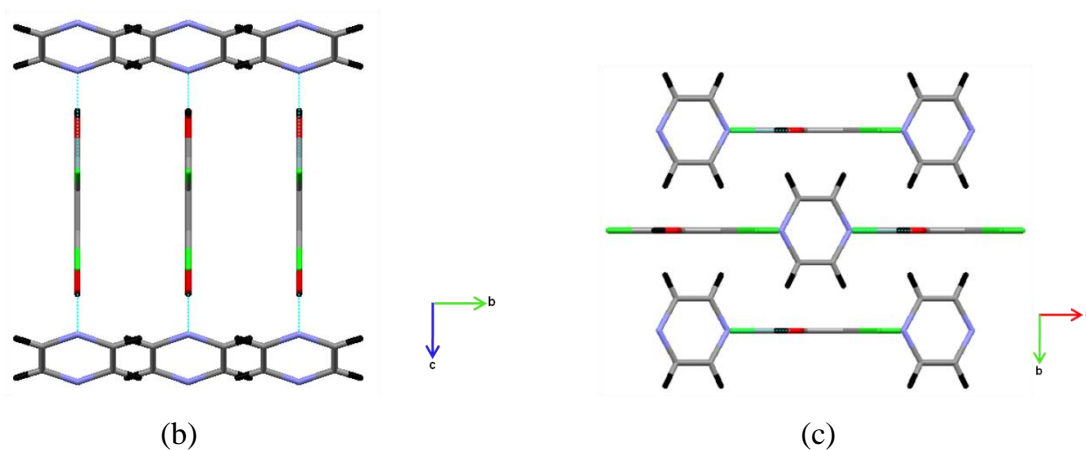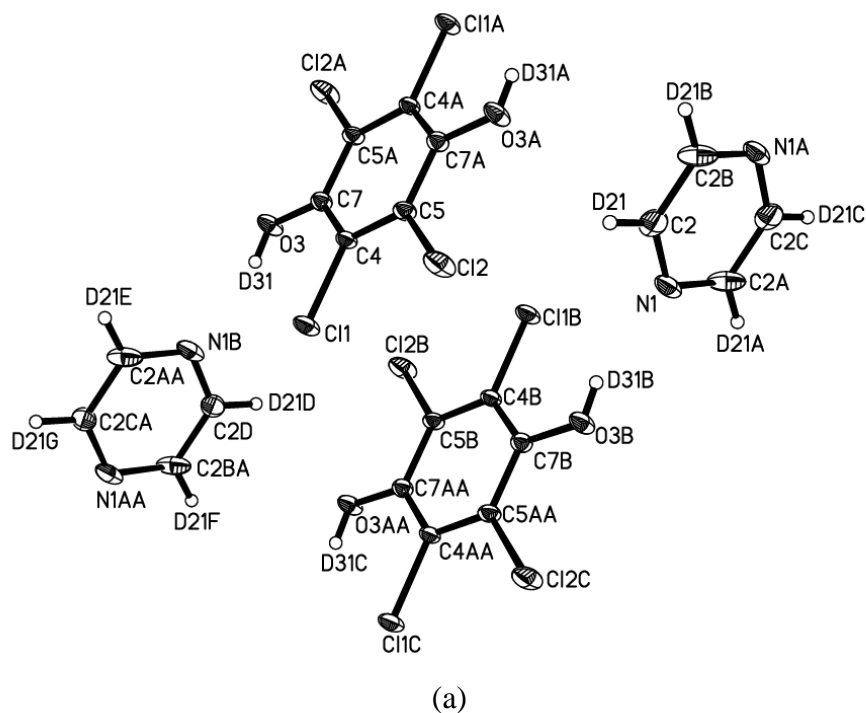
120 K



(a)



(b)



(c)

*Figure 7.3: a) The molecular structure of TCHQ-PZ at 120 K as determined by single crystal XRD (ADPs are plotted at the 50 % probability level and hydrogen atoms are labelled as D for consistency with the neutron data shown later), b) The molecular packing in TCHQ-PZ at 120 K, as viewed down the a axis and c) The molecular packing in TCHQ-PZ at 120 K, as viewed down the c axis.*

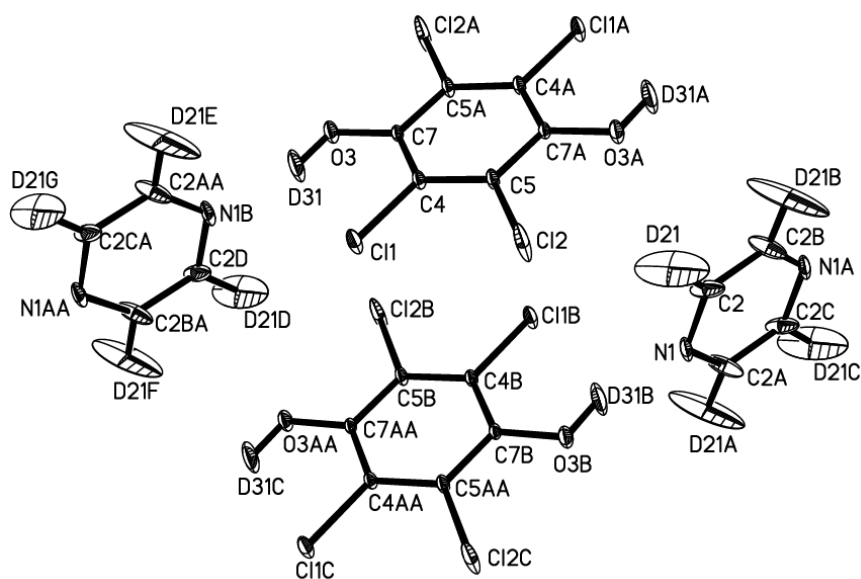### 7.1.2.2  Single Crystal Neutron Diffraction

In order to obtain an accurate structure with reliable hydrogen atom positions, it was necessary to use single crystal neutron diffraction. A summary of the crystallographic

data is given in Table 7.2 and the molecular structure at each temperature (30, 120 and 300 K) is shown in Figure 7.4. All lattice parameters were obtained using single crystal XRD, at 40, 120 and 300 K, respectively, since only ratios between unit cell dimensions can be determined by the white-beam Laue technique.

*Table 7.2: Crystallographic data for the structure of TCHQ-PZ, obtained by neutron diffraction at 30, 120 and 300 K.*

|  | 30K | 120 K | 300K |
|---|---|---|---|
| Chemical formula | $C_{10}H_6Cl_4N_2O_2$ | $C_{10}H_6Cl_4N_2O_2$ | $C_{10}H_6Cl_4N_2O_2$ |
| $M_r$ | 327.98 | 327.98 | 327.98 |
| Crystal system, space group | Monoclinic, $P12_1/a1$ | Monoclinic, $C12/m1$ | Monoclinic, $C12/m1$ |
| $a$/Å | 8.6270 (5) | 8.6087 (12) | 8.6537 (13) |
| $b$/Å | 7.0160(4) | 7.0247 (10) | 7.1597 (11) |
| $c$/Å | 9.8950 (6) | 9.8586 (13) | 9.9583 (15) |
| $\beta$/° | 92.392 (2) | 92.488 (2) | 92.680 (2) |
| $V$ /Å$^3$ | 596.22 (6) | 595.62 (14) | 616.32 (16) |
| $Z$ | 2 | 2 | 2 |
| $\mu$/mm$^{-1}$ | 0.07 | 0.07 | 0.07 |
| Data collection method | Laue | Laue | Laue |
| No. of measured, observed reflections | 10592, 2184 | 3546, 764 | 2481, 432 |
| $R_{int}$ | 0.129 | 0.141 | 0.102 |
| Refinement on | $F^2$ | $F^2$ | $F^2$ |
| $R[F^2 > 2\sigma(F^2)]$, $wR(F^2)$ | 0.132, 0.381 | 0.082, 0.217 | 0.121, 0.420 |
| No. of parameters | 109 | 77 | 77 |

30 K



(a)

120 K
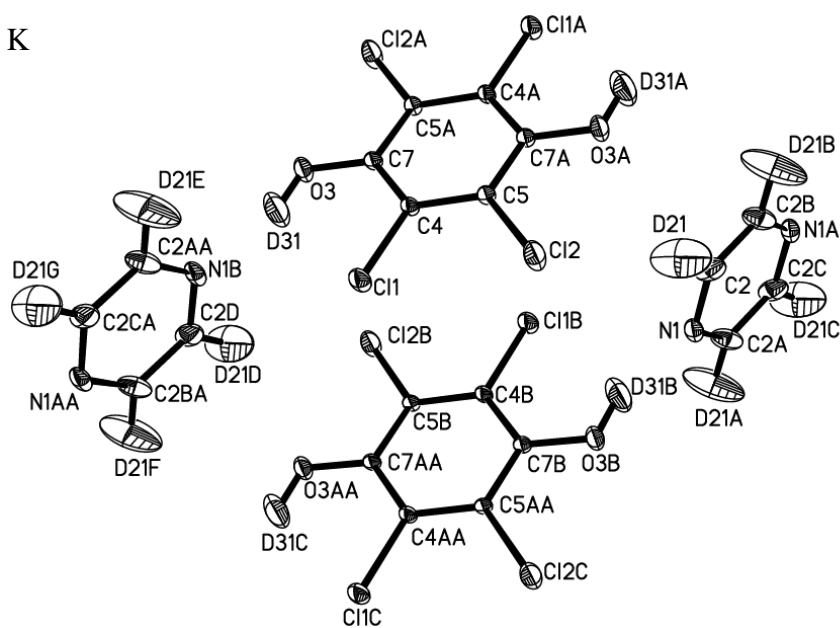


(b)

300 K
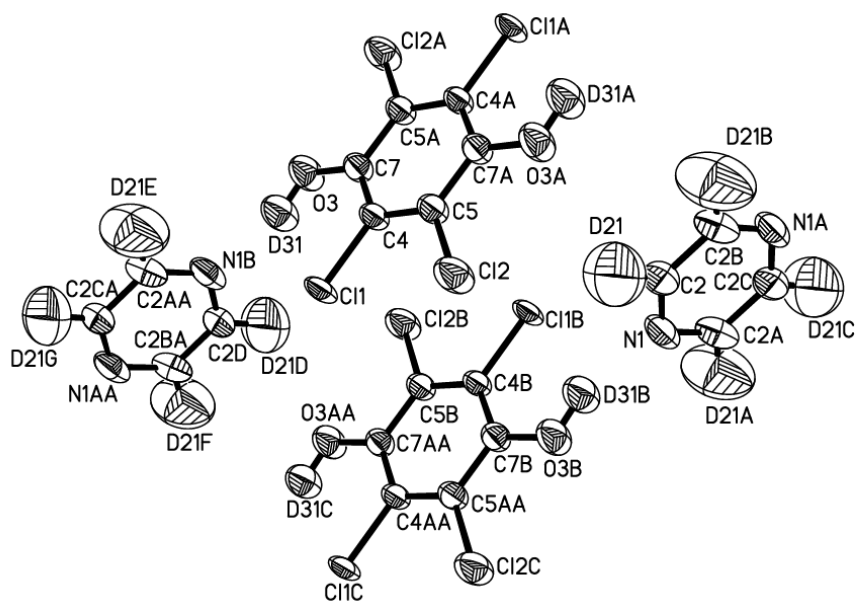


(c)

*Figure 7.4: The molecular structure of TCHQ-PZ obtained from single crystal neutron diffraction (modelled in space group C2/m) at a) 30 K, b) 120 K and c) 300 K. (ADPs are plotted at the 50 % probability level and all hydrogen atoms have been labelled as D to allow their refinement).*

The structure obtained from neutron diffraction data at 120 K is modelled well by *C*2/*m* symmetry, with a donor-acceptor, O···N, distance of 2.816(3) Å, an O–H distance of 0.983(6) Å and an N···H distance of 1.885(4) Å. At 300 K, Figure 7.4c, the structure is very similar, again with *C*2/*m* symmetry, but with a slightly expanded donor-acceptor distance of 2.844(3) Å. At this temperature the O–H distance is 0.963(5) Å and the N···H distance is 1.945(5) Å, suggesting that a small proton migration may be occurring, though this is likely to be a result of the overall changes in the donor-acceptor distance. In addition, increasing the temperature from 120 to 300 K causes a slight increase in the size of the ADPs, as expected.

While the structures obtained at 120 and 300 K are modelled well in the space group *C*2/*m*, that at 30 K, Figure 7.4a, does not appear to be correct; the long, flat shape of the thermal displacement parameters for each atom, compared to those at 120 K, suggests the assignment of an incorrect space group at 30 K. Closer inspection of the data showed a much larger number of reflections to be present, compared to those collected at higher temperatures, with the *C*-centred systematic absence of $h + k = 2n$ being violated. This suggested a decrease to primitive symmetry at this temperature.

Analysis using the monoclinic primitive subgroups of *C*2/*m* (*P*2/*m*, *P*2$_1$/*m*, *P*2/*a* and *P*2$_1$/*a*) was undertaken and a sensible refinement was found when using the space group *P*2$_1$/*a*. A further single crystal XRD experiment was performed at 40 K, in order to obtain a set of unit cell parameters suitable for using in the analysis of the neutron data collected at 30 K, and also to confirm the low temperature space group. The structure resulting from the analysis of the neutron data, in the *P*2$_1$/*a* space group, is shown in Figure 7.5.
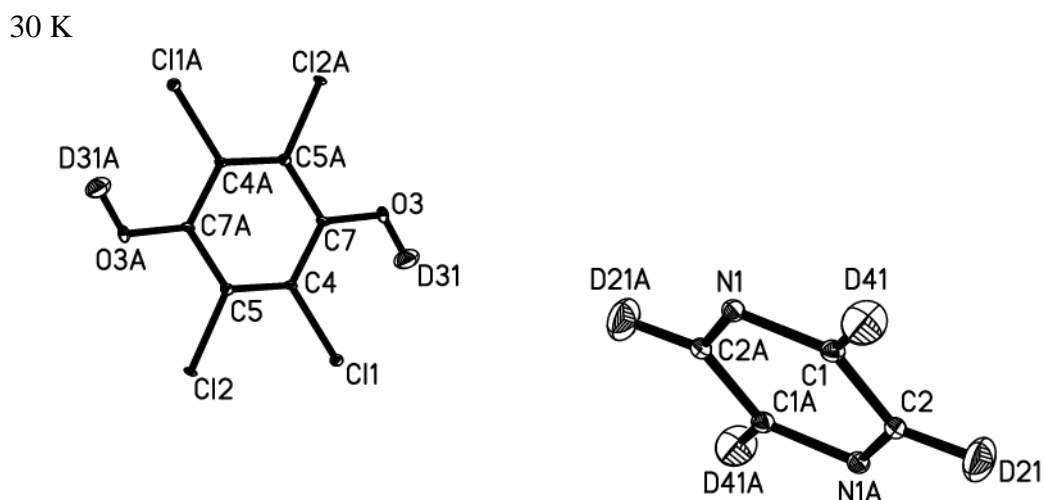
30 K



*Figure 7.5: The molecular structure obtained from single crystal neutron diffraction (modelled in space group P2₁/a) at 30 K. Hydrogen atoms have been labelled as D for refinement purposes and ADPs are drawn at the 50 % probability level.*

The molecular packing is given in Figure 7.6 (right-hand column), alongside that for the structure obtained from data collected at 120 K (left-hand column) for comparison, and the transition from $C2/m$ to $P2_1/a$ can be clearly seen. The rotational and mirror symmetry observed at high temperature (120 and 300 K) is broken by the slight rotation of the TCHQ and PZ components in an ordered fashion; the TCHQ molecule rotates out of the $ac$ plane (Figures 7.6b and 7.6f). The direction of this rotation alternates between the TCHQ components in the planes at $y = 0$ and those at $y = 0.5$. The PZ molecule rotates in a direction parallel to the $c$ axis (Figure 7.6b), with the direction alternating between those at (0,0,z) and those at (0.5,0.5,z). The loss of $C$-centring is clearly demonstrated in Figures 7.6e and 7.6f; at 120 K, Figure 7.6e, symmetry equivalent PZ are present at (0,0,0) and (0.5,0.5,0), whereas at 30 K, Figure 7.6f, this is no longer the case as a result of the alternating directions of the component rotations.

120 K                                    30 K



(a)                                      (b)



(c)                                      (d)
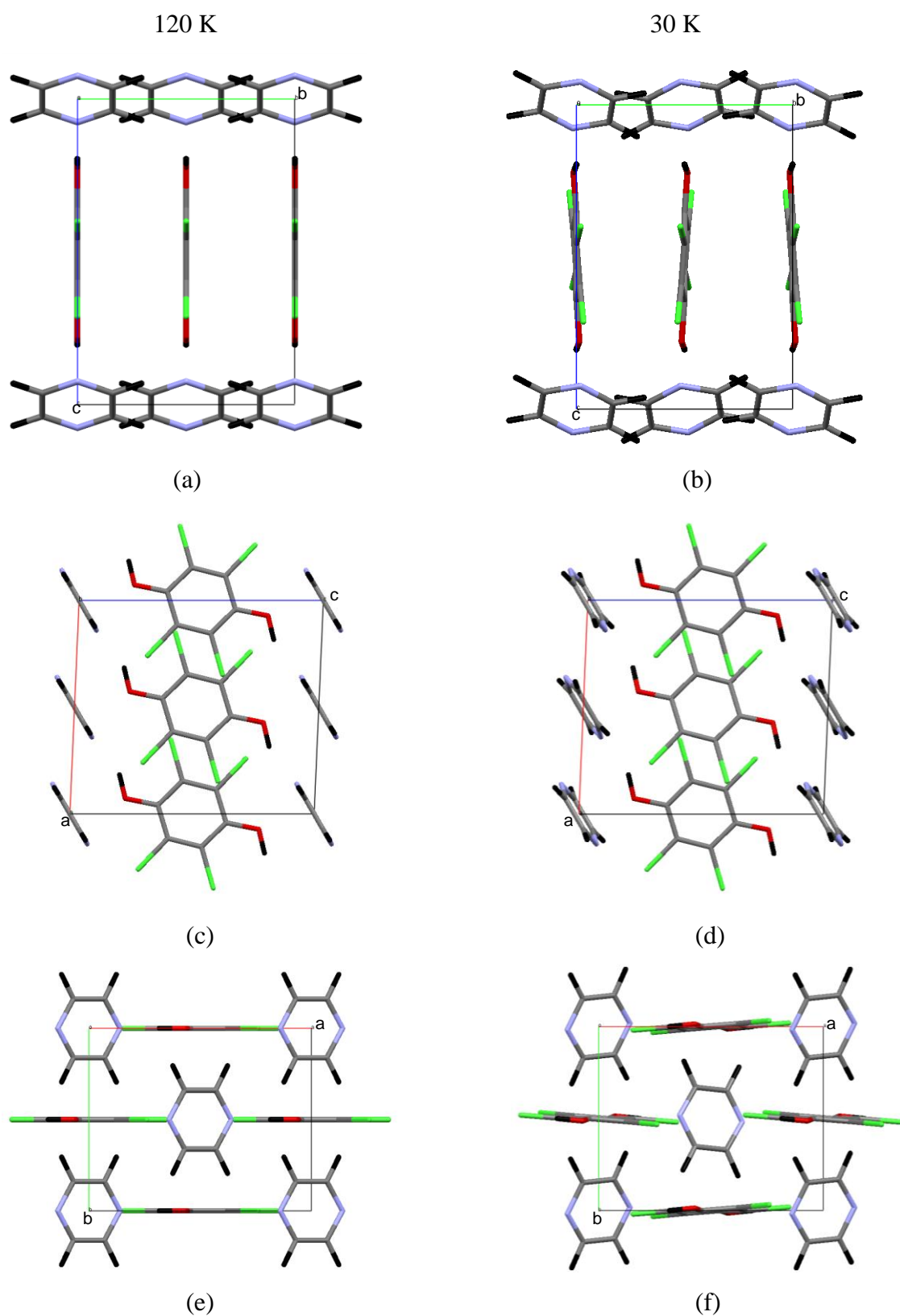


(e)                                      (f)

*Figure 7.6: The packing of TCHQ-PZ at 120 K (left column) and 30 K (right column),
as viewed down the a axis (top row), the b axis (middle row) and the c axis (bottom*

*row). In each case, carbon is drawn in grey, hydrogen in black, nitrogen in blue, oxygen in red and chlorine in green.*

At 30 K, the O–H distance is 0.993(12) Å, the N···H distance is 1.889(5) Å and the N···O distance is 2.819(5) Å, revealing an absence of proton migration between 120 and 30 K.

*Table 7.3: Summary of the hydrogen bond parameters obtained by single crystal neutron diffraction.*

|  | 30 K | 120 K | 300 K |
|---|---|---|---|
| **O3H31 distance/Å** | 0.99(1) | 0.983(6) | 0.963(5) |
| **O3N1 distance/Å** | 2.819(5) | 2.816(3) | 2.844(3) |
| **H31N1 distance/Å** | 1.889(5) | 1.885(4) | 1.945(5) |

The donor-acceptor distances found at all temperatures for TCHQ-PZ, summarised in Table 7.3, are much longer than those in comparable MP-PCP.[1] A large difference between MP-PCP and TCHQ-PZ, which may account for the observed differences in N···O separation, is the N–H–O angle. In general, in order to form the strongest hydrogen bonds, this bond must be as close to linear (180°) as possible. In TCHQ-PZ this is 156.90(15)° at 120 K, and in MP-PCP this is 169.6(10)° at 125 K, hence the stronger bond in MP-PCP.[1] In addition, the geometries of the structures differ. In the TCHQ-PZ structure the planes of the bulky tetrachlorohydroquinone groups lie perpendicular to the pyrazine planes, Figures 7.3 and 7.7a. In the MP-PCP dimer, Figure 7.7b, a dihedral angle of 59.4(1)° at 80 K exists between the planes of the phenol and 4-methylpyridine components.[10] This may reduce any steric hindrance caused by the bulky pentachlorophenol group, and the consequence of this is that a very short hydrogen bond can form.
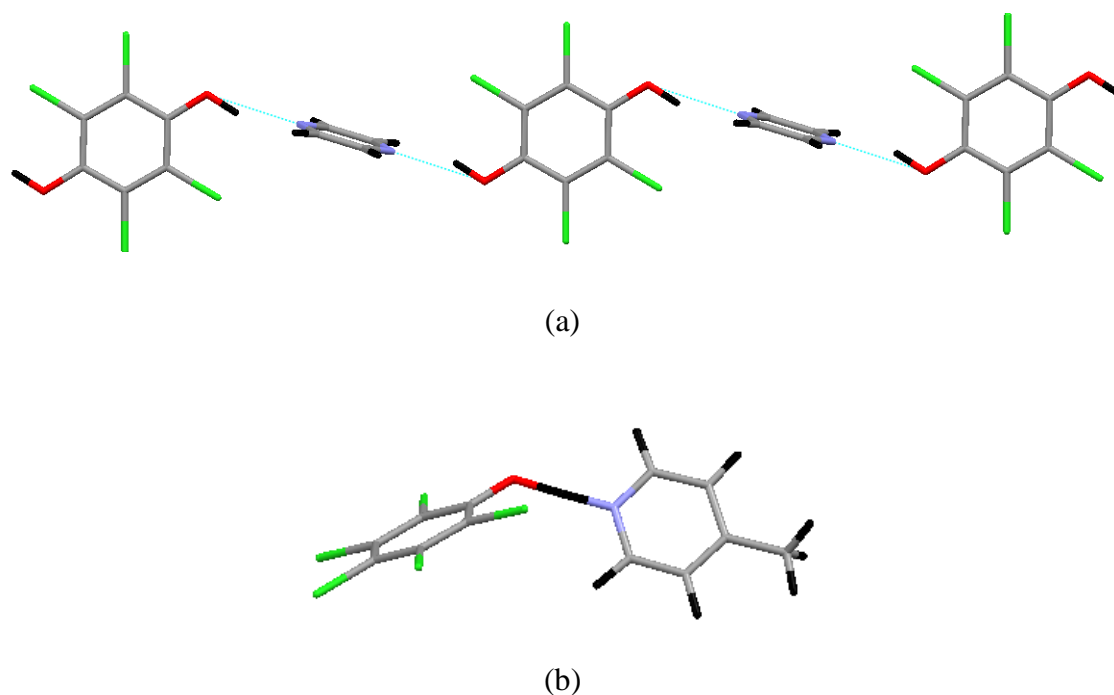
(a)



(b)

Figure 7.7: *a) Part of the TCHQ-PZ chain, showing the perpendicular TCHQ and PZ component and b) The MP-PCP dimer.*

The changes in the O–H and the N⋯H distances in TCHQ-PZ as the temperature is increased suggest that a very small proton migration, towards a more central position in the hydrogen bond, may be occurring between 300 and 120 K; however, the small changes that do occur are likely to be simply caused by the slight increase of the, already large, donor-acceptor distance. Given the fact that proton migration occurs in the moderate hydrogen bond (2.714 Å at 300 K) of the co-crystal of chloranilic acid and phenazine (H$_2$ca-Phz), Figure 7.8, it seems that a SSHB is not a necessary property for proton migration and that other factors may also be involved.

Additional factors have in fact been discussed for some proton migration compounds. For example, the co-crystal of isoniazid (isonicotinic acid hydrazide) and 4-aminosalicylic acid (INH-PAS), described in Chapter 1, has a complex structure, containing many O–H⋯O, N–H⋯O and O–H⋯N hydrogen bonds.[11] These hydrogen bonds are mostly medium or long in length (with donor-acceptor distances of approximately 2.8 to 3.4 Å). However, a shorter O–H⋯N bond on the boundary of a short/medium hydrogen bond length classification (with a donor-acceptor distance of 2.548(2) Å at 100 K and 2.576(3) Å at 280 K), forming between the nitrogen atom of a

pyridine ring and an oxygen atom of a carboxylic acid group, is also present. Temperature dependent proton migration has been found to occur in this shorter bond, from an asymmetric position closer to the donor oxygen atom at 280 K (O–H of 1.11(7) Å and N···H of 1.46(7) Å), to an almost central, symmetrical, position in the hydrogen bond at 100 K (O–H of 1.25(5) Å and N···H of 1.30(5) Å). Although this is a relatively short hydrogen bond at 100 K, particularly compared to that in TCHQ-PZ it was concluded that the migration was the result of a polar electronic environment for this bond.[11] This allows a stronger attraction between the proton and the acceptor atom, compared to the other, albeit longer, hydrogen bonds in the compound. Contrarily, this migration effect could be caused by the large changes in the donor-acceptor distance with temperature, from 2.576(3) Å at 280 K to 2.548(2) Å at 100 K.

Furthermore, in the co-crystal of phenazine and chloranilic acid ($H_2$ca-Phz), Figure 7.8, migration of one of the hydrogen bond protons, (H5, labelled) to a more symmetric position in the bond, has been explained as the result of the multi-centre nature of the hydrogen bond, in which the carbonyl oxygen (O2, labelled) could facilitate proton displacement.[12] In TCHQ-PZ, a chlorine atom resides in an equivalent position on the halide-containing ring. Due to the lower electronegativity of chlorine in comparison to oxygen, the hydrogen bond proton in TCHQ-PZ exists in a less polar environment, thereby reducing the attraction between it and the acceptor nitrogen atom and precluding any proton migratory behaviour.

In addition, the donor-acceptor distance in the $H_2$ca-Phz system is slightly shorter than in the current case (2.714 Å at 300 K, compared to 2.844(3) Å for TCHQ-PZ at 300 K), and this is likely to be a result of resonance assisted hydrogen bonding in each of the two enolone fragments (HO–C=C–C=O, one of which has been highlighted using a black rectangle in Figure 7.8). Again, such a stabilising interaction cannot occur in TCHQ-PZ due to it containing a chlorine atom in place of a carbonyl group. It is also possible that in TCHQ-PZ the bond is simply too long for proton migration to occur.
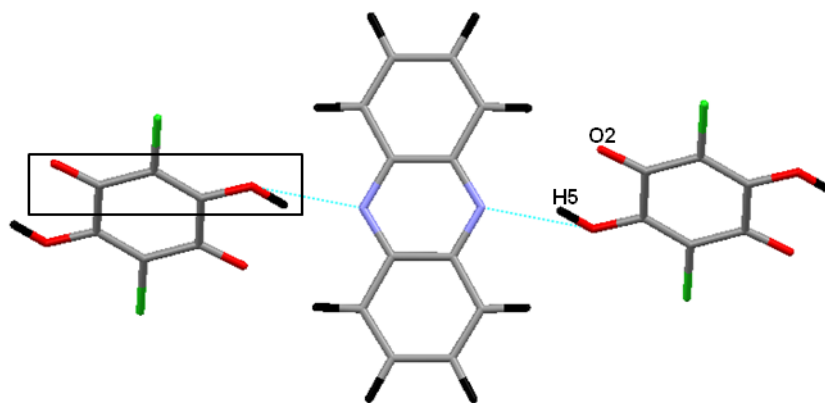
*Figure 7.8: The structure of the co-crystal of chloranilic acid and phenazine. One of the two enolone fragments (HO–C=C–C=O) has been highlighted with a black rectangle. Carbon atoms are drawn in grey, hydrogen in black, nitrogen in blue, oxygen in red and chlorine in green.*

### 7.1.2.3 Powder X-ray Diffraction

In order to determine the onset temperature of the phase transition in TCHQ-PZ, VT powder XRD data were collected, allowing for relatively rapid data collections with smaller temperature increments between each set of data. An initial diffraction pattern was recorded at room temperature, Figure 7.9, and Rietveld analysis confirmed that this sample was pure. However, on cooling it was found that the application of a vacuum to the sample chamber provided sufficient pressure to remove the PZ present in the sample, leaving the TCHQ starting material only. Therefore it was not possible to obtain data for the TCHQ-PZ co-crystal at any temperature lower than room temperature.
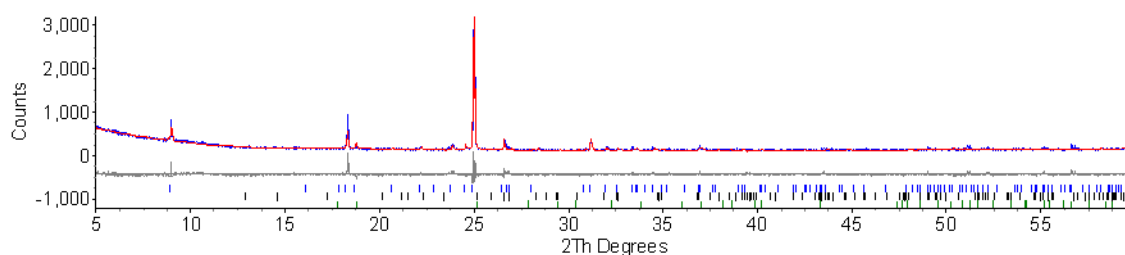


*Figure 7.9: The Rietveld fit of TCHQ-PZ, scan d9_04901, at room temperature; the calculated pattern in red, the observed pattern in blue and the difference plot in grey.*

## 7.2  Pentachlorophenol-Pyrazine

A further MP-PCP analogue attempted was that of the pentachlorophenol-pyrazine co-crystal (PCP-PZ), the components of which are shown in Figure 7.10.
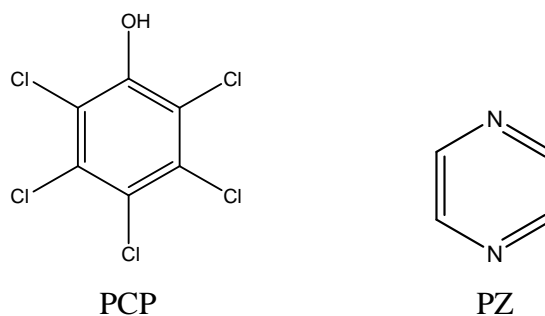


*Figure 7.10: The components of the pentachlorophenol-pyrazine co-crystal.*

### 7.2.1  Experimental

Following an initial solubility screen with a range of solvents, a successful method was found for the preparation of PCP-PZ co-crystals in solution. The starting reagents, pentachlorophenol (0.0430 g, 1.6 mmol, Aldrich, 98 %) and pyrazine (0.0065 g, 0.8 mmol, Aldrich, 99+ %) were separately dissolved in a minimum amount of methanol. These were then mixed in a sample vial and, using a pin, four small apertures were made in the cap. Colourless plate-like crystals were obtained after one week *via* slow evaporation of the solvent.

Single crystal XRD data were collected on the Bruker SMART 1000 diffractometer at 120 K. A number of crystals were found and tested, and a full data collection was carried out on a colourless, flat crystal, measuring $0.04 \times 0.16 \times 0.16$ mm$^3$. A full sphere of data was collected by a series of $\omega$ scans, using a frame width of $0.3°$ in $\omega$ and a time of 30 seconds per frame. The data were processed as described in Section 2.3.1.1. Structure solution using direct methods, followed by refinement on $F^2$, was carried out using CRYSTALS.[2] Atomic coordinates and anisotropic displacement parameters were refined for all non-hydrogen atoms. Hydrogen atoms were located using Fourier difference maps and their atomic coordinates were refined; a three parameter weighting scheme was also used.

235

## 7.2.2 Results and Discussion

As with the TCHQ-PZ co-crystal, several crystals were extracted from the sample vial and screened using single crystal XRD. An approximate unit cell of $a \sim 7.2$ Å, $b \sim 8.7$ Å, $c \sim 9.0$ Å, $\alpha \sim 72.3°$, $\beta \sim 86.5°$, $\gamma \sim 82.9°$ was found for the crystals. As this was unreported in the CSD it suggested that this was a new compound. A full data collection was then performed at 120 K and a summary of the crystallographic data is shown in Table 7.4.

*Table 7.4: Crystallographic data for the structure of PCP-PZ at 120 K.*

|  | 120K |
|---|---|
| Chemical formula | $C_{16}H_6Cl_{10}N_2O_2$ |
| $M_r$ | 612.76 |
| Crystal system, space group | Triclinic, $P\bar{1}$ |
| $a$/Å | 7.2078(4) |
| $b$/Å | 8.6284(5) |
| $c$/Å | 8.9514(6) |
| $\alpha$/° | 72.348(2) |
| $\beta$/° | 86.348(2) |
| $\gamma$/° | 82.898(2) |
| $V$/Å$^3$ | 526.22(6) |
| $Z$ | 1 |
| $\mu$/mm$^{-1}$ | 1.34 |
| Data collection method | $\omega/2\theta$ |
| No. of measured, independent and observed reflections | 7845, 5701, 4199 |
| Criterion for observed reflections | $I > 2.0\sigma(I)$ |
| $R_{int}$ | 0.027 |
| Refinement on | $F^2$ |
| $R[F^2 > 2\sigma(F^2)]$, $wR(F^2)$, $S$ | 0.037, 0.076, 0.42 |
| No. of parameters | 148 |

The crystal structure of PCP-PZ (Figure 7.11) was solved from the data collected at 120 K. The molecules in this compound form trimers, in the triclinic space group $P\bar{1}$ with the unit cell parameters as given in Table 7.4. The components, found in a 2:1 ratio of PCP:PZ, are joined by two N⋯H–O hydrogen bonds, parallel to the $b$ axis, with donor-acceptor distances of 2.691(3) Å; no significant interactions exist between the trimers. In each N⋯H–O hydrogen bond the hydrogen atoms are found located in an asymmetric position closer to the oxygen atoms of pentachlorophenol, while the nitrogen atoms of pyrazine act as the hydrogen acceptors. Additionally, the C–O bond lengths and unprotonated pyrazine C–N–C angles, of 1.340(2) Å and 116.47(18)°,

respectively, conform to the average values of 1.32 Å (Figure 3.12) and 116°, providing further evidence for an ordered O–H⋯N hydrogen bond.[8]
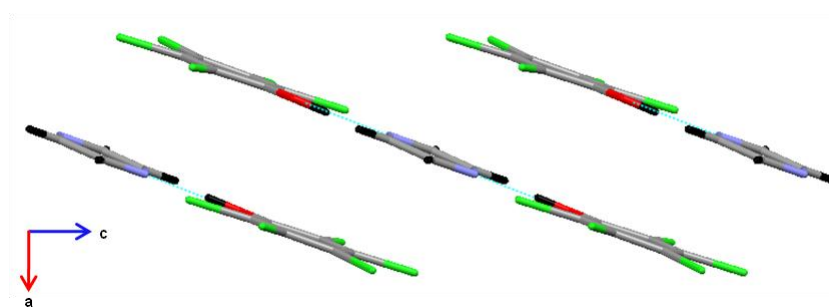
120 K
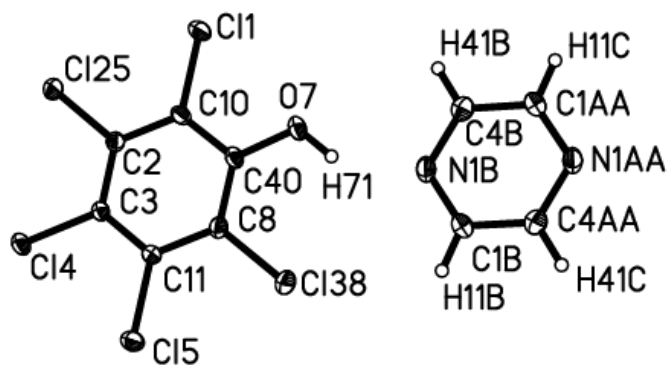


(a)
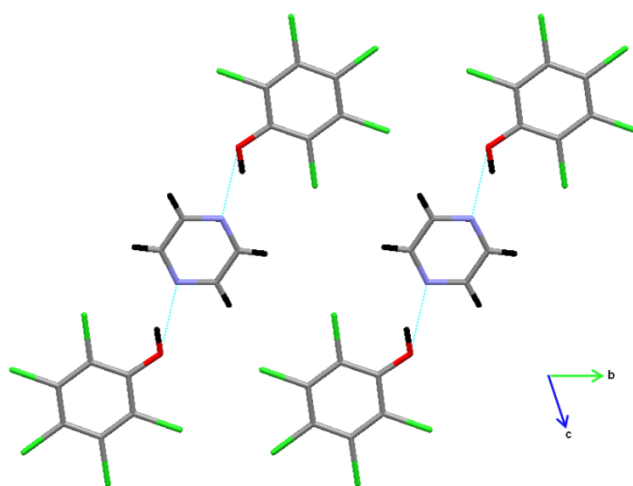


(b)



(c)

*Figure 7.11: (a) The molecular structure of PCP-PZ at 120 K, obtained using single crystal XRD (ADPs are plotted at the 50 % probability level), (b) The molecular*

*packing in PCP-PZ at 120 K, as viewed down the a axis and c) The molecular packing in PCP-PZ at 120 K, as viewed down the b axis.*

The N···O separation of 2.691 Å is relatively long, particularly when compared to the MP-PCP molecule with an N···O separation of 2.519 Å at 125 K;[1] however, it is similar in length to the normal hydrogen bond in $H_2$ca-Phz (discussed above) and is therefore potentially interesting.[9] In addition, the N–H–O angle of 149.04(15)° is much smaller than that of MP-PCP at 125 K (169.59°).[1] Although this angle in PCP-PZ is from an XRD study only, due to the fact that the C–O–H angle of pentachlorophenol (115(2)°) is similar to that of pentachlorophenol in the structure of MP-PCP (121.61°),[1] determined from neutron diffraction data, it seems that the proton position has been well determined.

The presence of a second nitrogen atom in PZ in place of the methyl group on MP leads to the bonding of a further PCP group and hence the formation of a trimer. A large difference between the geometries of MP-PCP and PCP-PZ, which may account for the observed differences in N–H–O angle and N···O separation, is the extent of planarity. In PCP-PZ the bulky pentachlorophenol groups lie flat, creating an almost entirely planar system, Figure 7.11c. As described previously, in the MP-PCP dimer, the pentachlorophenol component is twisted out of the plane and bent, Figure 7.7b, allowing for the formation of a very short hydrogen bond.

Attempts to study PCP-PZ using powder XRD showed that the polycrystalline samples were contaminated with the starting reagents and a further impurity, the identity of which could not established. Consequently, VT data were not collected. Furthermore, a number of larger crystals were also screened by neutron diffraction using VIVALDI at the ILL.[3] However, it was found that these larger crystals were not of sufficient crystallinity throughout, leading to very poor diffraction, and therefore a full single crystal neutron diffraction data collection was not carried out.

## 7.3  4-Methylpyridine-Tetrachlorohydroquinone

The final MP-PCP analogue for which the synthesis has been attempted is that of 4-methylpyridine-tetrachlorohydroquinone (MP-TCHQ), containing the components shown in Figure 7.12.
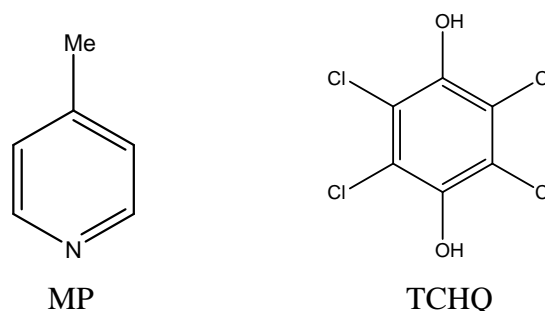


*Figure 7.12: The components of the 4-methylpyridine-tetrahydroquinone co-crystal.*

### 7.3.1  Experimental

Following an initial solubility screen with a range of solvents, the synthesis of a co-crystal of 4-methylpyridine-tetrachlorohydroquinone (MP-TCHQ) was attempted. The starting reagent, tetrachlorohydroquinone (0.050 g, 0.2 mmol, Acros Organics, 99 %), was dissolved in a minimum amount of ethanol. The liquid reagent, 4-methylpyridine (0.0375 g, 0.4 mmol, Aldrich, 99 %), was then added to this solution. Finally, this was sealed with a plastic cap containing four small apertures. The synthesis was repeated using methanol as the solvent; however, both methods have failed to produce crystals of MP-TCHQ to date, resulting only in an impure, poorly crystalline, powder material.

## 7.4  Conclusions

Two new materials (TCHQ-PZ and PCP-PZ), related to the temperature-dependent proton migration compound MP-PCP in terms of components, have been successfully synthesised, and their structures determined using single crystal XRD. In both cases, medium-length hydrogen bonds form between the donor and acceptor groups, similar in length to those in the ferroelectric anilic acid-phenazine compounds, and in contrast to

MP-PCP which contains one of the shortest N⋯H⋯O bonds reported in the literature. Attempts to synthesise a further compound, MP-TCHQ, remain unsuccessful to date.

PCP-PZ has $P\bar{1}$ symmetry and forms trimers which are arranged in a planar fashion. These trimers consist of PZ molecules which form N⋯H–O hydrogen bonds to two adjacent PCP molecules. TCHQ-PZ, however, has been shown to crystallise in $C2/m$, with chains of alternating TCHQ and PZ molecules, running perpendicular to the $b$ axis, bound by an N⋯H–O hydrogen bond. In addition, TCHQ-PZ undergoes a phase transition to $P2_1/a$ symmetry, between 120 and 30 K, as a result of slight rotations of the TCHQ and PZ components.

TCHQ-PZ has been further studied by variable temperature neutron diffraction at 30, 120 and 300 K. While a very small amount of proton migration has been observed, between 120 and 300 K, this is likely to be a result of overall changes in the hydrogen bond. No further migration has been found to occur between 120 and 30 K, though any changes occurring in this bond as a result of the temperature change are thought to be remnants of the structural changes taking place. To date, the exact temperature at which the phase transition occurs has not been established.

Recent literature suggests that a SSHB is not a necessary condition for proton migration, with a number of compounds seemingly exhibiting such a migration despite containing medium-length hydrogen bonds.[11, 12] However these medium-length hydrogen bond compounds do possess other structural factors which may assist this migration. INH-PAS, for example, has a polar electronic environment allowing a stronger attraction between the proton and the acceptor atom, and $H_2$ca-Phz, another example, has a multi-centre hydrogen bond, providing a further donor atom to facilitate proton displacement. In the case of the medium-length compounds discussed in this chapter, a lack of proton migration may be explained by the absence of such a supportive environment, or simply due to the longer donor-acceptor distances observed. In addition to the study of more compounds with medium-length bond distances, compounds with a variety of environments, thought to aid proton migration, should also be investigated.

## 7.5  References

1.  T. Steiner, I. Majerz and C. C. Wilson, *Angew. Chem. Int. Ed.*, 2001, **40**, 2651.
2.  P. W. Betteridge, J. R. Carruthers, R. I. Cooper, K. Prout and D. J. Watkin, *J. Appl. Crystallogr.*, 2003, **36**, 1487.
3.  C. J. Wilkinson, J. A. Cowan, D. A. A. Myles, F. Cipriani and G. J. McIntyre, *Neutron News*, 2002, **13**, 37.
4.  J. W. Campbell, J. Habash, J. R. Helliwell and K. Moffat, *Information Quarterly for Protein Crystallography, No. 18*, SERC, Daresbury Laboratory, Warrington, England, 1986.
5.  J. W. Campbell, Q. Hao, M. M. Harding, N. D. Nguti and C. J. Wilkinson, *J. Appl. Crystallogr.*, 1998, **31**, 23.
6.  C. J. Wilkinson, H. W. Khamis, R. F. D. Stansfield and G. J. McIntyre, *J. Appl. Crystallogr.*, 1988, **21**, 471.
7.  G. M. Sheldrick, *SHELXL* Bruker AXS Inc., University of Gottingen, Germany, 2000.
8.  M. Schmidtmann and C. C. Wilson, *Crystengcomm*, 2008, **10**, 177.
9.  S. Horiuchi, R. Kumai and Y. Tokura, *J. Am. Chem. Soc.*, 2005, **127**, 5010.
10. Z. Malarski, I. Majerz and T. Lis, *J. Mol. Struct.*, 1996, **380**, 249.
11. P. Grobelny, A. Mukherjee and G. R. Desiraju, *Crystengcomm*, 2011, **13**, 4358.
12. S. Horiuchi, R. Kumai and Y. Tokura, *J. Mater. Chem.*, 2009, **19**, 4421.

# 8 Overall Conclusions and Opportunities for Future Work

The work presented in this thesis has extended the study of hydrogen-bonded compounds at a fundamental level, focussing on the structure and dynamic behaviour of the protons therein. A range of experimental and computational methods have been employed in order to explore a number of chemical systems with short- and medium-length hydrogen bonds.

The structure and dynamics of 35PDCA have been investigated, using a combination of diffraction, spectroscopy, NMR and computational techniques, in order to understand changes in its phase transition, and the extent of the giant temperature-dependent proton migration, observed on full and selective deuteration. It has been demonstrated, using powder neutron diffraction, that in *d*-35PDCA, giant deuteron migration is driven by a non-classical first-order isosymmetric phase transition, which occurs *via* growth of domains of the pure high temperature species from the pure low temperature species. The partially deuterated compounds, *ring-d*-35PDCA and *acid-d*-35PDCA, show similar behaviour, although at slightly higher temperatures. DFT computational studies have shown that this phase transition is driven by vibrational free energy changes, where the stabilisation brought about by these is proportional to the degree of deuteration alone and is not affected by the position of the isotopic substitution.

Various spectroscopic techniques have been used in order to test a previous prediction of a two-site proton hopping model for 35PDCA.[1] In contrast to the gradual, continuous, temperature-dependent proton migration, from one side of the hydrogen bond to the other, determined by single crystal neutron diffraction for *h*-35PDCA and *d*-35PDCA, each of the isotopologues were found to be bistable; the proton being located in a position closer to the donor atom or a position closer to the acceptor atom, but never in a central position in the hydrogen bond. Two (or more) species, resulting from such proton migration were observed by IR, Raman and INS spectroscopy, in agreement with previous, and current, AIMD studies, and confirming the two-site model.

IR spectroscopy shows a pronounced migration in *d*-35PDCA (from a pure N–D···O species at low temperature to a pure N···D–O species at high temperature), occurring *via* a first-order phase transition accompanied by a small temperature range of phase co-existence, analogous to that observed by powder neutron diffraction. This is consistent with the domain model explanation for migration given using the diffraction data, the domains consisting of either the pure LT form or the pure HT form. For *acid-d*-35PDCA and *h*-35PDCA, evidence for the co-existence of the LT and HT species has been observed by Raman and INS spectroscopy and the temperature range for this co-existence has been shown to be greater than that of *d*-35PDCA. In addition, complete conversion between the pure N–H···O species and the pure N···H–O species occurs at a much higher temperature than in *d*-35PDCA. There is also evidence for possible disorder in these systems, from both Raman and INS spectroscopy. This disorder suggests that the proton migration behaviour in these isotopologues can be described by the AIMD domain model, in which a domain can be as small as a single molecule. This disorder cannot be resolved by diffraction, highlighting the limitation of diffraction in this case.

An NMR relaxometry experiment involving magnetic field-cycling techniques, performed by the Horsewill group at Nottingham University, reveals a non-zero dynamical rate at temperatures close to 0 K, providing evidence for the presence of a quantum tunnelling contribution to proton transfer in 35PDCA. Transition state calculations for the entire crystal, performed in this work, reveal the presence of a 2-well potential in the system which underpins the observation of tunnelling in the hydrogen bond. In addition, the proton hopping timescale predicted by various AIMD simulations was tested. Whilst NMR results reveal a dynamical rate on a nanosecond timescale, DFT AIMD calculations were found to over-estimate the dynamical rate, especially with VASP.

An activation energy (the energy required to form the N···H–O (HT) species from the N–H···O (LT) species for a single hydrogen bond) of 500 K was calculated from NMR data, AIMD dynamical rate calculations and vibrational spectroscopy, illustrating the reliability and consistency of all of the data obtained.

The role of low frequency lattice vibrations in proton migration in 35PDCA had previously been accounted for and explained.[1] In the current work, experimental evidence was provided in order to support this previous conclusion. In addition, a number of variable pressure experiments were undertaken during the course of this work in order to further understand this phenomenon by separating the effects of lattice expansion from the effects due to the activation of phonons in *d*-35PDCA. Whilst a single crystal neutron diffraction experiment was largely unsuccessful, a variable pressure powder neutron diffraction experiment was successfully performed. The results of this, at constant (room) temperature, suggest a potential phase transition, comparable to that observed at 150 K from various variable temperature diffraction experiments. In addition, transition state calculations for a single molecular sheet of 35PDCA show that it is the close proximity of the molecular sheets, caused by, for example, lowering the temperature of the system or increasing the pressure, that stabilises the LT zwitterionic form of the hydrogen bond. These, and the theoretical observation of the proton-transferred N–H$\cdots$O structure in the unit cell determined at 43 kbar, suggest that the proton-transferred structure may be obtained at higher pressures, meriting further investigation of this system as a function of pressure. In order to obtain reliable hydrogen bond distances and, hence, determine whether or not proton migration is occurring as a function of pressure, a further single crystal neutron diffraction experiment should be performed, possibly using a different method of obtaining pressure. For example, gas pressure cells, for which the exact accessible pressure is known, could be used. The disadvantage of this method is that only limited pressures are available. In addition, larger crystals could be grown in order to gain better neutron diffraction statistics.

A range of DFT calculations (geometry optimisation, molecular and lattice dynamics) have been used throughout this work in order to complement the experimental work. These calculations are all of limited accuracy due to the difficulty of using DFT to properly describe intermolecular forces, especially van der Waals forces (dispersion). Its incomplete treatment of dispersion can adversely affect the accuracy of DFT in the study of systems which are either dominated by dispersion or where dispersion competes significantly with other effects. As the *c* axis in 35PDCA is dominated by dispersion forces, the energy values resulting from these calculations may not be reliable. However, it is now be possible to add an improved correction for dispersion in

newer versions of Materials Studio and also in VASP, and therefore all of these calculations should be repeated at a higher level of accuracy in order to obtain more reliable values of energy.

A number of further SSHB systems, with the potential to exhibit interesting temperature-dependent proton migration and disorder effects, have also been identified and successfully synthesised; namely, 3,5-dinitrobenzoic acid-nicotinic acid (35DBNA), 4-aminobenzoic acid-nicotinic acid (4ABNA) and benzimidazolium hydrogen phenylmalonate (BHPM). It was found that the original published literature structures for these compounds were inaccurate, with protons located incorrectly.[2, 3] Subtle evidence for proton migration has been found in 35DBNA, although no significant migration through the hydrogen bond centre has been observed. 4ABNA exhibits a very short hydrogen bond of 2.48 Å at 300 K, and Fourier difference maps from XRD data show the existence of potential proton disorder. 4ABNA should, therefore, be further investigated using single crystal neutron diffraction in order to determine reliable hydrogen atom positions; future work should involve finding a method for growing crystals of a suitable size for this technique.

MD simulations were used in order to determine whether or not proton hopping behaviour can be calculated for 35DBNA and 4ABNA. In 35DBNA, these simulations show proton hopping over the hydrogen bond which increases with temperature; however for 4ABNA, no proton hopping behaviour was calculated, possibly as a result of the over-estimation of its donor-acceptor distance. It seems that such a calculation may be used as an initial screen of proton migration in order to determine whether or not temperature-dependent proton migration might be exhibited experimentally. However, these calculations are highly dependent on the structure resulting from a geometry optimisation calculation and have been found to be unsuccessful in certain cases where proton migration is in fact exhibited experimentally (particularly in systems where no long range interactions are present).[1] The possibility of adding an improved correction for dispersion in newer versions of Materials Studio should reduce such problems in geometry optimisation in the future and allow more wide-spread use of this MD method in the prediction of proton migration.

Finally, the synthesis and characterisation of two new compounds, tetrachlorohydroquinone-pyrazine (TCHQ-PZ) and pentachlorophenol-pyrazine (PCP-PZ), have been achieved; these materials are co-crystals, with their components based on those of the known SSHB and proton-migration material MP-PCP. Unlike MP-PCP, medium-length hydrogen bonds form in both TCHQ-PZ and PCP-PZ. A variable temperature neutron diffraction study on TCHQ-PZ showed that this compound does not exhibit a significant temperature-dependent proton migration. Although this phenomenon has been observed in compounds with hydrogen bonds of a similar length, for example, in $H_2$ca-Phz, it is thought that structural factors, such as a polar electronic environment or a multi-centre hydrogen bond, in these compounds aid/drive the proton migration.[4, 5] No such supportive environment is present in TCHQ-PZ, and this is a possible explanation for the absence of significant proton migration.

Although no new SSHB materials were found in this work, attempts at synthesising them, for example, by using reagents based on those of known SSHB systems, as described in this work, should be continued. In addition, the synthesis of new SSHB systems, using reagents with matching pKa's, could be attempted.

Whilst this work has focussed on a small number of systems, there are still many left to explore. Proton migration itself has only been observed in a limited number of small organic systems, predominantly in those containing SSHBs. However, the absence of significant proton migration in systems structurally similar to those in which it is observed, such as 35DBNA and 4ABNA, and its presence in compounds such as Phz-$H_2$ca, which contains a comparatively long hydrogen bond, suggests that SSHBs are neither a necessary nor a sufficient condition for this type of behaviour, and therefore other factors must be considered. In order to explore this, further systems, with a variety of hydrogen bond lengths, could be considered. Furthermore, very accurate methods for locating the electron density, such as charge density studies (experimental and theoretical), should be employed alongside this work, particularly when single crystal neutron diffraction is not possible, in order to provide insight into the interatomic interactions in the hydrogen bonds of these systems. These studies would allow the determination of the amount of covalency in the non-bonded H···Y bond (of a hydrogen bond of the form X–H···Y), and whether there is a relationship between this and any proton transfer.

In addition, this thesis has focussed on intermolecular hydrogen bonds. However, there are many hydrogen bond structures that possess intramolecular SSHBs. For example, 2-(2-(3-carboxypyridyl-4-isopropyl-4-methyl-5-oxo-imidazole (imazpyr), contains one of the shortest O–H⋯N hydrogen bonds reported in the literature, with a donor-acceptor, O⋯N, distance of 2.47 Å.[6] Whilst previous work using variable temperature single crystal X-ray diffraction suggests that proton migration occurs in this system, the use of variable temperature single crystal neutron diffraction would confirm and quantify this behaviour. This work could then be expanded to the study of further intramolecular hydrogen bond systems.

It has been found that two proton migration systems which have been successfully deuterated exhibit an interesting isotope effect; for example, 35PDCA and its associated isotopologues have been thoroughly studied in this thesis, and MP-PCP,[7] which has been found to undergo a drastic structural change involving a change of space group upon deuteration, has been studied elsewhere (see Chapter 1). The deuteration of other systems, such as urea-phosphoric acid (UPA) and benzene-1,2,4,5-tetracarboxylic acid-4,4'-bipyridyl (BTA-BPY) could be attempted in order to observe any such behaviour. The other systems described in this thesis, such as 35DBNA, 4ABNA, BHPM and TCHQ-PZ, as well as any new interesting intramolecular bonds, could also be deuterated in order to explore any possible differences between those systems which exhibit proton migration and those which do not.

Finally, in the long term there are many aspects of hydrogen bonding behaviour to be explored. In particular, hydrogen bonds play a significant role in many functional materials. For example, as mentioned previously, proton migration in hydrogen bonds is essential in certain ferroelectric materials. These are technologically important materials with potential future applications in electronics and optics. Known materials could be further explored by a combination of experimental and computational methods in order to fully understand the proton migration behaviour, which, in turn, may lead to the discovery of new, potentially exploitable systems.

One new aspect which could be explored is single component ferroelectrics. Recent work by Horiuchi *et al.*[8] has reported the first above room-temperature ferroelectricity in a single-component molecular crystal, croconic acid ($H_2C_5O_5$). The O⋯O

intermolecular hydrogen bonds in this material are medium in length (2.628(5) to 2.617(5) Å),[9] yet a proton switching behaviour, analogous to that in *d*-35PDCA, appears to be responsible for the ferroelectricity observed, further emphasising the lack of a necessity of a SSHB for such behaviour. Similar planar monocyclic $H_2C_nO_n$ systems are known, including squaric acid (n=4), an antiferroelectric material.[10] However, the solid state structure of rhodizonic acid (n=6) is still unknown.[11] This series of compounds could be further expanded, with initial focus on growing single crystals of rhodizonic acid, before attempting variable temperature single crystal neutron diffraction in order to observe any changes in the proton positions with temperature. The results of this study could be compared with those of the previous materials in this series in order to further determine the structural factors necessary for proton transfer and, ultimately, ferroelectric behaviour.

## 8.1  References

1.    F. Fontaine-Vive, M. R. Johnson, G. J. Kearley, J. A. Cowan, J. A. K. Howard and S. F. Parker, *J. Chem. Phys.*, 2006, **124**, 234503.
2.    S. R. Jebas and T. Balasubramanian, *Acta Crystallogr., Sect. E*, 2006, **62**, O5621.
3.    J. Zhu and J. M. Zheng, *Chin. J. Struct. Chem.*, 2004, **23**, 417.
4.    P. Grobelny, A. Mukherjee and G. R. Desiraju, *Crystengcomm*, 2011, **13**, 4358.
5.    S. Horiuchi, R. Kumai and Y. Tokura, *J. Am. Chem. Soc.*, 2005, **127**, 5010.
6.    P. Camilleri, C. A. Marby, B. Odell, H. S. Rzepa, R. N. Sheppard, J. J. P. Stewart and D. J. Williams, *Chem. Commun.*, 1989, 1722.
7.    Z. Malarski, I. Majerz and T. Lis, *J. Mol. Struct.*, 1996, **380**, 249.
8.    S. Horiuchi, Y. Tokunaga, G. Giovannetti, S. Picozzi, H. Itoh, R. Shimano, R. Kumai and Y. Tokura, *Nature*, 2010, **463**, 789.
9.    D. Braga, L. Maini and F. Grepioni, *Crystengcomm*, 2001, **3**, 27.
10.   D. Semmingsen, F. J. Hollander and T. F. Koetzle, *J. Chem. Phys.*, 1977, **66**, 4405.
11.   D. Braga, G. Cojazzi, L. Maini and F. Grepioni, *New J. Chem.*, 2001, **25**, 1221.